Defense Threat Reduction Agency
8725 John J. Kingman Road, MS
6201 Fort Belvoir, VA 22060-6201

DTRA-TR-16-37

TECHNICAL REPORT

Compendium of Photofission Signatures

Distribution Statement A. Approved for public release, distribution is unlimited.

August 2018

HDTRA1-08-1-0019

Dr. Alan W. Hunt

Prepared by:
Idaho State University
921 S. 8th Avenue
Pocatello, ID 83209

DESTRUCTION NOTICE:

Destroy this report when it is no longer needed.
Do not return to sender.

PLEASE NOTIFY THE DEFENSE THREAT REDUCTION AGENCY, ATTN: DTRIAC/ RD-NTF, 8725 JOHN J. KINGMAN ROAD, MS-6201, FT BELVOIR, VA 22060-6201, IF YOUR ADDRESS IS INCORRECT, IF YOU WISH IT DELETED FROM THE DISTRIBUTION LIST, OR IF THE ADDRESSEE IS NO LONGER EMPLOYED BY YOUR ORGANIZATION.

REPORT DOCUMENTATION PAGE

Form Approved
OMB No. 0704-0188

Public reporting burden for this collection of information is estimated to average 1 hour per response, including the time for reviewing instructions, searching existing data sources, gathering and maintaining the data needed, and completing and reviewing this collection of information. Send comments regarding this burden estimate or any other aspect of this collection of information, including suggestions for reducing this burden to Department of Defense, Washington Headquarters Services, Directorate for Information Operations and Reports (0704-0188), 1215 Jefferson Davis Highway, Suite 1204, Arlington, VA 22202-4302. Respondents should be aware that notwithstanding any other provision of law, no person shall be subject to any penalty for failing to comply with a collection of information if it does not display a currently valid OMB control number. **PLEASE DO NOT RETURN YOUR FORM TO THE ABOVE ADDRESS.**

1. REPORT DATE *(DD-MM-YYYY)*
00-08-2018

2. REPORT TYPE
Technical

3. DATES COVERED *(From - To)*
May 5, 2008 - July 4, 2014

4. TITLE AND SUBTITLE
Compendium of Photofission Signatures

5a. CONTRACT NUMBER

5b. GRANT NUMBER
HDTRA1-08-1-0019

5c. PROGRAM ELEMENT NUMBER

6. AUTHOR(S)
Dr. Alan W. Hunt, Dr. Mathew T. Kinlaw, Dr. Brandon Blackburn, Heather A. Seipel, Edward T. E. Reedy, Edna S. Cardenas, and Bruce H. Failor

5d. PROJECT NUMBER

5e. TASK NUMBER

5f. WORK UNIT NUMBER

7. PERFORMING ORGANIZATION NAME(S) AND ADDRESS(ES)
Idaho State University
921 S. 8th Avenue
Pocatello, ID 83209

8. PERFORMING ORGANIZATION REPORT NUMBER

9. SPONSORING / MONITORING AGENCY NAME(S) AND ADDRESS(ES)
Defense Threat Reduction Agency
8725 John J. Kingman Road, STOP 6201
Fort Belvoir, VA 22060-6201

10. SPONSOR/MONITOR'S ACRONYM(S)
DTRA

11. SPONSOR/MONITOR'S REPORT NUMBER(S)
DTRA-TR-16-37

12. DISTRIBUTION / AVAILABILITY STATEMENT
Distribution Statement A. Approved for public release, distribution is unlimited.

13. SUPPLEMENTARY NOTES

14. ABSTRACT

The capability to rapidly and accurately detect and attribute nuclear materials is essential for any national strategy to combat and deter the use of nuclear or radiological weapons. Unfortunately, nondestructive detection and quantification of fissionable materials in challenging national security settings is difficult. This difficulty stems in part from the large phase space of potential fissionable material signatures and the lack of a single signature that will be effective in all scenarios. Hence the research team executed a basic research program to increase the basic knowledge of how to utilize fission signals from bremsstrahlung induced fission for the detection of fissionable materials. The research began by examining the time and energy spectra of delayed neutron and y-ray spectra in order to develop unique fission signatures.

15. SUBJECT TERMS
fission signals, bremsstrahlung, radiological dispersal devices, fissionable materials

16. SECURITY CLASSIFICATION OF:			**17. LIMITATION OF ABSTRACT**	**18. NUMBER OF PAGES**	**19a. NAME OF RESPONSIBLE PERSON**
					Allen Dalton
a. REPORT	**b. ABSTRACT**	**c. THIS PAGE**	SAR	326	**19b. TELEPHONE NUMBER** *(include area code)*
Unclassified	Unclassified	Unclassified			(571) 616-6579

Standard Form 298 (Rev. 8-98)
Prescribed by ANSI Std. Z39.18

UNIT CONVERSION TABLE

U.S. customary units to and from international units of measurement*

U.S. Customary Units	Multiply by → / ← Divide by†		International Units
Length/Area/Volume			
inch (in)	2.54	$\times 10^{-2}$	meter (m)
foot (ft)	3.048	$\times 10^{-1}$	meter (m)
yard (yd)	9.144	$\times 10^{-1}$	meter (m)
mile (mi, international)	1.609 344	$\times 10^{3}$	meter (m)
mile (nmi, nautical, U.S.)	1.852	$\times 10^{3}$	meter (m)
barn (b)	1	$\times 10^{-28}$	square meter (m^2)
gallon (gal, U.S. liquid)	3.785 412	$\times 10^{-3}$	cubic meter (m^3)
cubic foot (ft^3)	2.831 685	$\times 10^{-2}$	cubic meter (m^3)
Mass/Density			
pound (lb)	4.535 924	$\times 10^{-1}$	kilogram (kg)
unified atomic mass unit (amu)	1.660 539	$\times 10^{-27}$	kilogram (kg)
pound-mass per cubic foot (lb ft^{-3})	1.601 846	$\times 10^{1}$	kilogram per cubic meter (kg m^{-3})
pound-force (lbf avoirdupois)	4.448 222		newton (N)
Energy/Work/Power			
electron volt (eV)	1.602 177	$\times 10^{-19}$	joule (J)
erg	1	$\times 10^{-7}$	joule (J)
kiloton (kt) (TNT equivalent)	4.184	$\times 10^{12}$	joule (J)
British thermal unit (Btu) (thermochemical)	1.054 350	$\times 10^{3}$	joule (J)
foot-pound-force (ft lbf)	1.355 818		joule (J)
calorie (cal) (thermochemical)	4.184		joule (J)
Pressure			
atmosphere (atm)	1.013 250	$\times 10^{5}$	pascal (Pa)
pound force per square inch (psi)	6.984 757	$\times 10^{3}$	pascal (Pa)
Temperature			
degree Fahrenheit (^oF)	$[T(^oF) - 32]/1.8$		degree Celsius (^oC)
degree Fahrenheit (^oF)	$[T(^oF) + 459.67]/1.8$		kelvin (K)
Radiation			
curie (Ci) [activity of radionuclides]	3.7	$\times 10^{10}$	per second (s^{-1}) [becquerel (Bq)]
roentgen (R) [air exposure]	2.579 760	$\times 10^{-4}$	coulomb per kilogram (C kg^{-1})
rad [absorbed dose]	1	$\times 10^{-2}$	joule per kilogram (J kg^{-1}) [gray (Gy)]
rem [equivalent and effective dose]	1	$\times 10^{-2}$	joule per kilogram (J kg^{-1}) [sievert (Sv)]

*Specific details regarding the implementation of SI units may be viewed at http://www.bipm.org/en/si/.

†Multiply the U.S. customary unit by the factor to get the international unit. Divide the international unit by the factor to get the U.S. customary unit.

Abstract

The capability to rapidly and accurately detect and attribute nuclear materials is essential for any national strategy to combat and deter the use of nuclear or radiological weapons. Unfortunately, nondestructive detection and quantification of fissionable materials in challenging national security settings is difficult. This difficulty stems in part from the large phase space of potential fissionable material signatures and the lack of a single signature that will be effective in all scenarios. Hence the research team executed a basic research program to increase the basic knowledge of how to utilize fission signals from bremsstrahlung induced fission for the detection of fissionable materials. The research began by examining the time and energy spectra of delayed neutron and γ-ray spectra in order to develop unique fission signatures. In order to compare the efficacy of these two signals, the detection limits were calculated and compared for bare ^{232}Th and ^{238}U targets. These signal were also combined to exploit correlated signals "islands" for use in fissionable material detection. In addition, the maximum interrogating bremsstrahlung endpoint energy was raised to over ~ 40 MeV to investigate fission signal interferences from non-fissionable materials.

Contents

1 Introduction **3**
1.1 Yields: What Is Actually Measured? 5
1.2 Critical Decision Level 6
1.3 Minimal Detectable Level and Mass 10
1.4 Extending the Critical Decision Level to a Multidimensional Signal Phase Space 14
1.5 Extending the Minimal Detectable Level to a Multidimensional Signal Phase Space 22

2 Delayed Neutrons **29**
2.1 Introduction and Experimental Setup 29
2.2 Aqueous Solutions 31
2.2.1 Yields and Minimal Detectable Masses 31
2.2.2 Specificity Techniques 35
2.3 SiO_2 Matrix 39
2.4 Delivered Dose and Beam Profile 43

3 Delayed γ-rays **45**
3.1 Introduction and Experimental Setup 45
3.2 Identification of the Photofission Signature 46
3.3 Minimal Detectable Mass of the 3 MeV Delayed γ-ray Signature 50
3.4 Using Discrete Delayed γ-rays for Isotopic Ratio Comparison 51
3.5 Prediction of Discrete Delayed γ-rays from ^{238}U and ^{232}Th 53
3.6 Delivered Dose and Beam Profile 55

4 Comparing Fission Signatures from Delayed γ-ray and Neutron Emissions **57**
4.1 Introduction and Experimental Setup 57
4.2 Energy and Time Spectra for Fission Signals 59
4.3 Total Fission Signal Yields 62
4.4 Detection Limits for Fissionable Materials 64
4.5 Two Dimensional Joint Yields 66

5 Fission Signal Interferences at Higher Bremsstrahlung Energies **70**
5.1 Introduction . . . 70
5.2 Interfering Reaction List/Database . . . 71
5.3 High-Energy Gross Interference Experiments . . . 79
5.4 Bremsstrahlung Weighted Integral Cross Sections . . . 88

6 Modeling Fission Signal Interferences **96**
6.1 Introduction . . . 96
6.2 Table Physics . . . 97
6.2.1 ^{9}Be(γ,p)^{8}Li . . . 97
6.2.2 ^{18}O(γ,np)^{16}N . . . 98
6.2.3 ^{19}F(γ,2pn)^{16}N . . . 98
6.2.4 ^{35}Cl(γ,n)^{34m}Cl . . . 99
6.2.5 ^{40}Ca(γ,np)^{38m}K . . . 99
6.3 CEM Physics . . . 100
6.4 Simulating a Representative Data Set . . . 103

A Targets **110**
A.1 Aqueous Solutions . . . 110
A.2 SiO_2Mixtures . . . 113

B A M.S. Thesis by Edward T. E. Reedy **116**

C A M.S. Thesis by Edna S. Cardenas **117**

Chapter 1

Introduction

Over the last decade, bremsstrahlung based techniques have been developed for the nondestructive detection, identification and quantification of concealed fissionable materials by the authors and other researchers[1–13]. The impetus for much of this recent research has been the needs of the Department of Defense, Department of Homeland Security and the Department of Energy to prevent the utilization of fissionable materials in nuclear weapons or radiological dispersal devices[14–17]. The bremsstrahlung beams used in these techniques are produced when energetic electrons from an accelerator impinge on a high-Z radiator. These high-energy photon beams are highly penetrating and forward directed, making them ideally suited for applications that require spatial resolution and standoff capabilities. In contrast, neutron sources, which can also be used for the nondestructive detection of fissionable materials, emit neutrons almost isotropically, making spatial resolution and standoff capabilities more difficult.

As the high-energy bremsstrahlung photons interact with materials containing fissionable isotopes, photofission reactions are induced, releasing on average 200 MeV of energy per fission reaction[18, 19]. The majority of this energy is in the kinetic energy of the fission fragments, which cannot be directly detected at any substantial distance. However, as these highly excited fission fragment decay they emit the following secondary radiation:

- **Prompt neutrons**
  - Yield: 2 to 3 per fission.
  - Timescale: 10^{-14} s.
- **Prompt γ-rays**
  - Yield: 7 per fission.
  - Timescale: 10^{-14} s.

- **Delayed neutrons**
  - Yield: 0.4%–5% of fissions.
  - Timescale: 100 ms to 55.6 s.
- **Delayed γ-rays**
  - Yield: 7 per fission.
  - Timescale: 100 ms to years.

These four emissions can be detected and form the basis for most of the active inspection techniques that have been studied and utilized for detecting fissionable materials. However, virtually every material can emit neutrons and γ-rays from photonuclear reactions other than fission (e.g. ^{A}Z(γ,n)$^{A-1}$Z). Consequently, any active inspection technique based on detecting these emissions must create a unique fissionable material signature from the distinctive characteristics of fission neutrons and/or γ-rays.

In this project, the research team studied how the emitted energy spectra, time-histories and particle yields performed as fissionable material signatures. A set of fission signatures for delayed neutrons and delayed γ-rays were identified and are detailed in Chapters 2 and 3. In addition, these signatures were combined into a multidimensional phase space to exploit signature "islands" for use in fissionable material forensic quantification. The fundamental questions answered by this research about these signatures and their combinations centered around experimentally determining:

- **Sensitivity**. What is the minimal detectable mass for the fissionable material?
- **Accuracy**. How accurately can the fissionable material be quantified?
- **Speed**. How quickly can the measurements be performed?
- **Specificity**. How well can different fissionable isotopes be identified?
- **Environment**. What are the effects of different operational environments?

A full and complete understanding of these SASSE properties is critical for the future development and deployment of any advanced fissionable material quantification technology. Furthermore, this data is relevant to the detection of concealed fissionable materials at standoff distances. In any application, compromises between the SASSE properties, spatial resolution and standoff distance will need to be made.

The main goal of many active inspection technologies is to detect concealed fissionable materials, thereby making the sensitivity of such systems the key question. The calculation and interpretation of this sensitivity is a little subtle and other requirements, such as the speed in which the inspection must be completed and dose limitations, heavily impact the overall sensitivity of the system. This has led many researchers and funding agencies

to define minimum inspection requirements that delineate the fissionable mass to be detected, maximum time, maximum dose, minimum probability of detection and maximum false alarm rate. While these requirements essentially dictate the required sensitivity of the active inspection system, the sensitivity can be better quantified by determining the minimal detectable mass for a given active inspection technique. The minimal detectable mass also provides a straightforward way to directly compare the efficacy of different fissionable material signatures. Throughout this compendium, the minimal detectable mass is the primary method used to evaluate different fissionable material signatures. Hence sections 1.1, 1.2 and 1.3 of this introduction chapter develop the framework for calculating the minimal detectable mass.

1.1 Yields: What Is Actually Measured?

The signals utilized for indicating the absence or presence of fissionable materials, all inevitably depend on tallying the number of neutrons and/or photons that are in the signature region of the data phase space. As an example, the delayed neutron signature consists of neutrons detected at long-times (e.g. $\sim$ 10 ms) after the inspection object has been interrogated by the probing neutron or photon beam. From the gross number of events in the signature region, C_g, the gross yield from a single inspection can then be calculated by

$$Y_g = \frac{C_g}{N_i}, \tag{1.1}$$

where N_i is an appropriate normalization for the inspection scenario. This normalization can be the inspection time, dose delivered, bremsstrahlung fluence, neutron fluence, electron charge on the bremsstrahlung radiator or some other logical normalization factor. Furthermore, detector solid angle, and detector efficiency can also be included in this normalization to allow easy comparisons between active inspection techniques and to easily estimate scaling up to larger inspection systems. Of course the normalization can be set to unity so that the gross yields are nothing more than the number of counts in the signature region.

The gross single inspection yield contains both the signal from fissionable isotopes in the inspection object, Y_s, and the total background, Y_{bk}, allowing it to be written as

$$Y_g = Y_s + Y_{bk}. \tag{1.2}$$

In the absence of fissionable isotopes, $Y_s \equiv 0$ and hence the gross yield is only caused by

the background, $Y_g = Y_{bk}$. This total background can have an active component, Y_{abk} and a passive component, Y_{pbk}, allowing equation 1.2 to be further expanded to

$$Y_g = Y_s + Y_{abk} + Y_{pbk}, \tag{1.3}$$

with $Y_{bk} = Y_{abk} + Y_{pbk}$. This distinction between active and passive components of the background becomes important when considering how these yields and their variances scale with the normalization. The normalization utilized in these yields is typically chosen so that the number of events from the fissionable isotopes is directly proportional, $C_s = Y_s N_i$. Similarly, the number of events from the active background is also proportional to the same normalization, $C_{abk} = Y_{abk} N_i$. Hence, the signal and active background yields are constants with respect to N_i. In contrast, the number of events in the signature region from the passive background is not directly proportional to the normalization and hence the passive background yield will not remain constant with respect to N_i. For example, the signal and active background events are directly proportional to the bremsstrahlung fluence, a measure of which makes an excellent normalization. The number of events from the passive background, however, is not directly proportional to the bremsstrahlung fluence but instead is directly proportional to the total detection time. Thus increasing the bremsstrahlung fluence, while keeping the total detection time constant, will cause the passive background yield to decrease.

1.2 Critical Decision Level

To make the determination that a fissionable material is "detected," the gross inspection yield must be significantly above the background. In contrast, a "not detected" determination is made when the gross inspection yield is below or not significantly above background. This comparison can be easily accomplished by subtracting the total background yield's limiting mean, $\Psi_{bk} = \langle Y_{bk} \rangle$, from the gross inspection yield to form a net inspection yield,

$$Y_n = Y_g - \Psi_{bk}. \tag{1.4}$$

This limiting mean of the total background yield, Ψ_{bk}, is determined from measurements of objects that contain no fissionable isotopes and measurements of the passive background. Presumably, these backgrounds can be measured with less uncertainty than the gross single inspection yield because the background measurements can include a large number of active

measurements and/or can be conducted over extended periods. A Greek letter is utilized to indicate that this total background is not necessarily from a single inspection. This convention of Roman letters representing quantities measured or inferred for a single inspection and Greek like letters representing quantities measured or inferred over extended periods is continued throughout this section. Keep in mind, when fissionable isotopes are not present in the inspection object, $\Psi_s = \langle Y_s \rangle \equiv 0$ and the net single inspection yield's limiting mean is inherently zero, $\Psi_n = \langle Y_n \rangle = 0$. Furthermore, when fissionable isotopes are present, $Y_s > 0$ and the net single inspection yield's limiting mean is $\Psi_n = \Psi_s$.

If a perfect measurement could be made without any errors, then $Y_n > 0$ would indicate that the signature is above background and hence the presence of fissionable materials. Of course, there are always at least counting statistic errors associated with any measurement because Y_n is at a minimum governed by the Poisson distribution. Thus, a critical decision level needs to be defined with $Y_n > L_c$ indicating a signal above background with some predefined confidence level. This critical decision level is chosen so that the probability of Y_n exceeding L_c is less than or equal to α when no fissionable isotopes are present. This definition can be expressed mathematically as

$$P\left(Y_n > L_c | \Psi_s \equiv 0\right) \leq \alpha, \tag{1.5}$$

where the inequality is used with distributions that have discrete α's (i.e. Poisson distribution). Hence, α is the false positive probability (i.e. the probability to incorrectly decide "detected" when no fissionable isotopes are present) and $1 - \alpha$ is the true negative probability (i.e. the probability to correctly decide "not detected" when no fissionable isotopes are present).

Assuming the number of events in the signature region is sufficiently large, the Poisson distribution, which describes the gross and background yields, is approximately Gaussian, leading to a Gaussian probability density for the net inspection yield. For an inspection without fissionable isotopes, Figure 1.1 illustrates this distribution, its relationship to the critical decision level, L_c, and the false positive probability α. The critical decision level for a given false positive probability can be found by solving for L_c in

$$\int_{L_c}^{\infty} \frac{1}{s_{no}\sqrt{2\pi}}\, e^{-\frac{{Y_n}^2}{2{s_{no}}^2}}\, \mathrm{d}Y_n = \alpha, \tag{1.6}$$

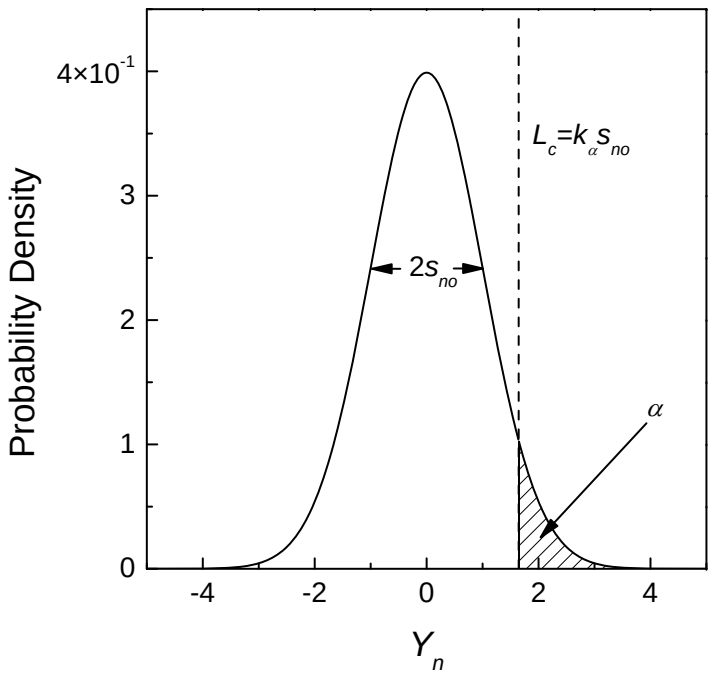

Figure 1.1: Representation of the net single inspection yield, Y_n, probability density when no fissionable isotopes are present. The critical decision level (dashed line), L_c, is shown for a false positive probability of α (cross hatched area). The standard deviation of the distribution, s_{no}, is also indicated.

where ${s_{no}}^2$ is the expected variance of the net single inspection yield without fissionable isotopes. The solution is quite readily found to be

$$L_c = k_\alpha s_{no}, \tag{1.7}$$

where k_α is the abscissas of the standard normal distribution with a cumulative probability of $1 - \alpha$. In more mathematical terms, k_α is given by

$$k_\alpha = \sqrt{2}\,\mathrm{erf}^{-1}\left(1 - 2\alpha\right). \tag{1.8}$$

Some care must be taken when choosing the false positive probability for a given inspection scenario; setting α too small will hurt the sensitivity and setting it too large will lead to an untenable false positive rate.

In the absence of fissionable materials, the expected variance of the net single inspection

yield is found from equation (1.4) to be

$$s_{no}{}^2 = s_{go}{}^2 + \sigma_{bk}{}^2, \tag{1.9}$$

where $s_{go}{}^2$ is the variance in the gross single inspection yield and $\sigma_{bk}{}^2$ is the variance in the limiting mean of the total background (i.e. the square of the error). While the limiting mean of the gross inspection yield equals the background yield without fissionable material (i.e. $\langle Y_{go} \rangle = \Psi_{bk}$), the variances are not necessarily equal. The expected variance of the gross inspection yield is

$$s_{go}{}^2 = \frac{\mathfrak{C}_{bk}}{N_i{}^2} = \frac{\mathfrak{C}_{abk} + \mathfrak{C}_{pbk}}{N_i{}^2} = \frac{\Psi_{abk} N_i + \mathfrak{C}_{pbk}}{N_i{}^2} = \frac{\Psi_{abk}}{N_i} + \frac{\mathfrak{C}_{pbk}}{N_i{}^2}, \tag{1.10}$$

and only depends on the background because there are no fissionable isotopes. Here $\mathfrak{C}_{bk}$, $\mathfrak{C}_{abk}$ and $\mathfrak{C}_{pbk}$ are the limiting means of the number of expected single inspection events in the signature region from the total, active and passive backgrounds, respectively (i.e. the centroids of the various background distributions). The total background is split into its active and passive components to explicitly delineate the expected scaling for the active background with respect to the inspection normalization, N_i. The full scaling for the passive background, $\mathfrak{C}_{pbk}$ with respect to the inspection parameters is not presented explicitly and needs to be determined for the inspection scenario. However, a truly passive background will scale as $\mathfrak{C}_{pbk} \propto \mathfrak{R}_{pbk} T_{di}$, where $\mathfrak{R}_{pbk}$ is the passive background rate in the signature region and T_{di} is the total detection time of the inspection. The critical decision level is then,

$$L_c = k_\alpha \sqrt{\frac{\Psi_{abk}}{N_i} + \frac{\mathfrak{C}_{pbk}}{N_i{}^2} + \sigma_{abk}{}^2 + \left(\frac{\Delta \mathfrak{C}_{pbk}}{N_i}\right)^2}, \tag{1.11}$$

where $\sigma_{abk}{}^2$ is the variance in the limiting mean of the active background (i.e. the square of the error) and $\Delta \mathfrak{C}_{pbk}{}^2$ is the variance in the limiting mean of the expected number of events in the signature region from the passive background. The first two terms in the square root are from the fluctuations in the gross single inspection yield and the second two terms are from subtracting the backgrounds. For a given false positive probability, α, the critical decision level is solely determined by the backgrounds and how well the backgrounds are known.

There are two limiting cases that are often discussed in the literature. The first limiting case is for paired measurements, where a known object without fissionable material is

measured under identical conditions as the unknown object and ${\sigma_{bk}}^2 = {s_{go}}^2$, leading to

$$L_c = k_\alpha \sqrt{2\left(\frac{\Psi_{abk}}{N_i} + \frac{\mathfrak{C}_{pbk}}{{N_i}^2}\right)}. \tag{1.12}$$

The second limiting case is for a well-known background, where the variance in the total background, ${\sigma_{bk}}^2$, is negligible compared to the variance in the gross inspection yield, ${s_{go}}^2$, leading to

$$L_c = k_\alpha \sqrt{\frac{\Psi_{abk}}{N_i} + \frac{\mathfrak{C}_{pbk}}{{N_i}^2}}. \tag{1.13}$$

Operationally, the appropriate critical decision level can be calculated quickly and compared to a measured net inspection yield from an unknown object to make a decision of "detected" or "not detected."

1.3 Minimal Detectable Level and Mass

While the critical decision level is used to make a posteriori decision of "detected" or "not detected," the minimal detectable level or mass is an a priori estimate of the detection capabilities of an active inspection system or technique. Adding fissionable material to the object under inspection, increases the limiting mean of the net inspection yield, $\Psi_n = \Psi_s$. This increases the probability that the observed net yield, Y_n, from a single inspection will be above the critical decision level, L_c, thereby correctly deciding "detected." The minimal detectable level, L_d, is defined as the required limiting mean, Ψ_n, so that the false negative probability is β for a given critical decision level, L_c. This definition can be expressed mathematically as

$$P\left(Y_n > L_c | \Psi_n = L_d\right) = \beta. \tag{1.14}$$

To be explicit, β is the the probability to incorrectly decide "not detected" when $\Psi_n = L_d$ (i.e. the false negative probability) and $1-\beta$ is the probability to correctly decide "detected" when $\Psi_n = L_d$ (i.e. the true positive probability).

Assuming the number of events in the signature region is sufficiently large, the Poisson distributions can again be approximated by Gaussian probability densities for the net inspection yield. For an inspection with enough fissionable material to exactly produce $\Psi_n = L_d$, Figure 1.2 illustrates the Y_n distribution and its relationship to the critical decision level, L_c, the false negative probability β, the Y_n distribution when no fissionable isotopes are present

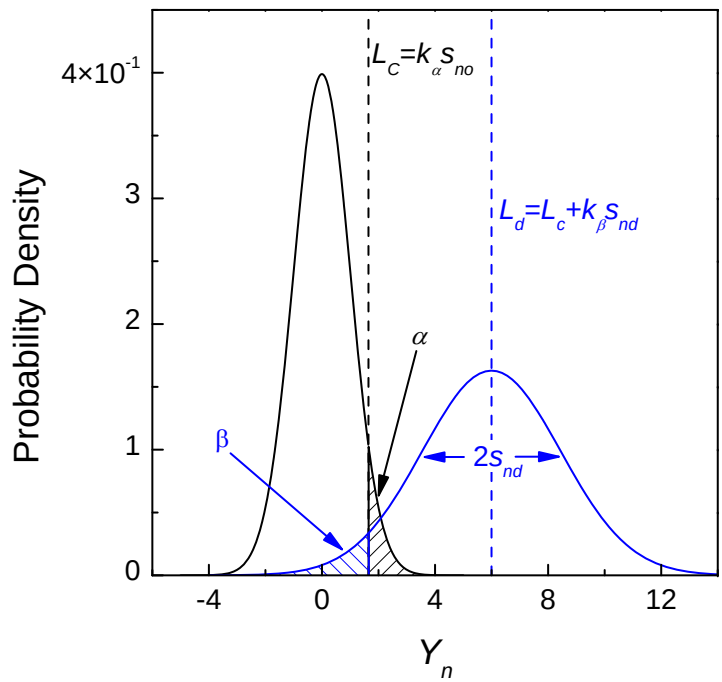

Figure 1.2: Representation of the net single inspection yield, Y_n, probability density (blue solid line) when there are enough fissionable isotopes present so that limiting mean of the net single inspection yield is equal to the minimal detectable level, $\Psi_n = \langle Y_n \rangle = L_d$. This distribution is compared to the net single inspection yield probability density when no fissionable isotopes are present (solid black line). The minimal detectable level (dashed blue line), L_d, is shown for a false negative probability of β (blue cross hatched area) along with the critical decision level (dashed black line), L_c, for a false positive probability of α (black cross hatched area). The standard deviation of the distribution, s_{nd}, is also indicated, when $\Psi_n = L_d$

and the false positive probability α. The minimal detectable level for a given false negative probability and critical decision level can be found by solving for L_d in

$$\int_{-\infty}^{L_c} \frac{1}{s_{nd}\sqrt{2\pi}}\, e^{-\frac{(Y_n - L_d)^2}{2{s_{nd}}^2}}\, \mathrm{d}Y_n = \beta, \tag{1.15}$$

where ${s_{nd}}^2$ is the expected variance when $\Psi_n = L_d$. The solution is found to be

$$L_d = L_c + k_\beta s_{nd}, \tag{1.16}$$

where k_β is the abscissas of the standard normal distribution with a cumulative probability of $1-\beta$. Again in more mathematical terms, k_β is given by

$$k_\beta = \sqrt{2}\,\mathrm{erf}^{-1}\left(1-2\beta\right). \tag{1.17}$$

The probability of $1-\beta$ is of course the true positive probability (i.e. the probability to correctly decide "detected" when fissionable isotopes are present).

When there is enough fissionable materials so that $\Psi_n = L_d$, the variance of the net inspection yield is found from equation (1.4) to be

$${s_{nd}}^2 = {s_{gd}}^2 + {\sigma_{bk}}^2, \tag{1.18}$$

where ${s_{gd}}^2$ is the variances in the gross single inspection yield with the presence of enough fissionable isotopes so that $\Psi_n = L_d$. Following the steps outlined in section 1.2, this expected variance can be expressed as

$${s_{gd}}^2 = \frac{\mathfrak{C}_{gd}}{{N_h}^2} = \frac{\mathfrak{C}_{nd}+\mathfrak{C}_{bk}}{N_h^2} = \frac{L_d N_h + \Psi_{abk} N_h + \mathfrak{C}_{pbk}}{{N_h}^2} = \frac{L_d}{N_h} + \frac{\Psi_{abk}}{N_h} + \frac{\mathfrak{C}_{pbk}}{{N_h}^2}, \tag{1.19}$$

where $\mathfrak{C}_{gd}$ and $\mathfrak{C}_{nd}$ are the limiting means of the gross and net single inspection events respectively. The variance in the net inspection yield is then

$${s_{nd}}^2 = \frac{L_d}{N_h} + \frac{\Psi_{abk}}{N_h} + \frac{\mathfrak{C}_{pbk}}{{N_h}^2} + {\sigma_{abk}}^2 + \left(\frac{\Delta\mathfrak{C}_{pbk}}{N_h}\right)^2. \tag{1.20}$$

Using the definition of the critical decision level in equation (1.11), the last four terms are nothing more than ${L_c}^2 \cdot {k_\alpha}^{-2}$ and the variance can be written as

$${s_{nd}}^2 = \frac{L_d}{N_h} + \frac{{L_c}^2}{{k_\alpha}^2}. \tag{1.21}$$

Substituting back into equation (1.16), the minimum detectable level is found by solving for L_d in

$$L_d = L_c + k_\beta\sqrt{\frac{L_d}{N_h} + \frac{{L_c}^2}{{k_\alpha}^2}}. \tag{1.22}$$

The larger root of this quadratic equation represents the minimum detectable level and is

given by

$$L_d = L_c + \frac{{k_\beta}^2}{2N_h} + {k_\beta}^2 \sqrt{\frac{1}{4{N_h}^2} + \frac{L_c}{{k_\beta}^2 N_h} + \frac{{L_c}^2}{{k_\alpha}^2 {k_\beta}^2}}. \tag{1.23}$$

Since the critical decision level is solely determined by the background yield and its variance for a given false positive probability, so to is the minimal detectable level. In the special case when $\alpha = \beta$, then $k_\alpha = k_\beta = k$ and equation (1.23) greatly simplifies to

$$L_d = \frac{k^2}{N_h} + 2L_c, \tag{1.24}$$

or substituting equation (1.11) in for L_c,

$$L_d = \frac{k^2}{N_h} + 2k \sqrt{\frac{\Psi_{abk}}{N_h} + \frac{\mathfrak{C}_{pbk}}{{N_h}^2} + {\sigma_{abk}}^2 + \left(\frac{\Delta\mathfrak{C}_{pbk}}{N_h}\right)^2}. \tag{1.25}$$

The minimal detectable levels are determined solely by backgrounds in the signature regions and do not consider the signal strength from the fissionable isotopes. Hence, these levels cannot be used to directly compare the fissionable material detection efficacy of one signature or inspection technique over another. The minimal detectable levels, however, can be related to the quantity of fissionable material required to generate a net yield of L_d. These minimal detectable masses (MDMs) provide an excellent way to directly compare efficacies. In general, the signal yield function relates the fissionable mass in the inspection object, m_f, to the limiting mean of the net inspection yield,

$$\Psi_n = \Psi_s \left(m_f, \dots\right). \tag{1.26}$$

This yield function, $\Psi_s \left(m_f, \dots\right)$, depends on all the parameters of the inspection such as photon fluence, fission cross sections, fission fragment yields, branching ratios, count periods, fissionable mass, detector efficiencies, attenuation of the probing beam, attenuation of the outgoing particles etc... In short, this can be a really complicated function for arbitrary inspection scenarios but one can imagine using Monte Carlo techniques to get a handle on it. For low mass targets, where the attenuation of the probing beam and outgoing particles in the target itself can be neglected, the net yield's limiting mean is directly proportional to the fissionable material mass

$$\Psi_n = \frac{\mathrm{d}\Psi_s}{\mathrm{d}m_f} \cdot m_f, \tag{1.27}$$

where $\mathrm{d}\Psi_s/\mathrm{d}m_f$ is the net yield per unit fissionable mass. The minimal detectable mass can then be easily found by setting $\Psi_n = L_d$ and solving for the mass

$$M_d = \left(\frac{\mathrm{d}\Psi_s}{\mathrm{d}m_f}\right)^{-1} \cdot L_d. \tag{1.28}$$

In essence, $\mathrm{d}\Psi_s/\mathrm{d}m_f$ can be thought of as a calibration constant for a fission signature or inspection system. This constant can be easily measured using low mass targets in which absorption is negligible.

1.4 Extending the Critical Decision Level to a Multidimensional Signal Phase Space

So far, the discussions of signatures, signals, critical decision levels, minimal detectable levels and minimal detectable masses have been limited to a single dimension in which a fission signal is treated independently of any other signals. During any inspection, multiple signals are produced and can be measured simultaneously. When the signals are treated independently, the minimum detectable masses discussed in Section 1.3 provide a methodology to impartially compare the fissionable material sensitivities from different fission signals. Furthermore, the simultaneous measurement of multiple fission signals opens up a multidimensional signal phase space in which the union of signals can be considered. These joint signals add considerable flexibility in choosing detection algorithms and make several advantages possible, including increased sensitivity, more robust shielding defeat, and minimization of interferences. While these advantages may not all be available concurrently they can be selected individually based on the requirements of a specific application.

The basic technique of making a decision that fissionable isotopes are "detected" or "not detected" in an inspection object does not fundamentally change with multiple fission signals. The goal is still to determine when the fission signal is significantly above the background, making the determination of "detected," or the signal is not significantly above the background, making the determination of "not detected." When multiple fission signals are considered jointly, the scalar yields in the previous sections become vectors in a

multidimensional signal phase space. Hence, the net single inspection yield becomes

$$\mathbf{Y_n} = \mathbf{Y_g} - \mathbf{\Psi_{bk}} = \begin{pmatrix} Y_{n_1} \\ Y_{n_2} \\ \vdots \\ Y_{n_j} \end{pmatrix} = \begin{pmatrix} Y_{g_1} - \Psi_{bk_1} \\ Y_{g_2} - \Psi_{bk_2} \\ \vdots \\ Y_{g_j} - \Psi_{bk_j}, \end{pmatrix} \tag{1.29}$$

where Y_{n_j}, Y_{g_j} and Ψ_{bk_j} are the appropriate scalar yields associated with the j'th signal. Because the net single inspection yield is now a vector, a critical decision surface, S_c, must be defined that divides the signal phase space into volumes for the decisions "detected" or "not detected." This critical decision surface is chosen so that the probability of a net single inspection yield, $\mathbf{Y_n}$, being outside the "not detected" volume, $V_{nd}\left(S_c\right)$, is less than or equal to α, when no fissionable isotopes are present. This definition can be expressed mathematically as

$$P\left(\mathbf{Y_n} \notin V_{nd}\left(S_c\right) | \Psi_s \equiv 0\right) \leq \alpha, \tag{1.30}$$

where the inequality is used with multivariate distributions that have discrete α's, like a multivariate Poisson distribution. Again, α is the false positive probability and $1-\alpha$ is the true negative probability.

As has been done previously, the number of detected events in each signal will be assumed large enough so that a multivariate Gaussian can be used to describe the probability density function for the net single inspection yield, $\mathbf{Y_n}$. Then equation (1.30) can be written as

$$\int\limits_{\mathbf{Y_n} \notin V_{nd}(S_c)} \frac{1}{\sqrt{\left(2\pi\right)^d \left|\mathbf{S_{no}}\right|}} e^{-\frac{1}{2}\mathbf{Y_n}^T \mathbf{S_{no}}^{-1} \mathbf{Y_n}} \, \mathrm{d}\mathbf{Y_n} = \alpha, \tag{1.31}$$

for a d–dimensional phase space. Here $\mathbf{S_{no}}$ is the expected variance-covariance matrix of the net single inspection yield without fissionable isotopes. If the Y_{n_j}'s are uncorrelated so that

$$\sigma\left(Y_{n_j}, Y_{n_l}\right) = \left\langle \left(Y_{n_j} - \left\langle Y_{n_j} \right\rangle\right)\left(Y_{n_l} - \left\langle Y_{n_l} \right\rangle\right) \right\rangle \Big|_{\mathbf{\Psi_n}=0} = \begin{cases} 0 & \text{if } l \neq j \\ {s_{no_j}}^2 & \text{if } l = j \end{cases}, \tag{1.32}$$

the multivariate Gaussian integrand can be simplified to

$$\int\limits_{\mathbf{Y_n} \notin V_{nd}(S_c)} \frac{1}{(2\pi)^{\frac{d}{2}} \prod\limits_{j=1}^{d} s_{no_j}} \prod_{j=1}^{d} \left(e^{-\frac{{Y_{n_j}}^2}{2{s_{no_j}}^2}} \right) \, \mathrm{d}\mathbf{Y_n} = \alpha, \tag{1.33}$$

where ${s_{no_j}}^2$ is the expected variance in the j'th net single inspection yield in the absence of fissionable materials. These variances are the same as given in equations (1.9) and (1.10). If correlations exist between the Y_{n_j}'s, additional terms arise in the integrand to account for the dependencies.

To make the critical decision surface, S_c, and the "not detected" volume, $V_{nd}\,(S_c)$, more concrete, the signal phase space will be limited to two dimensions (e.g. delayed neutrons and γ-rays). Figure 1.3 shows a false color representation of a two dimensional Gaussian distribution centered at the origin with both variances set to unity. In two dimensions, the critical decision surface becomes a boundary and the resultant "not detected" volume allows equation 1.33 to be written

$$\iint\limits_{\mathbf{Y_n} \notin V_{nd}(S_c)} \frac{1}{2\pi s_{no_1} s_{no_2}} \, e^{-\frac{{Y_{n_1}}^2}{2{s_{no_1}}^2}} \cdot e^{-\frac{{Y_{n_2}}^2}{2{s_{no_2}}^2}} \, \mathrm{d}Y_{n_1} \mathrm{d}Y_{n_2} = \alpha. \tag{1.34}$$

The integration is carried out over the region outside the "not detected" volume (i.e. the "detected" volume). The surface/volume, which defines the limits of integration, can have any shape as long as the false positive probability is α.

While there are many reasonable critical decision surfaces, two simple surfaces with tractable solutions are the logical "And" shown in Figure 1.3a and the logical "Or" shown in Figure 1.3b. The logical "And" boundary requires both signals to be above their respective critical decision levels and equation (1.34) becomes

$$\int\limits_{L_{c_2}}^{\infty} \int\limits_{L_{c_1}}^{\infty} \frac{1}{2\pi s_{no_1} s_{no_2}} \, e^{-\frac{{Y_{n_1}}^2}{2{s_{no_1}}^2}} \cdot e^{-\frac{{Y_{n_2}}^2}{2{s_{no_2}}^2}} \, \mathrm{d}Y_{n_1} \mathrm{d}Y_{n_2} = \alpha, \tag{1.35}$$

where L_{c_1} and L_{c_2} are the critical decision levels. The logical "Or" boundary requires one

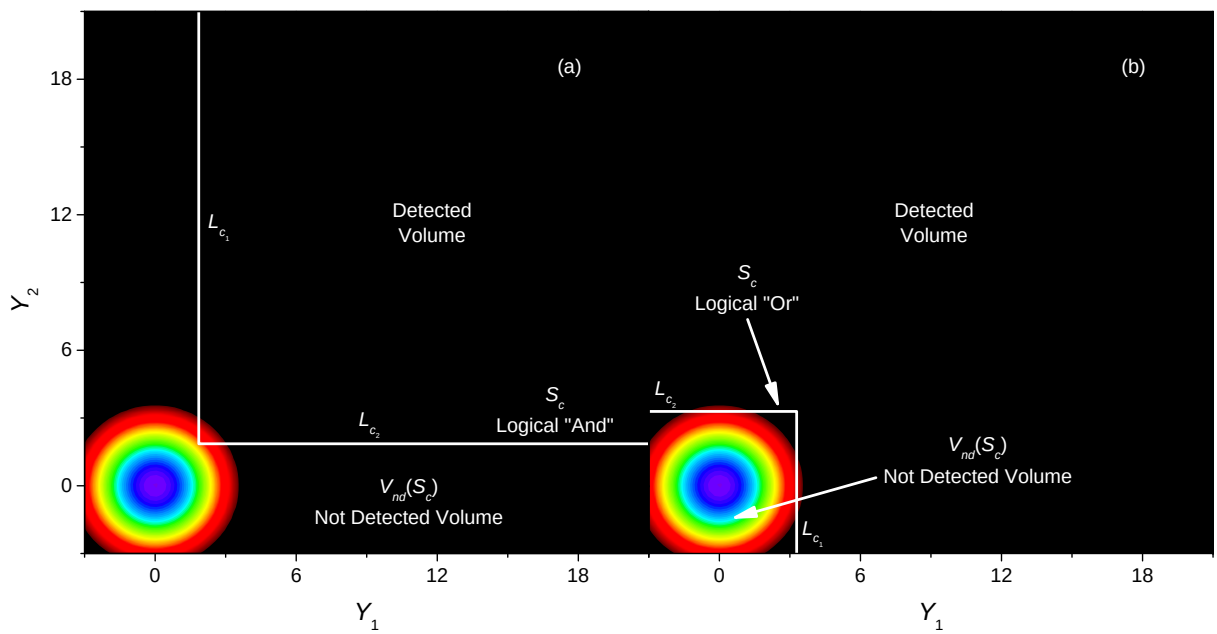

Figure 1.3: False color representation of a two dimensional Gaussian distribution centered at the origin with both variances set to unity. The critical decision surface for a logical "And" is overlaid on graph (a) and the critical decision surface for a logical "Or" is overlaid on graph (b). These two surfaces were calculated using equations (1.41) and (1.42) with $\alpha = 0.1\%$. A net single inspection yield vector located in the region labeled "Detected Volume" leads to a decision "detected."

signal to be above its respective critical decision levels and equation (1.34) becomes

$$1 - \int_{-\infty}^{L_{c_2}} \int_{-\infty}^{L_{c_1}} \frac{1}{2\pi s_{no_1} s_{no_2}} e^{-\frac{{Y_{n_1}}^2}{2{s_{no_1}}^2}} \cdot e^{-\frac{{Y_{n_2}}^2}{2{s_{no_2}}^2}} \, \mathrm{d}Y_{n_1} \mathrm{d}Y_{n_2} = \alpha. \tag{1.36}$$

For both boundaries, net single inspection yields in the upper right region produce the decision "detected." The solution to these integrals is relatively uncomplicated, resulting in a relationship between the two critical decision levels. This relationship for the logical "And" is

$$L_{c_{2,1}} = s_{no_{2,1}} \sqrt{2} \mathrm{erf}^{-1} \left(1 - \frac{4\alpha}{1 - \mathrm{erf}\left(\frac{L_{c_{1,2}}}{s_{no_{1,2}}\sqrt{2}} \right)} \right), \tag{1.37}$$

and for the logical "Or" is

$$L_{c_{2,1}} = s_{no_{2,1}}\sqrt{2}\mathrm{erf}^{-1}\left(\frac{4\left(1-\alpha\right)}{1+\mathrm{erf}\left(\frac{L_{c_{1,2}}}{s_{no_{1,2}}\sqrt{2}}\right)} - 1\right), \tag{1.38}$$

where $\mathrm{erf}\left(x\right)$ and $\mathrm{erf}^{-1}\left(x\right)$ are the error function and its inverse. These formulas are used by picking a desired critical decision level for one $L_{c_{1,2}}$ and this sets $L_{c_{2,1}}$ assuring that the false positive probability is α. The one dimensional (i.e. single signal) critical decision levels can be recovered by letting $L_{c_{1,2}} \longrightarrow -\infty$ for the logical "And" or letting $L_{c_{1,2}} \longrightarrow \infty$ for the logical "Or."

Equations (1.37) and (1.38) are little unsatisfying because there is no obvious way to pick one of the critical decision levels, L_{c_1} or L_{c_2}. This can be rectified by considering the multivariate distributions in a reduced coordinate system

$$\mathbf{y_n} = \begin{pmatrix} y_{n_1} \\ y_{n_2} \end{pmatrix} = \begin{pmatrix} \frac{Y_{n_1}}{s_{n_1}} \\ \frac{Y_{n_2}}{s_{n_2}} \end{pmatrix}, \tag{1.39}$$

thereby equalizing the importance of each signal relative to its expected variance without fissionable isotopes, ${s_{no_j}}^2$. The reduced coordinate critical decision levels at their intersection are set to be equal,

$$l_{c_1} = l_{c_2} = \frac{L_{c_1}}{s_{no_1}} = \frac{L_{c_2}}{s_{no_2}}, \tag{1.40}$$

and now only depend on the variances and the desired false positive rate. For the logical "And," the critical decision levels are given by

$$L_{c_j} = s_{no_j}\sqrt{2}\,\mathrm{erf}^{-1}\left(1-2\sqrt{\alpha}\right), \tag{1.41}$$

and for the logical "Or," the critical decision levels are given by

$$L_{c_j} = s_{no_j}\sqrt{2}\,\mathrm{erf}^{-1}\left(2\sqrt{1-\alpha}-1\right). \tag{1.42}$$

Since the multivariate Gaussian distributions in Figure 1.3 have their variances set to unity, these distributions are essentially in the reduced coordinate system. The logical "And" and "Or" boundaries were calculated using equations (1.41) and (1.42) with $\alpha = 0.1\%$.

Setting the intersection equal in a two-dimensional reduced coordinate signal phase space

results in simple closed form equations describing the logical "And" and logical "Or" critical decision surfaces. This simplicity continues in higher-dimension phase spaces. Furthermore, the logical "Or" boundary appears close to maximizing the fissionable isotope sensitivity, making a discussion of these simple boundaries in an arbitrary phase space worthwhile. Since the integrand is separable and the surfaces are only dependent at their common point of intersection, the integral in equation (1.33) can be written in the reduced coordinate phase space for the logical "And" surface as

$$\prod_{j=1}^{d}\left(\int_{l_{c_j}}^{\infty}\frac{1}{\sqrt{2\pi}}\,e^{-\frac{1}{2}{y_{n_j}}^2}\,\mathrm{d}y_{n_j}\right)=\alpha, \tag{1.43}$$

and for the logical "Or" surface as

$$1-\prod_{j=1}^{d}\left(\int_{-\infty}^{l_{c_j}}\frac{1}{\sqrt{2\pi}}\,e^{-\frac{1}{2}{y_{n_j}}^2}\,\mathrm{d}y_{n_j}\right)=\alpha. \tag{1.44}$$

Carrying out the integrals and setting a common point of intersection for all the reduced coordinate surfaces, quickly results in

$$\left[\frac{1}{2}-\frac{1}{2}\,\mathrm{erf}\left(\frac{l_c}{\sqrt{2}}\right)\right]^d=\alpha, \tag{1.45}$$

for the logical "And" surface and

$$1-\left[\frac{1}{2}+\frac{1}{2}\,\mathrm{erf}\left(\frac{l_c}{\sqrt{2}}\right)\right]^d=\alpha, \tag{1.46}$$

for the logical "Or" surface, where l_c is the common point. Solving for l_c and returning to the standard signal phase space, the logical "And" surface is described by

$$L_{c_j}=s_{no_j}\sqrt{2}\,\mathrm{erf}^{-1}\left(1-2\alpha^{\frac{1}{d}}\right), \tag{1.47}$$

and logical "Or" surface is described by

$$L_{c_j}=s_{no_j}\sqrt{2}\,\mathrm{erf}^{-1}\left[2\left(1-\alpha\right)^{\frac{1}{d}}-1\right], \tag{1.48}$$

providing a simple way to quickly calculate critical decision levels in an arbitrary dimensional signal phase space. Setting $d = 1$ for the one dimensional case (i.e. a single fission signal), both the logical "And" and logical "Or" critical decision points are equal and equivalent to the critical decision level for a single fission signal given by equations (1.7) and (1.8). Of course, the critical decision surface for two dimensions can be obtained by setting $d = 2$.

The critical decision surfaces discussed so far, all consist of intersecting flat planes that separate the "not detected" and "detected" volumes. While calculating these simple surfaces is easy using equations (1.37), (1.38), (1.41), (1.42), (1.47) or (1.48), the distance in the reduced coordinate system to the boundary from the origin is not constant in the important region where joint yields are expected from fissionable materials (i.e. the upper right quadrant in two dimensions). In many inspection scenarios, there will be very little a priori knowledge on where the joint yield is anticipated in the signal phase space and this location depends on the fissionable isotopes in and shielding of the inspection object. Hence a critical decision surface, which is equidistant from the origin in the detected region, is important. Figure 1.4 presents an equidistant logical "Or" surface in a two dimensional signal phase space along with the Gaussian distribution without fissionable isotopes from Figure 1.3. This simply connected surface consists of constant critical decision levels in the second and fourth quadrant and an elliptical surface in the first quadrant. Again, to equalize the importance of each signal relative to its expected variance, the signals and integrals will be considered in the reduced coordinate system with $y_1 = y_2 = l_c$ in the second and fourth quadrant and the ellipse in the first quadrant becomes a circular surface of radius l_c. To cover the entire "detected" volume, the integral in equation (1.34) is divided into three and becomes

$$\int_0^{\frac{\pi}{2}}\int_{l_c}^{\infty} \frac{1}{2\pi}\, e^{-\frac{{\rho_n}^2}{2}}\, \rho_n \mathrm{d}\rho_n \mathrm{d}\phi_n + \int_{l_c}^{\infty}\int_{-\infty}^{0} \frac{1}{2\pi}\, e^{-\frac{{y_{n_1}}^2+{y_{n_2}}^2}{2}}\, \mathrm{d}y_{n_1}\mathrm{d}y_{n_2} + \int_{-\infty}^{0}\int_{l_c}^{\infty} \frac{1}{2\pi}\, e^{-\frac{{y_{n_1}}^2+{y_{n_2}}^2}{2}}\, \mathrm{d}y_{n_1}\mathrm{d}y_{n_2} = \alpha, \tag{1.49}$$

where the first integral is in cylindrical coordinates to cover the "detected" volume in the first quadrant with ${\rho_n}^2 = {y_{n_1}}^2 + {y_{n_2}}^2$. The second and third integrals are equivalent and cover the second and fourth quadrants of the "detected" volume. Performing the integrations, this

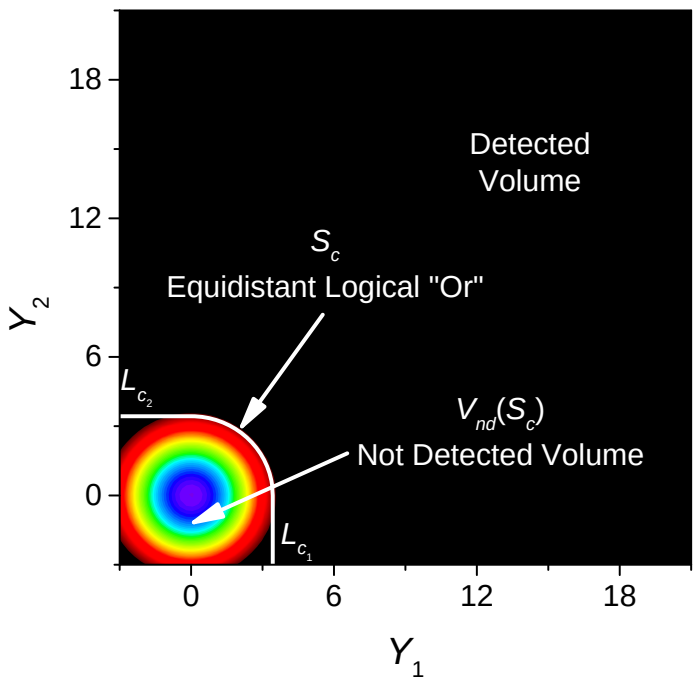

Figure 1.4: False color representation of a two dimensional Gaussian distribution centered at the origin with both variances set to unity. The critical decision surface is a logical "Or" that is equidistant from the origin in the first quadrant and is calculated using equation (1.50) with $\alpha = 0.1\%$. A net single inspection yield vector located in the region labeled "Detected Volume" leads to a decision "detected."

equation becomes

$$\frac{1}{4}\, e^{-\frac{l_c{}^2}{2}} + \frac{1}{2} - \frac{1}{2}\,\mathrm{erf}\left(\frac{l_c}{\sqrt{2}}\right) = \alpha, \tag{1.50}$$

and l_c can be found by simple numerical techniques. Returning to the standard signal phase space, $L_{c_1} = s_{no_1} l_c$ in the fourth quadrant, $L_{c_2} = s_{no_2} l_c$ in the second quadrant and the ellipse in the first quadrant is described by

$$\left(\frac{Y_{n_1}}{s_{no_1}}\right)^2 + \left(\frac{Y_{n_2}}{s_{no_2}}\right)^2 = l_c{}^2. \tag{1.51}$$

These equations were used to calculate the critical decision surface presented in Figure 1.4 with $\alpha = 0.1\%$, keeping in mind that both signal variances were set to unity.

1.5 Extending the Minimal Detectable Level to a Multidimensional Signal Phase Space

As with a single signal, making an a priori estimate of a technique's detection capabilities requires extending the mathematical framework to include fissionable materials. Adding fissionable material to the object under inspection, increases the net inspection yield's limiting mean, $\mathbf{\Psi_n}$. This increases the probability that the observed net yield, $\mathbf{Y_n}$, from a single inspection will be outside the "not detected" volume, $V_{nd}(S_c)$, thereby correctly deciding "detected." In a multidimensional signal phase space, the minimal detectable level becomes a surface, S_d, defined as the set of limiting means that have a false negative probability of β for a given critical decision surface, S_c . This definition can be expressed mathematically as

$$P\left(\mathbf{Y_n} \in V_{nd}(S_c) \,|\mathbf{\Psi_n} \in S_d\right) = \beta, \tag{1.52}$$

and the true positive probability when $\mathbf{\Psi_n}$ is on S_d is just $1-\beta$.

To demonstrate the addition of fissionable material, Figure 1.5a schematically illustrates the two dimensional distribution of a net single inspection yield, $\mathbf{Y_n}$, when $\mathbf{\Psi_n}$ is on S_d and $\Psi_{n_1} = \Psi_{n_2}$. The induced fission pushes the centroid of the distribution to higher values in the $\mathbf{Y_n}$ phase space and causes the variance to broaden. Overlaid on this graph is the logical "Or" critical decision surface, S_c, with a false positive probability of $\alpha = 0.1\%$ and the distribution of $\mathbf{Y_n}$'s without fissionable material both from Figure 1.3b. The use of two signatures with a logical "Or" critical decision surface decreases the minimal detectable surface compared to what can be obtained using a single signature. Figure 1.5b schematically shows the distribution and where the minimal detectable surface would reside, if the Y_1 yield was ignored. Only utilizing the Y_2 yield increases the minimal detectable level. The support provided by the Y_1 yield when both signatures are utilized allows the distribution's tails to extend below L_{c_1} or L_{c_2} and still be outside the "not detected" volume $V_{nd}(S_c)$. Hence, the minimal detectable surface, S_d, drastically decreases while maintaining the false negative probability β. A logical "And" critical decision surface does not permit a similar decrease in the minimal detectable surface, S_d. Furthermore, the advantage gained using a logical "Or" surface in a two dimensional signal phase space is highly dependent on the background yield, $\mathbf{\Psi_{bk}}$, and the relative signal strength between Y_1 and Y_2 when fissionable isotopes are present.

Once again, a multivariate Gaussian will be used to describe the probability density

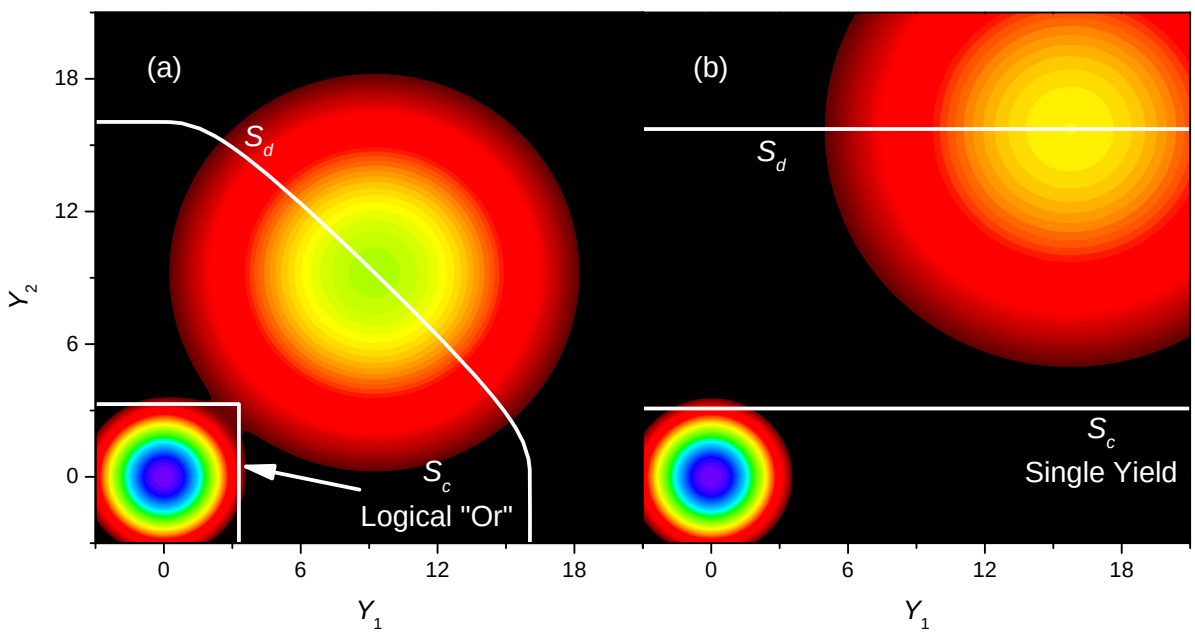

Figure 1.5: False color representation of a two dimensional Gaussian distributions representing the distribution of net single inspections yields, $\mathbf{Y_n}$. Graph (a) illustrates the distribution centered at $\mathbf{\Psi_n} = (L_{d_1}, L_{d_2})$ when $L_{d_1} = L_{d_2}$ for the overlaid logical "Or" boundary. Graph (b) illustrates the distribution centered at $\mathbf{\Psi_n} = (L_d, L_d)$ when the net single inspection yield Y_{n_1} is ignored, which reduces to the one dimensional problem. The single signal critical decision level is also overlaid on graph (b). In both graphs, the Gaussian centered at the origin represents the distribution without fissionable material with unity variances. The false positive and negative probabilities where set to $\alpha = \beta = 0.1\%$.

function for the net single inspection yield, $\mathbf{Y_n}$, based on the assumption that the number of detected events in each signal is large. Equation (1.52) can then be written as

$$\int\limits_{\mathbf{Y_n} \in V_{nd}(S_c)} \frac{1}{\sqrt{(2\pi)^d \left|\mathbf{S_{nd}}\right|}} e^{-\frac{1}{2}(\mathbf{Y_n}-\mathbf{L_d})^T \mathbf{S_{nd}}^{-1}(\mathbf{Y_n}-\mathbf{L_d})} \, \mathrm{d}\mathbf{Y_n} = \beta, \tag{1.53}$$

for a d–dimensional phase space. Here $\mathbf{L_d}$ is a minimal detectable level on S_d (i.e. $\mathbf{L_d} \in S_d$) and $\mathbf{S_{nd}}$ is the expected variance-covariance matrix of the net single inspection yield with $\mathbf{\Psi_n} = \mathbf{L_d}$. The integration is carried out over the region inside the "not detected" volume, giving the probability of a false negative decision, β. While the limiting means, Ψ_{n_j}, are presumably correlated to the fissionable mass and/or standoff distance, the Y_{n_j}'s from a

single inspection can remain uncorrelated so that

$$\sigma\left(Y_{n_j}, Y_{n_l}\right) = \left\langle \left(Y_{n_j} - \left\langle Y_{n_j}\right\rangle\right)\left(Y_{n_l} - \left\langle Y_{n_l}\right\rangle\right)\right\rangle\Big|_{\mathbf{\Psi_n}=\mathbf{L_d}} = \begin{cases} 0 & \text{if } l \neq j \\ {s_{nd_j}}^2 & \text{if } l = j \end{cases}. \tag{1.54}$$

This allows the multivariate Gaussian integrand to be simplified to

$$\int\limits_{\mathbf{Y_n}\in V_{nd}(S_c)} \frac{1}{(2\pi)^{\frac{d}{2}} \prod\limits_{j=1}^{d} s_{nd_j}} \prod_{j=1}^{d} \left(e^{-\frac{\left(Y_{n_j}-L_{d_j}\right)^2}{2{s_{nd_j}}^2}} \right) \mathrm{d}\mathbf{Y_n} = \beta, \tag{1.55}$$

where ${s_{nd_j}}^2$ is the expected variance in the j'th net single inspection yield when $\mathbf{\Psi_n} = \mathbf{L_d}$. These variances are the same as given in equations (1.20) or (1.21). If correlations exist between the Y_{n_j}'s, additional terms arise in the integrand to account for the dependencies.

For an arbitrary critical decision surface, S_c, the integrals in equation (1.55) can only be performed numerically. Furthermore, there are an infinite number of $\mathbf{L_d}$ points on S_d, making the number of required integrations large to describe the minimal detectable surface. However, the simple logical "And" and "Or" critical decision surfaces with common points of intersection make the integrals for each dimension completely separable. For the logical "And" critical decision surface, which requires all signals to be above their respective critical decision levels, equation (1.55) becomes

$$1 - \prod_{j=1}^{d} \left(\int\limits_{L_{c_j}}^{\infty} \frac{1}{s_{nd_j}\sqrt{2\pi}} e^{-\frac{\left(Y_{n_j}-L_{d_j}\right)^2}{2{s_{nd_j}}^2}} \mathrm{d}Y_{n_j} \right) = \beta. \tag{1.56}$$

For the logical "Or" critical decision surface, which requires only one signal to be above its respective critical decision level, equation (1.55) becomes

$$\prod_{j=1}^{d} \left(\int\limits_{-\infty}^{L_{c_j}} \frac{1}{s_{nd_j}\sqrt{2\pi}} e^{-\frac{\left(Y_{n_j}-L_{d_j}\right)^2}{2{s_{nd_j}}^2}} \mathrm{d}Y_{n_j} \right) = \beta. \tag{1.57}$$

Unlike the integrals for the critical decision surfaces, there is little advantage to transforming these minimal detectable integrals to the reduced coordinate system. However, these

integrals are very similar to those seen previously and the solutions are now easy. For the logical "And" surface, equation (1.56) can be written as

$$1 - \frac{1}{2^d} \prod_{j=1}^{d} \left[1 - \operatorname{erf}\left(\frac{L_{c_j} - L_{d_j}}{s_{nd_j}\sqrt{2}} \right) \right] - \beta = 0. \tag{1.58}$$

For the logical "Or" surface, equation (1.57) becomes

$$\frac{1}{2^d} \prod_{j=1}^{d} \left[1 + \operatorname{erf}\left(\frac{L_{c_j} - L_{d_j}}{s_{nd_j}\sqrt{2}} \right) \right] - \beta = 0. \tag{1.59}$$

While these equations may appear to have three independent parameters per dimension (i.e. L_{c_j}, L_{d_j} and s_{nd_j}), recall that many of them are related. Presumably, the critical decision surfaces have already been calculated using equations like (1.37), (1.38), (1.41), (1.42), (1.47) and (1.48). The expected single inspection variances, s_{nd_j}, when $\mathbf{\Psi_n} = \mathbf{L_d}$ are related to the L_{d_j}'s through equation (1.20) or (1.21). This leaves a single free L_{d_j} per signal phase space dimension. Hence, the roots of these equations produce a set of minimal detectable points, $\mathbf{L_d}$, all with a false negative probability of β, describing the minimal detectable surface S_d.

In one dimension (i.e. a single signal), equations (1.58) and (1.59) are equal and can be reduced to the minimal detectable level given in equation (1.23). To define the minimal detectable surface in greater than one dimension, the strategy is to solve equations (1.58) and (1.59) for one L_{d_m} as a function of the remaining L_{d_j}'s. Hence, the logical "And" surface equation is rewritten as

$$1 - \frac{1}{2^d} \left[1 - \operatorname{erf}\left(\frac{L_{c_m} - L_{d_m}}{s_{nd_m}\sqrt{2}} \right) \right] \prod_{\substack{j=1 \\ j \neq m}}^{d} \left[1 - \operatorname{erf}\left(\frac{L_{c_j} - L_{d_j}}{s_{nd_j}\sqrt{2}} \right) \right] = \beta, \tag{1.60}$$

and the logical "Or" surface equation becomes

$$\frac{1}{2^d} \left[1 + \operatorname{erf}\left(\frac{L_{c_m} - L_{d_m}}{s_{nd_m}\sqrt{2}} \right) \right] \prod_{\substack{j=1 \\ j \neq m}}^{d} \left[1 + \operatorname{erf}\left(\frac{L_{c_j} - L_{d_j}}{s_{nd_j}\sqrt{2}} \right) \right] = \beta. \tag{1.61}$$

Solving for L_{d_m}, both of the above equations result in

$$L_{d_m} = L_{c_m} + \frac{k_{\beta_m}^2}{2N_h} + k_{\beta_m} \left| k_{\beta_m} \right| \sqrt{\frac{1}{4{N_h}^2} + \frac{L_{c_m}}{k_{\beta_m}^2 N_h} + \frac{{L_{c_m}}^2}{{k_{\alpha_m}}^2 k_{\beta_m}^2}}, \tag{1.62}$$

which is nearly identical to the minimal detectable level in equation (1.23). However, k_{α_m} and k_{β_m} are more complicated functions than the simple one dimensional case and specifically, k_{β_m} is a function of the remaining L_{d_j}'s. For the logical "And" surface, the k_{α_m} and k_{β_m} are replaced by

$$k_{\alpha a_m} = \sqrt{2}\mathrm{erf}^{-1}\left[1 - \frac{2^d \alpha}{\prod\limits_{\substack{j=1 \\ j\neq m}}^{d}\left[1 - \mathrm{erf}\left(\frac{L_{c_j}}{s_{no_j}\sqrt{2}}\right)\right]}\right] \tag{1.63}$$

$$k_{\beta a_m} = \sqrt{2}\mathrm{erf}^{-1}\left[\frac{2^d\left(1-\beta\right)}{\prod\limits_{\substack{j=1 \\ j\neq m}}^{d}\left[1 - \mathrm{erf}\left(\frac{L_{c_j}-L_{d_j}}{s_{nd_j}\sqrt{2}}\right)\right]} - 1\right]. \tag{1.64}$$

For the logical "Or" surface, the k_{α_m} and k_{β_m} are replaced by

$$k_{\alpha o_m} = \sqrt{2}\mathrm{erf}^{-1}\left[\frac{2^d\left(1-\alpha\right)}{\prod\limits_{\substack{j=1 \\ j\neq m}}^{d}\left[1 + \mathrm{erf}\left(\frac{L_{c_j}}{s_{no_j}\sqrt{2}}\right)\right]} - 1\right] \tag{1.65}$$

$$k_{\beta o_m} = \sqrt{2}\mathrm{erf}^{-1}\left[1 - \frac{2^d \beta}{\prod\limits_{\substack{j=1 \\ j\neq m}}^{d}\left[1 + \mathrm{erf}\left(\frac{L_{c_j}-L_{d_j}}{s_{nd_j}\sqrt{2}}\right)\right]}\right]. \tag{1.66}$$

There is a further dependency on the L_{d_j}'s through the expected variances when $\mathbf{\Psi_n} = \mathbf{L_d}$, ${s_{nd_j}}^2$, which are given by equation (1.20) or (1.21). For completeness these expected variances are

$${s_{nd_j}}^2 = \frac{L_{d_j}}{N_h} + {s_{no_j}}^2 = \frac{L_{d_j}}{N_h} + \frac{{L_{c_j}}^2}{{k_{\alpha_j}}^2}, \tag{1.67}$$

where k_{α_j} is for the appropriate critical decision surface; either equation (1.63) or (1.65). When the dimensionality is one (i.e. $d = 1$), the k_{α_m}'s and k_{β_m}'s become the one dimensional k_α and k_β given in equations (1.8) and (1.17), resulting in the equation (1.62) being nothing

more than the one dimensional equation (1.23).

Equations (1.62), (1.65) and (1.66) were used to calculate the minimal detectable surface for the two dimensional logical "Or" critical decision surface, which is overlaid in Figure 1.5a. While there are an infinite number of minimal detectable levels, $\mathbf{L_d}$, on surface S_d, the distance from the origin to the minimal detectable surface can be minimized. In the somewhat artificial example of Figure 1.5a where $s_{no_1} = s_{no_2} = 1$, symmetry arguments dictate that this minimum distance occurs when $L_{d_1} = L_{d_2}$, which is where the schematic two dimensional net yield distribution with fissionable material is shown. In comparison, the single one dimensional minimal detectable level shown in Figure 1.5b is 70% larger than the $L_{d_1} = L_{d_2}$ point when two fission signals are utilized. This drastic improvement in the minimal detectable level is in the low count limit. In the high count limit, the one dimensional minimal detectable level is only 20% larger than the $L_{d_1} = L_{d_2}$ point when two fission signal are utilized. Furthermore, the improvement in the minimal detectable level assumes that the fission signals utilized have equal strength causing the centroid of the $\mathbf{Y_n}$ distribution with fissionable material to occur at $L_{d_1} = L_{d_2}$. Of course, there is no a priori reason for the fission signals to be of equal strength and their yields will depend on the signal yield function, $\mathbf{\Psi_s}(m_f, \dots)$. As in the one dimensional case, the yield function depends on all the parameters of the inspection such as photon fluence, fission cross sections, fission fragment yields, branching ratios, count periods, fissionable mass, detector efficiencies, attenuation of the probing beam, attenuation of the outgoing particles etc... Again, this can be a really complicated function for arbitrary inspection scenarios.

If only a single parameter is varied (e.g. fissionable mass, standoff distance, shielding thickness etc...), the signal yield function, $\mathbf{\Psi_s}(m_f, \dots)$, parameterizes a line through the signal phase space that starts at the origin with a trajectory that leaves the not detected volume, $V_{nd}(S_c)$, thereby entering the detected volume. This line will intersect the minimal detectable surface, S_d, determining the singular minimal detectable level, $\mathbf{L_d}$, and hence the minimal detectable mass, maximum standoff distance, shielding thickness etc... For low mass targets, the minimal detectable mass can be found easily because the net yield's limiting mean is directly proportional to the fissionable material mass

$$\mathbf{\Psi_n} = \frac{\mathrm{d}\mathbf{\Psi_s}}{\mathrm{d}m_f} \cdot m_f, \tag{1.68}$$

where $\mathrm{d}\mathbf{\Psi_s}/\mathrm{d}m_f$ is the net yield per unit fissionable mass. The minimal detectable mass can

then be easily found by setting $\mathbf{\Psi_n} = \mathbf{L_d}$ and solving for the mass

$$M_d = \left(\frac{\mathrm{d}\mathbf{\Psi_s}}{\mathrm{d}m_f}\right)^{-1} \cdot \mathbf{L_d}. \tag{1.69}$$

In essence, $\mathrm{d}\mathbf{\Psi_s}/\mathrm{d}m_f$ can be thought of as a calibration constant for a fission signature or inspection system. This constant can be easily measured using low mass targets in which absorption is negligible.

Chapter 2

Delayed Neutrons

2.1 Introduction and Experimental Setup

The experiments summarized in this chapter investigated photon induced delayed neutron emission for nuclear forensics applications. The primary goals were to measure the minimal detectable limits for fissionable isotopes in aqueous and sand matrices and to develop delayed neutron techniques that can identify these isotopes. Hence, the majority of the experiments used the 1 L aqueous and sand matrix targets that contained ^{232}Th and ^{238}U. More detailed information about these targets can be found in appendix A.

The high-energy bremsstrahlung beam that induced photofission reactions in the targets was produced by a 25 MeV electron linac. The electron energy and hence the bremsstrahlung end point energy was varied from 7 to 19 MeV. Each electron pulse from the accelerator contained $\sim$ 120 nC of charge in a 4 μs wide pulse, which was incident on a 4.2 g·cm^{-2} thick tungsten radiator. The accelerator was operated at repetition rates from 7.5 to 60 Hz, allowing the detection of delayed neutrons between bremsstrahlung pulses. The targets were placed $\sim$33 cm from the bremsstrahlung radiator, directly in the bremsstrahlung beam as seen in the experimental schematic of Figure 2.1. To prevent electrons from the accelerator striking the target or detectors, a 5.08 cm thick aluminum block was placed in front of the radiator to absorb electrons that transmitted through the radiator.

The delayed neutrons were detected by six photonuclear neutron detectors (PNDs) in close proximity to the target, three PNDs 11.1 cm on either side of target at 90° with respect to the bremsstrahlung beam. Each detector consisted of a 2.54 cm diameter ^{3}He filled proportional counter at a pressure of 10 atmospheres. Surrounding each tube is 2.54 cm of polyethylene, 110 μm of cadmium and 9.51 mm of a borated elastomer, with an outer casing

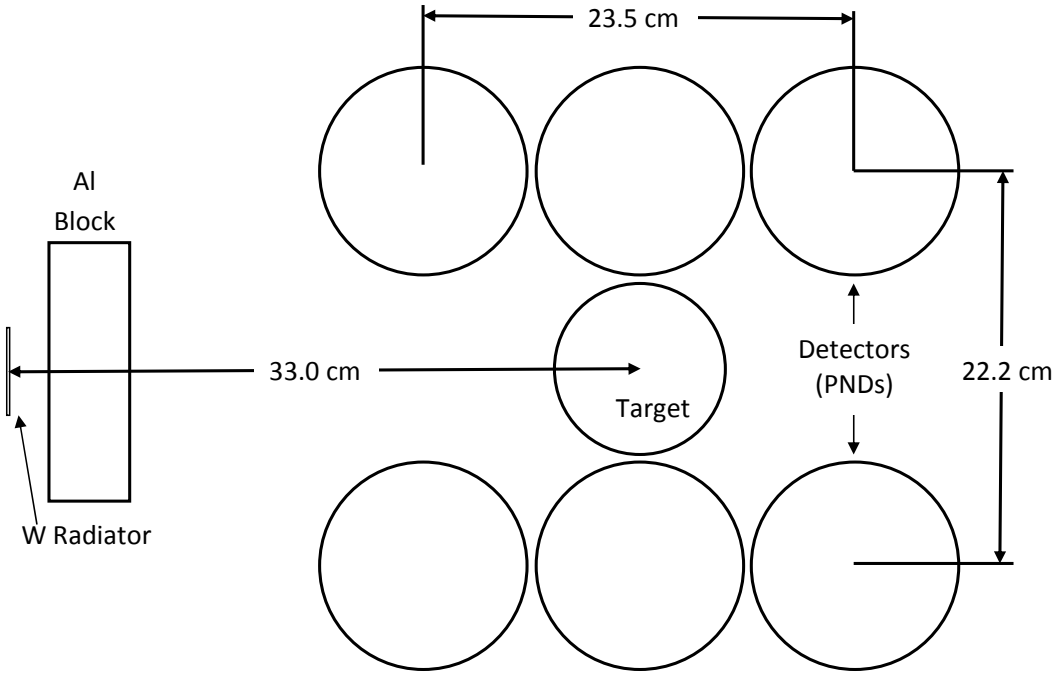

Figure 2.1: Schematic of the delayed neutron experimental setup. The electron beam from the accelerator (not shown) came from the left of the drawing and was incident on the tungsten radiator.

consisting of 2.4 mm of aluminum. The entire detector is 53.3 cm long with a 20.3 cm active region and is designed to detect neutrons with an energy of a few eV up to 10 MeV, although the peak efficiency occurs for 10 keV neutrons. With boron and cadmium's relatively high neutron capture cross sections for very low energy neutrons, the efficiency of the detectors is almost 400 times smaller for neutrons below 1 eV than for 10 keV neutrons[12, 20]. Hence, the neutrons that are produced from photonuclear reactions during the bremsstrahlung pulse and then thermalize in the environment, are not detected. The neutrons detected by the PNDs were counted by a latching scaler with a counting cycle starting $\sim$120 ns before each bremsstrahlung pulse and terminating just before the next pulse. A full description of these detectors can be found in the dissertation by M. T. Kinlaw[20].

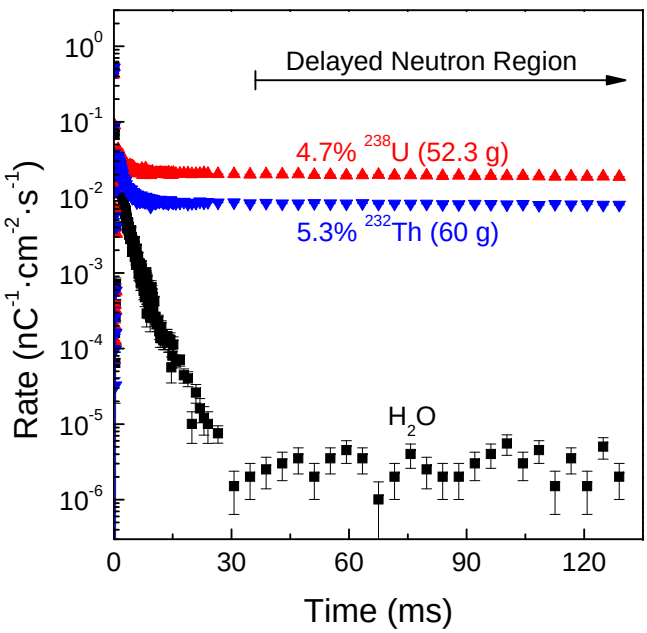

Figure 2.2: Neutron detection rates versus time after the bremsstrahlung pulse for the pure H_2O (■), 5.3% ^{232}Th (▼) and 4.7% ^{238}U (▲) 1 L aqueous targets. The bremsstrahlung beam endpoint energy was 16 MeV with a repetition rate of 7.5 Hz. The neutron detection rate has been normalized by the electron charge on the radiator and the detector area. The total inspection time was ∼300 s.

2.2 Aqueous Solutions

2.2.1 Yields and Minimal Detectable Masses

Figure 2.2 compares the detected neutron rates from the pure H_2O, 5.3% ^{232}Th and 4.7% ^{238}U aqueous targets, stimulated by a 16 MeV bremsstrahlung beam. These neutron detection rates have been normalized by the cross sectional detector area and by the total electron charge on the radiator as a proxy for the bremsstrahlung intensity. The detectors were inoperable during the first ∼900 μs as they recovered from the intense bremsstrahlung pulse. After the detectors were fully recovered, the rate decreased rapidly as neutrons created during the bremsstrahlung pulse scatter from objects in the environment and return to the detectors. For the pure H_2O target, this yield decreased over four orders of magnitude between its peak and ∼30 ms. In contrast, the yield stayed elevated for the aqueous solutions containing ^{232}Th or ^{238}U due to the emission of delayed neutrons following the induced photofission reactions. In the time range of 30 to 131 ms after the bremsstrahlung pulse, almost one million more neutrons were detected after 300 s of integration (2×10^3 bremsstrahlung pulses) for the

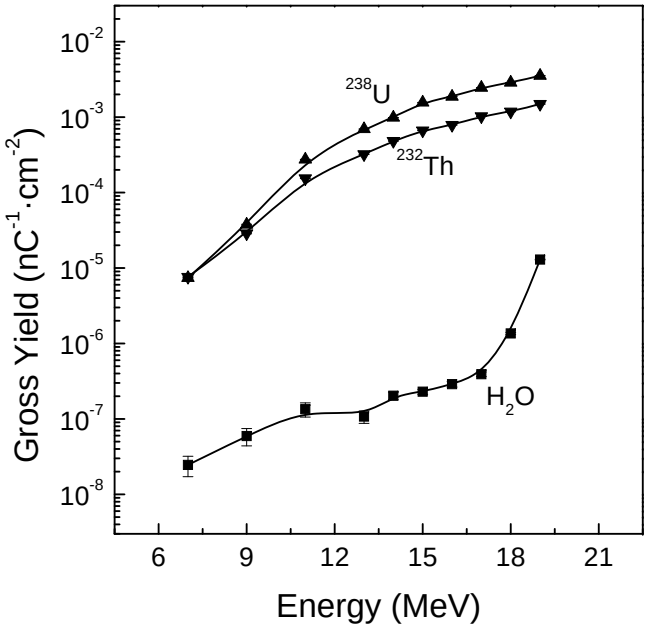

Figure 2.3: Detected delayed neutron yield versus bremsstrahlung endpoint energy for the 5.3% ^{232}Th (▼), 4.7% ^{238}U (▲) and pure H_2O (■) 1 L aqueous targets. The bremsstrahlung beam had a repetition rate of 7.5 Hz. The delayed neutron yield was calculated by integrating differential yield, like that presented in Figure 2.2 from 20 to 131 ms.

target containing ^{238}U than for the pure H_2O target. Hence, the delayed neutron fission signature in these experiments was defined as neutrons detected between 35 and 131 ms after the bremsstrahlung pulse in order to minimize interference from neutrons created in non-photofission processes.

The gross delayed neutron fission signal was calculated by integrating the detection rate from 35 to 131 ms and Figure 2.3 shows this gross yield as a function of the bremsstrahlung energy for the pure H_2O 5.3% ^{232}Th and 4.7% ^{238}U 1 L aqueous targets. From 7 to 16 MeV, the delayed neutron yield increased by a factor of $\sim$250 for the target containing ^{238}U isotopes. In contrast, the background, which is represented by the pure H_2O target, only increases by a factor of $\sim$11 from 7 to 16 MeV. Hence the delayed neutron fission signal from the ^{238}U containing target is $\sim$300 times above background at 7 MeV and grows to over $\sim$6000 times above background at 16 MeV. At 7 and 9 MeV the background from the pure H_2O target is indistinguishable from the natural passive neutron background but as the bremsstrahlung energy is increased above these energies there is an active background component. Below $\sim$16 MeV, the origin of this active background has not been conclusively identified but the research team suspects thermal neutron "streaming" through small un-

shielded sections of the detector. Above, $\sim$16 MeV, the background increases drastically due to the ^{18}O(γ,p)^{17}N reaction. This photonuclear reaction has a threshold of 15.9 MeV and ^{17}N is a neutron emitter with a 4.17 s half-life[21, 22]. The production of ^{17}N was verified in previous experiments by measuring the half-life of the parent nuclei that was emitting the neutrons from a pure H_2O target. The ^{18}O(γ,p)^{17}N reaction is the only known reaction accessible at bremsstrahlung energies below 20 MeV that can produce neutrons on the same timescale as fission delayed neutrons.

The minimal detectable level can be calculated from the yield data of Figure 2.3. For paired observations, where a known blank target without fissionable isotopes (i.e. a background measurement) is measured under the same conditions as an unknown target, the minimal detectable yield is found by combining equations (1.12) and (1.24). Hence for these experiments the minimal detectable level was given by [23]

$$L_d = \frac{k^2}{Q_t A_d} + k\sqrt{2\frac{\Psi_{abk}}{Q_t A_d}}, \tag{2.1}$$

where Q_t is the total charge on the radiator and A_d is the detector area for yield normalization and Ψ_{abk} is the background neutron yield from the blank target. For the low mass targets utilized here, the minimal detectable mass can then be found through equation (1.28). The minimal detectable mass as a function of bremsstrahlung endpoint energy for ^{232}Th and ^{238}U in aqueous solutions is presented in Figure 2.4. In calculating the minimal detectable mass, the concept of operations was an accelerator with 100 nC of charge per pulse at 7.5 Hz inspecting 1 L aqueous targets for 300 s; essentially the experimental conditions. The constant k was set at 1.645 which produces a symmetric 95% confidence interval; 5% false positives from solutions without fissionable isotopes and 5% false negatives for solutions with M_d of fissionable material. From 7 to 13 MeV, the minimal detectable mass decreases drastically because of the larger fission cross section and the increased bremsstrahlung production at higher energies. Between 13 and 17 MeV the minimal detectable mass continues to decrease but more slowly. Above 17 MeV the minimal detectable mass deteriorates as the background increases from ^{18}O(γ,p)^{17}N reactions. At 17 MeV the minimal detectable mass is 9.3 mg for ^{232}Th and 3.4 mg for ^{238}U. This corresponds to mole fractions of 720 and 260 ppb, respectively. Increasing the charge on the bremsstrahlung radiator either by increasing the charge per pulse or the inspection time, decreases the minimal detectable masses approximately as $\sim Q_t^{-\frac{1}{2}}$. For example, increasing the inspection time to $\sim$6 hr, decreases the minimal detectable masses to 1.1 mg (85 ppb) for ^{232}Th and 413 μg (30 ppb) for ^{238}U. In addition, the

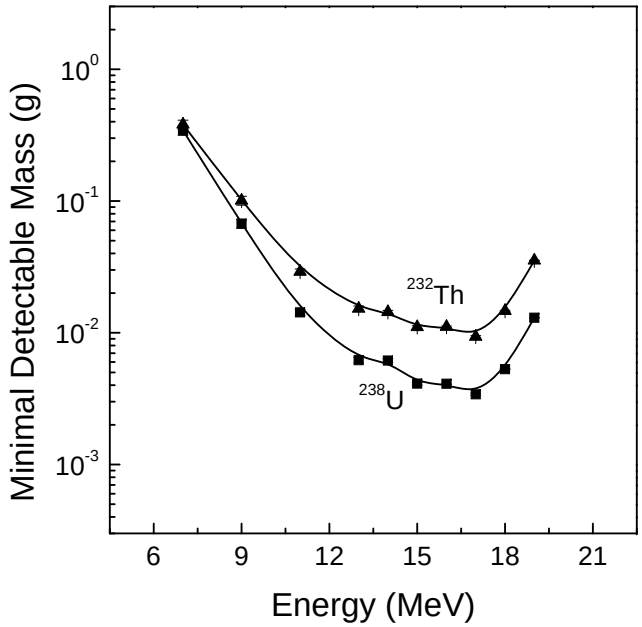

Figure 2.4: Minimal detectable mass versus bremsstrahlung endpoint energy for ^{232}Th (▲) and ^{238}U (■) in aqueous solutions. These minimal detectable masses were calculated using equations (2.1)and(1.28), $k = 1.645$ and the data in Figure 2.3. The concept of operations was an accelerator with 100 nC of charge per pulse at 7.5 Hz inspecting the aqueous solution for 300 s. This leads to a total charge on target of 225 μC.

minimal detectable masses can be decreased by increasing the neutron detection efficiency.

The minimal detectable masses presented in Figure 2.4 assume a linear relationship between the delayed neutron yield and fissionable mass in the solution, making equation (1.28) applicable. Delayed neutron yields were measured from the single component ^{232}Th and ^{238}U 1 L aqueous targets, which have fissionable isotope concentrations that vary from 1% to 8.8%. Figure 2.5 presents these mass calibrations for 11 and 16 MeV bremsstrahlung endpoint energies. At both energies the relationship between the delayed neutron yield and fissionable mass in the aqueous solution is very linear, demonstrating that the calibration factor $\mathrm{d}\Psi_s/\mathrm{d}m_f$ is indeed independent of fissionable mass. This linearity will breakdown when the concentration of the fissionable mass becomes large enough that the absorption characteristics of the incoming bremsstrahlung beam or the outgoing neutrons changes significantly. The calibration factor $\mathrm{d}\Psi_s/\mathrm{d}m_{232}$ for ^{232}Th is 2.31 ± 0.02 and 15.00 ± 0.09 mC^{-1}·cm^{-2}·g^{-1} at 11 and 16 MeV bremsstrahlung endpoint energy. The calibration factor $\mathrm{d}\Psi_s/\mathrm{d}m_{238}$ for ^{238}U is 4.73 ± 0.03 and 40.3 ± 0.1 mC^{-1}·cm^{-2}·g^{-1} at 11 and 16 MeV bremsstrahlung endpoint energy.

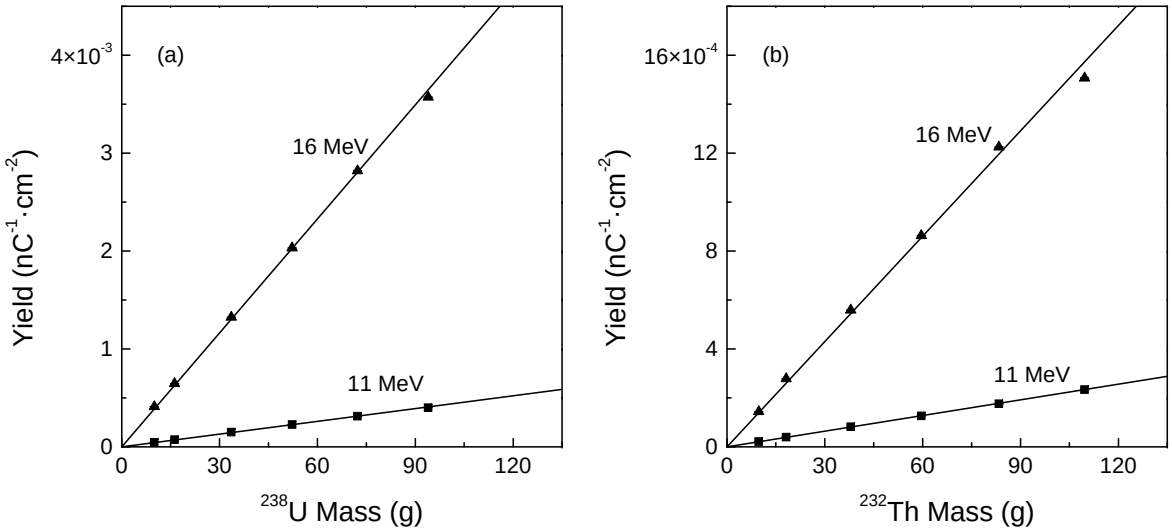

Figure 2.5: Delayed neutron yield versus the fissionable mass for the ^{238}U (a) and ^{232}Th (b) $\sim$1 L aqueous targets using 11 MeV (■) and 16 MeV (▲) bremsstrahlung endpoint energies. The accelerator was operated at 7.5 Hz with $\sim$66 and $\sim$120 nC of charge per pulse at 11 and 16 MeV, respectively.

2.2.2 Specificity Techniques

For nuclear forensics applications, it is necessary to not only detect and quantify fissionable materials but also to identify the fissionable isotopes present. M. T. Kinlaw and A. W. Hunt have demonstrated how the decay rate of delayed neutron emission can be used to identify fissionable materials[1, 3, 20]. Despite the large dynamic range of Figure 2.2, a slight decay in the delayed neutron emission from the solutions containing fissionable isotopes is observable from $\sim$30 to 131 ms. To clearly observe this decay, Figure 2.6 focuses on the normalized delayed neutron yield from the single component 5.3% ^{232}Th and 4.7% ^{238}U aqueous targets. While the decay of delayed neutron emission is inherently exponential in nature, the decays appear linear due to the short interval over which they are observed. The rate of decay from these isotopes are clearly different, permitting the discrimination of samples containing ^{238}U or ^{232}Th. The differences in these decay rates are the result of changes in the production of the delayed neutron emitting fission fragments for different fissionable isotopes[20, 24–26].

In addition to discriminating different fissionable isotopes, the change in the decay rate can be exploited to determine the isotopic ratio in bi-component solutions. Overlaid in Figure 2.6 is the normalized yield from two bi-component solutions containing $\sim$4.7% total fissionable mass with relative ^{232}Th(^{238}U) concentrations of 42.9%(57.1%) and 76.0%(24.0%).

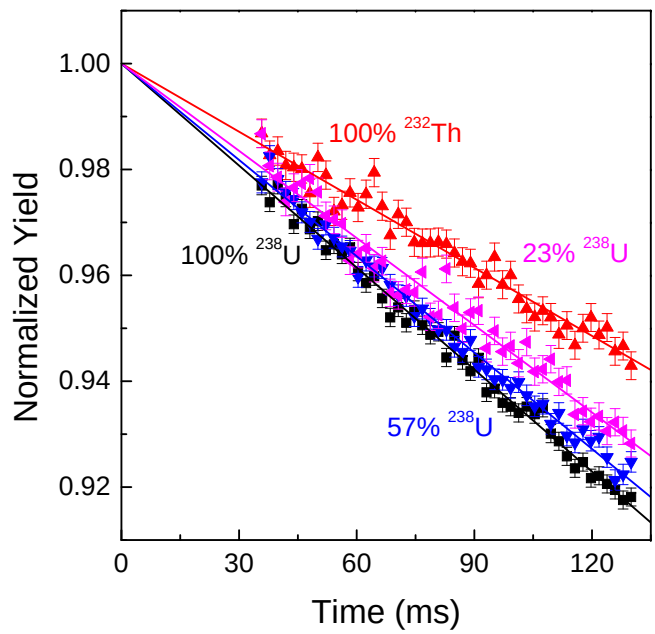

Figure 2.6: Normalized delayed neutron yields versus time after the bremsstrahlung pulse from the 5.3% ^{232}Th (▲), 4.7% ^{238}U (■), Mixed-B (▼) and Mixed-D (◀) aqueous targets. The data was normalized so that the y-intercept of the linear fit was unity. The accelerator was operated at 16 MeV at 7.5 Hz with $\sim$120 nC per pulse. The neutrons were detected between bremsstrahlung pulses for 75 min.

The normalized yields of the bi-component solutions fall between the single component solutions with the higher concentration of ^{232}Th(^{238}U) closer to the single component ^{232}Th(^{238}U) solution. For simplicity, linear least square fits were performed to determine the linearized decay rates of the normalized delayed neutron yield. These decay rates are shown in Figure 2.7 as a function of relative ^{238}U concentration for the two single component solutions and the four bi-component solutions. The differences in the rates are drastic, with a $\sim 45\sigma$ change between pure ^{232}Th and ^{238}U. The linearized decay rate monotonically increases with the ^{238}U concentration without saturating before a 100% relative ^{238}U concentration.

The expected linearized decay rates for bi-component solutions can be calculated from the calibration factors, $\mathrm{d}\Psi_s/\mathrm{d}m_f$, and the linearized decay rates from the single component solutions. The decay rate for a bi-component solution with a relative concentration of ^{238}U, f_{238}, is given by

$$\lambda_{bic}\left(f_{238}\right) = \frac{f_{238}\lambda_{238}{}^{2}\frac{\mathrm{d}\Psi_s}{\mathrm{d}m_{238}} + \left(1-f_{238}\right)\lambda_{232}{}^{2}\frac{\mathrm{d}\Psi_s}{\mathrm{d}m_{232}}}{f_{238}\lambda_{238}\frac{\mathrm{d}\Psi_s}{\mathrm{d}m_{238}} + \left(1-f_{238}\right)\lambda_{232}\frac{\mathrm{d}\Psi_s}{\mathrm{d}m_{232}}}, \tag{2.2}$$

where λ_{232} and λ_{238} are the linearized decay rates for the respective fissionable isotope.

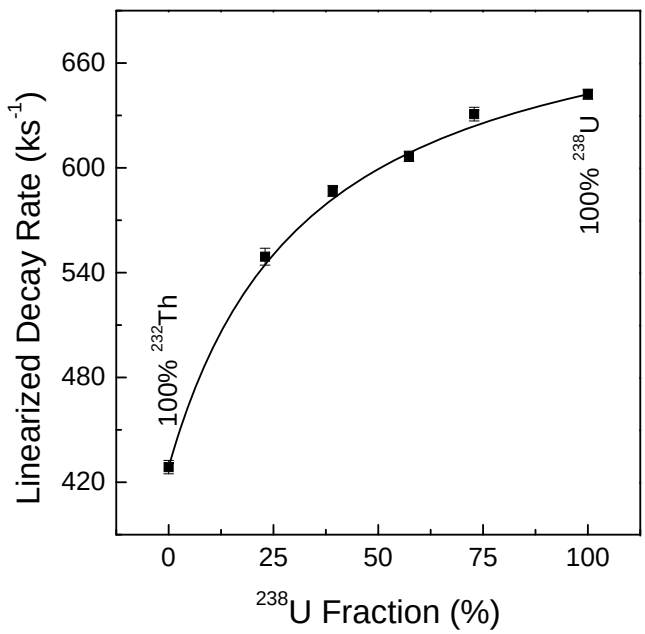

Figure 2.7: Delayed neutron linearized decay rates versus relative ^{238}U concentration. The targets were the two single component solutions containing 5.3% ^{232}Th or 4.7% ^{238}U and the four bi-component solutions, which contained both ^{232}Th and ^{238}U. The accelerator was operated at 16 MeV at 7.5 Hz with $\sim$120 nC per pulse. The neutrons were detected between bremsstrahlung pulses for 75 min. The solid line is the linearized decay rate as predicted by equation (2.2).

Using the calibration factors for ^{232}Th and ^{238}U from Figure 2.5 and the linearized decay rates from the single component ^{232}Th and ^{238}U solutions, the expected decay rate as a function of the relative ^{238}U concentration is overlaid in Figure 2.7. The agreement is striking with a maximum difference of only $\sim$1% between the predicted and measured rates. For a bi-component solution with an unknown isotopic ratio, f_{238}, equation (2.2) can be inverted to give

$$f_{238} = \frac{\lambda_{232}\frac{\mathrm{d}\Psi_s}{\mathrm{d}m_{232}}\left(\lambda_{232}-\lambda_{bic}\right)}{\lambda_{232}\frac{\mathrm{d}\Psi_s}{\mathrm{d}m_{232}}\left(\lambda_{232}-\lambda_{bic}\right)+\lambda_{238}\frac{\mathrm{d}\Psi_s}{\mathrm{d}m_{238}}\left(\lambda_{bic}-\lambda_{238}\right)}. \tag{2.3}$$

Hence, a system with measured calibration factors and linearized decay rates from "samples" containing a single fissionable isotopes can measure the isotopic ration of an unknown sample.

To measure the linearized decay rates, the neutrons were detected between bremsstrahlung pulses for 75 min, which is ten times longer than what was required for determining the minimal detectable masses. A faster method to obtain isotopic information using delayed neutrons is to measure the yield at multiple bremsstrahlung endpoint energies, thereby

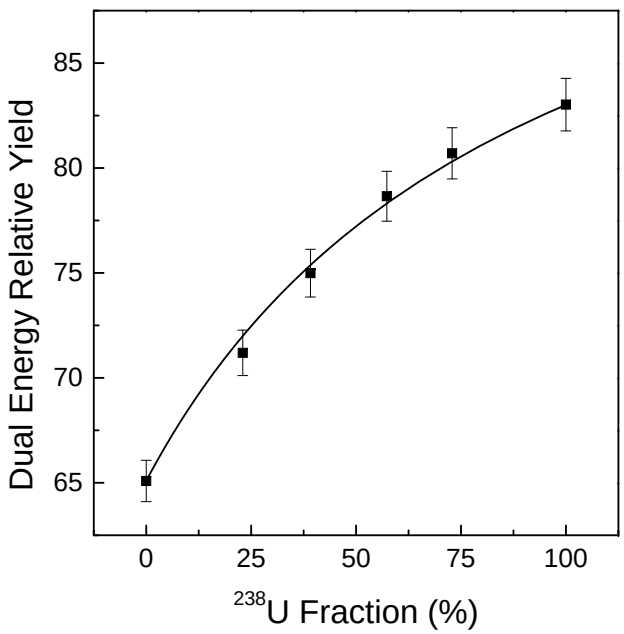

Figure 2.8: Delayed neutron dual energy relative yield versus relative ^{238}U concentration. The targets were the two single component solutions containing 5.3% ^{232}Th or 4.7% ^{238}U and the four bi-component solutions, which contained both ^{232}Th and ^{238}U. The accelerator was operated at 7.5 Hz with $\sim$66 and $\sim$120 nC of charge per pulse at 11 and 16 MeV. The neutrons were detected between bremsstrahlung pulses for 5 min at each bremsstrahlung endpoint energy. The solid line is the relative yield as predicted by equation (2.4).

exploiting differences in the sizes and shapes of the photofission cross sections. A simple example is the dual energy relative yield technique, which measures the delayed neutron yield at a bremsstrahlung energy relative to the yield at a reference energy. If a low bremsstrahlung energy is chosen as the reference energy, the relative delayed neutron yield is larger for ^{238}U compared to ^{232}Th because the ^{238}U cross section is relatively larger at higher bremsstrahlung energies. While the absolute neutron yield depends on the total mass of fissionable isotopes, this relative yield is independent of total fissionable mass. Figure 2.8 shows this relative yield from the single and bi-component solutions using a 16 MeV bremsstrahlung endpoint energy and 11 MeV as the reference energy. The difference between the relative yields were large with a $\sim 10\sigma$ change between pure ^{232}Th and ^{238}U. Furthermore, this relative yield monotonically increased with the ^{238}U concentration without saturating, demonstrating how the isotopic ratio can be determined. Combining the delayed neutron relative yield and decay rate techniques, isotopic ratios from more complicated solutions may be obtained.

The relative yield for bi-component solutions can be calculated solely from the calibration

factors, $\mathrm{d}\Psi_s/\mathrm{d}m_f$, at both energies and for both fissionable species. For a bi-component solution with a relative ^{238}U concentration, f_{238}, the relative yield is given by

$$D_{bic}(f_{238}) = \frac{f_{238}\frac{\mathrm{d}\Psi_{E_i}}{\mathrm{d}m_{238}} + (1 - f_{238})\frac{\mathrm{d}\Psi_{E_i}}{\mathrm{d}m_{232}}}{f_{238}\frac{\mathrm{d}\Psi_{E_o}}{\mathrm{d}m_{238}} + (1 - f_{238})\frac{\mathrm{d}\Psi_{E_o}}{\mathrm{d}m_{232}}}, \tag{2.4}$$

where the $\mathrm{d}\Psi_{E_o}/\mathrm{d}m_x$'s are the calibration factors at the reference energy and the $\mathrm{d}\Psi_{E_i}/\mathrm{d}m_x$'s are the calibration factors at the inspection bremsstrahlung endpoint energy. Using the calibration factors for ^{232}Th and ^{238}U in Figure 2.5, the expected relative yields as a function of the relative ^{238}U concentration is overlaid in Figure 2.8. The agreement is good with a maximum difference of $\sim 1\%$ between the predicted and measured relative yields. For a bi-component solution with an unknown isotopic ratio, f_{238} can be calculated by inverting equation (2.4) giving,

$$f_{238} = \frac{\frac{\mathrm{d}\Psi_{E_i}}{\mathrm{d}m_{232}} + D_{bic}\frac{\mathrm{d}\Psi_{E_o}}{\mathrm{d}m_{232}}}{\frac{\mathrm{d}\Psi_{E_i}}{\mathrm{d}m_{232}} - \frac{\mathrm{d}\Psi_{E_i}}{\mathrm{d}m_{238}} + D_{bic}\left(\frac{\mathrm{d}\Psi_{E_o}}{\mathrm{d}m_{238}} - \frac{\mathrm{d}\Psi_{E_o}}{\mathrm{d}m_{232}}\right)}. \tag{2.5}$$

Again, a properly calibrated system can measure the isotopic ration of an unknown samples.

2.3 SiO_2 Matrix

The next experimental campaign focused on measuring delayed neutrons from ^{232}Th, ^{238}U, ^{235}U and ^{239}Pu in a SiO_2 matrix. The primary goal was to study the effects of a different matrix on the minimal detectable masses and the specificity techniques developed with the aqueous solutions. Figure 2.9 shows the gross neutron yield detected in the delayed neutron region as a function of the bremsstrahlung energy for the pure SiO_2, 6% ^{232}Thand 6% ^{238}U 1.6 kg SiO_2 targets. In a similar manner to the aqueous targets, the delayed neutron yields increased with higher bremsstrahlung endpoint energy from the SiO_2 targets that contained fissionable isotopes. From 7 to 16 MeV, the delayed neutron yield increased by a factor of $\sim$190 for the target containing ^{238}U isotopes. As with the pure H_2O target, the background, which is represented by the pure SiO_2 target, only increased by a factor of ~ 8 from 7 to 16 MeV. Hence the delayed neutron fission signal from the ^{238}U containing target is $\sim$680 times above background at 7 MeV and grows to over $\sim 2 \times 10^4$ times above background at 16 MeV. This larger relative yield from the SiO_2 targets containing fissionable isotopes compared to the H_2O targets was the result of the larger ^{238}U and ^{232}Th mass in the SiO_2

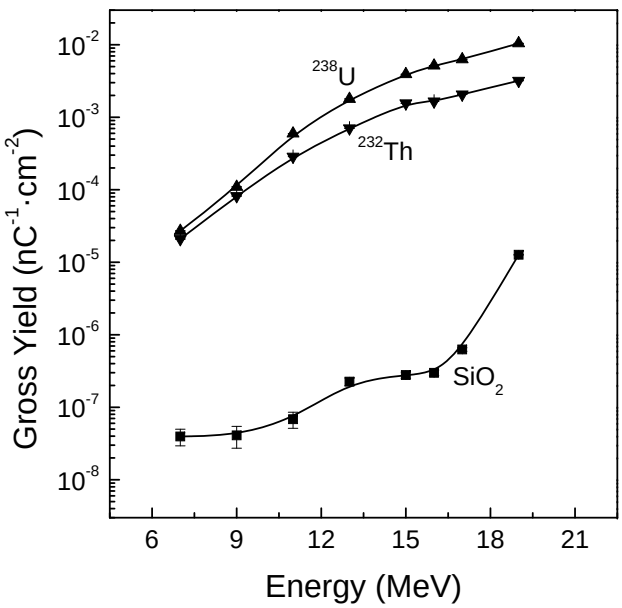

Figure 2.9: Detected delayed neutron yield versus bremsstrahlung endpoint energy for the 6% ^{232}Th (▼), 6% ^{238}U (▲) and pure SiO_2 (■) ∼1.6 kg SiO_2 matrix targets. The bremsstrahlung beam had a repetition rate of 7.5 Hz. The delayed neutron yield was calculated by integrating differential yield, like that presented in Figure 2.2 from 20 to 131 ms.

targets; ∼125 versus ∼52 g. At 7 and 9 MeV the background from the pure SiO_2 target is indistinguishable from the natural passive neutron background but as the bremsstrahlung energy increased above these energies there is an active background component. These gross yields from the pure SiO_2 target are nearly identical to those measured from the pure H_2O and below ∼16 MeV is a combination of natural passive background and thermal neutrons streaming into the detector. Above, ∼16 MeV, the background again increased drastically due to the $^{18}O(\gamma,p)^{17}N$ reaction.

The delayed neutron yields were measured at 11 and 16 MeV bremsstrahlung endpoint energies for the fissionable mass SiO_2 targets, which contained ^{232}Th or ^{238}U with mass concentrations between ∼0.5 and 8%. As for the aqueous solutions, the increasing mass targets which contained a single fissionable component were used to correlate the measured delayed neutron yields to the fissionable mass content. The results are presented in Figure 2.10. There is considerably more scatter from the least squares fit for the SiO_2 matrix mass calibration data than was observed for the aqueous targets. These inconsistencies arise primarily from an uneven distribution of the fissionable mass through the target. Whereas the aqueous solutions contained the fissionable masses in a nitrate form which dissolved and

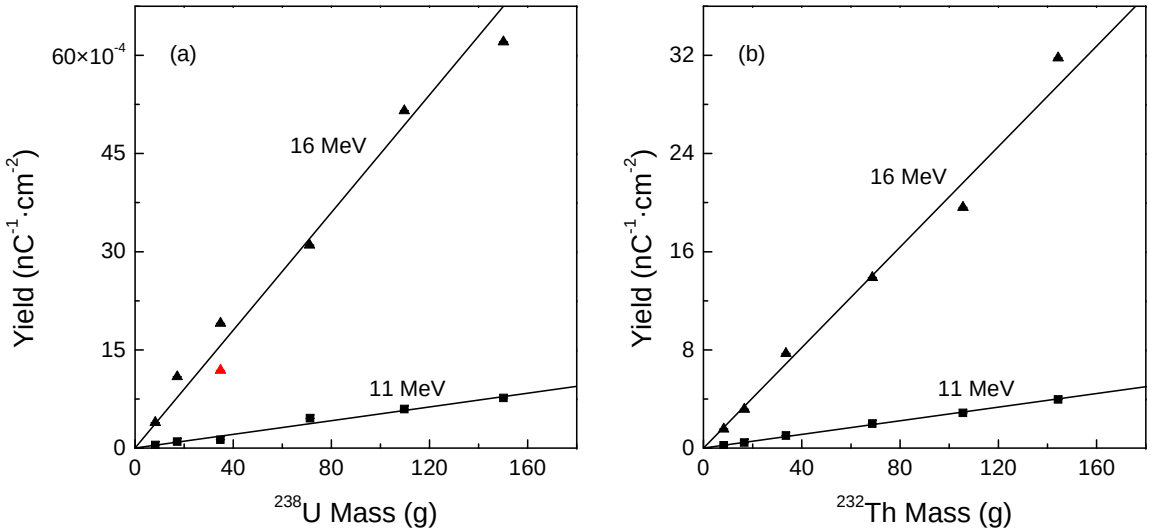

Figure 2.10: Delayed neutron yield versus the fissionable mass for the ^{238}U (a) and ^{232}Th (b) SiO_2 matrix targets using 11 MeV (■) and 16 MeV (▲) bremsstrahlung endpoint energies. The accelerator was operated at 7.5 Hz with $\sim$66 and $\sim$120 nC of charge per pulse at 11 and 16 MeV, respectively.

provided a uniform mass distribution of the target, the SiO_2 targets contain the fissionable mass in an oxide form, which are granular and did not distribute uniformly throughout the target. In essence, the sand and the fissionable oxides were not thoroughly mixed to produce a uniform distribution of ^{232}Th or ^{238}U. Overlaid on Figure 2.10 is a single data point for the 2% ^{238}U in an SiO_2 matrix in which the target was simply rotated by 180°. The yield from the rotated target was $\sim$38% lower than the original orientation, demonstrating the effects from the nonuniform distribution of the ^{238}U. Nevertheless, the calibration factor $d\Psi_s/dm_{232}$ for ^{232}Th is 2.78 ± 0.04 and 20.5 ± 0.7 mC^{-1}·cm^{-2}·g^{-1} at 11 and 16 MeV bremsstrahlung endpoint energy. The calibration factor $d\Psi_s/dm_{238}$ for ^{238}U is 5.2 ± 0.3 and 45 ± 2 mC^{-1}·cm^{-2}·g^{-1} at 11 and 16 MeV bremsstrahlung endpoint energy. On average, these sensitivities are $\sim$20% higher than the sensitivities from the aqueous targets because of the lack of the hydrogenous matrix material. The increased sensitivity to fissionable isotopes leads to a corresponding $\sim$20% decrease in the minimal detectable masses. However, the overall shape of the detection limit as a function of bremsstrahlung endpoint energy for the SiO_2 matrix targets is the same as the aqueous targets, just a little bit lower.

As for the aqueous solutions, long runs were acquired for the single component SiO_2 matrix targets containing 6% ^{232}Th and 6% ^{238}U by mass, and for the bi-component targets with the normalized yields presented in Figure 2.11. Again, the rate of decay from these

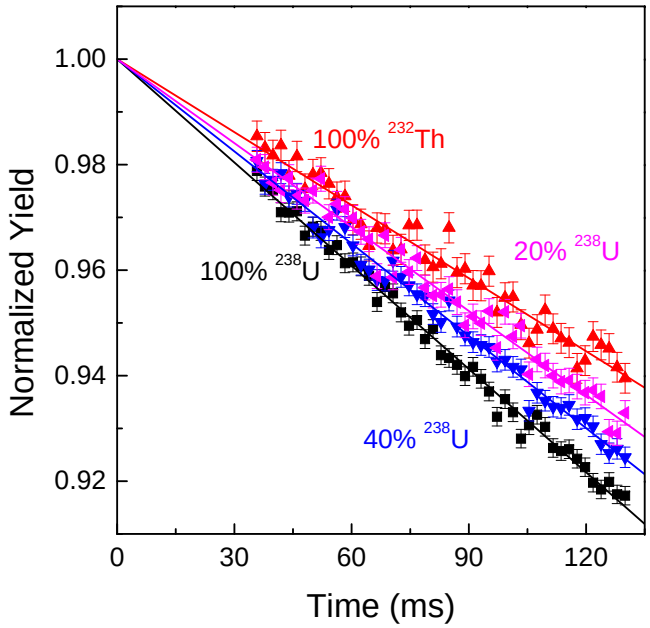

Figure 2.11: Normalized delayed neutron yields versus time after the bremsstrahlung pulse from the 6.0% ^{232}Th (▲), 6.0% ^{238}U (■), Mixed-C (▼) and Mixed-D (◀) SiO_2 matrix targets. The data was normalized so that the y-intercept of the linear fit was unity. The accelerator was operated at 16 MeV at 7.5 Hz with $\sim$120 nC per pulse. The neutrons were detected between bremsstrahlung pulses for 30 min.

pure targets are clearly different, permitting the discrimination of samples containing ^{238}U or ^{232}Th. Overlaid in Figure 2.11 is the normalized yield from two bi-component targets containing $\sim$6% total fissionable mass with relative ^{232}Th(^{238}U) concentrations of 60%(40%) and 80%(20%). The normalized yields of these bi-component targets fall between the single component targets with the higher concentration of ^{232}Th(^{238}U) closer to the single component ^{232}Th(^{238}U) target. To exploit these differences, least square linear fits were performed on the normalized yields to obtain the linearized decay rates for the targets. These decay rates are shown in Figure 2.12 as a function of relative ^{238}U concentration for the two single component targets and the four bi-component targets. The differences in the rates are drastic, with a $\sim 30\sigma$ change between pure ^{232}Th and ^{238}U. The linearized decay rate monotonically increased with the ^{238}U concentration without saturating before a 100% relative ^{238}U concentration. Using equation (2.2), the linearized decay rates from the single component ^{232}Th and ^{238}U targets, the expected decay rate as a function of the relative ^{238}U concentration is overlaid in Figure 2.12. The agreement is good with a maximum difference of only $\sim$3% between the predicted and measured rates. However, the agrement is

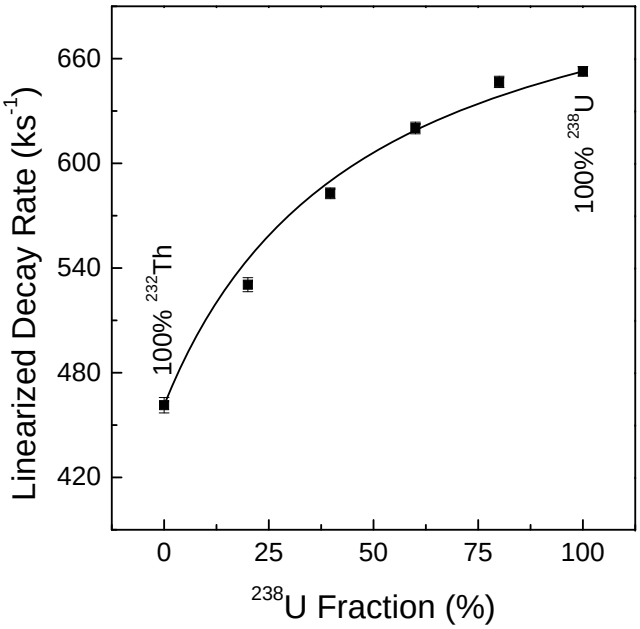

Figure 2.12: Delayed neutron linearized decay rates versus relative ^{238}U concentration. The targets were the two single component SiO_2 matrices containing 6.0% ^{232}Th or ^{238}U and the four bi-component matrices, which contained both ^{232}Th and ^{238}U. The accelerator was operated at 16 MeV at 7.5 Hz with $\sim$120 nC per pulse. The neutrons were detected between bremsstrahlung pulses for 30 min. The solid line is the linearized decay rate as predicted by equation 2.2.

not as good with the aqueous solution targets because of the previously discussed uneven distribution of the fissionable mass through the targets. Furthermore, this non-homogenous distribution made the results from the dual energy relative yield technique unreliable.

2.4 Delivered Dose and Beam Profile

All the delayed neutron data has been normalized to the dose delivered to the target and should therefore allow easy scaling of the experimental data to different applications. Measurements of the dose were performed at energies between 8 and 19 MeV by placing Gafchromic film in the location of the target. The film was in between $\sim$ 6.4 mm thick and $\sim$5.1 cm thick polyethylene blocks for electron equilibration. At 7 MeV the dose rate was too low to measure using Gafchromic film and hence the film was replaced with a more sensitive optically stimulated luminescence dosimeter. Figure 2.13 shows the measured dose per unit charge incident on the bremsstrahlung radiator at six different energies. Between 7

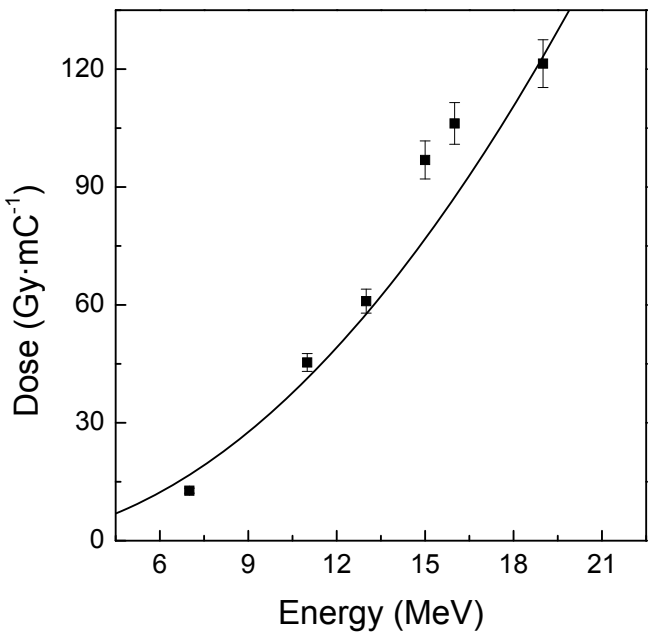

Figure 2.13: Measured dose per unit charge incident on the bremsstrahlung radiator versus energy. A dosimeter was positioned in the center of the bremsstrahlung beam 30.48 cm from the radiator. To ensure an electron equilibrium, the dosimeters were placed between ~ 6.4 mm and ~ 5.1 cm thick polyethylene blocks. The solid line is best fit to a pure quadratic.

and 19 MeV, this dose per unit charge is expected to transition from a cubic to a quadratic with respect to the bremsstrahlung endpoint energy, E_o[27]. The data agrees well with

$$D(E_o) = AE_o^2, \tag{2.6}$$

where $A = 0.341$ Gy·mC^{-1}·MeV^{-2}, which was found by a least squares fit to the data.

Chapter 3

Delayed γ-rays

3.1 Introduction and Experimental Setup

The experiments summarized in this chapter investigated photon induced delayed γ-ray emission for nuclear forensics applications. The primary goal was to verify that the delayed γ-ray signature could be detected from small quantities of fissionable materials in aqueous solutions. Hence, these experiments used the 5.3% ^{232}Th, 4.7% ^{238}U and pure H_2O aqueous solution targets. More detailed information about these targets can be found in Appendix A. In addition to theses targets, metal ^{232}Th, ^{238}U, and mixed aqueous solution targets that contained both ^{232}Th and ^{238}U were used to identify individual delayed γ-ray lines, which can be used for specifying the fissionable isotopes. Following these experiments, additional research investigated how delayed γ-ray techniques can be utilized for identifying and quantifying the fissionable isotopes. This follow on research is covered extensively in the thesis by E. T. E. Reedy, which is attached as Appendix B[28].

A 25 MeV pulsed electron linear accelerator was used to produce electron beams with energies ranging from 9 to 22 MeV at a pulse frequency of 15 Hz. Each pulse from the accelerator was 4 μs wide, contained approximately 120 nC of electron charge and was incident on a 4.2 g·cm^{-2} water cooled tungsten radiator. The resulting bremsstrahlung photon beam was collimated through a 2 m wall into a shielded experimental cell. Collimation consisted of a 1.25 cm diameter Pb collimator 61 cm downstream of the radiator on the accelerator hall side of the wall, followed by a 6 cm diameter Pb collimator on the experimental cell side. Each sample was placed 1.63 m from the experimental cell collimator for a total distance of 4.24 m from the tungsten radiator. This resulted in a 10 cm diameter beam spot on target, leading to $\sim$55% of the total fissionable mass in an aqueous target being in the bremsstrah-

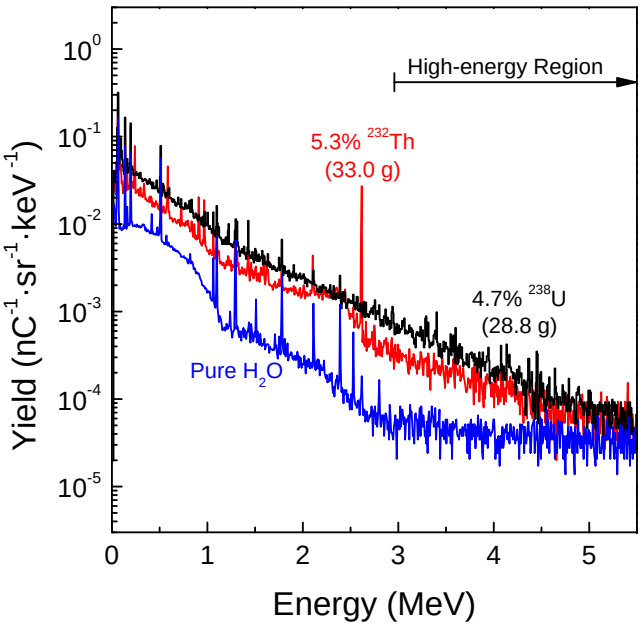

Figure 3.1: Energy spectra of 1 L solutions containing uranyl nitrate (black line), thorium nitrate (red line) and deionized water (blue line) taken between pulses at 19 MeV 15 Hz. The region above 3 MeV is indicated with an arrow as being high-energy.

lung beam. A mechanically cooled 104% relative efficiency high-purity germanium detector was placed 90° to the beam line at a distance of 25 cm to the target. This detector was placed in 5 cm of Pb shielding and 20 cm of borated poly to absorb neutrons. A 3.2 cm diameter by 5 cm deep Pb collimator was placed over the face of the detector. Energy spectra were collected from each target between irradiating bremsstrahlung pulses. The output from the HPGe detector was sent to a multi-parameter data acquisition system, which recorded both energy and time information in an event-by-event mode. The time data from the firing of the accelerator's electron gun identified when the bremsstrahlung pulse was incident on the target and by using this as a time fiducial, both energy and time information of the γ-rays detected by the HPGe detector could be examined.

3.2 Identification of the Photofission Signature

Figure 3.1 shows three typical energy spectra collected from the 5.3% ^{232}Th, 4.7% ^{238}U and pure H_2O aqueous targets using a 19 MeV bremsstrahlung beam. These spectra include γ-rays detected over all times between bremsstrahlung pulses and the presence of

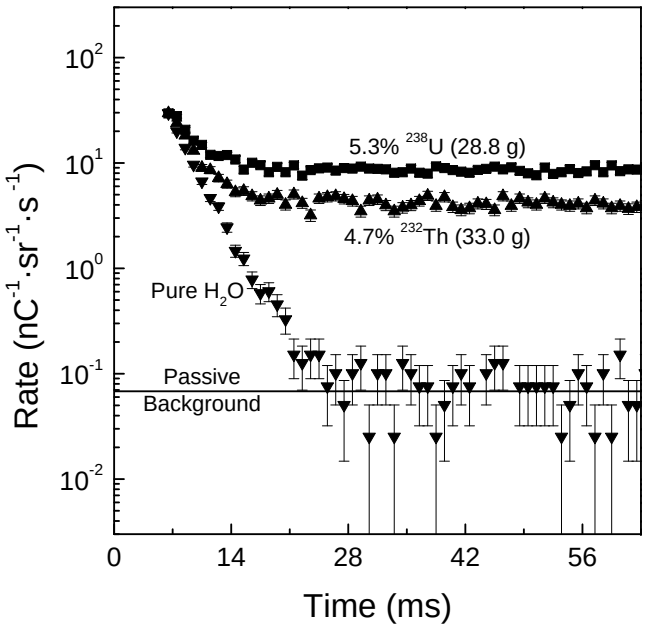

Figure 3.2: Delayed γ-ray yield above 3 MeV as a function of time after the bremsstrahlung pulse. The 1 L aqueous solutions of uranyl nitrate (■) and thorium nitrate (▲) are compared to deionized water (▼). The targets were subjected to a pulsed bremsstrahlung photon beam at 19 MeV 15 Hz. The delayed γ-ray region is indicated by the arrow above as being beyond 30 ms.

fissionable isotopes increases the yield throughout the entire energy range of the spectra. The high-energy region above 3 MeV shows promise as a signature of photofission; the cumulative yield of these γ-rays was five times larger for samples containing fissionable isotopes compared to samples with only non-fissionable materials. Unfortunately the observed high-energy "background," as represented by the pure water sample, increased with higher bremsstrahlung beam energies. Hence the cumulative yield of γ-rays above 3 MeV detected over all times does not produce a unique fission signature.

The difference between fissionable and non-fissionable materials can be enhanced by examining the timescales over which the high-energy γ-rays were detected. Figure 3.2 shows the time dependance of γ-rays above 3 MeV detected between bremsstrahlung pulses from ^{232}Th, ^{238}U and pure H_2O. These time spectra are from the same event-by-event data that generated the energy spectra of Figure 3.1. For the pure water target the high-energy γ-ray rate falls over two orders of magnitude to the passive background contribution within $\sim$28 ms after the bremsstrahlung pulse. These initial high-energy γ-rays are primarily from ^{A}Z(n,γ)^{A}Z reactions following the production of neutrons during the bremsstrahlung pulse.

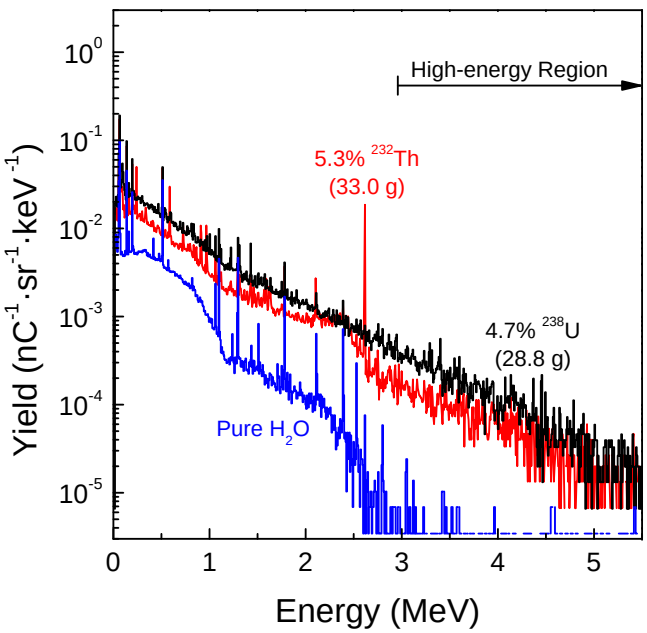

Figure 3.3: Energy spectra collected of 1 L solutions containing uranyl nitrate (black line), thorium nitrate (red line) and deionized water (blue line) taken between pulses at 19 MeV 15 Hz. The first 30 ms has been removed from the spectra.

In contrast, the fission fragments produced from the photofission of ^{232}Th and/or ^{238}U emit these high-energy γ-rays at an almost constant rate between pulses. Beyond $\sim$30 ms the detected high-energy γ-ray rate from the 4.7% ^{238}U target is over two orders of magnitude above targets without fissionable material. The measurable β-delayed γ-ray time window can vary depending on beam energy with longer time windows being utilized at higher beam energies.

By eliminating γ-rays detected between 0 ms and 30 ms, the background from non-fissionable materials can be minimized to the contribution from the natural passive background. Figure 3.3 shows the previous energy spectra from Figure 3.1 after removing γ-rays detected between 0 ms and 30 ms. The remaining spectra is from γ-rays detected after 30 ms and the high-energy γ-ray yield from the pure water target decreased by over a factor of 40. While the detected γ-ray yields from 5.3% ^{232}Th and 4.7% ^{238}U targets decreased with this time cut, the high-energy yield only decreased by $\sim$49%, leaving the the high-energy yield from the 4.7% ^{238}U sample over 65 times above the pure H_2O target. Hence, the delayed γ-ray fission signature was defined as γ-rays detected between 3 and 6 MeV at times between 30 and 66 ms after the bremsstrahlung pulse.

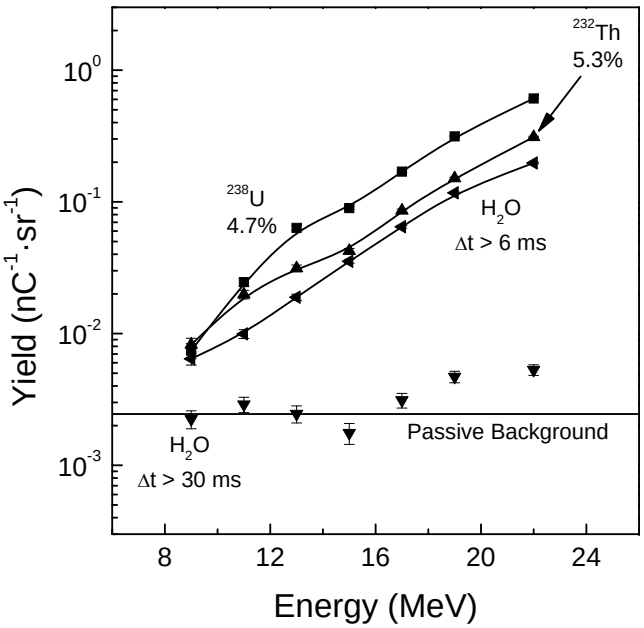

Figure 3.4: Delayed γ-ray yield above 3 MeV and beyond 30 ms as a function of bremsstrahlung endpoint energy. 1 L aqueous solutions of uranyl nitrate (■) and thorium nitrate (▲) are compared to deionized water (▼). Delayed γ-ray yields from deionized water are also represented without having removed the first 30 ms (◀).

Eliminating the early time high-energy γ-rays was effective across a wide range of bremsstrahlung endpoint energies. Figure 3.4 presents the gross γ-ray yield above 3 MeV and beyond 30 ms for each sample at bremsstrahlung energies from 9 to 22 MeV. The high-energy delayed γ-ray yield from samples containing fissionable isotopes increased by a factor of $\sim$60 as the bremsstrahlung endpoint energy was increased from 9 to 22 MeV. For the pure H_2O target, which represents the background, the gross yields are reasonably consistent with the natural passive background contribution up to $\sim$17 MeV. At 19 and 22 MeV the gross yield from the water target is above the passive background contribution, indicating the presence of some active beam induced background. Nevertheless, the relatively flat background from non-fissionable materials suggests that the delayed γ-ray signature is indeed unique to fissionable isotopes. These large signal to background ratios are only possible by removing the high-energy γ-rays detected in the first $\sim$30 ms after the bremsstrahlung pulse. To demonstrate the importance of this time cut, the gross high-energy γ-ray yield from the pure water target, including those detected in the first 30 ms, is overlaid in Figure 3.4. The inclusion of all times increases the gross high-energy γ-ray yield from the water target by a factor of $\sim$20, demonstrating the importance of the time cut.

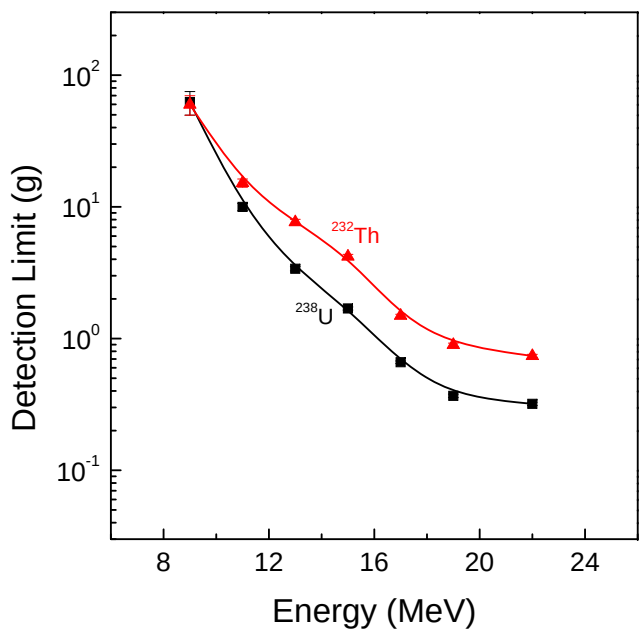

Figure 3.5: Minimal detectable mass as a function of bremsstrahlung endpoint energy for ^{238}U (■) and ^{232}Th (▲). Data in this graph represents a time and energy cut beyond 30 ms and above 3.0 MeV, respectively.

3.3 Minimal Detectable Mass of the 3 MeV Delayed γ-ray Signature

The minimal detectable level as outlined in Section 1.3 and implemented in Section 2.2.1 can be easily applied to the high-energy delayed γ-ray yield data of Figure 3.4. Again using the pure H_2O target as a known blank, the minimal detectable level for a paired observation is given by

$$L_d = \frac{k^2}{Q_t \Omega_d} + k\sqrt{2\frac{\Psi_{abk}}{Q_t \Omega_d}}, \tag{3.1}$$

where Q_t is the total charge on the radiator, Ω_d is the solid angle subtended by the HPGe detector (both for yield normalization) and Ψ_{abk} is the high-energy delayed γ-ray yield from the blank target. For the low mass targets utilized here, the minimal detectable mass can then be found through equation (1.28). The minimal detectable mass as a function of bremsstrahlung endpoint energy for ^{232}Th and ^{238}U in aqueous solutions is presented in Figure 3.5. In calculating the minimal detectable mass, the concept of operations was an accelerator with 100 nC of charge per pulse at 15 Hz inspecting 1 L aqueous targets for 300 s;

essentially the experimental conditions. The constant k was set at 1.645 which produces a symmetric 95% confidence interval; 5% false positives from solutions without fissionable isotopes and 5% false negatives for solutions with M_d of fissionable material. From 9 to 17 MeV, the minimal detectable mass decreases drastically because of the larger fission cross section and the increased bremsstrahlung production at higher energies. From 17 and 22 MeV the minimal detectable mass continues to decrease but more slowly. At 22 MeV the minimal detectable mass is $\sim$740 mg for ^{232}Th and 320 mg for ^{238}U. Again, increasing the charge on the bremsstrahlung radiator either by increasing the charge per pulse or the inspection time, decreases the minimal detectable masses approximately as $\sim Q_t^{-\frac{1}{2}}$.

3.4 Using Discrete Delayed γ-rays for Isotopic Ratio Comparison

Further investigation of the emissions from ^{232}Th and ^{238}U metal targets yielded several discrete γ-ray lines from photofission. Some of these discrete β-delayed γ-rays prove to be unique to either ^{238}U or ^{232}Th, while others are found in nearly equal intensity in both energy spectra. Figure 3.6 shows energy spectra of aqueous solutions ranging in concentration from 0.0% ^{232}Th and 100% ^{238}U to 100% ^{232}Th and 0.0% ^{238}U and a number of the fission fragments responsible for the discrete delayed γ-ray lines are labeled. Further information on these samples is found in appendix A. The more intense γ-ray lines have been labeled with their energy, corresponding fission fragment and half life. Of the six labeled delayed γ-ray lines, four are from fragments with half-lives less than one minute. The γ-rays from these short lived fission fragments are typically not observed in more traditional techniques, which irradiate the target for tens of minutes followed by an equally long data collection period. Furthermore, there are similarities and drastic differences between these delayed γ-ray spectra. For example, the $\sim$2662 keV line from ^{86}Se and ^{132m}Sb are approximately the same intensity in both spectra. In contrast, the line at $\sim$2944 keV from ^{98}Y, ^{88}Br and ^{106}Tc is almost nonexistent in the ^{232}Th spectrum but very strong in the ^{238}U spectrum. Additionally, the 2717 and the 2789 keV lines from ^{95}Sr and ^{106}Tc, respectively are present in the ^{238}U spectrum but absent from the ^{232}Th. Clearly the fissionable isotope can be uniquely identified based off of this type of fingerprint.

To determine the isotopic ratio of fissionable material contained within a sample, two peaks were selected that were present throughout the spectra collected in Figure 3.6. The intensity of the 2945 keV line is dominated by ^{88}Br and was selected due to its relatively

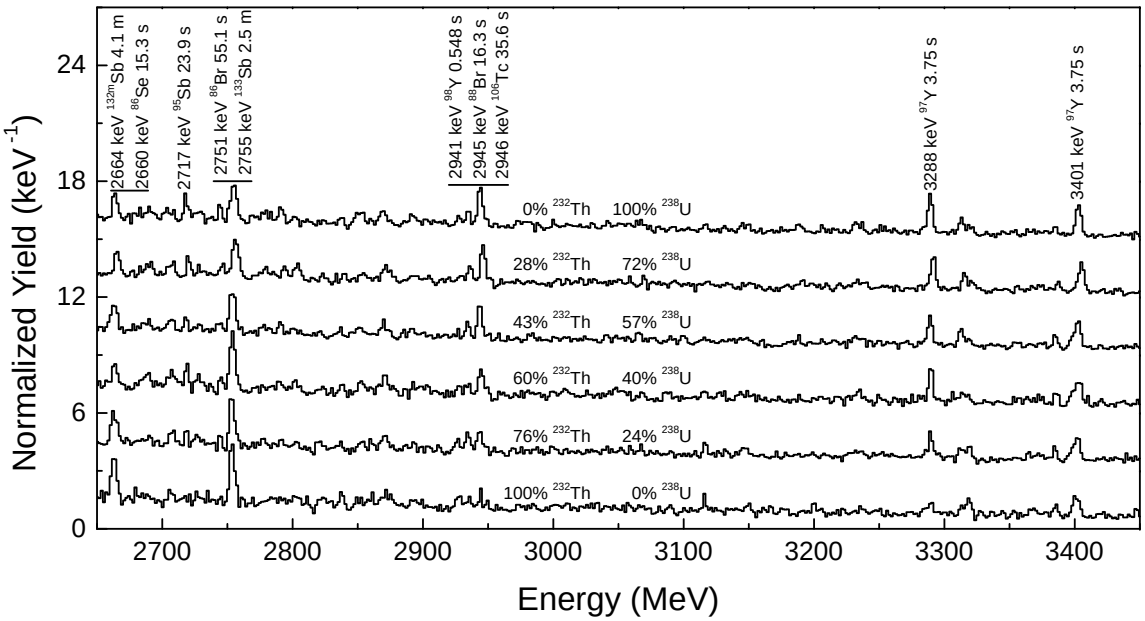

Figure 3.6: Energy spectra collected from aqueous bi-component solutions A, B, C and D as well as aqueous single component solutions containing 5.3% ^{232}Thand 4.7% ^{238}U beyond 13 ms. This gives a range of concentrations from 0.0% ^{232}Th and 100% ^{238}U to 100% ^{232}Th and 0.0% ^{238}U by mass. Relative concentrations of each sample are listed above their corresponding energy spectrum. Specific lines of interest as well as their generating fission fragment are also listed.

high intensity and appearance to vary as a function of concentration of ^{238}U in the sample. The $\sim$ 2753 keV line was selected as a fiducial peak for normalization since it appears invariant with concentration of either ^{238}U or ^{232}Th. This fiducial line is dominated by different fission fragments depending upon the fissioning isotope, with ^{86}Br dominating from the fission of ^{232}Th and ^{133}Sb dominating from ^{238}U fission. Figure 3.7 shows the ratio of the signal to fiducial ratio as a function of the relative concentration of ^{238}U and monotonically increases. The functional form of this ratio as a function of the relative ^{238}U concentration for a bi-component target is given by

$$R_{bic}(f_{238}) = \frac{f_{238}\frac{\mathrm{d}\Psi_{E_s}}{\mathrm{d}m_{238}} + (1 - f_{238})\frac{\mathrm{d}\Psi_{E_s}}{\mathrm{d}m_{232}}}{f_{238}\frac{\mathrm{d}\Psi_{E_f}}{\mathrm{d}m_{238}} + (1 - f_{238})\frac{\mathrm{d}\Psi_{E_f}}{\mathrm{d}m_{232}}}, \tag{3.2}$$

where the $\mathrm{d}\Psi_{E_s}/\mathrm{d}m_x$'s are the yield per unit mass of the signal discrete delayed γ-ray line and the $\mathrm{d}\Psi_{E_f}/\mathrm{d}m_x$'s are the yields per unit mass of the fiducial discrete delayed γ-ray line. This

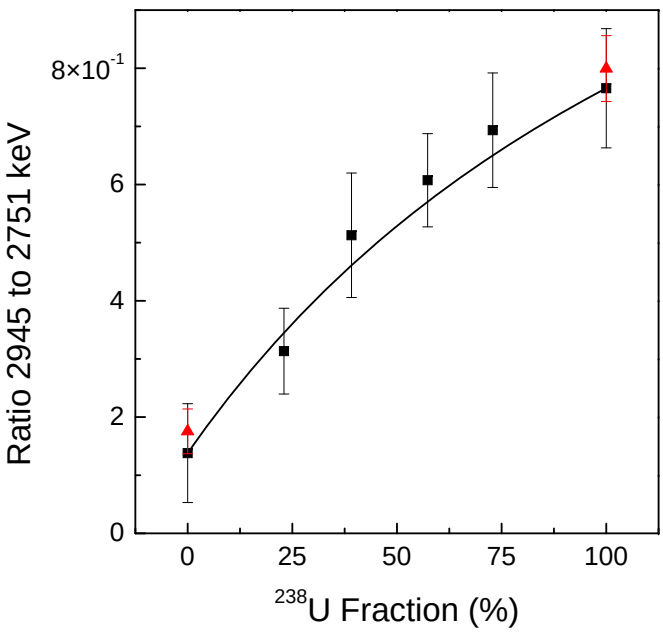

Figure 3.7: Ratios of 2945 keV and 2751 keV discrete γ-rays from ^{88}Br and ^{86}Br, respectfully, as a function of relative concentration of ^{238}U. Data is comprised of the same dataset as Figure 3.6 with added metal targets of ^{238}U and ^{232}Th under identical conditions expressed in red.

function is overlaid on Figure 3.7 and was calculated using the aqueous targets that contained only ^{232}Th or ^{238}U. The agreement with the ratios measured from the bi-component solution is good but the error bars from the measurements are rather large as result of the small net number of counts in each of the individual discrete γ-ray lines. These large error bars spurred the development of another technique that the team termed Spectral Composition Analysis which is described in the thesis by E. T. E. Reedy, which is attached at Appendix B[28].

3.5 Prediction of Discrete Delayed γ-rays from ^{238}U and ^{232}Th

These measured spectra can also be compared to what is expected based on the fission fragment yields published in nuclear reaction databases and/or the literature. In order to make this comparison, the neutron induced fission fragment yields were taken from T. R. England and B. F. Rider's technical report for incident neutrons with a fission energy spectrum [29]. For each fission fragment, the γ-ray branching ratio for every emitted γ-ray is multiplied

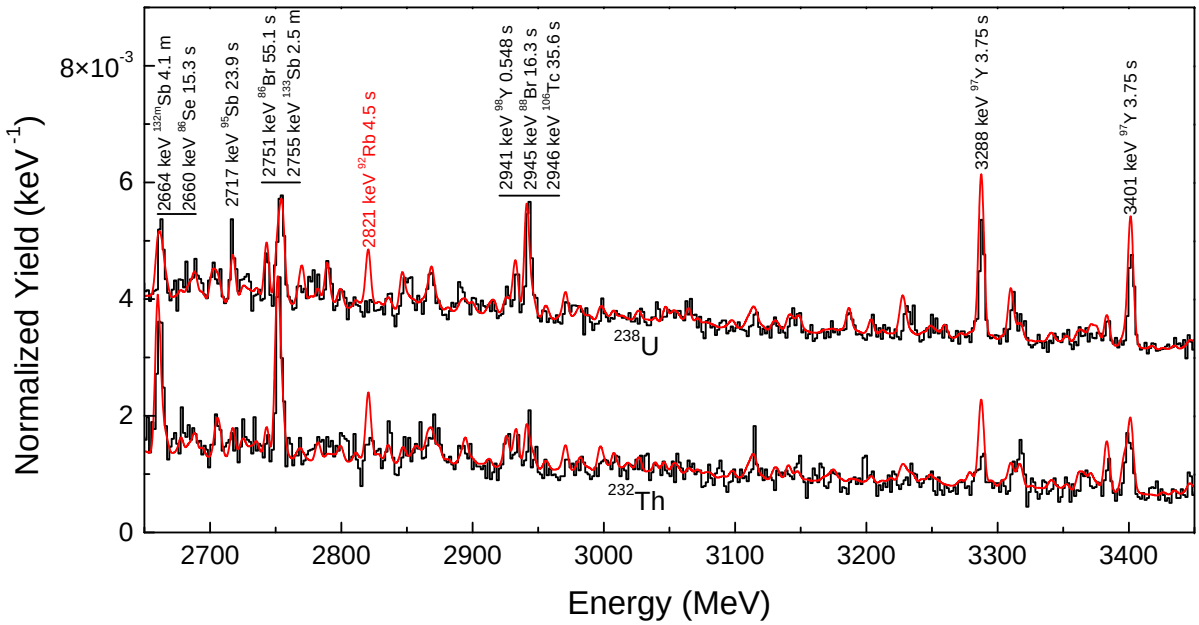

Figure 3.8: Energy spectra from ^{238}U and ^{232}Th collected at 19 MeV, 15 Hz with their associated energy spectrum calculated from neutron fast pool data overlaid. Major peaks are identified with their contributing fission fragments listed.

by the fission fragment yield. The resulting γ-ray yield distribution is then convoluted with the detector response function, which for simplicity has been assumed to be a Gaussian. These simulated spectra have been normalized to the $\sim$2753 keV line in the experimental data and overlaid in Figure 3.8. The simulated spectra are reasonably close to the observed experimental spectra but there are discrepancies. The fission fragment yields for the ^{98}Y, ^{88}Br and ^{106}Tc isotope trio, which produce the $\sim$2944 keV γ-ray line, are overestimated in ^{238}U. The fragment yields for the ^{86}Se and ^{132m}Sb isotope duo, which produce the 2662 keV γ-ray line, are overestimated in ^{232}Th. The largest discrepancy in the small energy region of Figure 3.8 is the tabulated fission fragment distributions suggestion that ^{92}Rb should be produced in large enough quantities to create a strong 2821 keV γ-ray line but this line is not observed in the ^{238}U nor ^{232}Th spectra. Over the full energy range there is a large number of discrepancies like those presented in this small energy region.

The discrepancies observed are not necessarily surprising and primarily arise from two possible inconsistencies in the fission fragment distribution. First, the fission fragment distributions are from a combination of theoretical calculations and experimental data. Hence, the yield of every fission fragment has not been measured independently, leading to possible

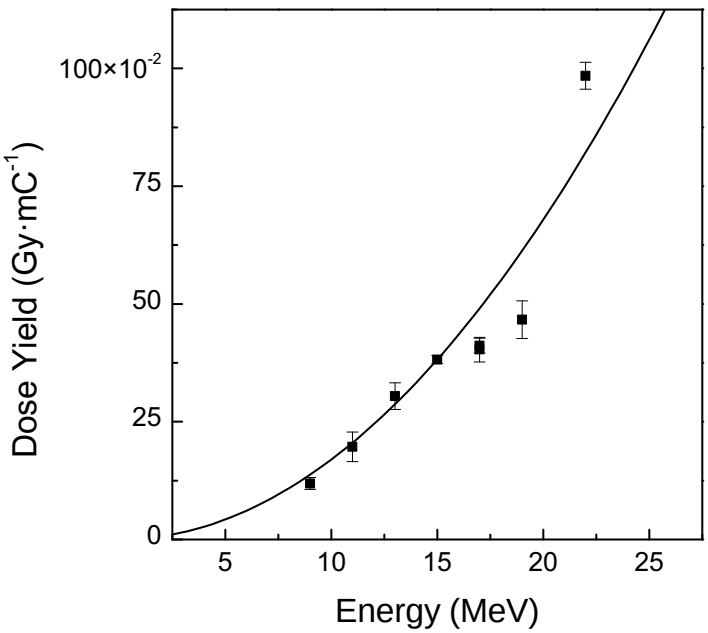

Figure 3.9: Measured dose per unit charge incident on the radiator as a function of bremsstrahlung endpoint energy. Four optically stimulated luminescence dosimeters were centered in the beam at the target location between two 0.63 cm thick polyethylene plates. The solid line indicates a best fit to the data using a pure cubic.

discrepancies when the distributions are compared to neutron induced fission data. This should be more problematic for short-lived fission fragments, which are the most difficult to measure and dominate the photofission data presented here. The second inconsistency can arise from comparing neutron induced fission fragment distributions to data collected from photofission because the fissioning systems are different. The fissioning system for ^{238}U(n,f) is ^{239}U (i.e. the ^{238}U nucleus absorbs the neutron and its kinetic energy, becoming ^{239}U, which fissions) but the fissioning system for ^{238}U(,f) is ^{238}U (i.e. the ^{238}U nucleus absorbs the γ-ray energy and fissions). While the exact cause of the discrepancies is not known and is outside of the scope of this project, the research team speculates that the latter issue dominates (i.e. neutron induced fission versus photofission).

3.6 Delivered Dose and Beam Profile

The data in this section is normalized to dose delivered to target and detector solid angle. Four optically stimulated luminescence dosimiters were centered in the beam at the target location at each electron beam energy. The dosimiters were placed between two 0.63 cm

thick polyethylene plates for electron equilibrium. The measurements from these dosimeters were used to produce a beam profile and determine the accumulated dose on target at each energy used. Figure 3.9 shows the results of the accumulated dose per unit charge on the converter as a function of bremsstrahlung endpoint energy. A least squares fit of the data was performed using a pure cubic,

$$D(E_o) = AE_o^2, \tag{3.3}$$

where $A = 1.70 \times 10^{-3}$ Gy·mC^{-1}·MeV^{-2}. This equation was used to normalize the data in this section to total delivered dose on target.

Chapter 4

Comparing Fission Signatures from Delayed γ-ray and Neutron Emissions

4.1 Introduction and Experimental Setup

In Chapters 2 and 3 delayed neutron and γ-ray emissions from fission reactions were measured and investigated independently as fission signatures. In the experiments presented in this chapter, the research team investigated fissionable material detection sensitivities of both delayed neutron and γ-ray signals from photofission in unshielded targets. The gross signature yields were measured simultaneously between intense bremsstrahlung pulses, allowing the minimal detectable fissionable masses to be easily calculated for each signature under identical inspection conditions. When the signatures are treated independently, these minimal detectable masses provide a methodology to impartially compare sensitivities. Furthermore, the simultaneous measurement of the two fission signatures opens up a multidimensional signature phase space in which the union of signature yields are considered. For the delayed neutron and γ-ray signatures the resulting two dimensional phase space of the joint yield adds considerable flexibility in choosing detection algorithms. This flexibility makes several advantages possible including increased sensitivity, a more robust shielding defeat, and minimization of interferences. While these advantages may not all be available concurrently they could be selected individually based on the requirements of a specific application.

The bremsstrahlung beams in these experiments originated from high-energy electrons generated by a 25 MeV electron linear accelerator impinging on a 4.2 g·cm^{-2} tungsten radiator. The accelerator produced 4 μs wide electron pulses at a 15 Hz repetition rate, leaving $\sim$66 ms intervals between pulses for detecting neutrons and γ-rays. The electron

charge contained in each pulse was between 50 and 225 nC and was dependent on the operating energy which varied from 7 through 22 MeV. The bremsstrahlung beam propagated from the accelerator hall into an adjoining experimental cell through a penetration in a 1.8 m thick wall. At the entrance and exit of the wall penetration the beam was collimated by 15.24 cm thick Pb collimators that were $\sim$ 300 cm and $\sim$ 4.8 m from the radiator with inner diameters of 1.3 and 3.8 cm, respectively. The target location was inside the experimental cell directly in the bremsstrahlung beam $\sim$ 6.4 m from the radiator, resulting in a $\sim$ 6.7 cm diameter bremsstrahlung beam spot. The target set included 13 fissionable and 19 non-fissionable targets with the fissionable targets containing either ^{238}U, ^{232}Th or ^{239}Pu; the fissionable mass in the bremsstrahlung beam ranged from 4.2 g to 1.7 kg. The non-fissionable targets included ^{9}Be, H_2O, D_2O, Fe, Cu and Pb, to name a few.

Unlike Chapter 3, the energy resolution was not a critical parameter and hence the HPGe detector was replaced with an array of six 5.08 cm diameter by 5.08 cm thick $Bi_4Ge_3O_{12}$ (BGO) scintillators coupled to negatively biased photomultiplier tubes. The utilization of BGO over NaI(Tl) crystals avoided neutron activation products from Na (primarily ^{23}Na(n,γ)^{24}Na) that interfere with the delayed γ-ray signature [30]. The comparison of BGO versus NaI(Tl) detectors in active inspection environments is covered extensively in the thesis by E. S. Cárdenas, which is attached as Appendix C[31]. To minimize energy deposited in the detectors during the intense bremsstrahlung pulse, 5.08 cm of Pb shielded the cylindrical sides of each detector in this 2 by 3 array. Additionally, 10.16 cm of Pb shielded the back and sides of the entire array leaving each detector with an unobstructed view of the target. The front face of the array was centered $\sim$1 m from the target with its surface normal perpendicular to the bremsstrahlung beam axis. Charge integrating preamplifiers conditioned the raw signals from each photomultiplier before being sent to the data acquisition system.

Neutrons were detected using a linear array of six 10 atm ^{3}He proportional counters surrounded by 2.54 cm of polyethylene moderator, 110 μm of Cd and 3.2 mm of borated elastomer. The neutron absorbing layers of cadmium and boron made the detection efficiency almost 400 times smaller for neutrons below 1 eV than for 10 keV neutrons[12, 20]. Hence, neutrons produced from photonuclear reactions during the bremsstrahlung pulse, which then thermalized in the environment, were not detected. The center of the linear array was $\sim$ 1 m from the target at an angle of $\sim 137^\circ$ with respect to the propagation direction of the bremsstrahlung beam. The pulse processing electronics were integrated into each neutron detector producing a logic pulse as neutrons were detected. More details about

these detectors can be found in the dissertation of M. T. Kinlaw[20].

A multi-parameter data acquisition system recorded the signals from the detectors along with the signal from the accelerator gun in an event-by-event list mode. After amplification, a set of analog to digital converters logged both the energy and time data of γ-rays detected by the BGO array. These analog to digital converters were gated off for 1 ms after the bremsstrahlung pulse to prevent data acquisition during detector recovery which occurred within $\sim$190 μs. A latched scaler counted the neutron pulses from the ^{3}He detector array with a time range that covered the period between bremsstrahlung pulses. The ^{3}He proportional counters recovered within $\sim$160 μs after the bremsstrahlung pulse. For both detector arrays, the time stamp of the accelerator gun trigger provided a reference that marked the detection time of neutrons and γ-rays relative to the bremsstrahlung pulse.

4.2 Energy and Time Spectra for Fission Signals

To maximize the difference between non-fissionable and fissionable materials, the delayed γ-ray fission signature exploited higher-energy γ-rays, which are not typically emitted by non-fission reaction products, naturally occurring radioactive materials, or commercially available radioisotopes[31–34]. Figure 4.1 compares γ-ray energy-time spectra collected between 16 MeV bremsstrahlung pulses irradiating metallic targets of 40.8 g·cm^{-2} Pb and 22.6 g·cm^{-2} ^{238}U. Both the Pb and ^{238}U targets fully subtended the bremsstrahlung beam with in-beam masses of $\sim$1.3 kg and $\sim$679 g respectively. The two dimensional false color histograms are the summation of $\sim 9 \times 10^{3}$ detection intervals with the initiating bremsstrahlung pulse of each 66.7 ms period aligned at $t = 0$. Emissions from the ^{238}U target drastically increased the high-energy photon intensity, making the two spectra strikingly distinct. The high-energy γ-ray yield, which was calculated by integrating the energy-time spectra from 3 to 5.5 MeV inclusive of all times, was over 3 times larger for the ^{238}U target. For the Pb target in Figure 4.1(a), over 99% of the high-energy γ-rays occurred within the first $\sim$15 ms after the bremsstrahlung pulse. Other non-fissionable targets produced similar sparsely populated high-energy spectra beyond $\sim$15 ms. In contrast, the ^{238}U target produced a fully populated high-energy spectrum at times beyond $\sim$15 ms due to emissions from short-lived fission fragments as seen in Figure 4.1(b). These high-energy γ-rays are not present in the passive spectrum of ^{238}U[35].

The decay and intensity of these high-energy γ-rays were more easily observed and quantified by integrating the energy-time spectra from 3 to 5.5 MeV, producing the time spectra

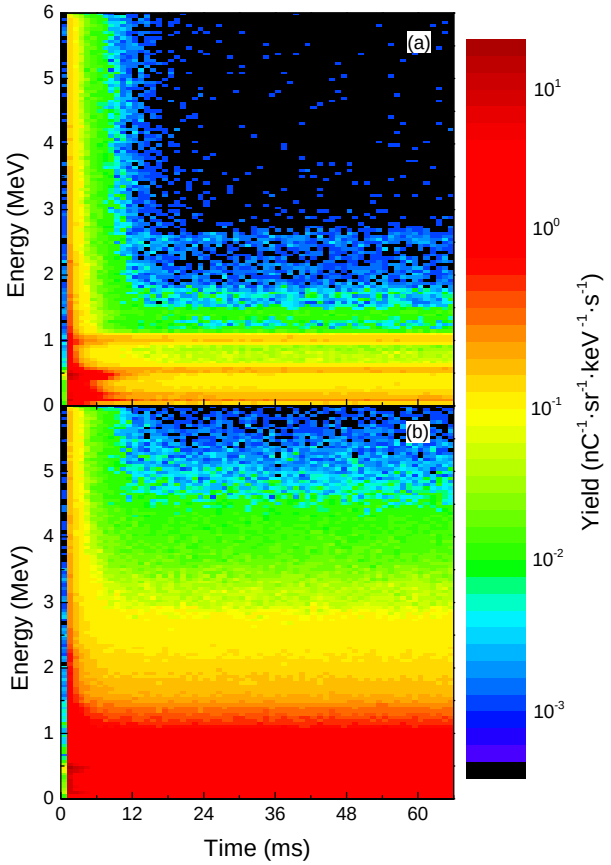

Figure 4.1: Energy-time spectra showing γ-ray intensity as a result of irradiating targets of metallic Pb in (a) and ^{238}U in (b). Operating parameters included a bremsstrahlung endpoint energy of 16 MeV, a pulse repetition rate of 15 Hz, an average charge on the radiator of $\sim$ 170 nC, and a target irradiation time of $\sim$ 600 s.

in Figure 4.2(a). In the first $\sim$30 ms, the rate plummeted three orders of magnitude for the Pb target until reaching the contribution from the natural passive background indicated by the solid line. The timescale of this initial decay suggested, and Monte Carlo simulations confirmed, that high-energy γ-rays from neutron capture reactions dominated the early times as neutrons produced in the radiator, target, and surrounding material thermalized in the environment[31]. In contrast to the Pb target, the ^{238}U target had only a slight decay during the first $\sim$ 13 ms and beyond $\sim$ 25 ms the high-energy γ-ray rate was over two orders of magnitude larger than the yield from the passive background. Consequently, the removal of γ-rays detected in the first 30 ms decreased the high-energy γ-ray yield for the Pb target by a factor of 370, leaving the yield for the ^{238}U target over 510 times larger. To take advantage of this dramatic increase in the differentiation between fissionable and non-fissionable

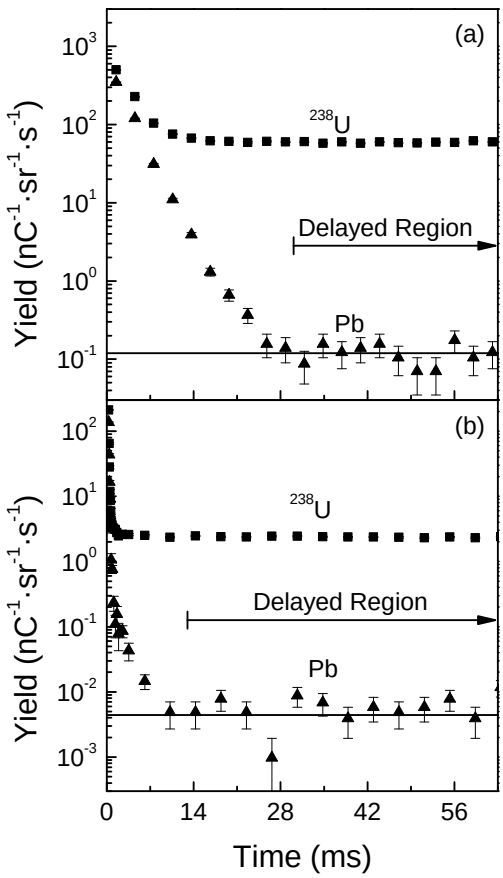

Figure 4.2: The high-energy γ-ray time spectra in (a) and neutron time spectra in (b) are normalized to an average charge per pulse of 170 nC, a pulsed repetition rate of 15 Hz, an average radiation time of 600 s, and solid angles of 0.012 sr and 0.159 sr for γ-ray and neutron detectors respectively. Spectra were produced by irradiating in-beam masses of 679 g of ^{238}U (■) and 1.3 kg of Pb (▲) with a bremsstrahlung photon endpoint energy of 16 MeV.

targets, the delayed γ-ray fission signature was defined as γ-rays above 3 MeV detected at times greater than 30.3 ms after the bremsstrahlung pulse.

Unlike delayed γ-rays, the delayed neutron signature relied solely on the detection of neutrons long after the bremsstrahlung pulse with neutron energy information only provided passively by the borated elastomer and cadmium filters around each detector. Figure 4.2(b) compares the neutron time spectra collected simultaneously with the γ-ray spectra presented in Figures 4.1 and 4.2(a). The neutron detection rate was initially very large for both targets and decreased rapidly as the copious quantity of neutrons created during the bremsstrahlung pulse scattered in the environment and returned to the detectors. For the Pb target, this rate decreased over five orders of magnitude within the first $\sim$13 ms until becoming equivalent

to the contribution from the natural passive background indicated by the solid line. The rate from the ^{238}U target did not decay to the passive background, but instead remained elevated over the Pb target by two orders of magnitude due to delayed neutron emissions. Nevertheless, the early time neutrons dominated the total yield inclusive of all times resulting in an integrated yield from the ^{238}U target only $\sim$20% larger than the Pb target. However, removing neutrons detected in the first 13.8 ms resulted in a yield for the ^{238}U target that was over 560 times larger than the Pb target and the passive background. To take advantage of this dramatic increase in the differentiation between fissionable and non-fissionable targets, the delayed neutron fission signature was defined as neutrons detected at times larger than 13.8 ms following the bremsstrahlung pulse.

4.3 Total Fission Signal Yields

Integrating the high-energy γ-ray and neutron yields over the signature regions, like those presented in Figure 4.2, resulted in the gross delayed γ-ray and neutron fission signals. Figure 4.3 presents these gross yields versus the bremsstrahlung end-point energy from the metallic ^{238}U target. The emission of delayed γ-rays and neutrons from the fission process dominated these yields and hence the γ-ray yield increased by over a factor of 600 and the neutron yield by over a factor of 500 from 7 to 22 MeV as the quantity of photofission reactions increased with bremsstrahlung energy. Moreover, the delayed γ-ray signal is on average $\sim$ 18 times larger than the delayed neutron signal primarily due to the increased yield of delayed γ-rays per fission reaction compared to neutrons.

For non-fissionable targets, the natural passive background dominated the high-energy γ-rays and neutrons detected in the signature region, resulting in detection rates that did not change drastically with bremsstrahlung energy. Furthermore, the gross yields scaled linearly with the total inspection time and not with bremsstrahlung intensity. To illustrate the magnitude of the background, the gross yield averaged over the non-fissionable targets and the passive background contribution are overlaid in Figure 4.3, assuming a bremsstrahlung beam generated by electron pulses with 150 nC of charge. The average yields from non-fissionable targets are consistent with the natural passive backgrounds up to 16 MeV, further verifying the uniqueness of the fission signatures. Above 16 MeV, the neutron yield remained consistent with the natural passive background but the high-energy γ-ray yield was 35% larger, indicating the presence of some actively induced background at the higher energies. Nevertheless, both fission signals from the ^{238}U target are $\sim$2.5 times larger than

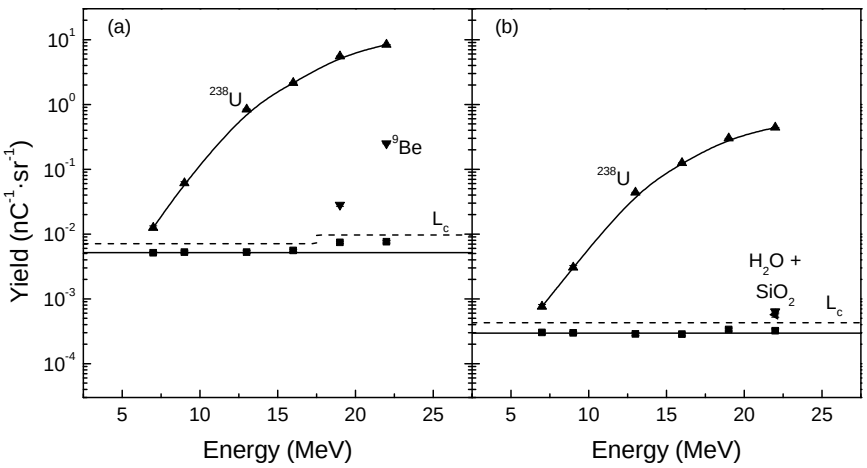

Figure 4.3: Gross integrated yields are presented for high-energy γ-rays in (a) and neutrons in (b). The ^{238}U target (▲) was irradiated with an average electron charge per pulse and time over all energies of 138 nC and 601 s respectively. Gross background yields (■) are an average of all non-fissionable targets irradiated excluding ^{9}Be for the high-energy γ-rays and oxygen containing targets for neutrons. This average yield assumes an electron charge per pulse of 150 nC.

the background at 7 MeV and this difference grows to over three orders of magnitude at 22 MeV, clearly demonstrating the fission signature. Similar to the fission signals, the background contribution from γ-rays is ~ 17 times larger than the contribution from neutrons due to larger natural passive background.

The background represented by the average non-fissionable gross yields shown in Figure 4.3 included measurements with no inspection object, Pb, H_2O, SiO_2 and ^{9}Be targets. Targets were excluded from these averages if they contained non-fissionable isotopes known to produce photonuclear reaction products that interfere with the fission signatures. The ^{9}Be target was excluded from the high-energy γ-ray averages at 19 and 22 MeV due to the ^{9}Be(γ,p)^{8}Li reaction. This reaction has a threshold of 16.9 MeV and the ^{8}Li reaction product has a 838 ms half-life, which β^--decays with an endpoint energy of 12.96 MeV, thereby interfering with the delayed γ-ray signature[36, 37]. The oxygen containing targets (i.e. H_2O and SiO_2) were excluded from the neutron average at 22 MeV due to the ^{18}O(γ,p)^{17}N reaction. This reaction has a threshold of 15.9 MeV and the ^{17}N reaction product has a 4.17 s half-life, which β^--decays followed by the emission of a neutron, thereby interfering with the delayed neutron signature[21, 36–38]. The yields from targets with known interfering reactions are shown separately in Figure 4.3. The high-energy γ-ray yield from the ^{9}Be target was ~ 4 and ~ 33 times larger than the yields from the remaining non-fissionable targets at 19 and

22 MeV respectively. The neutron yield from the oxygen containing targets was ~ 2 times larger than the yields from the remaining non-fissionable targets at 22 MeV. These interferences are clearly significant enough to lead to false positives in an inspection scenario but can be avoided by using lower bremsstrahlung energies. No interfering reactions were observed at or below 16 MeV. The ^{9}Be(γ,p)^{8}Li and ^{18}O(γ,p)^{17}N reactions do, however, portend the difficulties of utilizing higher-energy bremsstrahlung beams in which reaction channels are available that lead to interfering reaction products.

4.4 Detection Limits for Fissionable Materials

Excluding targets with interfering reaction products, the distinct differences in the gross yields between the fissionable target and the background, illustrated in Figure 4.3, were fairly consistent for both high-energy γ-rays and neutrons. In addition, the gross γ-ray yields were ~ 18 times larger than the neutron yields from the fissionable target but the γ-ray background was also ~ 17 times larger than the neutron background, making a comparison of the fission signals' detection efficacies difficult based on gross yields alone. The detection capabilities can be better quantified by estimating the detection limits, thereby allowing the minimum fissionable masses that can be reliably detected to be compared. As in Chapter 1, estimating the detection limit begins by calculating the critical decision level. Assuming a Gaussian is sufficient to describe the distribution of γ-rays or neutrons detected in the signature region during a single inspection, the critical decision level is given by

$$L_c = k_\alpha \sqrt{\frac{\psi_{abk}}{Q_i \cdot \Omega_d} + \frac{R_{pbk} \cdot T_d}{(Q_i \cdot \Omega_d)^2}}. \tag{4.1}$$

This expression is equivalent to the the critical decision level for a "Well-known" blank given by equation (1.13) with normalization by the total electron charge incident on the bremsstrahlung radiator, Q_i, and the solid angle subtended by the detector array, Ω_d[23]. The constant k_α is the abscissas of the standard normal distribution with a cumulative probability of $1 - \alpha$ with α being the false positive probability when no fissionable isotopes are present. In addition, the background has been explicitly separated into its active, ψ_{abk}, and passive, R_{pbk}, components with T_d being the total detection time. Hence the sum under the square root is the expected variance in the net yield due to the backgrounds alone.

The gross yield critical decision levels for a 1% false positive probability are overlaid on Figure 4.3 based on the average non-fissionable gross yields that excluded the interfering

reactions. Hence, the only discernable active background was in the high-energy γ-ray signature above a 16 MeV bremsstrahlung endpoint energy, resulting in a 35% increase in the critical decision level at higher energies. As expected, all signals from the ^{238}U target were substantially above the critical decision levels and the signals from the non-fissionable targets (not including interfering reactions) were below these levels, demonstrating the correct decisions of "detected" and "not detected" respectively. At higher bremsstrahlung endpoint energies, the yields from the ^{9}Be and oxygen containing targets were above the critical decision levels, causing them to be falsely identified as fissionable, due to the ^{8}Li and ^{17}N interfering reaction products.

For comparing fission signals, the detection limit is more important because it is an a priori estimate of the detection capabilities. The detection limit here is defined as the required mass, M_d, so that the false negative probability is β for a given critical decision level, L_c. For small mass targets where the yield is linearly related to the fissionable mass, the detection limit is given by combining equations (1.24) and (1.28) or explicitly

$$M_d = \left(\frac{dY_n}{dm_f}\right)^{-1} \cdot \left(\frac{k^2}{Q_i \cdot \Omega_d} + 2L_c\right), \tag{4.2}$$

when $k = k_\alpha = k_\beta$ so that the false positive and negative probabilities are equal. The first term in the equation, $\mathrm{d}Y_n/\mathrm{d}m_f$, is the net yield per unit fissionable mass and is essentially a calibration constant for the fission signal or inspection system. To minimize the attenuation of the probing bremsstrahlung beam, the calibration constant, $\mathrm{d}Y_n/\mathrm{d}m_f$, was measured from a uranyl nitrate aqueous target containing a 7.8% ^{238}U by mass, resulting in 24.3 g of ^{238}U in the bremsstrahlung beam. The detection limits as a function of bremsstrahlung endpoint energy for delayed neutrons and γ-rays is presented in Figure 4.4. In calculating the detection limits, the concept of operations was an accelerator with 150 nC of charge per pulse at 15 Hz inspecting a low mass target for 600 s; essentially the experimental conditions. Unlike the experiments, the γ-ray and neutron detector arrays were assumed to have the same active area of 1646 cm^2 and hence each subtended a solid angle of 159 msr. The false positive and negative probabilities were both 1%. From 7 to 13 MeV, the detection limits decreased by two orders of magnitude because of the larger fission cross section and the increased bremsstrahlung production at higher energies. Between 13 and 22 MeV the detection limits continued to decrease but only by a factor of $\sim$10. Furthermore, the delayed γ-ray signal was more sensitive to fissionable isotopes than the delayed neutron signal at all energies. At 7 MeV the delayed γ-ray detection limit was $\sim$4.3 times smaller than delayed neutrons with

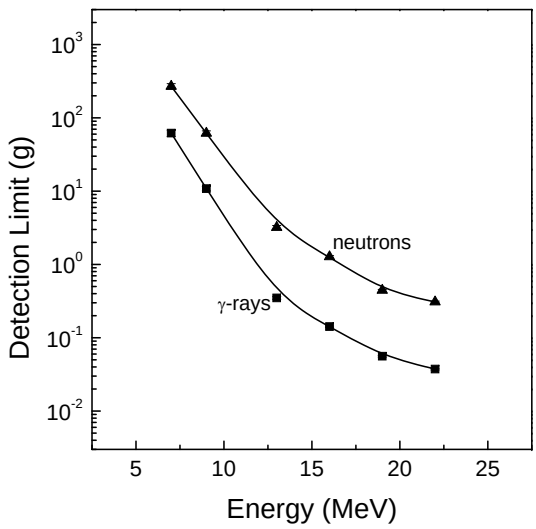

Figure 4.4: Minimal detectable mass presented for γ-rays (■) and neutrons (▲). An estimated average charge on target of 150 nC and 9000 inspection pulses were utilized. A detector solid angle of 0.159 sr was assumed identical for both γ-ray and neutron detectors. The detection system was calibrated with in-beam masses of 679 g at 7 and 9 MeV and 24.3 g for the larger bremsstrahlung energies. The detection sensitivity for γ-rays is greater than for neutrons for all energies examined.

an M_d of 61.9 g and this difference further increased to $\sim$8.2 times at 22 MeV with an M_d of 37 mg.

4.5 Two Dimensional Joint Yields

At bremsstrahlung endpoint energies up to 16 MeV, the gross high-energy γ-ray and neutron yields from the non-fissionable targets were dominated by the natural passive background. At higher energies, however, the reaction products from ^{9}Be(γ,p)^{8}Li and ^{18}O(γ,p)^{17}N were observed to interfere with the delayed γ-ray and neutron fission signals, respectively. To investigate the possibility of other interfering reaction products, the yields from a total of 19 non-fissionable targets were measured at 13 and 19 MeV. These targets included Al, ^{9}Be, Cu, Fe, Pb, H_2O, D_2O, LiF, SiO_2, C_2H_6O, $Na_2B_4O_7$ and a variety of commercial items (e.g. paper, wood, computer monitor etc...). In addition, the yields from 13 fissionable targets containing ^{232}Th, ^{238}U or ^{239}Pu were also measured with in-beam fissionable masses ranging from 4.2 g to 1.7 kg. Most of the low mass ^{232}Th and ^{238}U targets with less than 100 g of in-beam fissionable material were aqueous solutions of uranyl or thorium nitrate but also

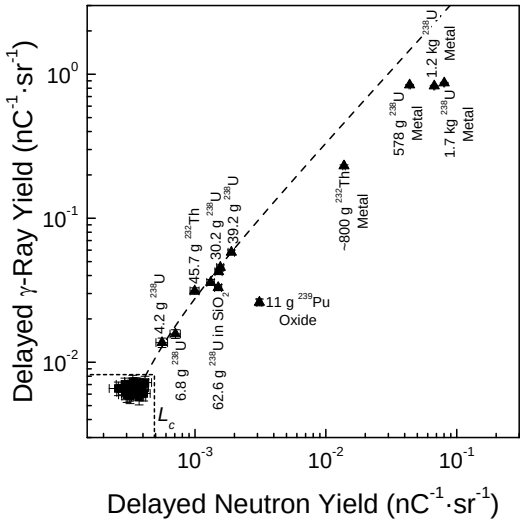

Figure 4.5: Two dimensional phase space presenting delayed γ-ray and neutron yields for 19 non-fissionable (■) and 13 fissionable (▲) targets. Targets were irradiated with a pulsed bremsstrahlung beam at an endpoint energy of 13 MeV for $\sim$ 600 s and a repetition rate of 15 Hz. The average charge per pulse was 119 nC.

included a few targets, which were SiO_2 mixed with uranium or thorium oxide. For a 13 MeV endpoint energy, Figure 4.5 presents the high-energy γ-ray and neutron yields as a scatter plot in the two dimensional gross signal phase space for all 32 targets. With the yield data displayed in this two dimensional joint form, the non-fissionable targets are grouped tightly together around the contribution from the natural passive background with a distribution consistent with Poisson counting statistics. The targets containing fissionable isotopes are spread out with significantly larger yields making them very distinct from the non-fissionable targets. Overlaid on Figure 4.5 is a linear parametric equation describing the relationship between the delayed γ-ray and neutron signal strengths that was determined from the low mass ^{238}U aqueous solution targets. Of course, the measured yields from the low fissionable mass targets agrees with this simple equation and the high fissionable mass targets deviate due to self absorption. The large neutron signal from the 11 g ^{239}Pu target was primarily from the spontaneous fission of ^{240}Pu, which constituted $\sim$5% of the target.

In addition to providing a clear way to visualize data from a large number of targets, the joint yields, comprised of multiple individual fission signals, allow flexibility in choosing the critical decision levels. In multiple dimensions these levels are surfaces and specifically in two dimensions there are essentially two flavors, logical "Or" or logical "And" boundaries. A simple logical "Or" boundary is shown in Figure 4.5 calculated using equation (1.42) with

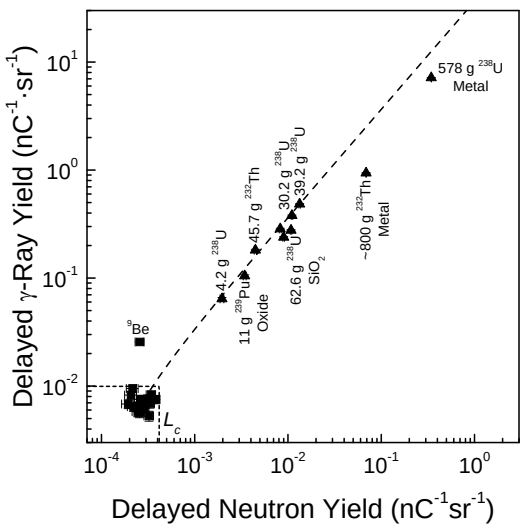

Figure 4.6: Two dimensional phase space examined with targets irradiated at a bremsstrahlung endpoint energy of 19 MeV for non-fissionable (■) and fissionable (▲) targets. All procedures and data analysis methods match those at 13 MeV as shown above with the exception of the average charge on target which was 167 nC.

the expected variance given by

$$s_{no_j} = \sqrt{\frac{\psi_{abk_j}}{Q_i \cdot \Omega_{d_j}} + \frac{R_{pbk_j} \cdot T_d}{(Q_i \cdot \Omega_{d_j})^2}}, \tag{4.3}$$

for the respective delayed neutron and γ-ray fission signals. The joint yields from all non-fissionable targets are within the "not detected" region in the lower left corner with no indication of any interfering reactions. In a complementary manner, the joint yields from all the fissionable targets are in the upper-right "detected" region. Increasing the bremsstrahlung energy to 19 MeV did not drastically change the distribution of the non-fissionable targets as seen in Figure 4.6, which shows the joint yield scatter plot along with the corresponding fission signal parametric equation and the logical "Or" decision boundary. The only observed interference was the already discussed ^{9}Be(γ,p)^{8}Li reaction, which was located in the detected region. The remaining 18 non-fissionable targets were within the "not detected" region and all the targets containing fissionable isotopes were in the "detected" region. The ^{9}Be(γ,p)^{8}Li and the ^{18}O(γ,p)^{17}N interferences can be eliminated by using a logical "And" boundary, requiring both the delayed γ-ray and neutron fission signals to be above their respective critical decision levels. However, the logical "And" boundary sacrifices sensitivity

and shielding defeat capabilities to prevent interferences.

Chapter 5

Fission Signal Interferences at Higher Bremsstrahlung Energies

5.1 Introduction

The experiments summarized in this chapter investigated the delayed neutron and γ-ray fission signal and more importantly interfering reactions from non-fissionable materials induced by interrogating bremsstrahlung beams with endpoint energies above $\sim$20 MeV. This research direction was spurred by a major Defense Threat Reduction Agency sponsored project to investigate standoff detection of fissionable materials utilizing endpoint energies up to $\sim$ 60 MeV. At these higher energies, there is a potential for opening up reaction channels in non-fissionable isotopes that lead to interferences.

In Chapters 2, 3 and 4 the delayed neutron and γ-ray fission signatures were developed using bremsstrahlung beams with endpoint energies up 22 MeV. For completeness these two signatures were defined as

- **Delayed neutron**. Generally, the signature is neutrons detected at long times after fission. For the photofission data presented in this report, the signature is neutrons detected $\sim$30 ms after the bremsstrahlung pulse until the beginning of the next pulse.
- **Delayed γ-ray**. Generally, the signature is high-energy γ-rays detected at long times after fission. For the photofission data presented in this report, the signature is γ-rays with energy above $\sim$ 3 MeV detected from $\sim$ 30 ms after the bremsstrahlung pulse until the beginning of the next pulse.

The exclusion of neutrons and γ-rays detected in the first tens of milliseconds immediately after the bremsstrahlung pulse from the fission signatures is necessitated by the large

number of neutrons generated by (γ,n), (γ,2n) etc... reactions in non-fissionable materials that are present in the target and/or the environment. As these "prompt" neutrons thermalize for tens of milliseconds, they are directly detected and produce high energy γ-rays through (n,γ) reactions. After excluding these early time neutrons and high-energy γ-rays the "background" from non-fissionable targets is dominated by the naturally occurring passive backgrounds, making the signatures unique and highly sensitive to fissionable materials.

The above fission signatures are effective at bremsstrahlung energies below $\sim$22 MeV because the dominant photonuclear absorption mechanism is through the giant dipole resonance (GDR), where the entire nucleus is excited. For fissionable materials, this excitation can lead to fission and the emission of the fission signals as the fission fragments, which are far from stability, decay to stable isotopes. For non-fissionable materials, photofission cannot occur but nucleons and few-nucleon particles (e.g. alphas) can evaporate from the target nuclei. At low excitation energies, a single nucleon or an alpha is typically emitted and the resulting daughter nuclei are stable or are close to the valley of stability. Hence, the vast majority of reaction products do not emit neutrons, high-energy γ-rays or high-energy β-particles that can interfere with the fission signals because radioisotopes close to the valley of stability tend to decay less energetically than those far from stability (many fission fragments are far from stability). Admittedly, the lack of significant interferences from non-fissionable materials with bremsstrahlung energies less than $\sim$22 MeV is somewhat serendipitous. However, two reaction products from ^{18}O(γ,p)^{17}N and ^{9}Be(γ,p)^{8}Li were found to interfere with the fission signatures at these bremsstrahlung energies. The former reaction product, ^{17}N, has a 4.2 s half-life decaying by neutron emission. The latter reaction product, ^{8}Li, has a 838 ms half-life decaying by β^{-}-particle emission with a 13 MeV endpoint energy. The thresholds for the reactions that produce these interfering reaction products have thresholds of 15.9 and 16.9 MeV, respectively. No significant interferences have been observed with bremsstrahlung endpoint energies below $\sim$16 MeV.

5.2 Interfering Reaction List/Database

With these higher bremsstrahlung energies, the possible excitation energies increases proportionally and a larger number of nucleons can evaporate after GDR absorption of the incident photon. In addition, quasideuteron absorption becomes important at higher energies, again increasing the probability of multiple nucleon losses for the target nuclei. In the end, the reaction products can be farther from the valley of stability with more energetic decays

that can interfere with the fission signatures. To identify potentially interfering reaction products, the research team started with the fission signature definitions and searched the Table of Isotopes and the Evaluated Nuclear Structure Data Structure File databases for radioisotopes that decay with the emission of one or more of the following [37, 39]

- **Neutrons**. Radioisotope with half lives greater than $\sim$3 ms, which decay by neutron emission. The half-life cutoff is 6 times smaller than the time region excluded in the delayed neutron fission signature.
- **Discrete high-energy γ-rays**. Radioisotope with half-lives greater than $\sim$ 5 ms, which decay by the emission of γ-rays above 3 MeV. The half-life cutoff is 6 times smaller than the time region excluded in the delayed γ-ray fission signature.
- **High-energy β-particle**. Radioisotope with half-lives greater than $\sim$ 5 ms, which decay by the emission of β-particles above 3 MeV. These high-energy particles primarily interfere with the delayed γ-ray signature through the production of bremsstrahlung photons above 3 MeV. The half-life cutoff is 6 times smaller than the time region excluded in the delayed γ-ray fission signature.

This search produced a long list of radioisotopes including the fission fragments responsible for the fission signatures. The vast majority of these radioisotopes cannot be produced in photonuclear reactions from naturally occurring non-fissionable isotopes, allowing the list to be greatly reduced by considering only the most probable reactions. Hence, the potential interfering reaction list was the intersection of the radioisotopes that emit neutrons, high-energy γ-rays and/or high-energy β-particles with the reaction products from the naturally occurring isotopes produced by the following 19 reactions, many of which lead to the same reaction products

- **Reaction product**. $^{A-1}$Z
  - (γ,n). Only reaction.
- **Reaction product**. $^{A-1}$(Z-1)
  - (γ,p). Only reaction.
- **Reaction product**. $^{A-2}$Z
  - (γ,2n). Only reaction.
- **Reaction product**. $^{A-2}$(Z-2)
  - (γ,2p). Only reaction.
- **Reaction product**. $^{A-2}$(Z-1)
  - (γ,d). Lowest threshold reaction.
  - (γ,np). Highest threshold reaction.

- **Reaction product**. $^{A-3}$Z
  - (γ,3n). Only reaction.
- **Reaction product**. $^{A-3}$(Z-2)
  - (γ,^{3}He). Lowest threshold reaction.
  - (γ,dp). Higher threshold reaction.
  - (γ,n2p). Highest threshold reaction.
- **Reaction product**. $^{A-3}$(Z-1)
  - (γ,t). Lowest threshold reaction.
  - (γ,dn). Higher threshold reaction.
  - (γ,p2n). Highest threshold reaction.
- **Reaction product**. $^{A-4}$(Z-2)
  - (γ,^{4}He). Lowest threshold reaction.
  - (γ,tp). Higher threshold reaction.
  - (γ,n^{3}He). Higher threshold reaction.
  - (γ,2d). Higher threshold reaction.
  - (γ,dpn). Higher threshold reaction.
  - (γ,2p2n). Highest threshold reaction.

The research team performed the intersection of the interfering radioisotope list with these reactions manually because it could not be automated easily. For neutron and discrete high-energy γ-ray interferences, this search and intersection process was relatively straight forward and has been performed for reaction products with atomic mass numbers from 1 to 100. For high-energy β-particle interferences, however, the search process was not straightforward because the available databases either were not complete (e.g. lacked β-particle emission data) or the database tools did not allow easy searches on β-particle endpoint energies. Consequently, the potential interfering reaction list for high-energy β-particles is hit and miss.

Each reaction identified as potentially interfering with the fission signatures was added to an appropriate list/database; neutron interferences, discrete high energy γ-ray interferences and high-energy β-particle interferences. A single reaction and reaction product can be and often is in multiple lists. As an example, ^{18}O(γ,p)^{17}N is in all three lists because the reaction product, ^{17}N, emits a neutron with a 95.2% branching ratio, a 3.8 MeV γ-ray with a 0.007% branching ratio and β-particles with 88.9% having endpoint energies above 3 MeV. For each reaction, the following data was compiled for the list/database

- **Target isotope**. The naturally occurring isotope, which is transmuted to the reaction product.
- **Elemental abundance in the earth's crust**. The weight percent of the element in the earth's crust.
- **Elemental abundance in earth's atmosphere**. Thee volume percent of the element in the earth's atmosphere.
- **Isotopic abundance**. The number percent for the specific isotope.
- **Reaction**. The photonuclear reaction that transmutes the target isotope to the reaction product.
- **Threshold**. The threshold in MeV of the reaction.
- **Reaction product**. The reaction product produced from the target isotope by the reaction.
- **Half-life**. The half-life in seconds of the reaction product.
- **Branch above 3 MeV**. For discrete high-energy γ-ray interferences, the fraction per decay above 3 MeV.
- **Branch neutron**. For delayed neutron interferences, the fraction of decays that emit neutrons.
- **Branch beta**. For high-energy β-particle inferences, the β-decay fraction.
- **Fraction above 3 MeV**. For high-energy β-particle inferences, the fraction of the β-decays with endpoint energies above 3 MeV.
- **Max beta endpoint energy**. For high-energy β-particle inferences, the maximum endpoint energy.
- **Tabulated cross section data**. Where tabulated cross section data can be found.
- **Experimental cross section**. First author of experimental cross section data reference on CSISRS [40].

With this information, the most concerning reactions can be easily identified by examining the abundance of the target isotope, reaction threshold, reaction product half-life, reaction product interfering branching ratio, etc... Of course, a crucial piece of information not captured directly in this list/database is the size of the reaction cross section. However, the availability of these cross sections in the tabulated databases and any known experimental measurements are both indicated. Either of these data sets can be easily downloaded [41].

Tables 5.1, 5.2 and 5.3 present the potentially interfering reaction lists for discrete high-energy γ-rays, neutrons and high-energy β-particles, respectively. For the interfering discrete high-energy γ-ray reactions in Table 5.1, 128 reactions have been identified after

searching atomic mass numbers 1 to 100. Of these reactions, only 24 have cross section measurements listed on the CSISRS database but somewhat surprisingly over 82% have cross section data on the ENDF or TENDL databases [36, 42]. Initially, 14 of the discrete γ-ray interferences were identified as being of greatest concern due to the target isotope abundance, reaction, reaction threshold, reaction product half-life and branching ratio above 3 MeV. Admittedly, the size of the reaction cross section was not considered with as much weight due to the lack of available data. For the interfering neutron reactions in Table 5.2, only five reactions were identified after searching reaction atomic mass numbers 1 to 230. Since all the target isotopes in these reactions are abundant, all were of concern. For the interfering high-energy β-particle reactions in Table 5.3, 45 reactions have been identified but as has been discussed previously, searching for high-energy β-particles is difficult. Hence, this list/database is not complete and some of these reactions were first discovered experimentally.

Table 5.1: Reactions and reaction products that can lead to interferences with the delayed γ-ray fission signal by the emission of discrete high-energy γ-rays. Reaction products with atomic mass numbers from 1 to 100 have been searched.

Index	Target Isotope	Elem. Abund. Crust Weight Percent	Elem. Abund. Atmosphere Volum Percent	Isotope Abund.	Reaction	Threshold (MeV)	Reaction Product	Half-life (s)	Branch above 3 MeV	Tabulated Cross Section Data	Experimental Cross Section Data
1	C-13	0.0300%	0.0383000%	1.1000%	(g,2p)	31.63	Be-11	13.81	0.105200	TENDL	None on CSISRS
2	C-13	0.0300%	0.0383000%	1.1000%	(g,p)	17.53	B-12	0.0202	Unquantified	ENDF	D. Zubanov
3	N-14	0.0050%	78.0840000%	99.6340%	(g,2p)	25.08	B-12	0.0202	Unquantified	ENDF	None on CSISRS
4	N-15	0.0050%	78.0840000%	0.3660%	(g,He-3)	28.20	B-12	0.0202	Unquantified	ENDF	None on CSISRS
5	N-14	0.0050%	78.0840000%	99.6340%	(g,2n)	30.62	N-12	0.011	Unquantified	ENDF	None on CSISRS
6	N-15	0.0050%	78.0840000%	0.3660%	(g,2p)	31.04	B-13	0.01736	0.090760	ENDF	None on CSISRS
7	O-16	46.6000%	20.9460000%	99.7620%	(g,3n)	52.06	O-13	0.00858	0.005600	No ENDF	None on CSISRS
8	O-16	46.6000%	20.9460000%	99.7620%	(g,2n)	28.89	O-14	70.606	0.000021	No ENDF	P. Carlos
9	O-17	46.6000%	20.9460000%	0.0380%	(g,2p)	25.26	C-15	2.449	0.633011	ENDF	None on CSISRS
10	O-18	46.6000%	20.9460000%	0.2000%	(g,He-3)	25.59	C-15	2.449	0.633011	TENDL	None on CSISRS
11	O-17	46.6000%	20.9460000%	0.0380%	(g,p)	13.78	N-16	7.13	0.720400	ENDF	None on CSISRS
12	O-18	46.6000%	20.9460000%	0.2000%	(g,np)	21.82	N-16	7.13	0.720400	ENDF	K. G. McNeil
13	F-19	0.0800%	0.0000000%	100.0000%	(g,He-3)	22.12	N-16	7.13	0.720400	TENDL	None on CSISRS
14	O-18	46.6000%	20.9460000%	0.2000%	(g,p)	15.94	N-17	4.173	0.000070	ENDF	J. G. Woodworth
15	F-19	0.0800%	0.0000000%	100.0000%	(g,2p)	23.90	N-17	4.173	0.000070	No ENDF	None on CSISRS
16	Ne-21	0.0000%	0.0018180%	0.2700%	(g,2p)	23.60	O-19	26.91	0.000244	No ENDF	None on CSISRS
17	Ne-22	0.0000%	0.0018180%	9.2500%	(g,He-3)	26.30	O-19	26.91	0.000244	No ENDF	None on CSISRS
18	Ne-21	0.0000%	0.0018180%	0.2700%	(g,p)	13.00	F-20	11	0.000083	No ENDF	None on CSISRS
19	Ne-22	0.0000%	0.0018180%	9.2500%	(g,np)	21.15	F-20	11	0.000083	TENDL	None on CSISRS
20	Na-23	2.8300%	0.0000000%	100.0000%	(g,He-3)	24.45	F-20	11	0.000083	ENDF	None on CSISRS
21	Na-23	2.8300%	0.0000000%	100.0000%	(g,3n)	40.59	Na-20	0.4479	0.033751	ENDF	None on CSISRS
22	Ne-22	0.0000%	0.0018180%	9.2500%	(g,p)	15.30	F-21	4.158	0.001365	No ENDF	V. V. Varlamov
23	Na-23	2.8300%	0.0000000%	100.0000%	(g,2p)	24.06	F-21	4.158	0.001365	ENDF	None on CSISRS
24	Mg-24	2.0900%	0.0000000%	78.9900%	(g,3n)	49.06	Mg-21	0.122	0.006640	ENDF	None on CSISRS
25	Mg-25	2.0900%	0.0000000%	10.0000%	(g,p)	12.06	Na-24	5.39E+04	0.000531	ENDF	None on CSISRS
26	Mg-26	2.0900%	0.0000000%	11.0100%	(g,np)	19.02	Na-24	5.39E+04	0.000531	ENDF	None on CSISRS
27	Al-27	8.1300%	0.0000000%	100.0000%	(g,He-3)	23.71	Na-24	5.39E+04	0.000531	ENDF	None on CSISRS
28	Mg-25	2.0900%	0.0000000%	10.0000%	(g,p)	12.53	Na-24m	2.02E-02	0.000000	ENDF None to MS	None on CSISRS
29	Mg-26	2.0900%	0.0000000%	11.0100%	(g,np)	19.49	Na-24m	2.02E-02	0.000000	ENDF None to MS	None on CSISRS
30	Al-27	8.1300%	0.0000000%	100.0000%	(g,He-3)	24.18	Na-24m	2.02E-02	0.000000	ENDF None to MS	None on CSISRS
31	Al-27	8.1300%	0.0000000%	100.0000%	(g,3n)	41.36	Al-24	2.053	1.015310	TENDL	None on CSISRS
32	Al-27	8.1300%	0.0000000%	100.0000%	(g,3n)	41.79	Al-24m	0.1313	0.005240	TENDL	None on CSISRS
33	Si-28	27.7200%	0.0000000%	92.2300%	(g,2n)	30.49	Si-26	2.234	0.000010	ENDF	None on CSISRS
34	Si-28	27.7200%	0.0000000%	92.2300%	(g,n)	17.18	Si-27	4.16	Unquantified	ENDF	R. E. Pywell
35	Si-29	27.7200%	0.0000000%	4.6700%	(g,3n)	38.96	Si-26	2.234	0.000010	ENDF	None on CSISRS
36	P-31	0.1200%	0.0000000%	100.0000%	(g,3n)	41.52	P-28	0.27	0.314902	TENDL	None on CSISRS
37	P-31	0.1200%	0.0000000%	100.0000%	(g,n)	12.30	P-30	149.88	0.000007	ENDF	V. V. Varlamov
38	S-32	0.0500%	0.0000000%	95.0200%	(g,3n)	47.07	S-29	0.187	0.558000	ENDF	None on CSISRS
39	S-32	0.0500%	0.0000000%	95.0200%	(g,pn)	21.18	P-30	149.88	0.000007	ENDF	A. Veyssiere
40	S-32	0.0500%	0.0000000%	95.0200%	(g,2n)	28.10	S-30	1.178	0.000100	ENDF	A. Veyssiere
41	S-33	0.0500%	0.0000000%	0.7500%	(g,3n)	36.74	S-30	1.178	0.000100	ENDF	None on CSISRS
42	S-32	0.0500%	0.0000000%	95.0200%	(g,n)	15.04	S-31	2.572	0.000391	ENDF	A. Veyssiere
43	S-33	0.0500%	0.0000000%	0.7500%	(g,2n)	23.68	S-31	2.572	0.000391	ENDF	None on CSISRS
44	S-34	0.0500%	0.0000000%	4.2100%	(g,3n)	35.10	S-31	2.572	0.000391	ENDF	None on CSISRS
45	Cl-35	0.0500%	0.0000000%	75.7700%	(g,3n)	39.90	Cl-32	0.298	0.318570	ENDF	None on CSISRS
46	Cl-35	0.0500%	0.0000000%	75.7700%	(g,2n)	24.15	Cl-33	2.511	0.000009	ENDF	None on CSISRS
47	Ar-36	0.0000%	0.9340000%	0.3370%	(g,t)	24.18	Cl-33	2.511	0.000009	ENDF	None on CSISRS
48	S-36	0.0500%	0.0000000%	0.0200%	(g,np)	21.47	P-34	12.43	0.002490	ENDF	None on CSISRS
49	Cl-37	0.0500%	0.0000000%	24.2300%	(g,He-3)	22.14	P-34	12.43	0.002490	ENDF	None on CSISRS
50	Cl-35	0.0500%	0.0000000%	75.7700%	(g,n)	12.80	Cl-34m	1920	0.125630	ENDF Not to MS	None on CSISRS
51	Ar-36	0.0000%	0.9340000%	0.3370%	(g,n)	15.25	Ar-35	1.775	0.001061	ENDF	None on CSISRS
52	Ar-38	0.0000%	0.9340000%	0.0630%	(g,3n)	35.88	Ar-35	1.775	0.001061	ENDF	None on CSISRS
53	K-39	2.5900%	0.0000000%	93.2581%	(g,3n)	40.60	K-36	0.342	0.218300	No ENDF	None on CSISRS
54	Ar-40	0.0000%	0.9340000%	99.6000%	(g,He-3)	23.07	S-37	303	0.943528	No ENDF	None on CSISRS
55	K-39	2.5900%	0.0000000%	93.2581%	(g,2n)	25.15	K-37	1.226	0.000190	No ENDF	None on CSISRS
56	Ca-40	3.6300%	0.0000000%	96.9410%	(g,He-3)	18.83	K-37	1.226	0.000190	ENDF	A. S. Gabelko
57	K-39	2.5900%	0.0000000%	93.2581%	(g,n)	13.08	K-38	458.16	0.001420	No ENDF	D. V. Webb
58	K-40	2.5900%	0.0000000%	0.0117%	(g,2n)	20.88	K-38	458.16	0.001420	No ENDF	None on CSISRS
59	K-41	2.5900%	0.0000000%	6.7302%	(g,3n)	30.97	K-38	458.16	0.001420	No ENDF	None on CSISRS
60	Ca-40	3.6300%	0.0000000%	96.9410%	(g,np)	21.40	K-38	458.16	0.001420	ENDF	A. Veyssiere
61	Ca-40	3.6300%	0.0000000%	96.9410%	(g,2n)	28.93	Ca-38	0.44	0.002900	ENDF	None on CSISRS
62	Ca-46	3.6300%	0.0000000%	0.0040%	(g,He-3)	26.09	Ar-43	322.2	0.015640	TENDL	None on CSISRS
63	Ti-46	0.5600%	0.0000000%	8.0000%	(g,3n)	39.02	Ti-43	0.509	0.000266	ENDF	None on CSISRS
64	Ca-46	3.6300%	0.0000000%	0.0040%	(g,np)	22.69	K-44	1327.8	0.097903	ENDF	None on CSISRS
65	Sc-45	0.0020%	0.0000000%	0.0000%	(g,n)	11.32	Sc-44	14137.2	0.000031	TENDL	A. Veyssiere
66	Ti-46	0.4400%	0.0000000%	8.0000%	(g,np)	21.67	Sc-44	14137.2	0.000031	ENDF	None on CSISRS
67	Ca-48	3.6300%	0.0000000%	0.1870%	(g,He-3)	29.43	Ar-45	21.48	0.353000	TENDL	None on CSISRS
68	Ca-46	3.6300%	0.0000000%	0.0040%	(g,p)	13.82	K-45	1038	0.006793	ENDF	None on CSISRS
69	Ca-48	3.6300%	0.0000000%	0.1870%	(g,np)	24.16	K-46	105	0.046000	ENDF	None on CSISRS
70	Fe-54	0.1000%	0.0000000%	5.8000%	(g,t)	22.96	Mn-51	2772	Unquantified	ENDF	None on CSISRS
71	Fe-54	0.1000%	0.0000000%	5.8000%	(g,3n)	40.25	Fe-51	0.305	0.003600	ENDF	None on CSISRS
72	Cr-53	0.0100%	0.0000000%	9.5010%	(g,p)	11.13	V-52	224.58	0.000019	ENDF	None on CSISRS
73	Cr-54	0.0100%	0.0000000%	2.3650%	(g,np)	20.85	V-52	224.58	0.000019	ENDF	None on CSISRS
74	Mn-55	0.1000%	0.0000000%	100.0000%	(g,He-3)	21.20	V-52	224.58	0.000019	ENDF	None on CSISRS
75	Fe-54	0.1000%	0.0000000%	5.8000%	(g,np)	20.91	Mn-52m	1266	0.000297	ENDF	S. S. Borodina
76	Fe-54	0.1000%	0.0000000%	5.8000%	(g,n)	13.38	Fe-53	510.6	0.000380	ENDF	S. S. Borodina
77	Fe-54	0.1000%	0.0000000%	5.8000%	(g,n)	16.42	Fe-53m	154.8	0.000590	ENDF Not to MS	S. S. Borodina
78	Fe-56	0.1000%	0.0000000%	91.8000%	(g,3n)	39.92	Fe-53	510.6	0.000380	ENDF	None on CSISRS
79	Fe-56	0.1000%	0.0000000%	91.8000%	(g,3n)	42.96	Fe-53m	154.8	0.000590	ENDF Not to MS	None on CSISRS
80	Ni-58	0.0100%	0.0000000%	68.0770%	(g,t)	21.15	Co-55	63108	0.000053	ENDF	None on CSISRS
81	Fe-57	0.1000%	0.0000000%	2.2000%	(g,p)	10.56	Mn-56	9282.6	0.001680	ENDF	None on CSISRS
82	Fe-58	0.1000%	0.0000000%	28.0000%	(g,np)	20.60	Mn-56	9282.6	0.001680	ENDF	None on CSISRS
83	Co-59	0.0020%	0.0000000%	100.0000%	(g,He-3)	20.25	Mn-56	9282.6	0.001680	TENDL	None on CSISRS
84	Ni-58	0.0100%	0.0000000%	68.0770%	(g,np)	19.55	Co-56	6676128	0.152870	ENDF	S. S. Borodina
85	Ni-58	0.0100%	0.0000000%	68.0770%	(g,n)	12.22	Ni-57	128160	0.000111	ENDF	S. S. Borodina
86	Ni-60	0.0100%	0.0000000%	26.2230%	(g,3n)	32.61	Ni-57	128160	0.000111	ENDF	None on CSISRS
87	Ni-64	0.0100%	0.0000000%	0.9260%	(g,He-3)	23.11	Fe-61	358.8	0.002280	TENDL	None on CSISRS
88	Zn-64	0.0075%	0.0000000%	48.6000%	(g,3n)	33.87	Zn-61	89.1	0.004440	ENDF	None on CSISRS
89	Ni-64	0.0100%	0.0000000%	0.9260%	(g,np)	21.04	Co-62	90	0.019200	ENDF	None on CSISRS
90	Ni-64	0.0100%	0.0000000%	0.9260%	(g,np)	21.06	Co-62m	834.6	0.002900	ENDF Not to MS	None on CSISRS

Table 5.1 cont: Reactions and reaction products that can lead to interferences with the delayed γ-ray fission signal by the emission of discrete high-energy γ-rays. Reaction products with atomic mass numbers from 1 to 100 have been searched.

Index	Target Isotope	Elem. Abund. Crust Weight Percent	Elem. Abund. Atmosphere Volum Percent	Isotope Abund.	Reaction	Threshold (MeV)	Reaction Product	Half-life (s)	Branch above 3 MeV	Tabulated Cross Section Data	Experimental Cross Section Data
91	Cu-65	0.0050%	0.0000000%	30.8300%	(g,He-3)	20.77	Co-62	90	0.019200	ENDF	None on CSISRS
92	Cu-65	0.0050%	0.0000000%	30.8300%	(g,He-3)	20.79	Co-62m	834.6	0.002900	ENDF Not to MS	None on CSISRS
93	Cu-63	0.0075%	0.0000000%	69.1700%	(g,n)	10.85	Cu-62	584.4	0.000097	ENDF	A. Veyssiere
94	Zn-64	0.0075%	0.0000000%	48.6000%	(g,np)	18.57	Cu-62	584.4	0.000097	ENDF	None on CSISRS
95	Zn-64	0.0075%	0.0000000%	48.6000%	(g,n)	11.86	Zn-63	2308.2	0.000055	ENDF	T. E. Rodrigues
96	Zn-66	0.0075%	0.0000000%	27.9000%	(g,3n)	30.90	Zn-63	2308.2	0.000055	ENDF	None on CSISRS
97	Ga-69	0.0020%	0.0000000%	60.1080%	(g,3n)	29.82	Ga-66	34164	0.136702	TENDL	None on CSISRS
98	Ge-70	0.0002%	0.0000000%	21.2300%	(g,3n)	32.12	Ge-67	1134	0.006937	ENDF	None on CSISRS
99	Se-74	0.0000%	0.0000000%	0.8900%	(g,3n)	33.32	Se-71	284.4	0.002360	TENDL	None on CSISRS
100	Ge-73	0.0002%	0.0000000%	7.7300%	(g,p)	9.99	Ga-72	50760	0.000306	ENDF	None on CSISRS
101	As-75	0.0002%	0.0000000%	100.0000%	(g,3n)	29.02	As-72	93600	0.004641	TENDL	None on CSISRS
102	Se-74	0.0000%	0.0000000%	0.8900%	(g,np)	19.34	As-72	93600	0.004641	TENDL	None on CSISRS
103	Ge-76	0.0002%	0.0000000%	7.4400%	(g,np)	20.52	Ga-74	487.2	0.037900	ENDF	J. J. McCarthy
104	Br-79	0.0002%	0.0000000%	50.6900%	(g,3n)	30.00	Br-76	58320	0.034566	TENDL	None on CSISRS
105	Kr-78	0.0000%	0.0001140%	0.3500%	(g,np)	19.25	Br-76	58320	0.034566	TENDL	None on CSISRS
106	Se-80	0.0000%	0.0000000%	49.6100%	(g,np)	18.08	As-78	5442	0.000650	TENDL	None on CSISRS
107	Br-79	0.0002%	0.0000000%	50.6900%	(g,n)	10.69	Br-78	387.6	0.000005	TENDL	None on CSISRS
108	Kr-80	0.0000%	0.0001140%	2.2500%	(g,np)	17.58	Br-78	387.6	0.000005	TENDL	None on CSISRS
109	Br-81	0.0002%	0.0000000%	49.3100%	(g,3n)	28.74	Br-78	387.6	0.000005	TENDL	None on CSISRS
110	Se-82	0.0000%	0.0000000%	8.7300%	(g,np)	18.57	As-80	15.2	0.001200	TENDL	None on CSISRS
111	Se-82	0.0000%	0.0000000%	8.7300%	(g,p)	9.28	As-81	33.3	0.000360	TENDL	None on CSISRS
112	Rb-85	0.0300%	0.0000000%	72.1650%	(g,3n)	30.20	Rb-82	76.38	0.000019	TENDL	None on CSISRS
113	Sr-84	0.0370%	0.0000000%	56.0000%	(g,np)	17.59	Rb-82	76.38	0.000019	ENDF	None on CSISRS
114	Kr-86	0.0000%	0.0001140%	17.3000%	(g,np)	18.60	Br-84	1908	0.146839	TENDL	None on CSISRS
115	Y-89	0.0030%	0.0000000%	100.0000%	(g,3n)	32.64	T-86	53064	0.003300	TENDL	Md. S. Rahman
116	Mo-92	0.0001%	0.0000000%	14.8400%	(g,n)	12.67	Mo-91	929.4	0.001542	ENDF	H. Bell
117	Mo-94	0.0001%	0.0000000%	9.2500%	(g,3n)	30.42	Mo-91	929.4	0.001542	ENDF	None on CSISRS
118	Zr-94	0.0200%	0.0000000%	17.3800%	(g,np)	17.80	Y-92	12744	0.000042	ENDF	None on CSISRS
119	Zr-96	0.0200%	0.0000000%	2.8000%	(g,He-3)	20.21	Sr-93	445.38	0.001870	TENDL	None on CSISRS
120	Ru-96	0.0000%	0.0000000%	5.5200%	(g,t)	17.42	Tc-93	9900	0.000160	TENDL	None on CSISRS
121	Ru-96	0.0000%	0.0000000%	5.5200%	(g,t)	17.81	Tc-93m	2610	0.036300	No ENDF or TENDL	None on CSISRS
122	Ru-96	0.0000%	0.0000000%	5.5200%	(g,3n)	33.03	Ru-93	59.7	0.021290	TENDL	None on CSISRS
123	Zr-96	0.0200%	0.0000000%	2.8000%	(g,np)	18.45	Y-94	1122	0.002600	ENDF	None on CSISRS
124	Ru-96	0.0000%	0.0000000%	5.5200%	(g,np)	15.19	Tc-94m	2610	0.016286	TENDL to GS+MS	None on CSISRS
125	Zr-96	0.0200%	0.0000000%	2.8000%	(g,p)	18.45	Y-95	618	0.086600	ENDF	None on CSISRS
126	Mo-100	0.0001%	0.0000000%	9.6300%	(g,np)	18.10	Nb-98m	3078	0.000248	ENDF to GS+MS	None on CSISRS
127	Mo-100	0.0001%	0.0000000%	9.6300%	(g,p)	11.52	Nb-99m	156	0.004240	ENDF to GS+MS	None on CSISRS
128	Pd-102	0.0000%	0.0000000%	1.0200%	(g,np)	17.69	Rh-100	74880	0.001371	ENDF	None on CSISRS

Table 5.2: Reactions and reaction products that can lead to interferences with the delayed neutron fission signals by the emission of neutrons. Reaction products with atomic mass numbers from 1 to 200 have been searched.

Index	Target Isotope	Elem. Abund. Crust Weight Percent	Elem. Abund. Atmosphere Volum Percent	Isotope Abund.	Reaction	Threshold (MeV)	Reaction Product	Half-life (s)	Branch Neutron	Tabulated Cross Section Data	Experimental Cross Section Data
1	B-11	0.0010%	0.0000%	80.1000%	(g,2p)	30.9	Li-9	0.1783	49.500%	TENDL	None on CSISRS
2	N-15	0.0050%	78.0840%	0.3660%	(g,2p)	31.04	B-13	1.74E-02	0.28%	ENDF	None on CSISRS
3	O-18	46.6000%	20.9460%	0.2000%	(g,p)	15.9	N-17	4.17	95.17%	ENDF	J. G. Woodworth
4	F-19	0.0800%	0.0000%	100.0000%	(g,2p)	23.9	N-17	4.17	95.17%	TENDL	None on CSISRS
5	O-18	46.6000%	20.9460%	0.2000%	(g,2p)	29.05	C-16	0.747	98.80%	TENDL	None on CSISRS

Table 5.3: Reactions and reaction products that can lead to interferences with the delayed γ-ray fission signal by the emission of high-energy β-particles. Due to difficulties searching for high-energy β-particle emissions this list/database is hit and miss.

Index	Target Isotope	Elem. Abund. Crust Weight Percent	Elem. Abund. Atmosphere Volum Percent	Isotope Abund.	Reaction	Threshold (MeV)	Reaction Product	Half-life (s)	Branch Beta	Faction above 3 MeV	Max Beta Endpoint (MeV)	Tabulated Cross Section Data	Experimental Cross Section Data
1	Li-7	0.0020%	0.0000%	92.5000%	(g,p)	9.98	He-6	0.806	100.0000%	100.00000%	3.508	TENDL	L. A. Kul
2	Be-9	0.0003%	0.0000%	100.0000%	(g,p)	16.89	Li-8	0.838	100.0000%	100.00000%	12.965	ENDF	K. Shoda
3	B-10	0.0009%	0.0000%	19.9000%	(g,2p)	23.50	Li-8	0.838	100.0000%	100.00000%	12.965	No ENDF/TENDL	None on CSISRS
4	B-11	0.0009%	0.0000%	80.1000%	(g,t)	27.25	Li-8	0.838	100.0000%	100.00000%	12.965	TENDL	None on CSISRS
5	B-11	0.0009%	0.0000%	80.1000%	(g,2p)	30.91	Li-9	0.178	100.0000%	96.50000%	13.606	No ENDF/TENDL	None on CSISRS
6	C-13	0.0300%	0.0383%	1.1000%	(g,2p)	31.63	Be-11	13.810	100.0000%	96.93600%	11.506	No ENDF/TENDL	None on CSISRS
7	C-13	0.0300%	0.0383%	1.1000%	(g,p)	17.53	B-12	0.020	100.0000%	100.00000%	13.368	ENDF	D. Zubanov
8	N-14	0.0050%	78.0840%	99.6340%	(g,2p)	25.08	B-12	0.020	100.0000%	100.00000%	13.368	ENDF	None on CSISRS
9	N-15	0.0050%	78.0840%	0.3660%	(g,He-3)	20.74	B-12	0.020	100.0000%	100.00000%	13.368	ENDF	None on CSISRS
10	N-14	0.0050%	78.0840%	99.6340%	(g,2n)	30.62	N-12	0.011	100.0000%	99.97000%	16.316	ENDF	None on CSISRS
11	N-15	0.0050%	78.0840%	0.3660%	(g,2p)	31.04	B-13	0.017	100.0000%	100.00000%	13.437	ENDF	None on CSISRS
12	O-17	46.6000%	20.9460%	0.0380%	(g,2p)	25.26	C-15	2.449	100.0000%	100.00000%	9.772	ENDF	None on CSISRS
13	O-18	46.6000%	20.9460%	0.2000%	(g,He-3)	25.59	C-15	2.449	100.0000%	100.00000%	9.772	TENDL	None on CSISRS
14	O-18	46.6000%	20.9460%	0.2000%	(g,2p)	29.05	C-16	0.747	100.0000%	100.00000%	7.890	No ENDF/TENDL	None on CSISRS
15	O-17	46.6000%	20.9460%	0.0380%	(g,p)	13.78	N-16	7.130	100.0000%	99.01200%	10.420	ENDF	None on CSISRS
16	O-18	46.6000%	20.9460%	0.2000%	(g,np)	16.27	N-16	7.130	100.0000%	99.01200%	10.420	ENDF	K. G. McNeil
17	F-19	0.0800%	0.0000%	100.0000%	(g,He-3)	22.12	N-16	7.130	100.0000%	99.01200%	10.420	TENDL	None on CSISRS
18	O-18	46.6000%	20.9460%	0.2000%	(g,p)	15.94	N-17	4.173	100.0000%	88.94000%	8.680	ENDF	J. G. Woodworth
19	F-19	0.0800%	0.0000%	100.0000%	(g,2p)	23.95	N-17	4.173	100.0000%	88.94000%	8.680	No ENDF/TENDL	None on CSISRS
20	Ne-21	0.0000%	0.0018%	0.2700%	(g,2p)	23.66	O-19	26.910	100.0000%	99.88200%	4.711	No ENDF/TENDL	None on CSISRS
21	Ne-22	0.0000%	0.0018%	9.2500%	(g,He-3)	26.31	O-19	26.910	100.0000%	99.88200%	4.711	TENDL	None on CSISRS
22	Ne-21	0.0000%	0.0018%	0.2700%	(g,p)	13.01	F-20	11.000	100.0000%	99.99130%	5.391	TENDL	None on CSISRS
23	Ne-22	0.0000%	0.0018%	9.2500%	(g,np)	21.15	F-20	11.000	100.0000%	99.99130%	5.391	TENDL	None on CSISRS
24	Na-23	2.8300%	0.0000%	100.0000%	(g,He-3)	24.45	F-20	11.000	100.0000%	99.99130%	5.391	ENDF	None on CSISRS
25	Ne-22	0.0000%	0.0018%	9.2500%	(g,p)	15.27	F-21	4.158	100.0000%	100.00000%	5.684	TENDL	V. V. Var;amov
26	Na-23	2.8300%	0.0000%	100.0000%	(g,2p)	24.06	F-21	4.158	100.0000%	100.00000%	5.684	ENDF	None on CSISRS
27	Mg-25	2.0900%	0.0000%	10.0000%	(g,p)	12.06	Na-24	53850.000	100.0000%	0.00003%	4.147	ENDF	None on CSISRS
28	Mg-26	2.0900%	0.0000%	11.0100%	(g,np)	19.02	Na-24	53852.400	100.0000%	0.00003%	4.147	ENDF	None on CSISRS
29	Al-27	8.1300%	0.0000%	100.0000%	(g,He-3)	23.71	Na-24	53852.400	100.0000%	0.00003%	4.147	ENDF	None on CSISRS
30	Mg-25	2.0900%	0.0000%	10.0000%	(g,p)	12.53	Na-24m	0.020	0.0005%	0.00050%	5.988	ENDF None to MS	None on CSISRS
31	Mg-26	2.0900%	0.0000%	11.0100%	(g,np)	19.49	Na-24m	0.020	0.0005%	0.00050%	5.988	ENDF None to MS	None on CSISRS
32	Al-27	8.1300%	0.0000%	100.0000%	(g,He-3)	24.18	Na-24m	0.020	0.0005%	0.00050%	5.988	ENDF None to MS	None on CSISRS
33	Mg-26	2.0900%	0.0000%	11.0100%	(g,p)	14.14	Na-25	59.100	100.0000%	62.50000%	3.835	ENDF	B. S. Ishkhanov
34	Al-27	8.1300%	0.0000%	100.0000%	(g,2p)	22.41	Na-25	59.100	100.0000%	62.50000%	3.835	ENDF	None on CSISRS
35	Cl-35	0.0500%	0.0000%	75.7700%	(g,n)	12.65	Cl-34	1.526	100.0000%	100.00000%	4.469	ENDF	K. Kuriyama
36	Cl-35	0.0500%	0.0000%	75.7700%	(g,2n)	24.15	Cl-33	2.511	100.0000%	98.99000%	4.561	ENDF	None on CSISRS
37	Ca-40	3.6300%	0.0000%	96.9410%	(g,3n)	45.93	Ca-37	0.181	100.0000%	100.41000%	10.617	TENDL	None on CSISRS
38	Ca-40	3.6300%	0.0000%	96.9410%	(g,t)	25.00	K-37	1.226	100.0000%	98.10000%	5.127	ENDF	None on CSISRS
39	Ca-40	3.6300%	0.0000%	96.9410%	(g,n)	15.65	Ca-39	0.860	100.0000%	100.00000%	5.509	ENDF	A. Veyssiere
40	Ca-40	3.6300%	0.0000%	96.9410%	(g,np)	27.33	K-38m	0.924	100.0000%	100.00000%	5.022	ENDF None to MS	A. Veyssiere
41	Ca-40	3.6300%	0.0000%	96.9410%	(g,2n)	28.94	Ca-38	0.440	100.0000%	99.70000%	5.591	ENDF	None on CSISRS
42	Ca-43	3.6300%	0.0000%	0.1350%	(g,p)	10.68	K-42	44496.000	100.0000%	81.90000%	3.525	ENDF	None on CSISRS
43	Ca-44	3.6300%	0.0000%	2.0860%	(g,np)	21.81	K-42	44496.000	100.0000%	81.90000%	3.525	ENDF	None on CSISRS
44	Ar-40	0.0000%	0.9340%	99.6000%	(g,np)	20.61	Cl-38	2234.400	100.0000%	57.60000%	4.916	ENDF	None on CSISRS
45	Ti-46	0.5600%	0.0000%	8.0000%	(g,3n)	39.02	Ti-43	0.509	100.0000%	99.73400%	5.845	ENDF	None on CSISRS
46	Ca-46	3.6300%	0.0000%	0.0040%	(g,He-3)	26.09	Ar-43	322.200	100.0000%	49.20000%	4.620	TENDL	None on CSISRS
47	Ca-46	3.6300%	0.0000%	0.0040%	(g,np)	22.69	K-44	1327.800	100.0000%	37.80000%	5.660	ENDF	None on CSISRS
48	Ca-46	3.6300%	0.0000%	0.0040%	(g,p)	15.81	K-45	1038.000	100.0000%	12.90000%	4.205	ENDF	None on CSISRS

5.3 High-Energy Gross Interference Experiments

Based on the potentially interfering reaction lists/databases, the research team simultaneously measured the delayed neutron and γ-ray signal interferences from 27 non-fissionable chemical targets, containing 66 different isotopes. These targets are summarized in Table 5.4 along with 5 commercial products that were used as targets. To provide a comparison, the fission signature strengths from ^{232}Th, ^{238}U and ^{239}Pu were also measured. These experiments were conducted using a 15 to 45 MeV endpoint energy pulsed bremsstrahlung beam generated from ~ 2 μs electron pulses containing 50 to ~ 450 nC of charge that struck a 2.2 mm tungsten radiator. The bremsstrahlung repetition rate was 15 Hz and the inspection time was varied from 5 to ~ 80 min in order to ensure a significant number of counts. A rough schematic of the experimental setup is shown in Figure 5.1. The radiator to target distance was $\sim$6 m during which the bremsstrahlung beam passed through 1.27 and 3.81 cm diameter Pb collimators, thereby creating 2.7 cm diameter beam spot on the target. The detectors for measuring the gross fission signal yields consisted of 5 shielded/moderated ^{3}He tubes for neutron detection and 6 collimated BGO detectors for γ-ray detection; both were ~ 1 m from the target. The ^{3}He tubes had a frontal surface area of 1372 cm^2 and hence subtended a solid angle of 137 msr with respect to the target. The BGO detectors had a frontal surface area of 122 cm^2 and hence subtended a solid angle of 12.2 msr with respect to the target. To measure the discrete γ-ray emission from the target, an 80% relative efficient HPGe detector was ~ 37 cm from the target. Both photon detectors (i.e. BGO array and HPGe detector) were surrounded by at least two inches of Pb shielding excluding the front of the detectors. The front of the BGO array had no filter, while the HPGe detector had a $\sim$0.6 cm Pb filter. The 2.54 cm diameter ^{3}He tubes were surrounded by 2.54 cm of virgin polyethylene, 110 m of Cd and 6.34 mm of borated elastomer. The details of these detectors and their associated electronics can be found in the dissertation of Dr. M. T. Kinlaw [20]. The data was acquired using a multiparameter data acquisition system, which collected the detector events in an event-by-event mode for post experiment analysis. The time and energy cuts used for extracting the delayed neutron and γ-ray signatures are described at the beginning of this section.

Table 5.4: List of non-fissionable materials uses as taregts with their total in-beam mass.

Target	Mass (g)
Al	128.0
Ar	0.462
Be	561.0
BN	67.6
$Na_2B_4O_7 \cdot 10H_2O$	105.2
Ca	62.5
Cu	766.6
Fe	396.2
C (graphite)	598.5
KBr	176.0
$C_6H_{11}KO_7$	72.9
KF	59.1
LiF	65.7
Na	5.9
NaCl	127.3
$H_2{}^{18}O$	50.0
Pb	487.0
PbBe	347.1
S	88.0
Na	5.9
H_2O - NaCl (2.9%)	782.8
SiO_2	148.0
SiN	63.3
C_2F_4	553.4
H_2O	757.2
Zn	316.4
Zr	164.9
Beef	403.2
Concrete	337.7
Diesel Fuel	234.8
Watermelon	217.4
Wood	151.8

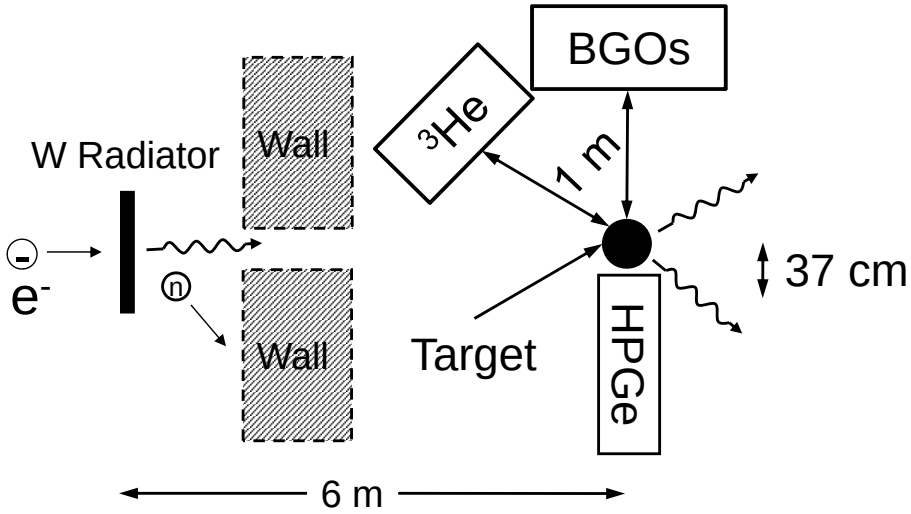

Figure 5.1: Schematic diagram of the delayed neutron and γ-ray interference experiments.

Before delving into high-energy bremsstrahlung inspections, delayed neutron and high-energy γ-ray gross yield measurements from $\sim$15 MeV endpoint energy are presented first in order to set a baseline and demonstrate the lack of interferences from non-fissionable materials. Figure 5.2 shows the measured gross delayed neutron and γ-ray single inspection yields from these targets, presented as a two dimensional signal plot as in Chapter 4. The raw neutron and high-energy γ-ray counts in the fission signature regions were normalized by the total electron charge on the bremsstrahlung radiator and the solid angle subtended by the detectors; the electron charge is a proxy for the bremsstrahlung fluence impinging on the target and the detector solid angle allows the data to be easily scaled to different detector sizes. As with the 13 MeV inspection yields in Figure 4.5, the non-fissionable targets were grouped tightly together around the contribution from the natural passive background with a distribution consistent with Poisson counting statistics; the natural passive background completely dominated the signal. The logical "Or" critical decision surface calculated from equations (1.42) and (1.10) with 0.1% false positive probability based on the passive background and non-fissionable targets is also shown in Figure 5.2. Unlike the experiments in Chapter 4, the targets in these experiments were specifically chosen due to their potential for interferences with the fission signals but no interferences were observed at 15 MeV. The targets containing fissionable isotopes were spread out due to the differences in the fissionable masses. Overlaid on Figure 5.2 is a linear parametric equation describing the relationship between the delayed γ-ray and neutron signal strengths that was determined from the low

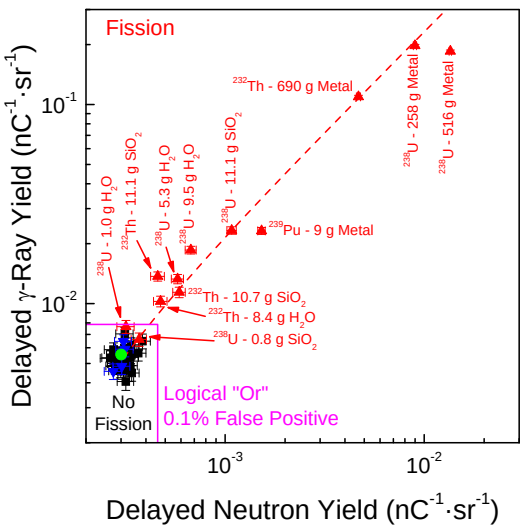

Figure 5.2: Gross single delayed neutron and γ-ray inspection yields from 42 bare targets including 29 that did not contain any fissionable materials (■), 12 that contained fissionable materials (▲) and a number of inspections with no target (▼). The bremsstrahlung endpoint energy was 15 MeV and was generated by electron pulses containing $\sim$ 225 nC of charge. The total inspection time was $\sim$ 600 s. Overlaid on this graph is the linear relationship between the delayed neutron and γ-ray yields (red dashed line), the logical "Or" critical decision surface (solid magenta line) and the passive background contribution (●).

mass ^{238}U aqueous solution targets. The majority of the targets containing fissionable isotopes were correctly identified as "detected" but the two targets with the lowest fissionable mass were within the "not detected" region.

The high-energy bremsstrahlung inspection experiments increased the endpoint energies to 22.5, 30 and 37.5 MeV and measured the gross delayed neutron and high-energy γ-ray yield. Figure 5.3 shows these gross yields as the bremsstrahlung endpoint energy is increased along with the linear parametric equations describing the fission signal and logical "Or" critical decision surfaces with a 0.1% false positive probability. Since the non-fissionable targets produced a number of interferences with the fission signal at these higher energies, these critical decision surfaces are based on the passive background and no target yields. When the bremsstrahlung endpoint energy was increased to 22.5 MeV, which is shown in Figure 5.3(a), the already discussed ^{18}O(γ,p)^{17}N and ^{9}Be(γ,p)^{8}Li interfering reactions were immediately obvious. Recall the ^{17}N reaction product is a neutron emitter, interfering with the delayed neutron fission signal, and the ^{8}Li reaction product is a high-energy β-particle emitter, interfering with the delayed γ-ray fission signal. The threshold for these reactions are

15.9 and 16.9 MeV respectively. Furthermore, the 50 g $H_2{}^{18}O$ target produced an increased high-energy γ-ray yield due to the $^{18}O(\gamma,d)^{16}N$ reaction, which has a threshold of 19.6 MeV. The ^{16}N reaction product has a 7.1 s half-life and decays with the emission of a 6.1 and 7.1 MeV γ-rays, thereby interfering with the delayed γ-ray fission signal. The largest delayed γ-ray fission signal interference at 22.5 MeV was from the 771 g C_2F_4 target due to the $^{19}F(\gamma,{}^3He)^{16}N$ reaction, which has a threshold of 22.1 MeV. The large interference from this C_2F_4 target was due to its large mass as demonstrated by the smaller 58 g LiF target, which produced a $\sim$19 smaller interference.

In addition to the large interferences in the ^9Be, $H_2{}^{18}O$ and C_2F_4, 9 other targets displayed smaller interferences, mostly in the high-energy γ-ray yield. All of these interfering targets contained either oxygen and/or fluorine except the 62.5 g Ca and 127.3 g NaCl targets. The underlying dominant interfering reaction from Ca was $^{40}Ca(\gamma,n)^{39}Ca$, which has a threshold of 15.6 MeV. The ^{39}Ca reaction product has a half-life of 860 ms and decays by the emission of a high-energy β-particle with a 5.5 MeV endpoint energy. For the NaCl target, the dominant interfering reaction was $^{35}Ca(\gamma,n)^{34m}Ca$, which has a threshold of 12.8 MeV. The ^{34m}Cl reaction product has a half-life of 32 min and decays by the emission of a 3.2 MeV γ-ray. One commercial product, concrete, also interfered with both fission signals. Concrete is of course a common construction material including a large number of elements with variability due to a changing source materials. Major elements include oxygen, calcium and potential ^{238}U or ^{232}Th in the aggregate.

As the bremsstrahlung energy is increased further, the distribution of the targets on the dual signal scatter plots continued to evolve. First, the contribution from the natural passive background and the yields measured without a target begin to separate, indicating that there is an active background. The root cause of this active background is unknown but there is of course oxygen in the atmosphere and the experiment was conducted in a concrete bunker. The research team did their best to shield the concrete that was directly in the bremsstrahlung beam's path with lead but only so much could be done. Second, the interferences that were already observed at 15 and 22.5 MeV continued to increase in strength. Finally, additional targets began to interfere with the fission signals and by 37.5 MeV every target was outside the "not detected" region. One of the major new reactions was $^{19}F(\gamma,2p)^{17}N$, which has a threshold of 23.9 MeV. The reaction product, ^{17}N, is the same as from the $^{18}O(\gamma,p)^{17}N$ reaction, interfering with the delayed neutron fission signal. The addition of this reaction combined with the $^{19}F(\gamma,{}^3He)^{16}N$ reaction made the C_2F_4, LiF and KF targets appear almost exactly like fissionable materials.

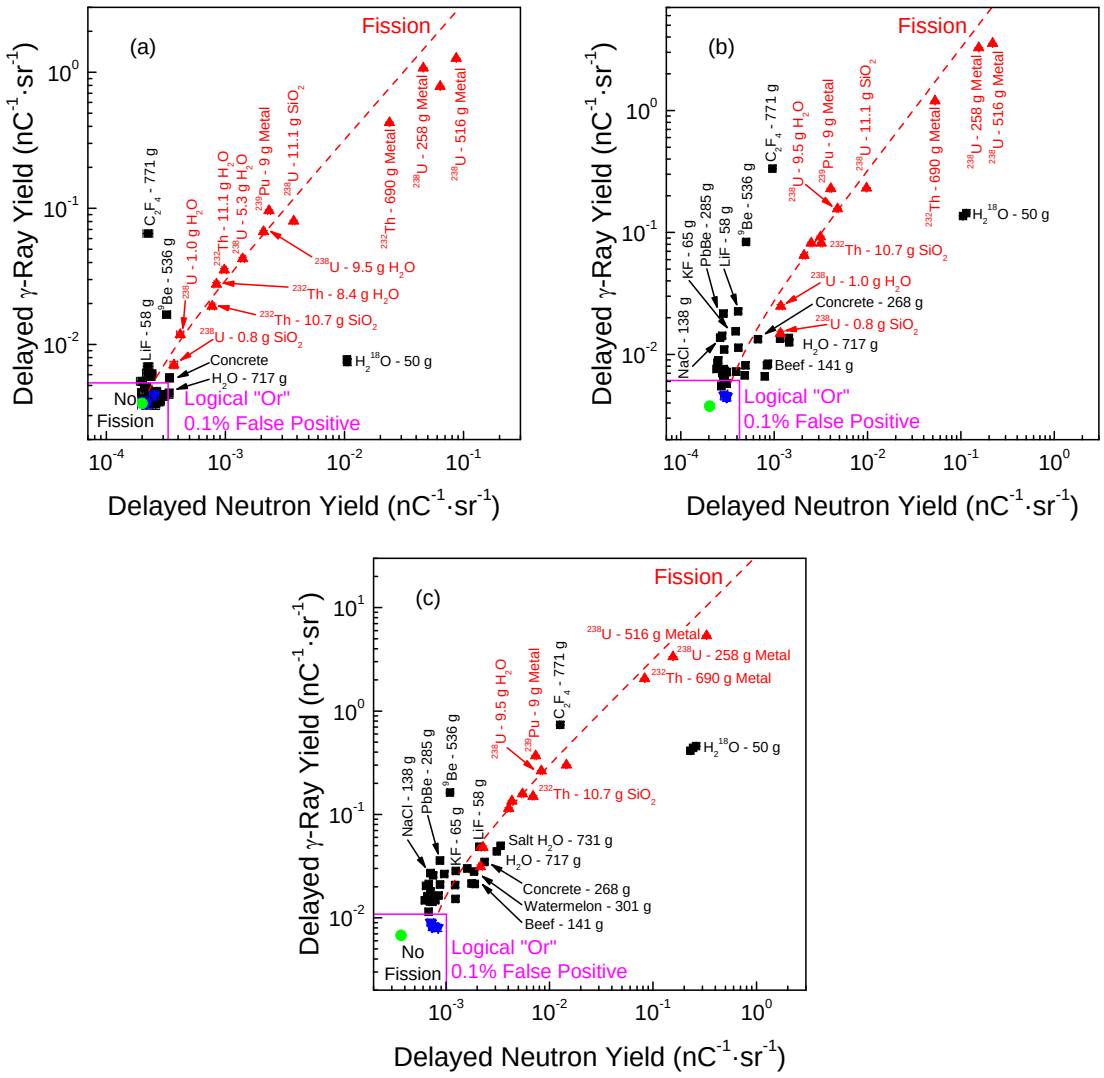

Figure 5.3: Gross single delayed neutron and γ-ray inspection yields from 42 bare targets including 29 that did not contain any fissionable materials (■), 12 that contained fissionable materials (▲) and a number of inspections with no target (▼). The bremsstrahlung endpoint energies were 22.5 (a), 30 (b) and 37.5 MeV (c); generated by electron pulses containing $\sim$340 and $\sim$335 and $\sim$185 nC, respectively. The total inspection time was $\sim$600 s. Overlaid on these graphs is the linear relationship between the delayed neutron and γ-ray yields (red dashed line), the logical "Or" critical decision surface (solid magenta line) and the passive background contribution (●).

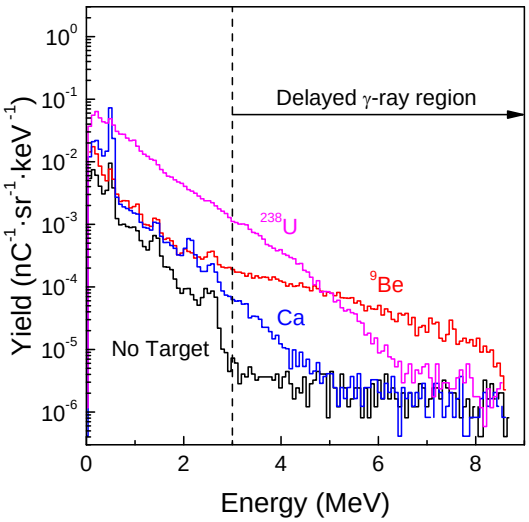

Figure 5.4: Photon energy spectra collected by the BGO detector array from the irradiation of no (black line), Ca (blue line), ^{9}Be (red line) and ^{238}U (magenta line) targets. The inspections were conducted using a pulsed 38 MeV bremsstrahlung beam generated from 2 μs electron pulses containing $\sim$80 nC of charge that struck a 2.2 mm tungsten radiator. The bremsstrahlung repetition rate was 15 Hz and the inspection times varied depending on the precision required for integral cross section measurements. Photon detected in the first $\sim$25 ms after the bremsstrahlung pulse have been removed, hence the indicated region above $\sim$3 MeV represents the photons counted in the delayed ray signal.

During the first experiments, the large number of non-fissionable targets that caused interferences with the high-energy delayed γ-ray fission signal surprised the research team because some of the target isotopes did not have intense discrete high-energy γ-ray emissions identified. As an example, the Ca target had a gross delayed γ-ray single inspection yield that was $\sim$3 times larger than the no target backgrounds without intense discrete high-energy γ-ray emissions. The γ-ray spectrum collected by the BGO detector array suggested the emission of high-energy β-particles as seen in Figure 5.4, which compares spectra from no, ^{9}Be, Ca and ^{238}U target irradiations. Above $\sim$ 3 MeV, the spectrum is featureless (i.e. no discrete γ-ray lines) and falls exponentially before reaching the no target background at $\sim$5 MeV. This featureless decrease with an endpoint energy is indicative of high-energy particle emissions creating high-energy bremsstrahlung photons. The spectrum from the ^{238}U target is similar but with a different endpoint energy because many of the fission fragments emit even higher energy particles in addition to the high-energy discrete γ-rays. The γ-ray lines from ^{238}U cannot be resolved in the spectrum from the BGO array due to the poor energy resolution. With the 13 MeV endpoint energy of the ^{8}Li - decay, the spectrum from

the ^{9}Be target stays above the no target background. Getting back to the spectrum from the Ca target, the root cause of the interference was the emission of high-energy β^{+}-particles from at least 10 different reactions listed in Table 5.3. The most concerning of these reactions is ^{40}Ca(γ,n)^{39}Ca, which only has a 15.6 MeV threshold with $\sim$15 mb maximum cross section at $\sim$20 MeV. In addition, calcium is the 5th most abundant element in the earth's crust and the ^{40}Ca target nuclei's isotopic abundance 96.4%. The ^{39}Ca reaction product β^{+}-decays 100% of the time with a 5.5 MeV endpoint energy in agreement with the spectrum observed by the BGO detector array. Searching for high-energy β^{+}-particles emissions in the available radioisotope decay databases has been challenging and β^{+}-decay is in many ways the most probable decay mode for photonuclear reaction products because they tend to produce proton rich radioisotopes.

The non-fissionable targets were chosen for their potential of interfering reactions and may not be representative of a normal mix of materials. One mitigation strategy is to switch from the logical "Or" critical decision surface of Figure 5.3 to a logical "And" surface. Figure 5.5 displays the same 37.5 MeV bremsstrahlung data as in Figure 5.3(c) but overlays the logical "And" critical decision surface with a 0.1% false positive probability. Switching to the logical "And" surface eliminated half of the interferences by requiring both the delayed neutron and high-energy γ-ray fission signals to be elevated. Of course, half of the targets were still in the "detected" region of the logical "And" surface. However, the underlying interfering reactions was limited to six reactions

- **^{9}Be(γ,p)^{8}Li**. threshold $\sim$16.9 MeV; $\sim$13 MeV β^{-} emitter endpoint energy $\sim$13 MeV; half-life 838 ms. The bremsstrahlung produced by the high-energy β^{-}-particles lead to neutron emission through ^{9}Be(γ,n)^{8}Be reactions, which has only a 1.7 MeV threshold.
- **^{11}B(γ,2p)^{9}Li**. threshold $\sim$30.9 MeV; neutron emitter and β^{-} emitter endpoint energy $\sim$13.6 MeV; half-life 178 ms.
- **^{18}O(γ,p)^{17}N**. threshold $\sim$15.9 MeV; neutron emitter; half-life 4.2 s.
- **^{18}O(γ,d)^{16}N**. threshold $\sim$19.6 MeV; $\sim$6.1 MeV γ-ray emitter; half-life 7.1 s.
- **^{19}F(γ,2p)^{17}N**. threshold $\sim$23.9 MeV; neutron emitter; half-life 4.2 s.
- **^{19}F(γ,^{3}He)^{16}N**. threshold $\sim$22.1 MeV; $\sim$6.1 MeV γ-ray emitter; half-life 7.1 s.

In the interfering reaction lists of Tables 5.1, 5.2 and 5.3, the lowest energy threshold reaction was displayed but keep in mind any reaction that emits the correct number of neutrons and protons will lead to the same reaction product.

While only six reactions interfere with both the delayed neutron and high-energy γ-ray fission signatures, the target isotopes are from some of the most abundant elements. To

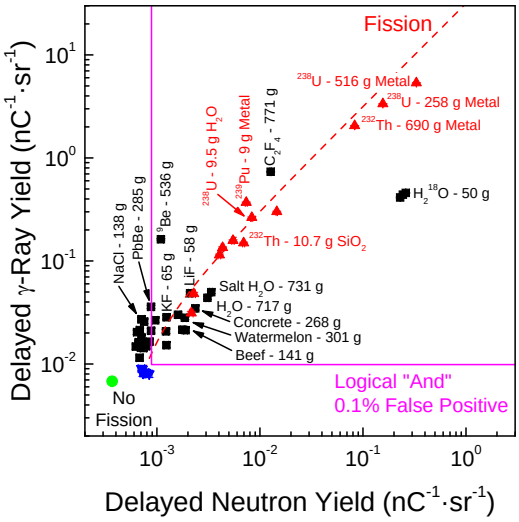

Figure 5.5: Gross single delayed neutron and γ-ray inspection yields from 42 bare targets including 29 that did not contain any fissionable materials (■), 12 that contained fissionable materials (▲) and a number of inspections with no target (▼). The bremsstrahlung endpoint energies was 37.5 MeV and was generated by electron pulses containing $\sim$185 nC, respectively. The total inspection time was $\sim$ 600 s. Overlaid on these graphs is the linear relationship between the delayed neutron and γ-ray yields (red dashed line), the logical "And" critical decision surface (solid magenta line) and the passive background contribution (●).

start, oxygen is the most abundant element in the earth's lithosphere (i.e. the outermost shell of a rocky planet) and it is of course the second most abundant element after hydrogen in the 1.4×10^{15} L of water on the planet [43]. Not to mention the atmosphere, which is approximately 20% oxygen molecules. The isotopic fraction of the target isotope ^{18}O is only 0.2% but the large quantity of oxygen makes it easily within the top 15 most abundant isotopes on earth. Hence, relatively small quantities of materials containing oxygen can cause interferences with both fission signatures as seen in Figures 5.5 for H_2O (i.e. water), SiO_2 (i.e. sand), watermelon, beef etc.... Fluorine is not nearly as prevalent as oxygen but it is still the 13th most abundant element in the earth's lithosphere by mass [44]. However, 100% of elemental fluorine is the target isotope ^{19}F, making it only slightly less abundant than ^{18}O. The target isotope ^{19}F has an isotopic abundance by mass (i.e. elemental abundance multiplied by the isotopic fraction) in the lithosphere of $\sim$0.08% versus $\sim$0.09% for ^{18}O.

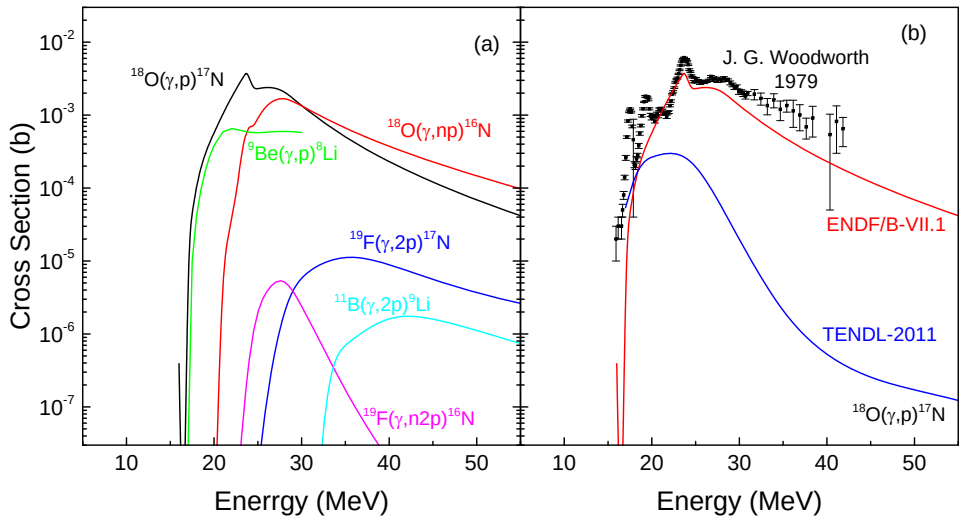

Figure 5.6: Cross sections of ^{18}O(γ,p)^{17}N (black line), ^{18}O(γ,np)^{16}N (red line), ^{19}F(γ,2p)^{17}N (blue line), ^{19}F(γ,n2p)^{16}N (magenta line), ^{9}Be(γ,p)^{8}Li (green line) and ^{11}B(γ,2p)^{9}Li reactions (cyan line) in graph (a). The ^{18}O and ^{9}Be reactions were from the ENDF/B-VII.1 evaluated cross section database [36]. The ^{19}F reactions were from the TENDL-2011 calculated cross section database [42]. Graph (b) compares the cross section for the ^{18}O(γ,p)^{17}N from ENDF/B-VII.1 (red line), TENDL-2011 (blue line) and measurements from J. G. Woodworth (■) [22].

5.4 Bremsstrahlung Weighted Integral Cross Sections

The likelihood that a target isotope will be encountered is one of the important pieces of information needed to evaluate the potential intensity of an interfering reaction in a high-energy inspection scenario. The intensity of the reaction products interfering decay (i.e. branching ratios and half-life) and the production cross section for the reaction also need to be considered. The decay intensity was summarized in Tables 5.1, 5.2 and 5.3, but only the location of the available cross section data was given in these tables. Figure 5.6(a) shows the cross sections for the six reactions that interfere with both delayed neutrons and high-energy γ-ray fission signals. The ^{18}O(γ,p)^{17}N, ^{18}O(γ,d)^{16}N and ^{9}Be(γ,p)^{8}Li cross sections are from the ENDF/B-VII.1 evaluated cross section database [36]. In contrast, the ^{19}F(γ,2p)^{17}N, ^{19}F(γ,n2p)^{16}N and ^{11}B(γ,2p)^{9}Li cross sections are from the TENDL-2011 calculated cross section database because evaluated cross section data was not available. The cross sections for the ^{18}O reactions are over two orders of magnitude larger than the cross sections for the ^{19}F reactions that lead to the same products. However, significant discrepancies can exist between calculated, evaluated and even experimentally measured cross sections as can

be seen in Figure 5.6(b), showing the ^{18}O(γ,p)^{17}N cross sections from ENDF/B-VII.1 and TENDL-2011 databases compared to the measured cross section from J. G. Woodworth et al. [22]. The most striking difference is between the ENDF/B-VII.1 evaluated cross section and TENDL-2011 calculated cross section, which is orders of magnitude smaller with a drastically different shape. The evaluated cross section roughly matches the experimentally measured cross section but is missing the structure in the cross section seen experimentally below $\sim$ 20 MeV. Furthermore, the evaluated cross section is $\sim$ 4 times below the measurements at high photon energies. These discrepancies highlight the difficulty in calculating/simulating interferences because only 35 of the 181 interfering reactions identified in Tables 5.1, 5.2 and 5.3 have experimental cross section data listed on the CSISRS database.

While the bremsstrahlung beam's broad energy distribution prevents any easy measurement of the production cross sections, the bremsstrahlung weighted integral cross sections is closely related to the production rate of the reaction product. This production rate is given by

$$P = N_T \int_{E_o}^{E_f} \frac{\mathrm{d}\Phi}{\mathrm{d}E_\gamma} \, \sigma\left(E_\gamma\right) \mathrm{d}E_\gamma, \tag{5.1}$$

where N_T is the number of target isotope atoms in the target, $\mathrm{d}\Phi/\mathrm{d}E_\gamma$ is the bremsstrahlung flux in the target and $\sigma\left(E_\gamma\right)$ is the reaction cross section. Of course in the experiments, the interfering reaction products were created in a pulse and the decay radiation was detected between irradiating pulses. Hence, the reaction products are created and then exponentially decay, with this process repeated thousands of times. Starting with the first bremsstrahlung pulse, the number of reaction products at any time after the pulse is

$$N_{0d} = \frac{P}{\lambda}\left(1 - e^{-\lambda t_p}\right) e^{t - \lambda t_p}, \tag{5.2}$$

where λ is the decay constant and t_p is the pulse width. Assuming a discrete γ-ray from the decay of the reaction product is being counted, the detection rate is given by

$$R_{0d} = \epsilon \beta P \left(1 - e^{-\lambda t_p}\right) e^{-\lambda (t - t_p)}, \tag{5.3}$$

where ϵ is the absolute photo peak efficiency for the γ-ray emitted with branching ratio of

β. The photons detected between the beginning, t_o, and end, t_f, of the counting period is

$$C_{0d} = \int_{t_o}^{t_f} R_{0d}\left(t\right) \mathrm{d}t = \epsilon\beta\frac{P}{\lambda}\left(1 - e^{-\lambda t_p}\right)\left[e^{-\lambda(t_o - t_p)} - e^{-\lambda\left(t_f - t_p\right)}\right]. \tag{5.4}$$

When multiple bremsstrahlung pulses irradiate a target, the photons detected after the last pulse contains contributions from the reaction products produced in all the previous bremsstrahlung pulses. Hence, the photons detected after an arbitrary number of pulses contains a sum,

$$C_{nd} = \epsilon\beta\frac{P}{\lambda}\left(1 - e^{-\lambda t_p}\right)\sum_{k=0}^{n}\left[e^{-\lambda(t_o + k\Delta t - t_p)} - e^{-\lambda\left(t_f + k\Delta t - t_p\right)}\right]. \tag{5.5}$$

Here the sum is in "reverse" order with $k = 0$ and $k = n$ representing the last and first pulse respectively. This sum can be written as a simple geometric series

$$C_{nd} = \epsilon\beta\frac{P}{\lambda}\left(1 - e^{-\lambda t_p}\right)\left[e^{-\lambda(t_o - t_p)} - e^{-\lambda\left(t_f - t_p\right)}\right]\sum_{k=0}^{n}\left(e^{-\lambda\Delta t}\right)^k, \tag{5.6}$$

and the solution to geometric series can be applied, resulting in

$$C_{nd} = \epsilon\beta\frac{P}{\lambda}\left(1 - e^{-\lambda t_p}\right)\left[e^{-\lambda(t_o - t_p)} - e^{-\lambda\left(t_f - t_p\right)}\right]\frac{1 - e^{-\lambda(n+1)\Delta t}}{1 - e^{-\lambda\Delta t}}. \tag{5.7}$$

Presumably, the photons are detected between every pulse, requiring that the photons detected after each pulse be summed together

$$C_T = \sum_{n=0}^{n_p - 1} C_{nd} = \epsilon\beta\frac{P}{\lambda}\left(1 - e^{-\lambda t_p}\right)\frac{e^{-\lambda(t_o - t_p)} - e^{-\lambda\left(t_f - t_p\right)}}{1 - e^{-\lambda\Delta t}}\sum_{n=0}^{n_p - 1}\left[1 - e^{-\lambda(n+1)\Delta t}\right]. \tag{5.8}$$

Again the sum on the right hand side of the equation is a geometric series and applying the solution results in

$$C_T = \epsilon\beta\frac{P}{\lambda}\left(1 - e^{-\lambda t_p}\right)\frac{e^{-\lambda(t_o - t_p)} - e^{-\lambda\left(t_f - t_p\right)}}{1 - e^{-\lambda\Delta t}}\left[n_p - e^{-\lambda\Delta t}\frac{1 - e^{-\lambda n_p\Delta t}}{1 - e^{-\lambda\Delta t}}\right]. \tag{5.9}$$

Every term in the above equation was measured in the experiments except the production rate, P, which is related to the bremsstrahlung weighted integral cross section. Using

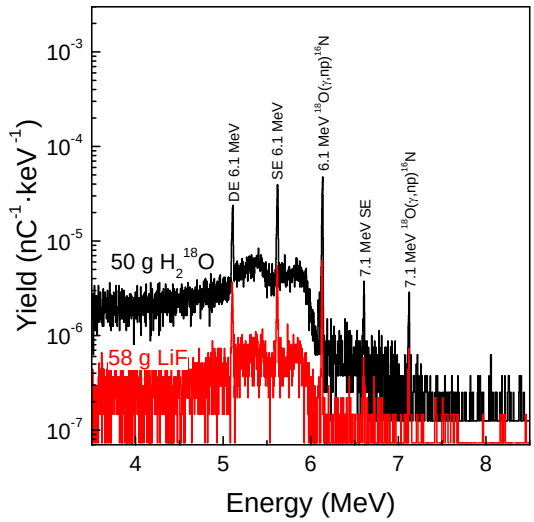

Figure 5.7: Photon energy spectra collected by the HPGe detector from the irradiation of the $H_2{}^{18}O$ (black line) and LiF (red line) targets. The inspections were conducted using a pulsed 38 MeV bremsstrahlung beam generated from 2 μs electron pulses containing $\sim$80 nC of charge that struck a 2.2 mm tungsten radiator. The bremsstrahlung repetition rate was 15 Hz and the inspection times were 1.2 and 3.4 hr for the $H_2{}^{18}O$ and LiF targets. Photon detected in the first $\sim$25 ms after the bremsstrahlung pulse have been removed.

Equation (5.9), the bremsstrahlung weighted integral cross section can be determined from

$$\Sigma_{brem} = \int_{E_o}^{E_f} \frac{\mathrm{d}\Phi}{\mathrm{d}E_\gamma}\,\sigma\left(E_\gamma\right)\mathrm{d}E_\gamma = \frac{C_T}{\epsilon\beta N_T N_{mp}} \cdot \frac{\lambda}{1-e^{-\lambda t_p}}, \tag{5.10}$$

where

$$N_{mp} = \frac{e^{-\lambda(t_o-t_p)} - e^{-\lambda\left(t_f-t_p\right)}}{1-e^{-\lambda\Delta t}}\left[n_p - e^{-\lambda\Delta t}\frac{1-e^{-\lambda n_p \Delta t}}{1-e^{-\lambda\Delta t}}\right]. \tag{5.11}$$

These measured bremsstrahlung weighted integral cross sections can then be compared to integral cross sections calculated using the Monte Carlo models to simulate the bremsstrahlung flux and the cross section data like those presented in Figure 5.6.

Equation (5.10) is most easily applied to discrete γ-rays emitted from a reaction product as opposed to the gross high-energy γ-ray yield. As an example, Figure 5.7 presents the discrete γ-ray spectrum collected by the HPGe detector from the ^{16}N reaction product created in ^{18}O(γ,np)^{16}N and ^{19}F(γ,n2p)^{16}N reactions. The primary decay lines from ^{16}N are clearly visible at 6.1 and 7.1 MeV followed by the single escape peaks 511 keV below these lines. In

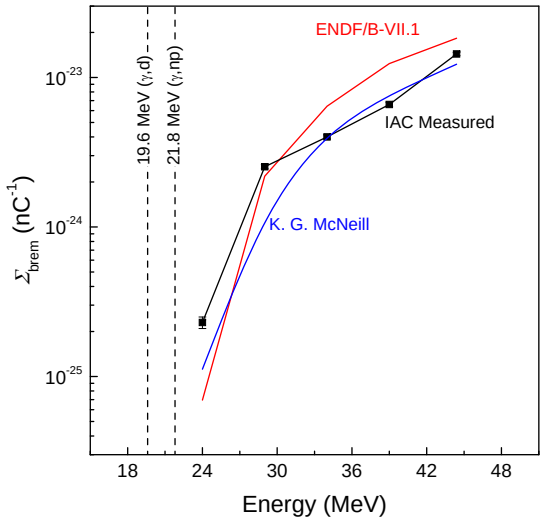

Figure 5.8: Measured integral cross section for the ^{18}O(γ,np)^{16}N reaction (■) as a function of bremsstrahlung endpoint energy. The measurements were conducted using a bremsstrahlung endpoint energy that was changed from 19 to 45 MeV. Overlaid on this graph is integral cross sections from the ENDF/B-VII.1 database (red line) and measurements by K. G. McNeill (blue line) [36, 45].

addition, the double escape peak is visible from the 6.1 MeV γ-ray line. These high-energy photons are largely responsible for the interference with the delayed γ-ray fission signature. The integration of the primary lines provides the number of detected photons needed in Equation (5.10) for calculating the integral cross section. While the discrete rays from ^{16}N are directly responsible for the interferences from ^{18}O and ^{19}F, any intense discrete γ-ray from a reaction product can be utilized.

The research team has so far used the discrete γ-ray yield from ^{16}N, ^{17}N, ^{20}F and ^{34m}Cl to investigate the bremsstrahlung weighted integral cross section from ^{18}O(γ,np)^{16}N, ^{18}O(γ,p)^{17}N, ^{19}F(γ,n2p)^{16}N, ^{23}Na(γ,n2p)^{20}F and ^{35}Cl(γ,n)^{34m}Cl reactions. Figure 5.8 shows the measured integral cross section for the ^{18}O(γ,np)^{16}N compared to the cross section from the ENDF/B-VII.1 database and the experimentally measured cross section by K. G. McNeill et. al [36, 45]. The integral cross section is presented per unit electron charge on the bremsstrahlung radiator because the research team used this charge as a proxy; the conversion to more natural units (i.e. b·MeV) is ongoing. As expected, the integral cross section monotonically increases by over three orders of magnitude between 24 and 45 MeV bremsstrahlung endpoint energy. At the lowest bremsstrahlung energy of 24 MeV, the IAC measured integral cross section over a factor of two larger than the comparison cross sec-

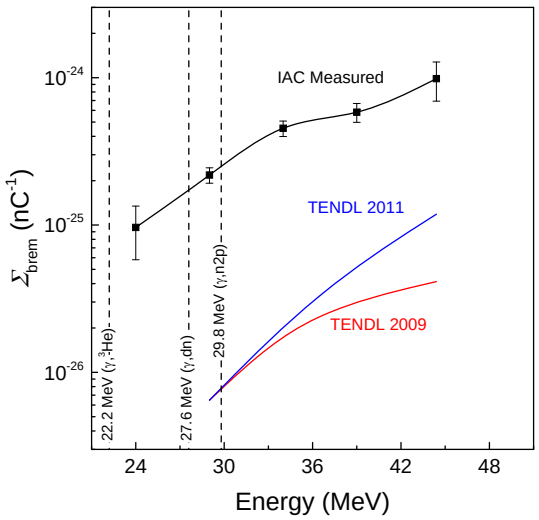

Figure 5.9: Measured integral cross section for the ^{19}F(γ,n2p)^{16}N reaction (■) as a function of bremsstrahlung endpoint energy. The measurements were conducted using a bremsstrahlung endpoint energy that was changed from 19 to 45 MeV. Overlaid on this graph is integral cross sections from the TENDL-2009 (redred line) and TENDL-2011 (blue line) databases [42].

tions. This discrepancy may be caused by ^{17}O contamination in our $H_2{}^{18}O$ sample through the ^{17}O(γ,p)^{16}N reaction, which has a low threshold of 13.8 MeV. The IAC team has not corrected for this contribution. At higher energies, the measured integral cross section is in good agreement with the cross section from K. G. McNeill, both of which are $\sim$60% below the evaluated cross section provided by ENDF/B-VII.1.

The ^{18}O(γ,np)^{16}N provides a good test case of our integral cross section measurements because both evaluated cross sections and measurements by other research teams are available. The ^{19}F(γ,^{3}He)^{16}N, ^{19}F(γ,dp)^{16}N and ^{19}F(γ,n2p)^{16}N reactions do not have measured cross sections available and no evaluated cross section is available in ENDF/B-VII.1. Figure 5.9 shows the measured integral cross section for the collective ^{19}F(γ,n2p)^{16}N reactions compared to the calculated cross section from the TENDL-2009 and TENDL-2011 database. Again, the integral cross section monotonically increases by over an order of magnitude between 24 and 45 MeV bremsstrahlung endpoint energy. Most importantly the measured integral cross section is over an order of magnitude above the calculated cross sections. Any simulation/calculation based on the calculated TENDL cross sections would grossly underestimate the strength of the interferences from ^{19}F. Hence, these cross sections are a prime candidate for a standard cross section measurement utilizing a monoenergetic photon beam as the irradiation source. A word of caution is warranted, ^{16}N can also be produced from

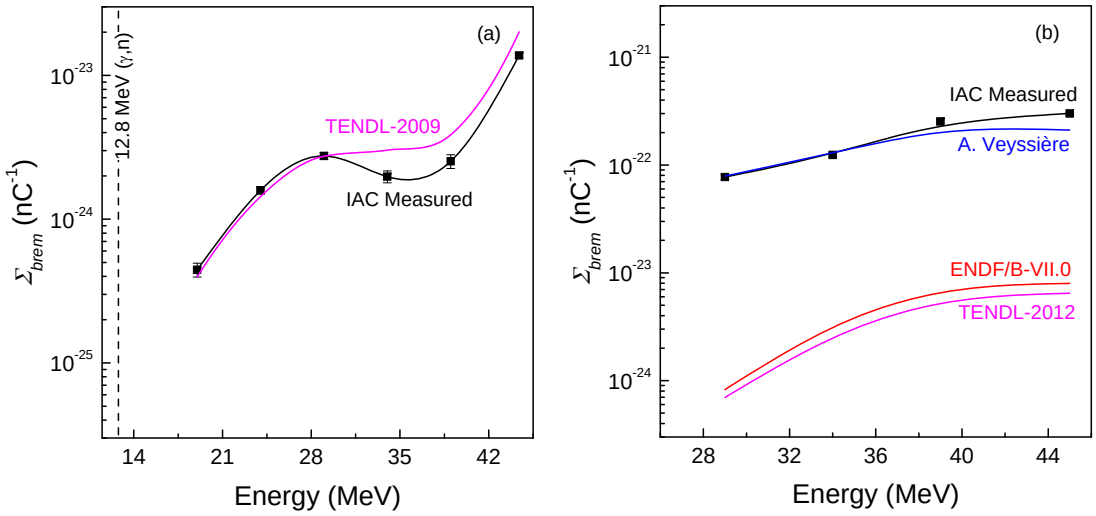

Figure 5.10: Measured integral cross sections (■) for the ^{35}Cl(γ,n)^{34m}Cl (a) and ^{40}Ar(γ,np)^{38}Cl (b) reactions as a function of bremsstrahlung endpoint energy. The measurements were conducted using a bremsstrahlung endpoint energy that was changed from 19 to 45 MeV. Overlaid on this graph is integral cross sections calculated from cross section by the ENDF/B-VII.0 (red line), TENDL (magenta line) and TENDL-2011 (blue line) A. Veyssiére et. al [36, 42, 46].

^{19}F by ^{19}F(n,^{4}He)^{16}N and any other neutron reaction emitting 2 neutrons and 2 protons. All the available reactions have neutron thresholds over 20 MeV, except the ^{19}F(n,^{4}He)^{16}N reaction, which has a low threshold of only 1.6 MeV. Hence, there is a possibility that neutrons produced in (γ,nx)reactions in the environment then induce ^{19}F(n,^{4}He)^{16}N reactions. The research team suspects that this interfering contribution is small due to the low efficiency of neutron production but further research is required.

The photonuclear reactions in ^{18}O and ^{19}F are of the greatest concern because their reaction products interfere with both the delayed neutron (^{17}N) and γ-ray (^{16}N) fission signals and the target isotopes have some of the highest natural abundances. However, there are a large number of other interfering reactions that were observed, mostly for the delayed γ-ray fission signal, for which bremsstrahlung weighted cross sections were also measured. Figure 5.10 shows the measured bremsstrahlung weighted integral cross sections from the ^{35}Cl(γ,n)^{34m}Cl and ^{40}Ar(γ,np)^{38}Cl reactions. Both reactions are compared to calculated integral cross sections based on standard cross sections when available from TENDL, ENDF/B and experimental measurements. The ^{35}Cl(γ,n)^{34m}Cl reaction in Figure 5.10a has a threshold of 12.8 MeV with the reaction product ^{34m}Cl having a half-life of 32 min that interferes

with the delayed γ-ray signal through the emission of a 3.3 MeV γ-rays. In addition, the isomeric transition daughter ^{34}Cl has a half-life of 1.5 s and interferes with the delayed γ-ray fission signal through the emission of high-energy β^+-particles with an endpoint of 4.5 MeV. As with almost all reactions that lead to metastable products, no ENDF/B or experimental cross section data was available but data was available from TENDL-2009 and this integral cross section is overlaid with the measurements. The experimentally measured integral cross section agreed exceptionally with the TENDL-2009 data below $\sim$28 MeV with minor discrepancies at higher energies. The flat region in the integral cross section from $\sim$28 to $\sim$37 MeV arises as multiple particle emission reactions begin to open up. The ^{40}Ar(γ,np)^{38}Cl reaction in Figure 5.10b has a threshold of 15.6 MeV with the reaction product ^{38}Cl having a half-life of 37 min that interferes with the delayed γ-ray signal through the emission of high-energy β^--particles with an endpoint of 4.5 MeV. While the interference from ^{38}Cl is minor, standard cross section data is available from ENDF/B-VII.0, TENDL-2012 and experimentally measured by A. Veyssiére et. al [46], allowing a broad comparison. The experimentally measured integral cross section agree well with the data from A. Veyssiére et. al but the cross section data in ENDF/B-VII.0 and TENDL-2012 under predicts the integral cross section by over an order of magnitude. Further demonstrating the potential pitfalls of relying on data in the standard cross section databases.

Chapter 6

Modeling Fission Signal Interferences

6.1 Introduction

The research into fission signature interferences sought to identify and measure reactions that produce similar signals to those used to indicate the presence of fissionable materials. Once measured, the integral cross sections for the interfering reactions were compared with those available in the various databases. For these comparisons, the Monte Carlo-based simulation software MCNPX 2.7 was employed to provide well-defined bremsstrahlung flux distributions in the targets; this process is discussed in Section 6.4. Additionally, for the following 5 photonuclear reactions of interest, the corresponding ACE files, from which the cross section information is extracted in a standard MCNPX simulation, were examined:

- ^{9}**Be(**γ**,p)**^{8}**Li**
- ^{18}**O(**γ**,np)**^{16}**N**
- ^{19}**F(**γ**,2pn)**^{16}**N**
- ^{35}**Cl(**γ**,n)**^{34m}**Cl**
- ^{40}**Ca(**γ**,np)**^{38m}**K**

This provided an understanding of the specific reactions available when using table physics. A final focus of the modeling and simulation effort centered on demonstrating the efficacy of simulating representative data sets with MCNPX 2.7. For Version 2.7, delayed γ-ray emission from residual nuclei is included for neutron library interactions, but is excluded for all photonuclear (non-fission) and proton library interactions [47]. Model interactions also allow for residuals to be created and tracked, with corresponding delayed γ-ray emission, and include photonuclear interactions. Hence, for this phase, model physics were forced and the CEM03 models were utilized to create representative data sets.

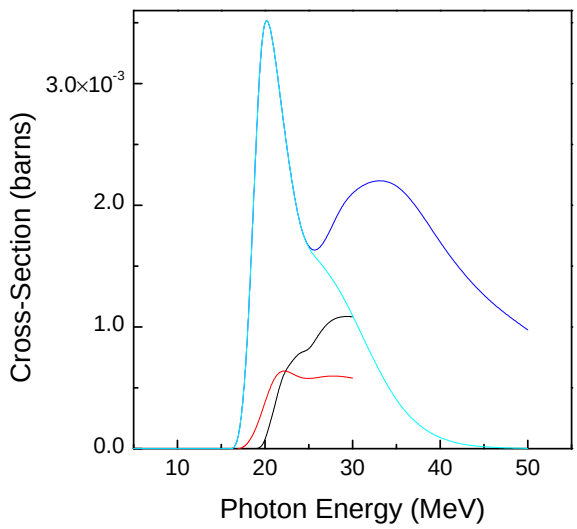

Figure 6.1: Comparison of particle production cross sections for photon interactions in ^{9}Be. (black line) proton production, ENDF/B-VII.0 ACE file; (redline) reaction MT=103, ENDF/B-VII.0 database; (blue line) proton production, TENDL 2011 ACE file; and (cyan line) ^{8}Li production, TENDL 2011 database.

6.2 Table Physics

It is understood that utilizing table physics does not allow for tracking of residual nuclei or delayed γ-ray emission with photonuclear interactions. However, assuming the cross sections contained in the ACE files are sufficiently accurate, it could then be possible to extract the corresponding reaction cross sections and create empirical data sets based on these cross sections. This would be particularly useful since, as discussed in Section 6.3, the CEM03 models do not consider photo-absorption below $\sim$ 30 MeV. While ACE files exist for several databases (e.g., KAERI, CNDC, BOFOD, etc.), the current investigation was limited to ACE files representing the ENDF/B-VII.0 (*.70u) and TENDL 2011 (*.00u) libraries.

6.2.1 ^{9}Be(γ,p)^{8}Li

The 4009.70u ACE file contains particle production cross sections for neutrons, γ-rays, protons, and ^{4}He. Further, the ENDF/B-VII database contains a cross section for ^{9}Be(z,p) (MT=103); however, as shown in Figure 6.1, the proton production cross section included in the .70u ACE file is significantly different from the ^{9}Be(z,p) cross section. In either case, the cross sections only contain entries for incident photon energies up to 30 MeV, which is inadequate for applications where the incident energies are much higher. Aside from the

contents of the .70u ACE file, the ENDF/B-VII.0 database does not appear to include a cross section for the photonuclear production of ^{8}Li from ^{9}Be.

The TENDL .00u ACE file contains particle production cross sections for neutrons, γ-rays, protons, deuterons, tritons, ^{3}He, and ^{4}He. While not included in the ACE file, the TENDL 2011 database does contain a cross section for the ^{9}Be(γ,p)^{8}Li reaction. Shown in Figure 6.1, the proton production and ^{9}Be(γ,p)^{8}Li cross sections are identical below $\sim$ 25 MeV, although they strongly deviate for higher energies.

6.2.2 ^{18}O(γ,np)^{16}N

The 8018.70u ACE file contains particle production cross sections for neutrons, γ-rays, protons, deuterons, tritons, ^{3}He, and ^{4}He. The ENDF/B-VII.0 database provides the ^{18}O(γ,np)^{16}N cross section; however, the ^{16}N production is not available from the ACE file. The deuteron and ^{16}N production cross sections are identical from the threshold slightly above 20 MeV, but quickly deviate above $\sim$ 22 MeV.

The TENDL .00u ACE file contains particle production cross sections for neutrons, γ-rays, protons, deuterons, tritons, ^{3}He, and ^{4}He. As with ENDF/B-VII.0, the TENDL 2011 database also includes a ^{16}N production cross section that is not present within the ACE file. This cross section is equivalent to the deuteron production cross section below 22 MeV, but is shown to be much less probable for energies above 22 MeV.

6.2.3 ^{19}F(γ,2pn)^{16}N

The ENDF/B-VII.0 database does not appear to contain any cross sections for photonuclear reactions from ^{19}F. Consequently, there is no 9019.70u section in the ENDF/B-VII.0 ACE files. TENDL .00u ACE file contains particle production cross sections for neutrons, γ-rays, protons, deuterons, tritons, ^{3}He, and ^{4}He. The TENDL 2011 database also includes ^{16}N production, although this cross section is excluded in the ACE file. Further, while the ^{3}He and ^{16}N production cross sections from TENDL 2011 are identical from the threshold slightly above 20 MeV, significant discrepancies are present above 26 MeV. Similar to the TENDL 2011 cross sections for ^{18}O, substituting the ^{3}He production cross section for all ^{16}N production may suffice for incident photons between 20 and 26 MeV, although careful considerations would be warranted for higher incident energies.

6.2.4 ^{35}Cl(γ,n)^{34m}Cl

The 17035.70u ACE file contains particle production cross sections for neutrons, γ-rays, protons, deuterons, tritons, and ^{4}He. The total neutron production and the ^{34}Cl production (included in the ENDF/B-VII.0 database) cross sections are identical from the threshold at 12.6 MeV until $\sim$ 18.5 MeV, where the two deviate. Further, it is understood the delayed γ-ray of interest at 3304 keV is emitted from the metastable state ^{34m}Cl, for which the production cross section does not appear to be included in either the 17035.70u ACE file nor the ENDF/B-VII.0 database as a whole.

The TENDL .00u ACE file contains particle production cross sections for neutrons, γ-rays, protons, deuterons, tritons, ^{3}He, and ^{4}He. In this case, the TENDL 2011 database also includes cross sections for ^{34}Cl and ^{34m}Cl production. All three cross sections differ across the entire energy range of incident photons. Regardless, the ^{34m}Cl production cross section is excluded from the ACE file.

The cindergl.dat file includes the necessary information to generate the 3304 keV γ-rayfrom the ^{35}Cl(γ,n)^{34m}Cl reaction. However, even if either the .70u or .00u libraries allowed for ^{34m}Cl production, MCNPX 2.7 does not provide a mechanism for the passing of a metastable state to cinder [48]. This restriction is not limited to photonuclear reactions, but also occurs with neutron interactions. As an example, most, if not all, of the experimental measurements collected with the HPGe detector showed strong γ-ray lines at 570 and 1064 keV. These γ-rays are emitted via de-excitation of the third excited level of ^{207}Pb, which is a metastable state, first by emission of the 1064 keV γ-ray followed by the 570 keV γ-ray. The de-excitation of this 1633 keV level has a half-life of $\sim$ 800 ms and was likely produced via ^{208}Pb(n,2n)^{207m}Pb reactions. Nevertheless, each of these metastable states is absent in the MCNPX 2.7 simulations, since branching of specific nuclides to metastable states is not processed in the ACE files [48].

6.2.5 ^{40}Ca(γ,np)^{38m}K

The 20040.70u ACE file has particle production cross sections for neutrons, γ-rays, protons, deuterons, tritons, and ^{4}He. The ENDF/B-VII.0 database includes a ^{38}K production cross section, although ^{38m}K production is not available. The deuteron and ^{38}K production cross sections are substantially different above $\sim$ 22 MeV.

The TENDL .00u ACE file contains particle production cross sections for neutrons, γ-rays, protons, deuterons, tritons, ^{3}He, and ^{4}He. Similar to ^{35}Cl, the TENDL 2011 database

provides cross sections for both ^{38}K and ^{38m}K production. For these reactions, the ^{38}K and ^{38m}K production cross sections are only slightly different below $\sim$ 24 MeV, although above this incident energy all three cross sections are considerably different.

6.3 CEM Physics

In MCNPX 2.7, residual nuclei are tracked for neutron-induced and model reactions; however, photon and proton library reactions do not produce residuals [47]. Hence, simulating delayed γ-ray production from photonuclear reaction products requires the use of physics models (Bertini, ISABEL, CEM03, etc.). For photonuclear interactions, MCNPX automatically calls the CEM03 model physics, despite what may be called for on the corresponding LCA card [47]. The CEM03 code uses the Cascade-Exciton Model for nuclear reactions, which is based on the Dubna IntraNuclear Cascade (INC) and the Modified Exciton Model [49]. The code generally assumes reactions induced by nucleons, pions, or photons occur in three stages, the first of which is the INC. This is followed by the pre-equilibrium stage, finishing with relaxation of the nuclear excitation via a modified exciton model of equilibrium evaporation/fission [49].

The code uses the Dubna INC model for reactions induced by photons above the Giant Dipole Resonance (GDR) and below the pion-production threshold, where photon absorption is considered to occur on quasi-deuteron pairs [49]. Above the pion-production threshold, the INC employs a Monte Carlo method, based on partial cross sections, to choose the specific reaction mode [49]. There remains an issue, however, when simulating lower-energy photonuclear interactions, since the INC does not apply for energies within the GDR. Based on the literature and confirmatory simulations, CEM03 does not consider photon absorption for energies below $\sim$ 30 MeV [49, 50]. Despite the fact that a driving motivation of the current research is higher-energy photonuclear reactions, many of the reactions of interest have thresholds well below $\sim$ 30 MeV. However, since the only option available in MCNPX 2.7 to generate the delayed γ-rays is to employ model physics, the CEM03 model were used, despite the exclusion of interactions within, and below, the GDR.

To extract the cross sections from the CEM, monoenergetic photons from 10 to 50 MeV were incident on 10 μm thick targets. Residual nuclei tallies were produced with the FT RES Special Treatment option in MCNPX. The associated cross section at each incident energy was then calculated by

$$\sigma = \frac{Tally}{\rho_A \cdot V \cdot \Phi}, \tag{6.1}$$

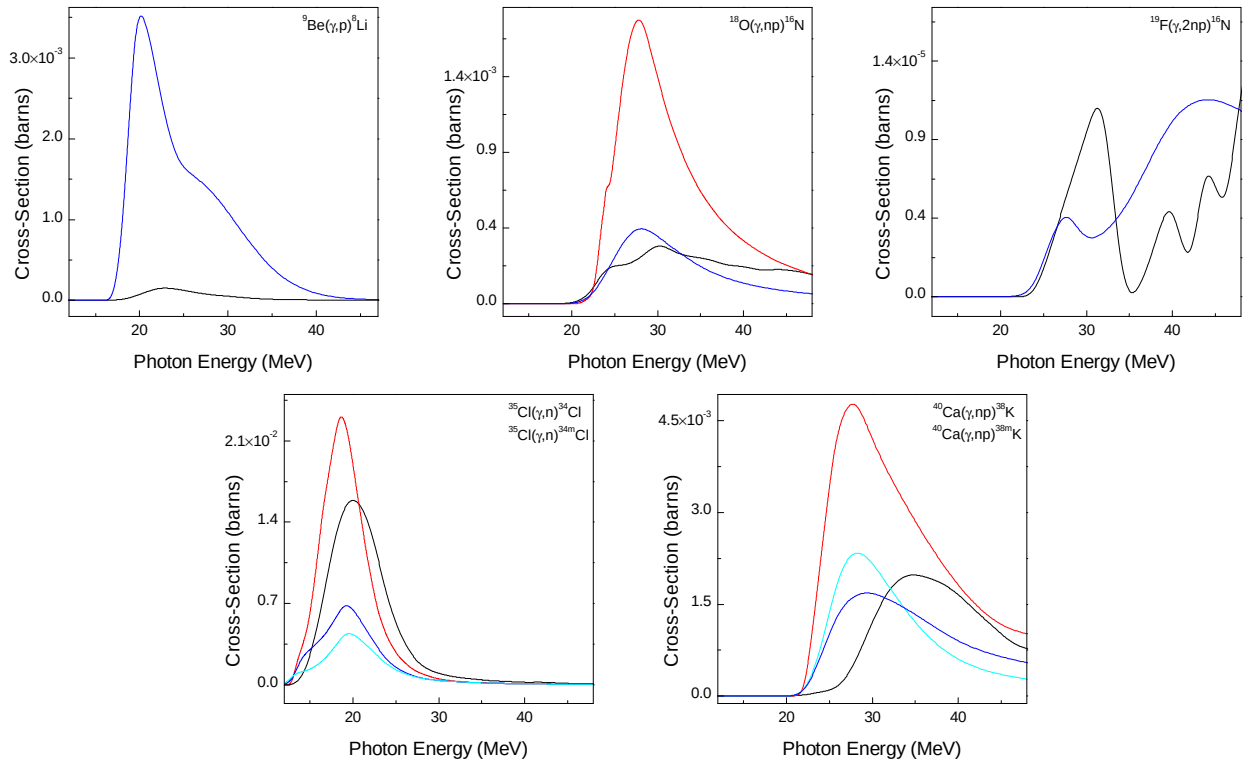

Figure 6.2: Comparisons of photonuclear reaction cross sections from (black line) CEM03, (red line) ENDF/B-VII.0 database, (blue line) TENDL 2011 database, and (cyan line) metastable states from TENDL 2011 database. The CEM03 cross sections were calculated from the results of each simulation.

where ρ_A is the atomic density, V is the cell volume, and Φ is the incident photon flux. To support this method, a preliminary simulation using neutron library interactions (.70c) on ^{3}He and tallying for residual ^{3}H showed strong agreement with the well-known ^{3}He(n,p)^{3}H reaction cross section across all energies examined. Figure 6.2 compares the cross sections calculated from the CEM03 model with corresponding cross sections from the ENDF/B-VII.0 and TENDL 2011 databases. For all 5 cases, the cross sections extracted from the CEM03 model and those provided by the two databases are contradictory across all incident photon energies examined. While such disagreements were identified from previous investigations within this research, it is, nevertheless, concerning for applications where similar predictive models may be relied upon to inform the direction of the research.

Section 6.4 describes a process for creating representative data sets for comparison with measured spectra. Due to the exclusion of photonuclear reactions below $\sim$ 30 MeV with CEM03, it is understood that the cross sections will undoubtedly differ; hence, direct head-

to-head comparisons via normalization (e.g., nC^{-1}) were not expected to produce precise agreements between simulated and measured spectra. Nevertheless, it is still possible to generate representative spectra, albeit with artificial normalization, for cases where the correct delayed γ-rays are included within CEM03. To assess the availability of delayed γ-rays from the reactions listed in Section 6.1, simulations were completed for 40 MeV γ-rays incident on 5.08 cm thick targets (natural beryllium, ^{18}O-enriched water, polytetrafluoroethylene, sodium chloride, and natural calcium). The resulting delayed ($>$ 20 ms) γ-ray spectra are shown in Figure 6.3. Both the 6129 and 7115 keV γ-rays are present from the ^{18}O(γ,np)^{16}N and ^{19}F(γ,2np)^{16}N reactions in Figure 6.3 A and B, respectively. Figure 6.3 B also contains a 1633 keV γ-ray, which likely resulted from neutron capture on the ^{19}F. It is expected that ^{19}F(n,^{4}He)^{16}N reactions contributed at some level to the production of the 6129 and 7115 keV lines.

The simulation with the beryllium target did not produce any delayed γ-rays for times $>$ 20 ms. While discrete γ-ray emission was not expected, ^{8}Li decays with 13 MeV β^- emission. This decay was observed experimentally from the γ-rays that were emitted via bremsstrahlung of the β^- particles within the target itself. Nevertheless, the simulated data contained no delayed γ-rays; hence, this spectrum is not included in the figure. As seen in Figure 6.3 C, the sodium chloride target produced a 1634 keV γ-ray from the ^{23}Na(γ,^{3}He)^{20}F and/or ^{23}Na(n,α)^{20}F reactions. This is, however, essentially the only γ-ray produced by the model above 511 keV. In reality, photonuclear absorption on ^{35}Cl produces a 3304 keV delayed γ-ray and 4.47 MeV β^+ particles via the ^{35}Cl(γ,n)^{34m}Cl and ^{35}Cl(γ,n)^{34}Cl reactions, respectively. Finally, the simulation with natural calcium also failed to generate any delayed γ-rays above 3 MeV. In this case, the delayed γ-rays were expected from the bremsstrahlung of 5.02 MeV β^+ particles that result from the ^{40}Ca(γ,np)^{38m}K reaction. As was the case for beryllium, the bremsstrahlung process from the delayed β^+ particles was observed experimentally, but is, nevertheless, absent in the simulations. Section 6.2.4 discussed the inability of MCNPX 2.7 to produce delayed γ-rays from metastable states, even in cases where the decay transitions are included in the cinder.dat and/or cindergl.dat files. It is not entirely clear at the time this report was written whether their omission from CEM03 is due to a similar issue.

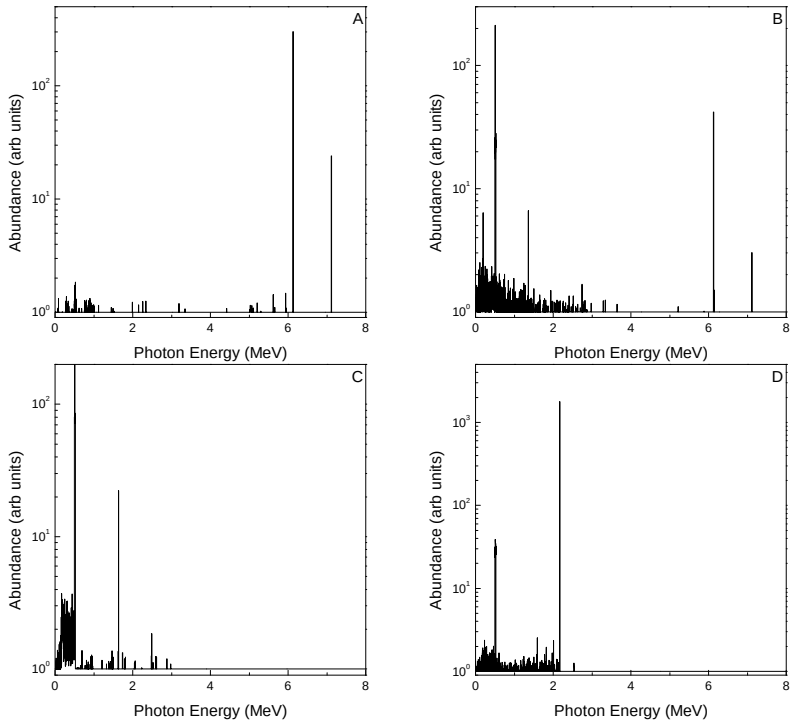

Figure 6.3: CEM-generated delayed γ-ray spectra. These spectra show γ-rays inside (A) ^{18}O-enriched water, (B) polytetrafluoroethylene, (C) sodium chloride, and (D) natural calcium, at times > 20 ms following photon irradiation.

6.4 Simulating a Representative Data Set

For the simulations aimed at reproducing experimentally-measured delayed γ-ray spectra, the 80% relative efficiency HPGe detector was used as the primary detector. The simulated data sets were generated with a multi-step process, beginning with a simulated bremsstrahlung beam. This distribution is utilized as the source for a subsequent simulation that tallies (cell-averaged flux) photons emitted within the targets on timescales greater than 20 ms following source emission. Results from this tally are then used as the source for a final simulation that generates pulse height spectra in a high-fidelity model of the HPGe detector. Here, the F8 pulse-height tally was used with the Gaussian Energy Broadening (GEB) option to produce pulse-height distributions comparable in resolution to the experimental data. Completing this process in multiple stages was largely driven by two factors. Based on the percentage of delayed γ-rays that reach the HPGe active volume (per source electron), it is unlikely that acceptable precision can be achieved with a realistic number of starting source particles. Further, the standard Tally Time option is unavailable with the F8 pulse-height tally. It

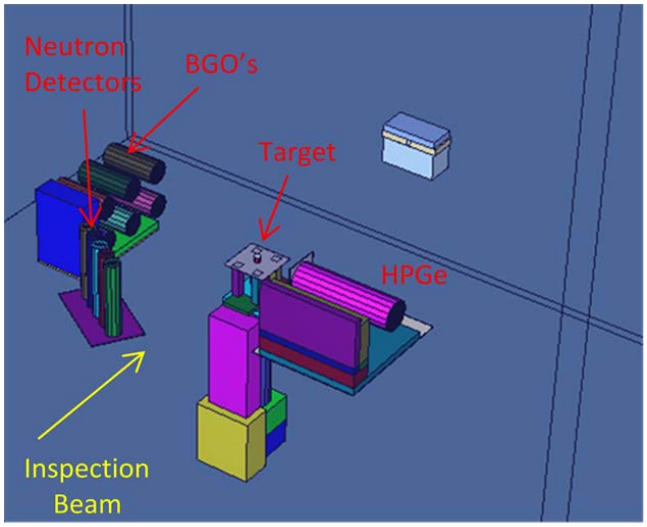

Figure 6.4: VisEd dynamic 3D display of the simulated measurement setup. The image illustrates the relative position of the target and detector arrays; the incident beam direction is from the lower left corner to the upper right. The polyethylene shielding around the HPGe and BGO detectors has been removed in the image to better illustrate the interior components. Using the simulated bremsstrahlung distribution as the source, the cell-averaged flux inside the target was tallied for times greater than 20 ms.

is possible to generate time-dependent F8 tallies by running a more standard F8 tally in coincidence with a time-dependent F6 tally. However, based on the additional convolution this presents along with the desire for statistical precision, a multi-stage approach was chosen.

The bremsstrahlung beam was simulated with 45 MeV electrons incident on a 4.2 g·cm^{-2} tungsten radiator, which included a 2.54 cm aluminum plate on the downstream side. The model geometry included two initial collimators of radii 1.27 cm and 5.08 cm, which were included in the experimental setup immediately downstream from the radiator. The 1.83 m thick concrete wall separating the linac hall from the measurement hall had a first collimator with a radius of 6.35 cm and a second with a radius of 1.905 cm. For the simulation, an additional cell, which was 5.08 cm thick and had a 1.905 cm radius, was created immediately downstream from the last collimator and served as the tally cell. The resulting bremsstrahlung photon distribution was determined with an F4 cell-averaged flux (particles per cm^2) tally. It should be noted that the simulations assume a completely monoenergetic electron beam energy. In reality, there is inherently some energy spread carried by the electrons; however, this assumption does not appear to produce any noticeable inconsistencies between the measurements and the simulations.

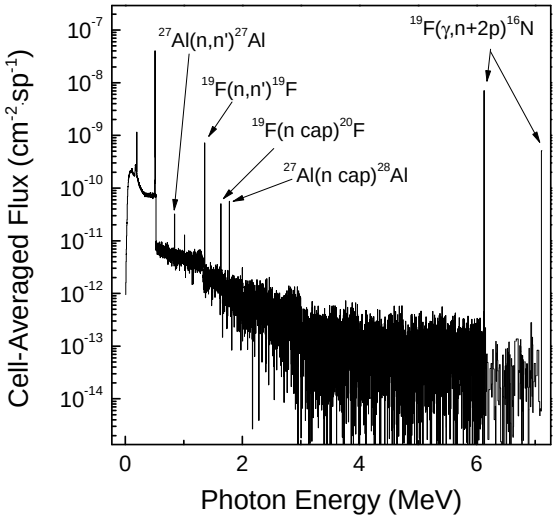

Figure 6.5: Simulated cell-averaged flux in a LiF target after 20 ms. Particular γ-ray lines of note are those at 6129 and 7115 keV, resulting from ^{19}F(γ,2pn)^{16}N, and at 1779 keV from neutron capture in ^{27}Al. These data comprised the source distribution for the final simulation, which generated the simulated HPGe response.

Figure 6.4 provides a 3D schematic of the setup geometry, illustrating the relative position of the target location and detector arrays. The model included high-fidelity geometries for the six BGO detectors, five ^{3}He-based neutron detectors, and two HPGe detectors. A natural lead beam stop, seen as the blue and grey structure towards the upper right of Figure 6.4, was also included. In this orientation, the incident beam travels from the lower left corner to the upper right. With the simulated bremsstrahlung distributions as the source, F4 cell-averaged flux tallies inside the targets-of-interest as well as the materials immediately surrounding the target (e.g. aluminum target stand, etc.) were collected to assess the delayed γ-ray spectra generated by the various isotopes. Time cuts were performed, coinciding with the experimental data, to select only those γ-rays and neutrons that were emitted on timescales longer than 20 ms after source particle creation. Additional F4 tallies, excluding the time cut, were also collected to provide the bremsstrahlung flux distribution within the target. These flux distributions were used for calculating the experimentally-measured, integrated cross sections.

Figure 6.5 presents the results of the F4 tally for photons inside a LiF target, at times $>$ 20 ms. The 6129 and 7115 keV γ-rays, as indicated, are from ^{19}F(γ,2pn)^{16}N reactions and are readily observable. Several additional γ-ray lines are present, although they are likely produced via neutron capture and/or inelastic scattering reactions, specifically ^{27}Al(n,n$'$)^{27}Al

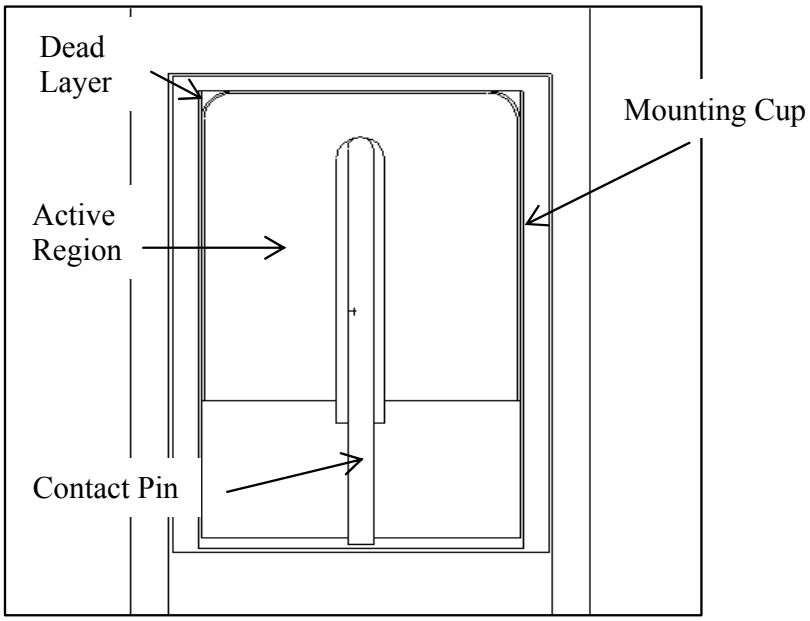

Figure 6.6: 2D representation of the HPGe detector geometry. The model geometry included a 700 micron dead layer, brass pin, aluminum mounting cup, and aluminum pop top. Pulse-height tallies (F8) were collected across the active region of the Ge crystal; energy binning corresponded in scale to the experimental data acquisition software. Gaussian energy broadening parameters were determined from the FWHM of selected experimentally-measured peaks.

and ^{19}F(n,n′)^{19}F. While neutron capture in ^{27}Al produces ^{28}Al, which undergoes β^- decay with a 2.2 minute half-life, the other two inelastic scattering reactions are not delayed reactions. Further, while these reactions do not produce interferences themselves, the appearance of these reactions on delayed timescales (likely due to room-return and delayed neutron emission) suggests alternative reactions, despite being relatively fast, are possible on delayed timescales and could potentially compound gross γ-ray and/or neutron interferences.

Figure 6.6 shows a 2D representation of the HPGe detector geometry used to collect the pulse-height distributions for the final stage of the simulations. The model geometry included a 700 micron dead layer, brass pin, aluminum mounting cup, and aluminum pop top. Exact dimensions were taken from the manufacturer's data sheets, and although slight inconsistencies may exist compared with the actual detector, these differences did not significantly affect the results. The in-target spectra (see Figure 6.5) were utilized as the source distribution for this stage; pulse-height tallies (F8) were collected across the active region of the germanium crystal. Energy binning corresponded in scale to the data acquisition system

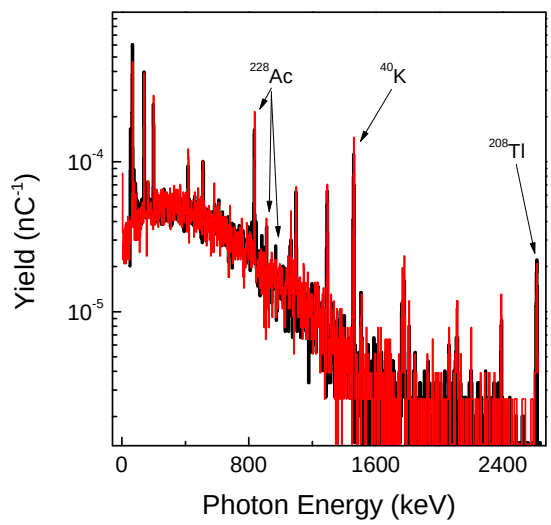

Figure 6.7: Comparison of (black line) measured and (red line) simulated active background in the HPGe detector. The simulated background does reasonably well to reproduce the prominent lines at 2614 keV (^{208}Tl) and 1460 keV (^{40}K), as well as several additional γ-rays emitted by ^{228}Ac and Bi.

used to collect the experimental data. The FT GEB Special Treatment feature was employed to reproduce the Gaussian energy broadening seen in the actual HPGe detector. For this, the required parameters were determined from the FWHM of selected experimentally-measured peaks with the following:

$$W_{FWHM} = a + b \cdot (E + c \cdot E^2)^{0.5}, \tag{6.2}$$

where a = -3.08 keV, b = 0.206 keV$^{0.5}$, and c = 4.716×10^{-5} keV^{-1}. To ensure the extracted parameters were valid across the energy scale expected, experimentally-measured data from the ^{18}O-enriched target were utilized, which included γ-ray peaks up to 7115 keV.

Representative data sets involved two components, the active background and the delayed γ-ray emission from the target. Many of the γ-rays present in the active background data are natural emissions produced from the environment. The more prominent of these are at 2614 keV (^{208}Tl) and 1460 keV (^{40}K), with several additional γ-rays emitted by ^{228}Ac and Bi. Experimentally-measured active background spectra were examined to extract initial relative abundances of the prominent emissions. The abundances were then further refined by accounting for the effect the energy-dependent detector efficiency had on the measured spectra. The next step utilized the refined abundances as the source distribution for a sim-

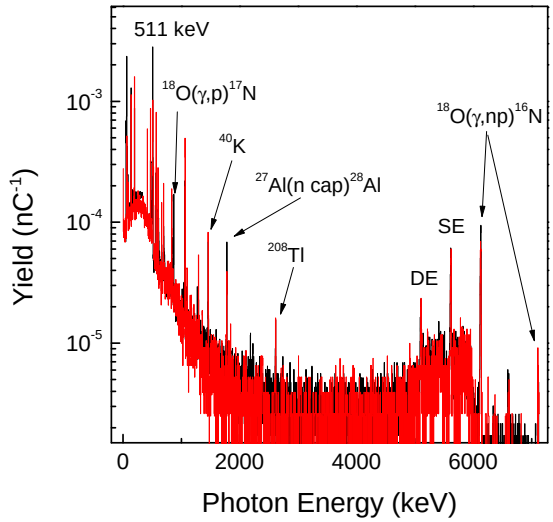

Figure 6.8: Comparison of the (black line) measured and (red line) simulated delayed γ-ray spectra from an ^{18}O-enriched water target. Overall, the simulations reproduced the experimental data reasonably well. These data have been artificial normalized to the 6129 keV peaks.

ulation wherein a F4 tally recorded the cell-average photon flux inside a concrete wall. This provided an estimate for the downscattering of the natural emissions and produced a more-realistic energy distribution. The final step in generating a simulated active background used the energy distribution from the previous step as the source, positioned at the primary target location, for a final simulation with the modeled HPGe detector. The "final simulation" here was actually a series of small, iterative adjustments to the source distribution, which allowed for stronger agreement between the measured and simulated active background spectra. Figure 6.7 compares the measured (black data) and simulated (red data) HPGe responses from the active background. In this case, the simulated response was normalized to the yield of the 2614 keV peak. Ideally, the simulated data should be normalized on a per nC or per source electron basis; however, with the *a priori* understanding that the CEM03 cross sections exclude any photoabsorption below $\sim$ 30 MeV, inclusion of the complete data set (active background and target emissions) makes artificial normalization necessary regardless of how the simulated background is treated.

With the delayed γ-ray spectrum from the target and the active background well-defined, the complete representative data set could be generated. The target and active background spectra were combined and run, from the target location, as the source distribution. As previously described, the F8 tally provided the pulse-height distribution across the active

region of the germanium crystal and represented the delayed γ-ray spectrum collected by the HPGe detector. Figure 6.8 presents a comparison of experimental data (black lines) and simulation results (red data) for the ^{18}O-enriched water target. Both the 6129 and 7115 keV γ-ray peaks show strong agreement, as do the single and double escape peaks from the 6129 keV peak. The simulation also produced several γ-rays from the surrounding materials (e.g., the 1779 keV line from ^{27}Al(n,γ)^{28}Al). The simulation appears to have failed to produce a significant contribution from the 871 keV γ-ray that is present in the experimental data. This omission is notable, as the 871 keV γ-ray results from the ^{18}O(γ,p)^{17}N reaction. This reaction is not a high-energy delayed γ-ray emitter, but rather produces delayed neutrons.

Peaks resulting from neutron interactions within the germanium crystal appear in the experimental data. At least some portion of these can be generated in the simulations given a sufficient number of delayed neutrons can be produced. However, the simulated interactions do not produce the high-energy tail seen in the measured spectra. In Figure 6.8, these peaks were generated separately and are included in the source definition. For completeness, γ-rays at 570 and 1064 keV were also artificially included in the source definition. As explained in Section 6.2.4, these γ-rays are emitted by ^{207m}Pb and are unavailable from the simulation software. As a final note, in previous iterations of these simulations, the models failed to produce the 511 keV peak and corresponding lower-energy continuum with an abundance comparable to the measured data. While that energy region of the spectrum is not of primary interest here, it is worth mentioning the cause of the underestimation stemmed from the material definitions used. In the case of the ^{18}O-enriched water target, the material definition for the glass container called for elemental Si (14000.60c). Modifying this definition to include the appropriate isotopics, the ^{28}Si in the glass was able to generate ^{27}Si via photonuclear interactions, resulting in delayed β^+ emission and subsequent annihilation photons. Although seemingly inconsequential, inclusion of the improved material definition had a noticeable effect on the final spectrum and was, therefore, included in subsequent efforts.

Appendix A

Targets

A.1 Aqueous Solutions

The aqueous targets containing ^{232}Th and ^{238}U were produced by dissolving thorium nitrate ($Th(NO_3)_4(H_2O)_4$) and uranyl nitrate ($UO_2(NO_3)_2(H_2O)_6$) in 1 L of deionized water. Table A.1 shows the masses that were mixed to create the aqueous solutions. Table A.2 shows the resulting fissionable masses and concentrations in the 16 aqueous solution targets.

Table A.1: The masses of thorium and uranyl nitrate used to create the aqueous solutions.

Target	Thorium Nitrate (g)	Uranyl Nitrate (g)	H_2O (kg)
^{232}Th-1	23.2	0.0	1.0
^{232}Th-2	43.2	0.0	1.0
^{232}Th-4	90.3	0.0	1.0
^{232}Th-5	141.8	0.0	1.0
^{232}Th-7	198.4	0.0	1.0
^{232}Th-9	260.9	0.0	1.0
^{238}U-1	0.0	21.1	1.0
^{238}U-2	0.0	34.2	1.0
^{238}U-3	0.0	70.9	1.0
^{238}U-5	0.0	110.2	1.0
^{238}U-6	0.0	152.5	1.0
^{238}U-8	0.0	198.2	1.0
Mixed-A	27.1	65.0	1.0
Mixed-B	55.8	66.9	1.0
Mixed-C	77.4	44.5	1.0
Mixed-D	82.3	21.9	1.0

Table A.2: The ^{232}Th and ^{238}U masses and concentrations in the aqueous targets.

Target	^{232}Th Mass (g)	^{238}U Mass (g)	Concentration	Relative ^{232}Th	Relative ^{238}U
^{232}Th-1	9.8	0.0	1.0%	100%	0%
^{232}Th-2	18.3	0.0	1.7%	100%	0%
^{232}Th-4	38.2	0.0	3.5%	100%	0%
^{232}Th-5	60.0	0.0	5.3%	100%	0%
^{232}Th-7	84.0	0.0	7.0%	100%	0%
^{232}Th-9	110.5	0.0	8.8%	100%	0%
^{238}U-1	0.0	10.0	1.0%	0%	100%
^{238}U-2	0.0	16.2	1.6%	0%	100%
^{238}U-3	0.0	33.6	3.1%	0%	100%
^{238}U-5	0.0	52.3	4.7%	0%	100%
^{238}U-6	0.0	72.4	6.3%	0%	100%
^{238}U-8	0.0	94.1	7.8%	0%	100%
Mixed-A	11.5	30.9	4.0%	27.8%	72.2%
Mixed-B	23.6	31.7	5.2%	42.9%	57.1%
Mixed-C	32.8	21.1	5.1%	60.0%	40.0%
Mixed-D	34.8	10.4	4.2%	76.0%	24.0%

A.2 SiO_2Mixtures

The SiO_2 targets containing ^{232}Th and ^{238}U were produced by mixing thorium dioxide (ThO_2) and uranium oxide (U_3O_8 with 1.64 kg of SiO_2. Table A.3 shows the masses that were mixed to create these SiO_2 mixtures. Table A.4 shows the resulting fissionable masses and concentrations in the 16 SiO_2 targets.

Table A.3: The masses of thorium dioxide and uranium oxide used to create the SiO_2 mixtures.

Target	Thorium Dioxide (g)	Uranium Oxide (g)	SiO_2 (kg)
^{232}Th-0.5	9.4	0.0	1.64
^{232}Th-1	18.9	0.0	1.64
^{232}Th-2	38.2	0.0	1.64
^{232}Th-4	78.2	0.0	1.64
^{232}Th-6	120.2	0.0	1.64
^{232}Th-8	164.2	0.0	1.64
^{238}U-0.5	0.0	9.7	1.64
^{238}U-1	0.0	19.6	1.64
^{238}U-2	0.0	39.6	1.64
^{238}U-4	0.0	81.2	1.64
^{238}U-6	0.0	124.9	1.64
^{238}U-8	0.0	170.8	1.64
Mixed-A	24.1	99.8	1.64
Mixed-B	48.1	74.8	1.64
Mixed-C	72.2	49.9	1.64
Mixed-D	96.2	24.9	1.64

Table A.4: The ^{232}Th and ^{238}U masses and concentrations in the SiO_2targets.

Target	^{232}Th Mass (g)	^{238}U Mass (g)	Concentration	Relative ^{232}Th	Relative ^{238}U
^{232}Th-0.5	8.25	0.0	0.5%	100%	0%
^{232}Th-1	16.59	0.0	1.0%	100%	0%
^{232}Th-2	33.56	0.0	2.0%	100%	0%
^{232}Th-4	68.73	0.0	4.0%	100%	0%
^{232}Th-6	105.61	0.0	6.0%	100%	0%
^{232}Th-8	144.34	0.0	8.0%	100%	0%
^{238}U-0.5	0.0	8.25	0.5%	0%	100%
^{238}U-1	0.0	17.21	1.0%	0%	100%
^{238}U-2	0.0	34.81	2.0%	0%	100%
^{238}U-4	0.0	71.35	4.0%	0%	100%
^{238}U-6	0.0	109.74	6.0%	0%	100%
^{238}U-8	0.0	150.14	8.0%	0%	100%
Mixed-A	21.17	84.66	6.0%	20.0%	80.0%
Mixed-B	42.31	63.47	6.0%	40.0%	60.0%
Mixed-C	63.43	42.29	6.0%	60.0%	40.0%
Mixed-D	84.54	21.14	6.0%	80.0%	20.0%

Appendix B

A M.S. Thesis by Edward T. E. Reedy

Discrete γ-rays from Photofission for Nuclear Forensics Applications

In presenting this thesis in partial fulfillment of the requirements for an advanced degree at Idaho State University, I agree that the Library shall make it freely available for inspection. I further state that permission for extensive copying of my thesis for scholarly purposes may be granted by the Dean of the Graduate School, Dean of my academic division, or by the University Librarian. It is understood that any copying or publication of this thesis for financial gain shall not be allowed without my written permission.

Signature _____

Date _____

Discrete γ-rays From Photofission for Nuclear Forensics Applications

A thesis presented

by

Edward Thomas Elzea Reedy

to

The Department of Physics

in partial fulfillment of the requirements

for the degree of

Masters in Science

in the subject of

Physics

Idaho State University

December 2011

©2011 - Edward Thomas Elzea Reedy

All rights reserved.

To the Graduate Faculty:

The members of the committee appointed to examine the thesis of Edward Thomas Elzea Reedy find it satisfactory and recommend that it be accepted.

Major Advisor

Committee Member

Graduate Faculty Representative

For Winifred

Acknowledgments

I would like to thank my collaborators Heather A. Seipel and Edna S. Cárdenas for their help with my research. I would also like to thank my advisor, Alan W. Hunt, for his knowledge and guidance. And last, but not least, my parents for encouraging me to do whatever the hell I want.

Contents

List of Figures ix
List of Tables xiv
Abstract xv

1 Introduction **1**
1.1 Introduction 1

2 Theory and Fundamentals **7**
2.1 The Fission Process 7
2.1.1 Fission Fragment Distribution 9
2.1.2 Prompt and Delayed Emissions 11
2.2 Detectors 12
2.2.1 High Purity Germanium Photon Detectors 12
2.2.2 ^{3}He Neutron Detectors 15
2.3 Calculated Spectra via ENDF/B 16

3 Experiment **23**
3.1 Setup 23
3.1.1 Physical Setup 23
3.2 Targets 25
3.3 Data collection 26

4 Results and Analysis **30**
4.1 Identifying Fission 30
4.1.1 (n,γ) Interference 31
4.2 Discrete Line Prediction and Identification via ENDF/B 35
4.3 Peak Ratio Analysis (PRA) 41
4.4 Spectral Contribution Analysis (SCA) 46
4.4.1 Using Measured Energy Spectra as a Basis Set 47
4.4.2 Using Calculated Energy Spectra as a Basis Set 55

5 Conclusions **60**
5.1 Summary/Findings 60
5.2 Applications and Future Work 61

A A Note on Calculated Spectra **63**

Bibliography **65**

List of Figures

1.1 The cumulative fission fragment mass distribution of ^{238}U (□) and ^{232}Th (■) for 14 MeV neutron induced fission. The overall cumulative yield is normalized to 2 [8]. 3

1.2 Energy spectra of low mass ^{238}U and ^{232}Th samples collected between intense bremsstrahlung pulses with an endpoint energy of 22 MeV and a repetition rate of 15 Hz. 5

2.1 The photofission process. At time zero a photon strikes the nucleus and excites it. In less than 10^{-21} s the nucleus has deformed and coulomb repulsion forces the fission fragments apart. The fission fragments then emit promt neutrons and γ-rays within 10^{-13} s following fission. The fragments then undergo β-decay and emit delayed γ-rays and neutrons on the order of 10^{-3} to 100s of seconds after fission has occurred [13]. 9

2.2 The cumulative fission fragment mass distribution of ^{238}U (□) and ^{232}Th (■) for 14 MeV neutron induced fission. The overall cumulative yield is normalized to 2. 10

2.3 High mass (▲) and low mass (■) distribution centroids for fissionable materials with nucleonic masses between 232 and 242. 11

2.4 Cross sectional view of coaxial p-type (a) and n-type (b) high purity germanium detector crystals. Thick lines indicate the surface p^+ and n^+ contacts respectively. For reverse bias the n^+ contact is positive bias and the p^+ contact is negative bias. Each detector is shown with incident radiation track and the ensuing electron-hole pairs produced. 12

2.5 The absolute efficiency as a function of energy for a 48% relative efficient p-type HPGe detector at 25 cm to the photon source. 15

2.6 The six region curve for gas filled detectors. Region I: Recombination, Region II: Ionization, Region III: Proportional, Region IV: Limited Proportional, Region V: Geiger-Mueller, Region VI: Continuous Discharge. The scale of this curve depends on the geometry of the detector as well as the gas utilized [21]. 17

2.7 A portion of the calculated energy spectra for ^{238}U high-energy neutron induced fission (a) and fast pooled fission on ^{237}U (b). The two spectra are nearly identical. 21

3.1 Schematic of the experimental setup used to measure β-delayed γ-rays from photofission as viewed from above. The total distance from radiator to target was 4.0 m. A well shielded HPGe detector was placed at 90° to the bremsstrahlung beam at a distance of 25 cm from the center of the target. Directly opposite the HPGe detector, an array of MHND detectors was placed at a distance of 63.5 cm from the center of the target to the center of the array. 24

3.2 Poloroid^{TM}image of the bremsstrahlung photon beam at the target location. Image is a large format Polaroid 52 placed at the target location and exposed to a 22 MeV bremsstrahlung photon beam at 15 Hz for 40 s. The scale across the bottom is in cm. 25

3.3 The pulse structure of the electron beam. Each pulse has a duration of 4 μs and contains approximately 120 nC of charge. The pulses are separated by 66 ms. 26

3.4 Diagram of the low mass liquid targets. Each canister is made of $\sim$ 0.5 mm thick 18/8 stainless steel. The contents are sealed with a stainless steel and plastic screw cap and extend vertically 18.5 cm from the bottom of the canister. 27

3.5 Schematic of the electronics portion of the experimental setup. The data acquisition system (DAQ) records both the HPGe and ^{3}He neutron detectors as well as the TTL pulse from the accelerator gun trigger. 29

4.1 Energy spectra of three 15.4 g·cm^{-2} ^{238}U plates with and without incident bremsstrahlung photon beam. For the spectrum with photon beam, the accelerator was operated at 22 MeV and 15 Hz with a charge of 170 nC per pulse. The data was collected for 8 h and 400 s, respectively. A demarcation line at 3 MeV indicates the effective limit of γ-ray emissions from natural decays. 31

4.2 Energy spectra of low mass ^{238}U (U-5, 0.41 g·cm^{-2}), ^{232}Th (Th-5, 0.46 g·cm^{-2}) and nonfissionable H_2O collected at 22 MeV and 15 Hz. The accelerator was operated with 4 μs wide pulse containing 150 nC of charge. Total collection time for both spectra is 2 h. Spectra is shown with a demarcation line at 3 MeV. 32

4.3 The γ-ray rate as a function of time for emissions greater that 3 MeV for low mass ^{232}Th (▲),^{238}U (■) and the nonfissionable sample of H_2O (▼) from the energy spectra in Figure 4.2. The accelerator was operated at 22 MeV, 15 hz with a pulse width of 4 μs, containing 150 nC of charge. Total collection time for each spectrum is 2 h. 33

4.4 Neutron rate as a function of time after the pulse for ^{238}U (■), ^{232}Th (▲) and H_2O (▼). The accelerator was operated at 22 MeV, 15 Hz with a pulse width of 4 μs, containing 150 nC of charge. Total collection time for each spectrum is 2 h. 34
4.5 Energy spectra of aqueous ^{238}U, 0.41 g·cm^{-2}, ^{232}Th, 0.46 g·cm^{-2} and nonfissionable H_2O from Figure 4.2 with the first 35 ms after the accelerator pulse removed. The accelerator was operated at 22 MeV, 15 Hz with a pulse width of 4 μs, containing 150 nC of charge. Total collection time for each spectrum is 2 h. 35
4.6 Calculated energy spectra from fission fragment distributions for ^{238}U fission with 14.5 MeV neutrons and ^{237}U fast pooled fission overlaid on a measured energy spectrum from a low mass aqueous sample of ^{238}U (U-5, 0.41 g·cm^{-2}). For measured energy spectra, the accelerator was operated at 22 MeV, 15 hz with a pulse width of 4 μs, containing 150 nC of charge. Total collection time was 2 h. The energy spectra are normalized to total charge on radiator and given an artificial offset to accentuate differences between calculated energy spectra. Labeled photopeaks indicate the presence of overly estimated fission fragments in the calculated spectra. 36
4.7 Energy spectra of ^{238}U, 0.41 g·cm^{-2}, ^{232}Th, 0.46 g·cm^{-2}, low mass aqueous samples collected at 22 MeV and 15 Hz overlaid with the calculated energy spectra from high energy neutron induced fission on ^{238}U and ^{232}Th, respectively. The measured spectra were collected over a period of 2 h and are normalized to total charge on radiator. ^{238}U spectra are shown with an arbitrary offset to accentuate differences between spectra. Several notable energy peaks are labeled. Those labeled in black have been calculated accurately, red have been predicted but are not present in data, blue have been over predicted but are present in data, and green have not been predicted and thus are not identified. . 39
4.8 Energy spectra of ^{238}U, 0.41 g·cm^{-2}, ^{232}Th, 0.46 g·cm^{-2}, low mass aqueous samples collected at 22 MeV and 15 Hz overlaid with the calculated energy spectra from high energy neutron induced fission on ^{238}U and ^{232}Th, respectively. The measured spectra were collected over a period of 2 h and are normalized to total charge on radiator. ^{238}U spectra are shown with an arbitrary offset to accentuate differences between spectra. Several notable energy peaks are labeled. Those labeled in black have been calculated accurately, red have been predicted but are not present in data, blue have been over predicted but are present in data, and green have not been predicted and thus are not identified. . 40

4.9 Energy spectra of low mass liquid targets U-5, A, B, C, D and Th-5 collected at 22 MeV, 15 Hz. Each spectrum is normalized to total charge on radiator with the first 35 ms following the pulse has been removed. An artificial offset is employed to emphasize differences as well as similarities between energy spectra. The combined photopeaks of ^{98}Y & ^{96}Tc and ^{86}Br & ^{133}Sb are labeled. 42
4.10 a) Graph of the peak ratios of 2941 & 2946 keV and the 2751 & 2755 keV gamma peaks from Figure 4.9. b) Peak ratios have been transformed into Relative ^{238}U concentration. Error bars in both graphs are representative of 1σ standard deviation. 43
4.11 A closer look at the combined photopeak of 2751 keV from ^{86}Br and 2755 keV from ^{133}Sb. The dashed line shows the shift in energy due to the transition in dominance from one to the other, respectively. . . . 44
4.12 Energy spectra of 10 μCi button sources of ^{137}Cs and ^{60}Co taken at 25 cm from the detector both individually and separately. Energy spectra were collected for 1 m each and normalized to time. Spectra are given artificial offset to emphasize individual photopeaks. 45
4.13 Energy spectrum obtained from the fitting algorithm utilizing measured energy spectra as basis sets (red) overlaid on their respective energy spectra (black). Figures to the right indicate the relative percent of ^{238}U present in the sample. 48
4.14 Relative spectral contribution from ^{238}U as a function of relative mass in the target. A line is shown at equality between calculated and actual. Error bars are representative of 1σ standard deviation. 49
4.15 Normalized ^{238}U (a) and ^{232}Th (b) coefficients as a function of mass for spectral contribution analysis utilizing measured energy spectra from low mass ^{238}U and ^{232}Th as a basis set. Error bars in both graphs are representative of 1σ standard deviation. 50
4.16 A portion of the energy spectrum collected from 1 L H_2O at 22 MeV and 15 Hz. The spectrum is normalized to total charge on the radiator and has the first 35 ms following the accelerator pulse removed. The spectrum was collected over a period of 2 h. 51
4.17 Relative spectral contribution from ^{238}U as a function of relative ^{238}U concentration in the target. A line is shown at equality between calculated and actual. Error bars are representative of 1σ standard deviation. 53
4.18 Normalized ^{238}U (a) and ^{232}Th (b) coefficients as a function of mass for spectral contribution analysis utilizing measured energy spectra from low mass ^{238}U and ^{232}Th as a basis set. Error bars in both graphs are representative of 1σ standard deviation. 54

4.19 The predicted energy spectra overlaid on the respective energy spectra of low mass ^{238}U, 0.41 g·cm^{-2}, and ^{232}Th, 0.46 g·cm^{-2} in aqueous solution. Each spectrum was collected over a period of 2 h at 22 MeV and 15 Hz with the first 35 ms following the pulse removed. Notable discrete lines are labeled above. ^{92}Rb has been removed from ^{238}U calculated energy spectra to better match experimental data. Notable fission fragment contributors have been labeled with their respective energy and half-life. 55
4.20 Relative ^{238}U spectral contribution as a function of relative ^{238}U concentration. Error bars indicate 1σ standard deviation. 56
4.21 Normalized ^{238}U (a) and ^{232}Th (b) coefficients as a function of mass for spectral contribution analysis utilizing calculated energy spectra from low mass ^{238}U and ^{232}Th as a basis set. Error bars in both graphs are representative of 1σ standard deviation. 57
4.22 Energy spectrum obtained from the fitting algorithm utilizing calculated energy spectra as basis sets (red) overlaid on their respective energy spectra (black). Figures to the right indicate relative percent of ^{238}U present in the target. 58

5.1 Comparison of peak ratio analysis (a) versus spectral contribution analysis (b) utilizing identical data sets. 60

A.1 Energy spectra of ^{238}U, 0.41 g·cm^{-2}, ^{232}Th, 0.46 g·cm^{-2}, low mass aqueous samples collected at 22 MeV and 15 Hz overlaid with the calculated energy spectra from high energy neutron induced fission on ^{238}U and ^{232}Th, respectively. The measured spectra were collected over a period of 2 h and are normalized to total charge on radiator. ^{238}U spectra are shown with an arbitrary offset to accentuate differences between spectra. The position of where the 3235 keV peak from ^{136}Te should appear is indicated 64

List of Tables

3.1 ^{232}Th and ^{238}U aqueous target masses and concentrations. 28

4.1 ^{238}U and ^{232}Th aqueous target masses, relative concentration and calculated sum of coefficients α_{238} and α_{232}. 52

Thesis advisor
Alan W. Hunt

Author
Edward Thomas Elzea Reedy

Discrete γ-rays From Photofission for Nuclear Forensics Applications

Abstract

Emissions from induced fission events provide indicative signatures of fission that have proven useful in methods of isotope identification and quantification. Many of these methods utilize broad spectrum yields from prompt and delayed neutrons or γ-rays from fission fragments with some emphasis on the time dependence of these emissions. This research looks at discrete β-delayed γ-rays from photofission as a means to detect, identify and quantify fissionable material. A 25 MeV linear electron accelerator was used to produce a pulsed bremsstrahlung photon beam to interrogate several aqueous solutions containing varied concentrations of ^{238}U and ^{232}Th as well as nonfissionable targets. A high purity germanium (HPGe) detector was used to collect γ-ray energy spectra from the targets between accelerator pulses. The resulting spectra were then time and energy analyzed to identify signatures unique to the fission process. This revealed discrete lines from short-lived fission fragments that are unique to the fissioning isotope. Using a broad energy range containing several of these discrete lines it is possible to form a unique vector for each isotope. A basis set can then be formed to deconvolve energy spectra containing contributions from multiple fission sources into their base components.

Chapter 1

Introduction

1.1 Introduction

Recently, considerable emphasis has been placed on active nondestructive techniques that can detect, identify and quantify fissionable material in a variety of situations [1, 2, 6, 19, 24, 26, 27, 30, 32, 34]. These often include applications to cargo inspection, treaty verification, safeguards and nuclear forensics. While passive methods have proven useful in some situations, they are often ineffective due to the low-energy and low yield of primary emissions, many of which cannot penetrate small amounts of shielding or are not present significantly enough to be accurately measured over that of natural background [17]. Active techniques utilize a probing source of neutrons or high-energy photons to induce activation and/or fission events and monitor for secondary emissions. These secondary emissions have a drastically increased yield and energy over that of natural decay [10, 35]. This increase allows for increased penetration of shielding, shorter inspection times and an overall increase in detection probability over that of passive systems.

In most security applications, it is only necessary to identify whether fissionable material is present, as is the case with cargo inspection [18, 31]. Two commonly used fissionable material signatures are delayed neutrons and delayed γ-rays. These delayed emissions follow the β-decay of fission fragments and are emitted at relatively long timescales after fission has occurred [13]. However, delayed neutrons are only emitted

from $0.3 - 5\%$ of fission reactions and are easily shielded by hydrogenous material [5, 33]. This is in stark contrast to the abundant β-delayed γ-rays, which average seven per fission event [10, 35]. Multiple methods to detect fissionable material have been developed utilizing β-delayed γ-rays following irradiation from both neutron and photon sources [12, 28, 30, 31, 36].

While these methods take advantage of unique signatures of fissionable material to identify whether material is present, they do little to quantify the material or resolve its composition. Typically these methods focus on broad spectrum yields of β-delayed γ-rays or neutrons with some emphasis on the time dependence of these emissions [12, 28, 30, 31, 36]. This increased yield is then indicative of fissionable material. However, the capability to quantify and differentiate fissionable materials is at the core to nuclear forensics and safeguards applications [7]. In nuclear forensics the goal is to determine the composition of fissionable material in order to attribute it to a source [25]. If illicit nuclear material is found, its origin may be determined by first measuring the isotopic composition and then making a comparison to known nuclear materials. This analysis must be done quickly so that an appropriate response can be implemented. For safeguards applications, like nuclear fuel reprocessing, the goal is typically to measure the amount of fissile material, i.e. ^{235}U, ^{239}Pu, etc. present in a sample in order to determine whether materials diversion has occurred. As an example, the safeguards community is interested in techniques that can independently measure the fissile mass in spent nuclear fuel before reprocessing has begun. Once it is reprocessed, the resulting mass of uranium or plutonium can be compared to prior measurements to determine the efficiency of reprocessing and if material diversion has taken place. Passive systems can be encumbered by the presence of shielding, as with nuclear forensics applications, and instances of high background levels, as with spent fuel recycling. While the high yield of neutrons and γ-rays from induced fission can provide signatures above that of naturally occurring radioactive material, these applications require techniques that go beyond simple detection.

Figure 1.1 shows the fission fragment mass distributions for ^{238}U and ^{232}Th for 14.5 MeV neutron induced fission. Each fissionable isotope has a unique fission fragment distribution, and similarly, each fission fragment emits a characteristic set of dis-

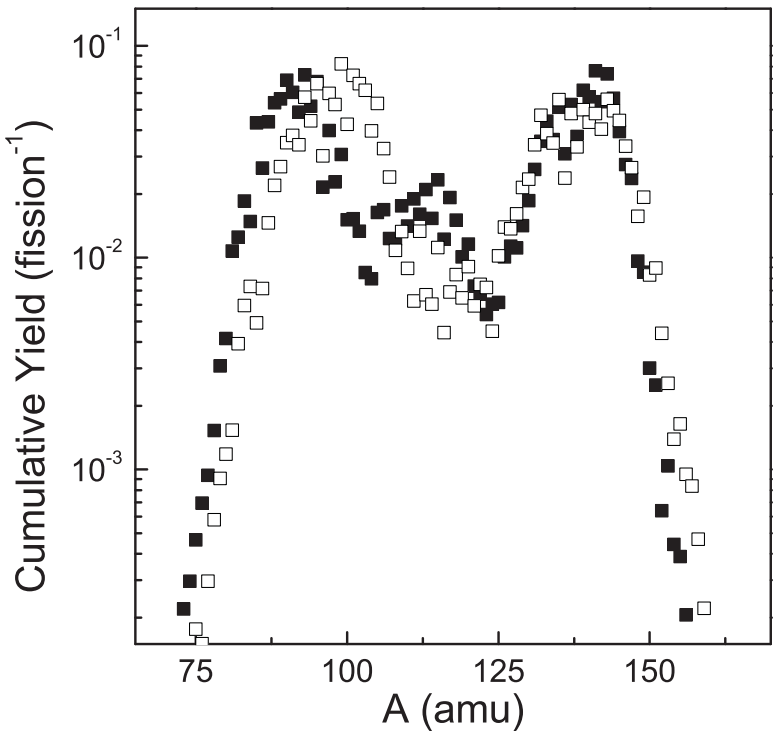

Figure 1.1: The cumulative fission fragment mass distribution of ^{238}U (□) and ^{232}Th (■) for 14 MeV neutron induced fission. The overall cumulative yield is normalized to 2 [8].

crete γ-rays [3]. The unique distribution combined with the fragments' characteristic γ-rays results in unique energy spectra that correlates to the original fissioning nuclei. Thus, discrete β-delayed γ-rays from induced fission offer a unique active inspection signature capable of differentiating between fissioning isotopes. With fission fragments releasing on average $\sim$ 7 MeV into β-delayed γ-rays, a significant high-energy γ-ray yield persists well after fission has occured [15, 16]. Many of these γ-rays lay above the limit of lines from naturally occurring radioactive material ($\sim$ 2.6 MeV) as well as those from spent nuclear fuel ($\sim$ 3 MeV) [3, 30, 31]. Since high-energy γ-rays are predominantly emitted from short-lived fission fragments, these γ-rays are indicative of the current amount of fissionable material in the sample. In contrast, longer-lived fission fragments tend to emit lower-energy γ-rays over much longer timescales. Techniques that focus on lower-energy γ-rays can be limited by background and shielding

or inaccurate due to long term population buildup. Thus, the analysis of higher-energy discrete lines may have the capability to more accurately identify and quantify fissioning isotopes with less influence from background or shielding.

A method that has been used traditionally in nuclear forensics to narrow the composition of fissionable material samples is the ratios between discrete γ-ray lines [27]. Figure 1.2 shows a portion of typical energy spectra collected from ^{238}U and ^{232}Th between interrogating bremsstrahlung photon pulses. Energy spectra such as this contain discrete high-energy γ-rays unique to the fissioning material. By relating the yields of multiple discrete γ-rays, the contributors of those γ-rays can then be identified. However, this method presents multiple challenges. Not all fission fragments may be present in a high enough yield to produce effective discrete γ-ray lines. This is further exacerbated since a majority of fission fragments that emit γ-rays above ~ 3 MeV are short-lived with half-lives on the order of hundreds of milliseconds to seconds [3, 8]. Such lines may also be contaminated and convoluted by other fission fragments which produce discrete γ-rays at or near the energy of interest.

This thesis seeks to overcome the challenges of peak ratio analysis. By first predicting and then measuring the spectrum of β-delayed γ-rays from photofission, multiple peaks unique to ^{238}U and ^{232}Th were identified. This information was used to deconvolve the energy spectra of β-delayed γ-rays from the photofission of multiple fissionable materials into their base components. In the process of deconvolving the spectra, information regarding the composition of fissionable material used to make it is obtained. A pulsed linear electron accelerator was used to produce an intense bremsstrahlung photon beam with an endpoint energy of 22 MeV to interrogate a variety of low mass aqueous solutions containing varying quantities of ^{238}U and ^{232}Th. The resulting energy spectra were collected using a high purity germanium detector between accelerator pulses. From these spectra discrete high-energy β-delayed γ-ray lines were identified that can be utilized to differentiate distinct fissionable isotopes. Two methods of determining isotopic composition were compared: peak ratio analysis and spectral contribution analysis. In spectral contribution analysis, a portion of the measured energy spectra from photofission of ^{238}U and ^{232}Th was used to formulate a basis set. This basis set was applied using a fitting algorithm to deconvolve

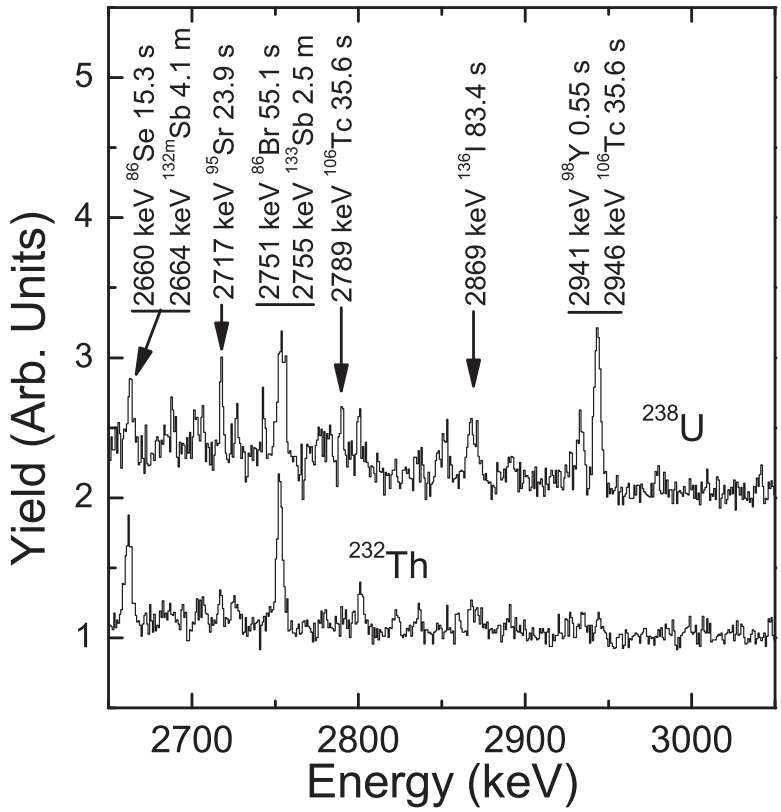

Figure 1.2: Energy spectra of low mass ^{238}U and ^{232}Th samples collected between intense bremsstrahlung pulses with an endpoint energy of 22 MeV and a repetition rate of 15 Hz.

energy spectra from samples containing mixed quantities of ^{238}U and ^{232}Th in order to narrow their respective compositions beyond the capability of peak ratio analysis. By utilizing a broad portion of the energy spectrum, spectral contribution analysis takes advantage of multiple peaks over a wide energy range while simultaneously overcoming the difficulties in fitting those peaks individually. In addition to utilizing measured energy spectra, fission fragment mass distributions from ENDF/B, the evaluated nuclear structure data files (ENSDF), and the detector characteristics were combined to produce calculated energy spectra. The calculated energy spectra were also used as a basis set to deconvolve the measured energy spectra into their principal components through spectral contribution analysis. This thesis will thus provide the physics background, formulation and comparison of these techniques with emphasis

on these main areas:

- **The physics of induced fission.** An introduction to the fission process, how it occurs, fission fragment mass distributions, and prompt and delayed emissions.
- **Characteristics of HPGe and ^{3}He detectors.** The fundamentals of high purity germanium and ^{3}He detectors and their response to radiation.
- **Prediction of β-delayed γ-rays from photofission.** The available fission fragment distributions from ENDF/B VII and the detector response function are combined to predict the delayed γ-ray spectra from photofission.
- **The identification and isolation of β-delayed γ-rays from photofission.** Predicted energy spectra along with the information from the detectors are used to identify discrete β-delayed γ-rays from photofission.
- **Peak Ratio Analysis.** Construction of an analysis method utilizing two discrete β-delayed γ-rays from photofission to identify and quantify different types of fissionable material and the difficulties it presents.
- **Spectral Contribution Analysis.** The utilization of a portion of the energy spectra containing discrete γ-rays to construct a basis set unique to both ^{238}U and ^{232}Th in an effort to resolve issues present in prior methods.

Chapter 2

Theory and Fundamentals

2.1 The Fission Process

Nuclear fission was discovered by Hahn and Strassmann in 1939 following bombardment of natural uranium with neutrons in an effort to make new elements with ever increasing mass [14]. When one of the products of this experiment was found to be barium, they quickly realized that the regular decay channels from an excited uranium nucleus could not be responsible and ultimately, the nuclei had undergone fission. Following this, Meitner and Frisch proposed the Liquid Drop Model of a nucleus to explain the fission process [23]. In this model, a nucleus behaves in much the same was as a liquid drop with the nucleons forming an incompressible and uniform nuclear fluid with the short range strong force playing the role of surface tension and holding the nucleus together.

Based off this model, Weizsäcker formulated the equation,

$$E_b(Z,N) = \alpha_1 A - \alpha_2 A^{2/3} - \alpha_3 \frac{Z(Z-1)}{A^{1/3}} - \alpha_4 \frac{(N-Z)^2}{A} + \Delta, \tag{2.1}$$

to calculate the binding energy of a nucleus given the number of protons and neutrons [37]. The first term, $\alpha_1 A$, dictates that the nuclear binding energy increases linearly with respect to the total number of nucleons because the strong force affects both neutrons and protons equally. The surface term, $\alpha_2 A^{2/3}$, allows for the change in binding energy due to nucleon proximity. While nucleons at the center contribute

significantly, the contributions of those at the surface is reduced due to their lower proximity to other nucleons. Term three accounts for Coulomb repulsion between protons. During the fission process this repulsion works to drive the nucleus apart. Term four adjusts the binding energy to account for isospin considerations. Nuclear binding energy is maximized for cases where N=Z. For larger nuclei, the total number of neutrons is greater than protons and decreases the binding energy. Estimated values for the α's in these terms are given by Wong as $\alpha_1 = 16$ MeV, $\alpha_2 = 17$ MeV, $\alpha_3 = 0.6$ MeV and $\alpha_4 = 25$ MeV [37]. Term five, Δ, arises from spin coupling. For odd atomic mass nuclei $\Delta = 0$. If the total atomic mass is even, Δ is positive when Z and N are both even and Δ is negative when Z and N are both odd.

The Weizsäcker formula accurately calculates the binding energy of nuclei and can be utilized to show why nuclei fission. As in the case with Hahn and Strassmann, ^{238}U is bombarded with neutrons to form ^{239}U [14]. Assuming the resulting fission fragments are ^{139}Ba and ^{100}Kr, the difference in binding energy between a ^{239}U nucleus and these two fission fragments is 112 MeV. Along with the added energy from absorbing a high-energy neutron, the total energy released from fission for this scenario would be in excess of 130 MeV. Thus, it is energetically favorable for a ^{239}U nucleus to undergo fission. Even without the addition of a neutron to ^{238}U the difference in binding energy between a ^{238}U nucleus and its resulting ^{139}Ba and ^{99}Kr fission fragments is in excess of 100 MeV allowing for fission to proceed spontaneously in such heavy nuclei.

For a nucleus to undergo fission Coulomb repulsion between protons must exceed the affect of the strong force. It is theoretically feasible for nuclei to spontaneous fission for $Z^2/A \geq 48$ [4]. In contrast to spontaneous fission, induced fission utilizes a probing source of radiation to impart energy to the nucleus and incite fission. Two forms of radiation are primarily used for this purpose, neutrons and high-energy γ-rays. Figure 2.1 shows a schematic of the photofission process. In photofission, incident γ-rays impart energy to the nucleus. If the energy of the γ-ray lies within the giant dipole resonance, oscillatory motion is induced which deforms the nucleus. This deformation allows Coulomb repulsion to overcome the short range strong force within the nucleus and scission occurs. Once scission occurs, the fission fragments are

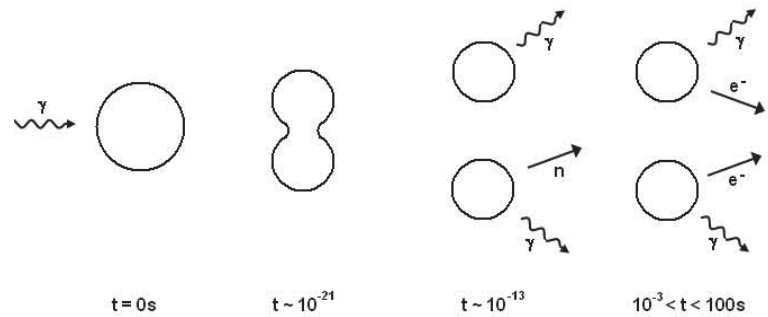

Figure 2.1: The photofission process. At time zero a photon strikes the nucleus and excites it. In less than 10^{-21} s the nucleus has deformed and coulomb repulsion forces the fission fragments apart. The fission fragments then emit promt neutrons and γ-rays within 10^{-13} s following fission. The fragments then undergo β-decay and emit delayed γ-rays and neutrons on the order of 10^{-3} to 100s of seconds after fission has occurred [13].

quickly accelerated apart. On average $\sim$ 200 MeV of energy is released from fission. Approximately 80% of this release goes to kinetic energy of the fission fragments from this acceleration. The remaining energy is released into prompt and delayed emissions from the decay of the fission fragments.

2.1.1 Fission Fragment Distribution

Figure 2.2 shows the fission fragment mass distribution for ^{238}U and ^{232}Th 14.5 MeV neutron induced fission. For each fission event, typically 2 fission fragments are produced. While the liquid drop model accurately describes many aspects of the nucleus, it fails to explain the asymmetry of the fission fragment mass distribution. This asymmetry is best explained by the shell model of the nucleus. Similar to the the atomic shell model, nucleons fill shells of increasing energy following the Pauli Exclusion Principle. For large nuclei, the binding energy of the nucleus decreases as nucleons are added. However, for certain numbers of neutrons and protons, the binding energy is significantly greater than predicted by the Weizacker mass formula for a liquid drop. The number of nucleons where this increase in binding energy occurs are referred to as magic numbers and occur at N or Z equal to 2, 8, 20, 50, 82 and 126. Instances

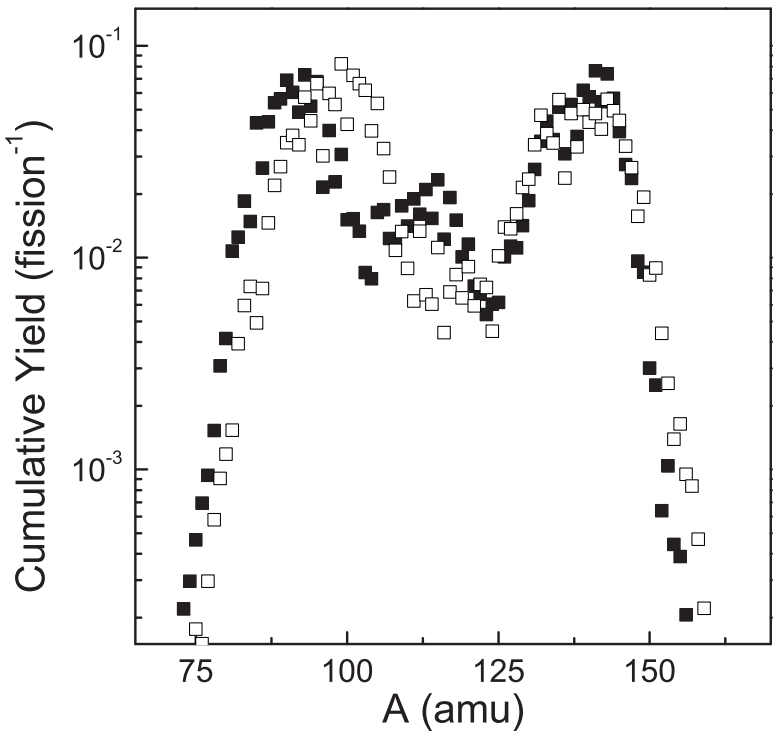

Figure 2.2: The cumulative fission fragment mass distribution of ^{238}U (□) and ^{232}Th (■) for 14 MeV neutron induced fission. The overall cumulative yield is normalized to 2.

where both neutrons and protons occupy magic numbers, such as $^{16}_{8}O_8$ and $^{208}_{82}Pb_{126}$, are referred to as doubly magic. Magic numbers occur where the nucleons present completely fill a nuclear shell making that isotope very stable.

Fission fragments containing magic numbers for neutrons (82) and/or protons (50) lay at the lower edge of the high mass distribution effectively "pinning" the high mass distribution above 132 u. Figure 2.3 shows the centroid locations of the high mass and low mass distributions as a function of the fissioning isotope mass. While the high-mass centroid remains relatively unchanged, the low-mass centroid shifts to accommodate the increase in mass of the fissioning isotope. Due to this increase and the subsequent shift of the low mass distribution, the fission fragment distribution is unique to the fissioning isotope. Since these fission fragments are responsible for the delayed emissions, the resulting delayed γ-ray spectra are also unique to the fissioning

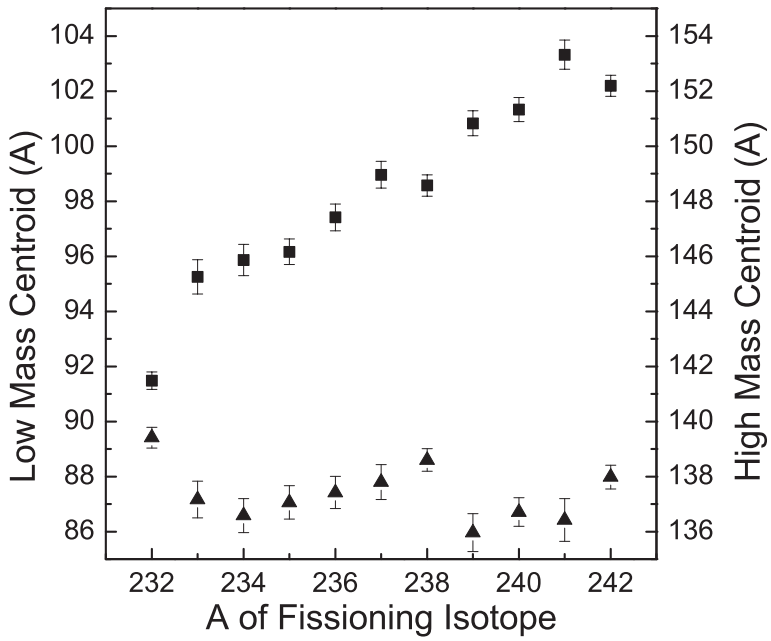

Figure 2.3: High mass (▲) and low mass (■) distribution centroids for fissionable materials with nucleonic masses between 232 and 242.

isotope.

2.1.2 Prompt and Delayed Emissions

Prompt emissions of γ-rays and neutrons occur within 10^{-13} s following scission [13]. On average, 7 prompt γ-rays and $2-3$ prompt neutrons are released per fission event [13]. Despite this high yield, prompt neutrons and γ-rays are emitted on a short timescale, making it difficult to detect and isolate them in an accelerator environment. In contrast, delayed emissions follow the β-decay of fission fragments and are emitted on the order of milliseconds out to years following fission. While ~ 7 delayed γ-rays are released per fission event, delayed neutrons are only emitted from $0.3-5\%$ of fission reactions and are easily shielded by hydrogenous materials [5,9,10,33,35]. With approximately 6 to 8 MeV divided between these γ-rays, a significant portion of them lay above 2.6 MeV, the limit of naturally occurring radioactive material [10,15,16,35].

High-energy γ-rays, in general, come from short-lived fission fragments [3,8]. The

fission fragments that emit high-energy γ-rays lay far from the line of stability and decay quickly releasing large amounts of energy. Because these emissions are short-lived, with half-lives on the order of milliseconds to seconds, they are indicative of the amount of fission currently going on in a sample. Longer lived fission fragments, as well as γ-rays from natural decay, tend to be lower in energy. Hence, high-energy β-delayed γ-rays from induced fission can provide a substantial and accurate signature of fission capable of penetrating various types of shielding.

2.2 Detectors

2.2.1 High Purity Germanium Photon Detectors

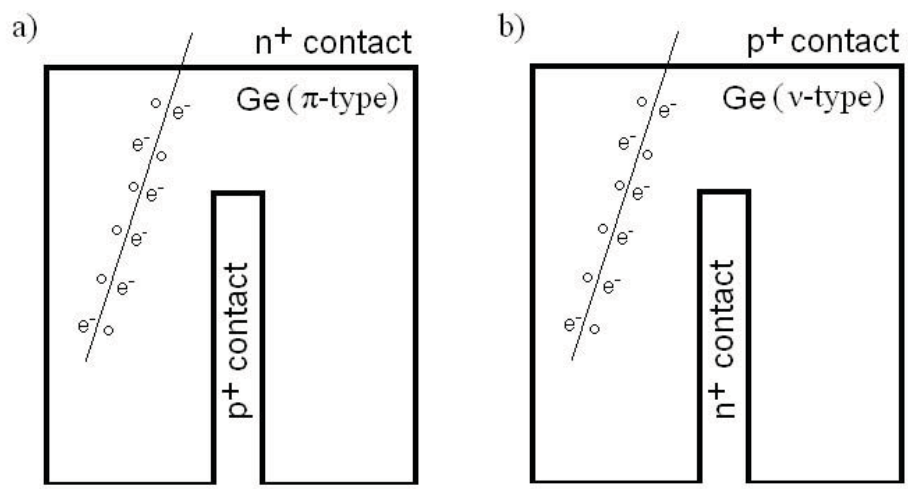

Figure 2.4: Cross sectional view of coaxial p-type (a) and n-type (b) high purity germanium detector crystals. Thick lines indicate the surface p^+ and n^+ contacts respectively. For reverse bias the n^+ contact is positive bias and the p^+ contact is negative bias. Each detector is shown with incident radiation track and the ensuing electron-hole pairs produced.

High purity germanium (HPGe) detectors are solid state semiconductor photon detectors. Figure 2.4 shows cross sectional views of coaxial p-type and n-type HPGe detector crystals. Single crystal germanium comprises the bulk of the detectors. If

the germanium crystal contains acceptor impurities left during growth, the resulting crystal is π-type and will comprise a p-type detector. Germanium containing donor impurities, ν-type, will comprise an n-type detector. Electrical contacts, as well as the n-p junction, are typically formed using boron implantation and lithium diffusion. Lithium diffusion is used to form an n^+ contact while boron implantation is used to make a p^+ contact [21].

HPGe detectors operate in reverse bias such that the crystal is fully depleted. While reverse biasing of both n-type and p-type detectors is done by applying positive voltage to the n^+ contact and negative voltage to the p^+ contact, the role of these contacts depends on the impurities present in the germanium crystal. If the germanium crystal is π-type the n^+ contact serves as the rectifying contact, whereas for ν-type germanium the p^+ contact serves at the rectifying contact. The depletion region begins at the rectifying contact and grows into the germanium crystal as bias is applied [21].

The depleted germanium crystal serves as the active region of the detector. As radiation penetrates the detector it interacts with the germanium crystal to produce electron-hole pairs. When a γ-ray enters the crystal it inelastically scatters with electrons, ejecting them from the atom as each electron absorbs part of the momentum of the γ-ray. These electrons create further ionization and electron-hole pairs as they lose energy. The γ-ray continues to scatter through the crystal to produce a track of electron-hole pairs until the photon is completely absorbed or scatters out of the crystal. The electric field across the crystal serves to transport the electrons and holes out of the crystal, creating an electric pulse. The amplitude of the pulse is directly proportional to the number of charge carriers generated by the incident photon. Since the number of charge carriers is linearly related to absorbed energy, the resulting pulse amplitude can be used to determine the energy of the photon [21].

While Compton scattering is the dominant interaction method for photons in the typical energy range of HPGe detectors from 10s of keV to $\sim$ 10 MeV, the photoelectric effect and pair production also play significant roles. The less dominant photoelectric effect produces an electron-hole pair by ejecting an electron from a bound shell of one of the atoms in the crystal. Unlike Compton scattering the γ-ray is en-

tirely absorbed by the atom and the result is an electron that is ejected with the total energy of the photon less the separation energy of that electron. The ejected electron scatters through the crystal and subsequent interactions result in the detection and absorption of the original incident photon energy. However, not all interactions result in total absorption of the photon. If an incident γ-ray is above 1022 keV it may create an electron-positron pair. While the energy of the electron is easily captured, the positron annihilates within the crystal, resulting in two 511 keV photons. If either of these photons escapes the detector, the resulting energy captured is 511 keV less than the incident photon. Likewise, if any of these interaction processes occur near the edge of the active region of the detector, ejected electrons or scattered photons may leave the active region and fail to be absorbed. The remaining captured energy contributes to escape peaks, from pair production, and the Compton continuum. Loss of energy information will also occur if the photon is of significant enough energy to pass entirely through the active region without being fully absorbed. Additionally, because thermal excitations can cause valence electrons to migrate to the conduction band, causing false output signals, HPGe detectors require low temperatures to operate and are typically cooled to liquid nitrogen temperatures, 77 K.

These factors in photon absorption directly contribute to the efficiency of the HPGe detector. Figure 2.5 shows the absolute efficiency at 25 cm as a function of photon energy for a typical p-type HPGe detector. The significant drop in efficiency at low energies is due to the presence of a dead layer around the germanium crystal. This dead layer is comprised of the ohmic n^+ contact. Since the outer lithium diffusion layer is typically several hundred microns thick, low-energy photons are blocked before entering the active region of the crystal. Contrary to p-type, n-type HPGe detectors have a thinner, on the order of a few tenths of a micron, outer boron implantation layer. This allows for easier penetration of low-energy photons into the active region of the detector and a significant increase in low-energy efficiency.

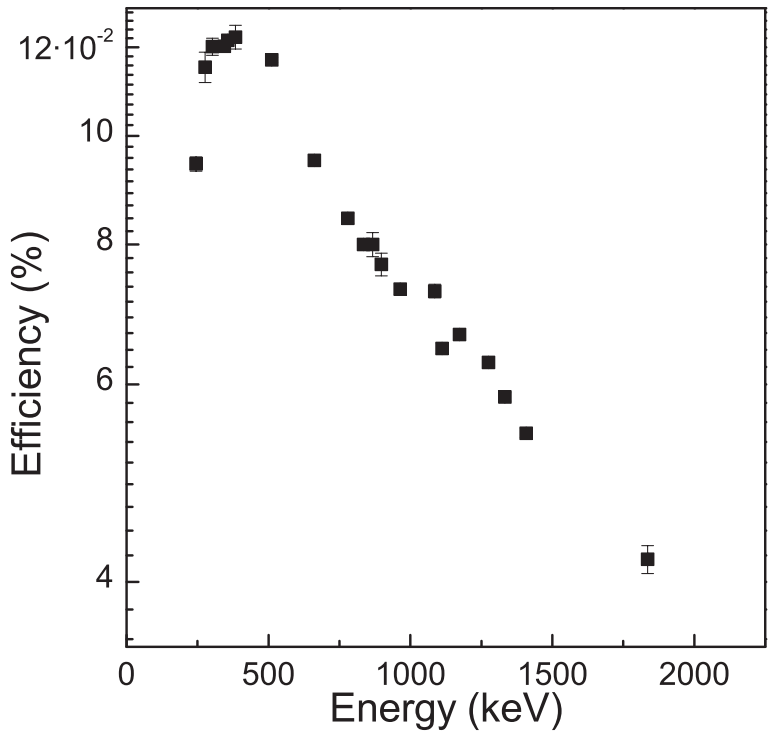

Figure 2.5: The absolute efficiency as a function of energy for a 48% relative efficient p-type HPGe detector at 25 cm to the photon source.

2.2.2 ^{3}He Neutron Detectors

The ^{3}He neutron detector is a gas filled proportional counter that is commonly used to detect slow neutrons. Since neutrons cannot ionize material directly, ^{3}He neutron detectors utilize the ^{3}He(n,p)^{3}H reaction to indirectly detect neutrons. The cross section for this reaction is $\sim$ 5300 b for thermal neutrons and falls rapidly as ν^{-1} as neutron energy increases. The cross section increases for neutron energies near 1 MeV before continuing its downward trend. The ^{3}He(n,p)^{3}H reaction produces an energetic proton and triton pair with energies of 0.573 and 0.191 MeV respectively. As the proton and triton drift apart they ionize the ^{3}He gas. To collect the resulting ions, and thereby detect the incident neutron, an electric field is placed across the gas.

Typically, ^{3}He neutron detectors are coaxial detectors with a conductive outer

casing and an inner conductive wire. The electric field is created by biasing the casing or wire and either grounding or negatively biasing the opposing conductor. Figure 2.6 shows relative pulse amplitude with respect to the applied bias for gas filled detectors. The applied voltage must be sufficient to overcome recombination of the electron-ion pair, Region I. If the voltage is beyond Region I to the ionization region, Region II, every ionization event created is collected. In the proportional region, the electron-ion pair cause secondary ionizations as they drift through the gas. These secondary electron-ion pairs subsequently drift in the electric field and continue to produce more ionization events. This form of gas multiplication increases the amplitude of the output signal and is proportional to the voltage applied. Above the proportional and limited proportional region is the Geiger-Mueller plateau, Region V. In this voltage region a single ionization event causes the complete ionization of the gas in the chamber. This results in a nearly constant pulse amplitude as a function of applied voltage. Beyond the Geiger-Mueller region the applied bias is greater than the breakdown voltage of the gas and causes a continuous discharge of the electric field [21].

2.3 Calculated Spectra via ENDF/B

Energy spectra from photofission were calculated to predict and identify high-energy discrete lines from fission fragments. Fission fragment distribution information for fissionable materials (ENDF/B) was used in combination with the characteristics of the high purity germanium detector and the evaluated nuclear structure data files (ENSDF) to generate simulated photofission spectra for ^{238}U and ^{232}Th.

Because fission fragments are produced during the accelerator pulse and subsequently decay into their daughter products between pulses, the yield of each fission fragment must be calculated with respect to this decay. The general differential equation for coupled decay and production of a given fission fragment, N_n, is given by,

$$\frac{dN_n(t)}{dt} = \overline{P_n} + N_{n-1}(t)\gamma_{n-1} - N_n(t)\beta_n, \tag{2.2}$$

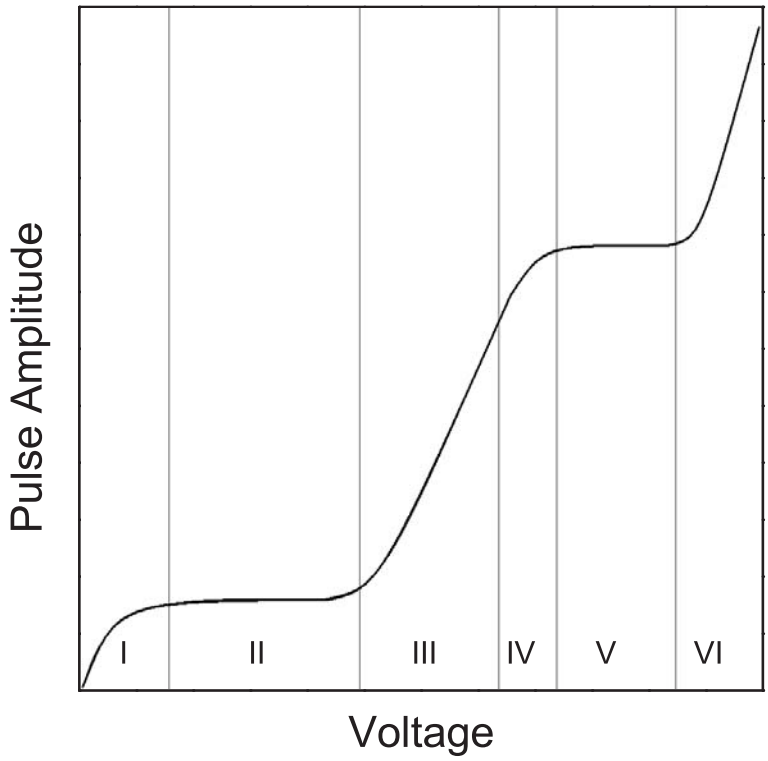

Figure 2.6: The six region curve for gas filled detectors. Region I: Recombination, Region II: Ionization, Region III: Proportional, Region IV: Limited Proportional, Region V: Geiger-Mueller, Region VI: Continuous Discharge. The scale of this curve depends on the geometry of the detector as well as the gas utilized [21].

where γ_{n-1} is the probability of nuclide N_{n-1} decaying to N_n, β_n is the total decay probability of nuclide N_n and $\overline{P_n}$ is the production rate of N_n. Because the detector is only operational between bremsstrahlung pulses, the production term $\overline{P_n}$ can be negated. Thus, the general solution to this equation is,

$$N_n(t) = \sum_{m=1}^{n}\{\prod_{k=m}^{n-1}\gamma_k\}N_m^0\sum_{j=m}^{n}\frac{e^{-\beta_j(t-t_p)}}{\prod_{i=m,\neq j}^{n}(\beta_i-\beta_j)}, \tag{2.3}$$

where t_p is the pulse width and N_m^0 is the initial number of N_m atoms. However, this equation is for the number of fission product N_n after a single bremsstrahlung pulse. For additional pulses $N_n(t)$ becomes,

$$N_n(t) = N_n(t) + N_n(t-\Delta t) + N_n(t-2\Delta t) + ... = \sum_{q=0}^{q_p-1} N_n(t-q\Delta t). \tag{2.4}$$

Substituting this into Equation 2.3 gives,

$$N_n(t) = \sum_{q=0}^{q_p-1}\sum_{m=1}^{n}\{\prod_{k=m}^{n-1}\gamma_k\}N_m^0\sum_{j=m}^{n}\frac{e^{-\beta_j(t-t_p-q\Delta t)}}{\prod_{i=m,\neq j}^{n}(\beta_i-\beta_j)}. \tag{2.5}$$

Because time is measured after the last pulse, t becomes,

$$t = t' + t_p + (q_p-1)\Delta t, \tag{2.6}$$

and Equation 2.5 can be written as,

$$N_n(t) = \sum_{m=1}^{n}\{\prod_{k=m}^{n-1}\gamma_k\}N_m^0\sum_{j=m}^{n}\frac{e^{-\beta_j t}}{\prod_{i=m,\neq j}^{n}(\beta_i-\beta_j)}\sum_{q'=0}^{q_p-1}e^{-\beta_j q'\Delta t}, \tag{2.7}$$

where $q' \equiv q_p - 1 - q$. The summation over index q' is a geometric series. For large values of q' Equation 2.7 becomes,

$$N_n(t) = \sum_{m=1}^{n}\{\prod_{k=m}^{n-1}\gamma_k\}N_m^0\sum_{j=m}^{n}\frac{e^{-\beta_j t}}{\prod_{i=m,\neq j}^{n}(\beta_i-\beta_j)}\frac{1}{1-e^{-\beta_j\Delta t}}. \tag{2.8}$$

By integrating the rate, $\beta_n N_n(t)$, from the time after the pulse where measurement begins, t'', to when measurement ceases ,Δt, we arrive at the overall measured yield, Y_n of the fission fragment N_n for a pulsed accelerator system. This integration yields,

$$\int_{t''}^{\Delta t} \beta_n N_n(t) dt = \sum_{m=1}^{n} \{\prod_{k=m}^{n-1} \gamma_k\} N_m^0 \sum_{j=m}^{n} \int_{t''}^{\Delta t} \frac{\beta_n e^{-\beta_j t}}{\prod\limits_{i=m,\neq j}^{n} (\beta_i - \beta_j)} \frac{1}{1 - e^{-\beta_j \Delta t}} dt, \tag{2.9}$$

and,

$$Y_n = \sum_{m=1}^{n} \{\prod_{k=m}^{n-1} \gamma_k\} N_m^0 \sum_{j=m}^{n} \frac{\beta_n}{\beta_j \prod\limits_{i=m,\neq j}^{n} (\beta_i - \beta_j)} \frac{e^{-\beta_j t''} - e^{-\beta_j \Delta t}}{1 - e^{-\beta_j \Delta t}}. \tag{2.10}$$

Utilizing the identity,

$$\frac{1}{\prod_{i=m}^{n} \beta_i} = \sum_{j=m}^{n} \frac{1}{\beta_j \prod\limits_{i=m,\neq j}^{n} (\beta_i - \beta_j)}, \tag{2.11}$$

Equation 2.10 becomes,

$$Y_n = \sum_{m=1}^{n} \{\prod_{k=m}^{n-1} \gamma_k\} N_m^0 \frac{\beta_n}{\prod\limits_{i=m}^{n} \beta_i} \frac{e^{-\beta_j t''} - e^{-\beta_j \Delta t}}{1 - e^{-\beta_j \Delta t}}. \tag{2.12}$$

The probability of decay, β_j, is determined by the half-life of the N_j fission fragment. The shortest fission fragment half-life given by ENDF/B is 68 ms and half-lives increase substantially from there [8]. Because the probability of decay for a majority of the fission fragments during Δt is very small, $\beta_j t''$ and $\beta_j \Delta t$ are much less than 1, and the exponents can be expanded in a Taylor series. Neglecting second order terms and above this expansion yields,

$$Y_n = \sum_{m=1}^{n} \{\prod_{k=m}^{n-1} \gamma_k\} N_m^0 \frac{\beta_n}{\prod\limits_{i=m}^{n} \beta_i} \frac{\Delta t - t''}{\Delta t} =$$

$$= \frac{\Delta t - t''}{\Delta t} (N_n^0 + \frac{\gamma_{n-1}}{\beta_{n-1}} N_{n-1}^0 + \frac{\gamma_{n-1}\gamma_{n-2}}{\beta_{n-1}\beta_{n-2}} N_{n-2}^0 + ...). \tag{2.13}$$

This result is simply the cumulative yield of a given fission fragment with a modification accounting for fraction of time between pulses measurement occurs.

Utilizing the cumulative yield, Y_n, given by ENDF/B, the absolute peak intensities were calculated for a given fission fragment distribution using the equation,

$$I(E_\gamma) = \sum_n \sum_i Y_n I_{n,i} \int N \frac{d\phi}{dE_\gamma} \cdot \sigma(E_\gamma) dE_\gamma. \tag{2.14}$$

In this equation, $I_{n,i}$ is the branching ratio for each γ-ray given by ENSDF and the remaining integral calculates the total fission yield in the sample. The absolute intensities are then put into a gaussian response function,

$$S(E) = \sum_{E_\gamma} I(E_\gamma)\varepsilon(E_\gamma) \frac{1}{\sqrt{\pi}\sigma_{det.}(E_\gamma)} e^{\frac{-(E-E_\gamma)^2}{2\sigma_{det.}(E_\gamma)}}, \tag{2.15}$$

yielding the energy spectrum for a given fission fragment distribution. Equation 2.15 contains the detector efficiency and the resolution as a function of energy, $\varepsilon(E_\gamma)$ and $\sigma_{det.}(E_\gamma)$, respectively.

The available fission fragment distribution from ENDF/B is almost exclusively for neutron induced fission. While data is available for ^{238}U(γ,f) it is identical to that of ^{237}U(n,f). Because the data available is for thermal, fast-pooled and high-energy neutrons, the equation,

$$E_{ave} = \frac{\int_{E_{min}}^{E_{max}} E_\gamma \cdot \frac{d\phi}{dE_\gamma} \cdot \sigma(E_\gamma) dE_\gamma}{\int_{E_{min}}^{E_{max}} \frac{d\phi}{dE_\gamma} \cdot \sigma(E_\gamma) dE_\gamma}, \tag{2.16}$$

was used to calculate the average excitation energy for a 22 MeV bremsstrahlung photon beam on ^{238}U in an attempt to match the excitation energies of available data. The average excitation energy of a 22 MeV bremsstrahlung photon beam on ^{238}U is 13.2 MeV. This lays directly between the excitation energy of fast pooled fission on ^{237}U, $\sim$ 8.5 MeV, and 14.5 MeV neutron fission on ^{238}U, $\sim$ 19 MeV, the data available through ENDF/B [8]. Equation 2.15 was then used to produce energy spectra for both ^{237}U fast pooled fission and ^{238}U high-energy fission. Figure 2.7 shows a portion of the calculated energy spectra for ^{238}U and ^{237}U. In this energy

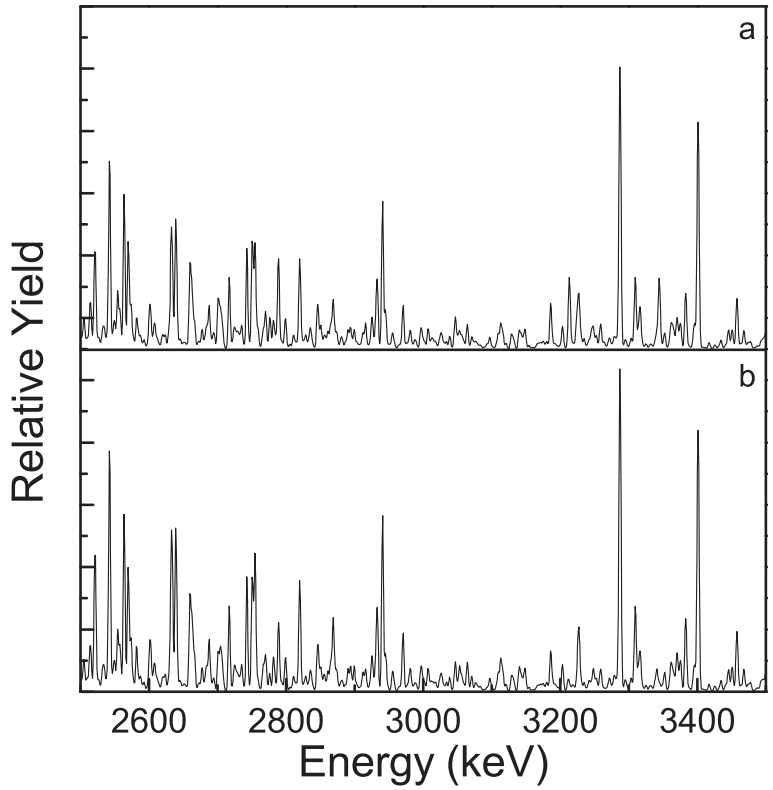

Figure 2.7: A portion of the calculated energy spectra for ^{238}U high-energy neutron induced fission (a) and fast pooled fission on ^{237}U (b). The two spectra are nearly identical.

region the two spectra have few differences and are likely to match experimental data equally well.

Chapter 3

Experiment

3.1 Setup

3.1.1 Physical Setup

Figure 3.1 shows a diagram of the experimental setup. A 25 MeV pulsed linear electron accelerator was operated at an energy of 22 MeV. The electron beam was incident on a 4.2 g$\cdot$ cm^{-2} tungsten radiator to produce a bremsstrahlung photon beam with the corresponding endpoint energy. The resulting photon beam was collimated through a 1.8 m concrete and earth wall into a shielded experimental cell to help limit exposure due to the intense bremsstrahlung beam. Collimation consisted of a 1.27 cm diameter Pb collimator 15.2 cm in length on the accelerator hall side 61 cm from the radiator and a 3.81 cm diameter Pb collimator 15.2 cm long in the experimental cell, 2.4 m from the radiator. This resulted in a 6.5 cm diameter beam spot at the target location, 4.0 m from the radiator.

Figure 3.2 shows an image of the bremsstrahlung beam taken at the target location, using large format film that was exposed to a 22 MeV bremsstrahlung photon beam at 15 Hz for 40 s. This image shows the overall size of the bremsstrahlung beam due to collimation and its relative intensity profile. Beam current was measured via an inductive loop placed before the radiator and is directly related to bremsstrahlung intensity. Figure 3.3 shows the structure of the pulsed beam. The accelerator was op-

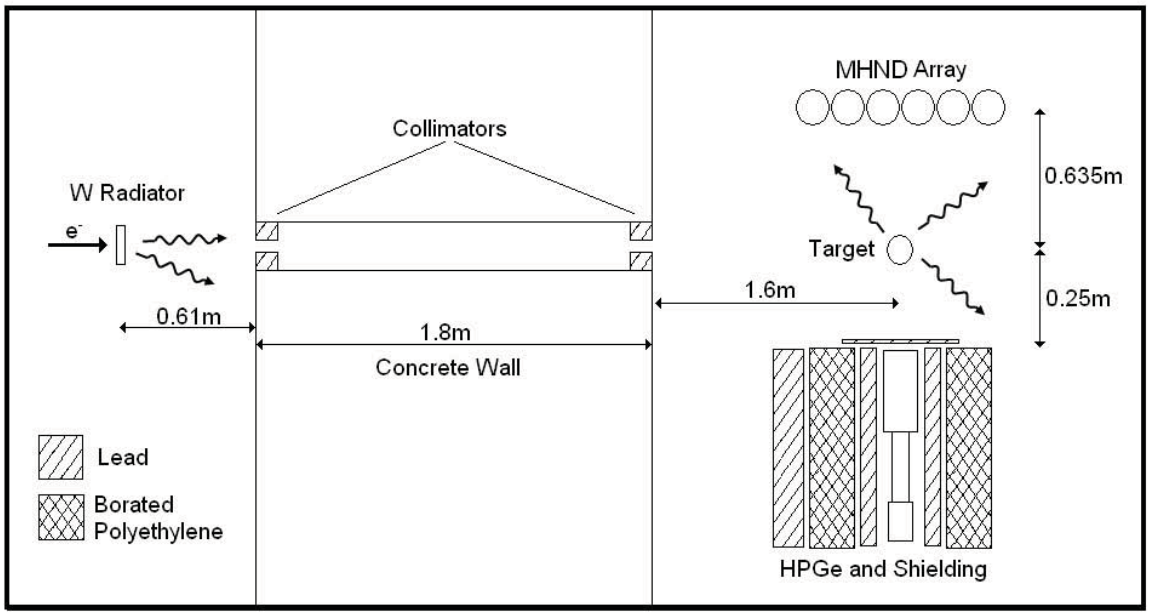

Figure 3.1: Schematic of the experimental setup used to measure β-delayed γ-rays from photofission as viewed from above. The total distance from radiator to target was 4.0 m. A well shielded HPGe detector was placed at 90° to the bremsstrahlung beam at a distance of 25 cm from the center of the target. Directly opposite the HPGe detector, an array of MHND detectors was placed at a distance of 63.5 cm from the center of the target to the center of the array.

erated at a repetition rate of 15 Hz leaving 66 ms between each pulse. Each electron pulse had a width of 4 μs and contained approximately 120 nC of charge.

A 48% relative efficient p-type high purity germanium (HPGe) detector was placed at 90° to the beam line, at a distance of 25 cm from the target center. The detector was cooled using a mechanical cryostat. To reduce background and minimize exposure to the bremsstrahlung pulse the detector was encased in 5 cm of Pb shielding and placed inside 20 cm of borated polyethylene. An additional 10 cm of Pb shielding was added on the accelerator side of the detector exterior to the borated polyethylene. A 635 mm Pb filter was placed over the face of the detector to minimize low-energy background contributions to the energy spectrum and reduce detector dead time.

Directly opposite the HPGe detector was an array of moderated ^{3}He neutron detectors (MHND), consisting of 6 neutron detectors aligned perpendicular to the

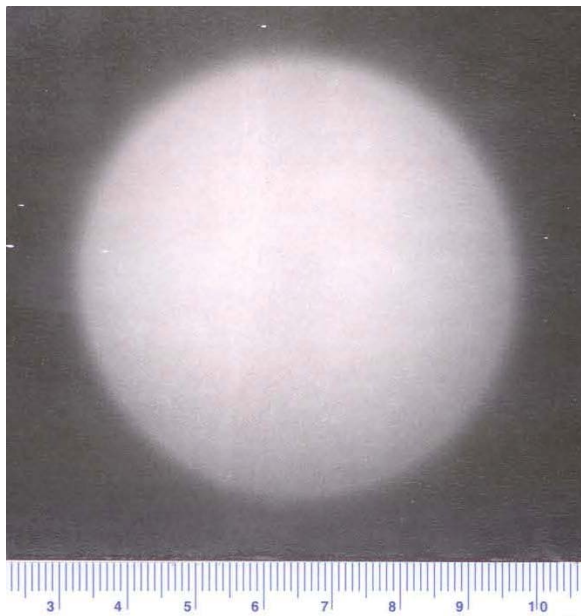

Figure 3.2: Poloroid^{TM}image of the bremsstrahlung photon beam at the target location. Image is a large format Polaroid 52 placed at the target location and exposed to a 22 MeV bremsstrahlung photon beam at 15 Hz for 40 s. The scale across the bottom is in cm.

target at a distance of 63.5 cm to the center of the array. The detectors were made using 2.54 cm diameter ^{3}He proportional counters filled to 10 atmospheres. The ^{3}He tubes are encapsulated in 2.54 cm of polyethelene, 110 μm of cadmium and 9.51 mm of borated elastomer. Each detector was encased in a 2.4 mm thick aluminum housing. The detectors have an overall length of 53.3 cm with an active region of 20.3 cm. This arrangement allows for the detection of neutrons with an energy less than 10 MeV and greater than $\sim$ 1 eV with a peak efficiency of 10 keV [20].

3.2 Targets

The bulk of the targets investigated consisted of 1 L aqueous solutions of ^{238}U and ^{232}Th in various concentrations. Figure 3.4 shows a diagram of the liquid targets. These targets provided a small and diffuse sample to minimize self absorbtion of the outgoing γ-rays. Table 3.1 contains data on the contents of the aqueous solutions

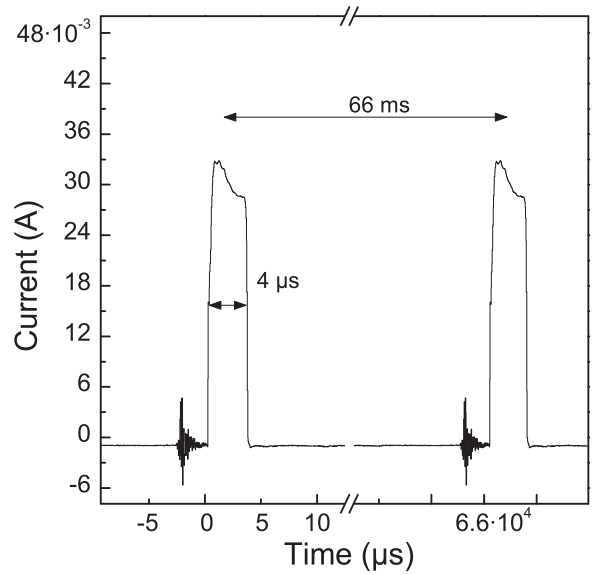

Figure 3.3: The pulse structure of the electron beam. Each pulse has a duration of 4 μs and contains approximately 120 nC of charge. The pulses are separated by 66 ms.

used. Water soluble forms of ^{238}U and ^{232}Th, $UO_2(NO_3)_2$ and $Th(NO_3)_4$ respectively, were combined with 1 L of deionized water to form each of the targets. The solutions were then sealed in 1.18 L stainless steel bottles. The bottles were manufactured from $\sim$ 0.5 mm thick 18/8 stainless steel, which is comprised of 18% chromium, 8% nickel and 74% iron. The bottles are 8.9 cm diameter, which intersected with the 6.5 cm diameter beam results in $\sim$ 260 ml of the liquid contents being directly exposed to the bremsstrahlung beam. In addition to the liquid based targets, 3 large mass 15.4 g$\cdot$ cm^{-2} ^{238}U plates were also used in the "proof of concept" portions of the experiment.

3.3 Data collection

Figure 3.5 shows a schematic of the data acquisition system. Output from the HPGe detector's preamplifier was sent to a spectroscopy amplifier, which provided pulse amplification and shaping before input into a Wilkinson analog to digital con-

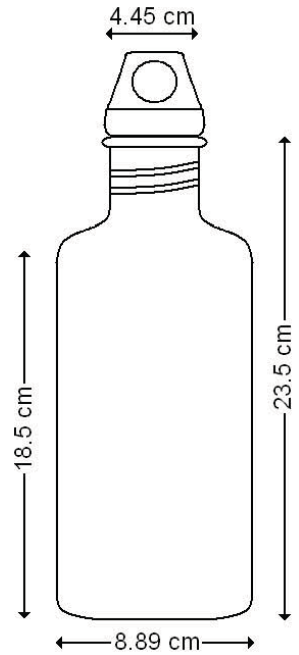

Figure 3.4: Diagram of the low mass liquid targets. Each canister is made of ~ 0.5 mm thick 18/8 stainless steel. The contents are sealed with a stainless steel and plastic screw cap and extend vertically 18.5 cm from the bottom of the canister.

verter. This allowed for energy spectra to be collected via pulse height analysis. Energy spectra and timing information were collected from the HPGe detector using a multi-parameter data acquisition system. The acquisition system allowed for data storage in event-by-event mode with a timestamp resolution of 50 ns. Energy spectra from the HPGe detector as well as a TTL pulse from the accelerator trigger were recorded.

The output signals from the moderated ^{3}He neutron detectors (MHND) were recorded via a latched scaler. The scaler was triggered from the accelerator gun and set to histogram the data from the array in 32 μs bins spanning 2048 channels. Hence, data from the MHNDs was recorded during the entire timespan from pulse to pulse allowing for a direct measurement of the neutron emission from the target as well as the neutron die-away time in the experimental cell.

Due to the intensity of the bremsstrahlung pulse, the HPGe detector was unable

Table 3.1: ^{232}Th and ^{238}U aqueous target masses and concentrations.

Target	^{232}Th Mass (g)	^{238}U Mass (g)	Concentration	Relative ^{232}Th	Relative ^{238}U
^{232}Th-1	9.8	0.0	0.95%	100%	0%
^{232}Th-2	18.1	0.0	1.7%	100%	0%
^{232}Th-4	37.9	0.0	3.5%	100%	0%
^{232}Th-5	59.6	0.0	5.2%	100%	0%
^{232}Th-7	83.4	0.0	7.0%	100%	0%
^{232}Th-9	109.7	0.0	8.7%	100%	0%
^{238}U-1	0.0	10.0	0.98%	0%	100%
^{238}U-2	0.0	16.2	1.6%	0%	100%
^{238}U-3	0.0	33.6	3.1%	0%	100%
^{238}U-5	0.0	52.2	4.7%	0%	100%
^{238}U-6	0.0	72.3	6.3%	0%	100%
^{238}U-8	0.0	94.0	7.8%	0%	100%
Mixed-A	11.4	30.8	3.9%	27.0%	73.0%
Mixed-B	23.4	31.7	4.9%	42.5%	57.5%
Mixed-C	32.5	21.1	4.8%	60.6%	39.4%
Mixed-D	34.6	10.4	4.1%	76.9%	23.1%

to resolve individual events during the irradiating pulse and shortly thereafter. Thus it was necessary to gate the detectors until they were fully recovered. Recovery time was approximately 5 ms and was proportional to the mass of fissionable material and bremsstrahlung intensity. Thus, the ADCs were gated accordingly using a digital gate and delay generator triggered via the accelerator pulse. The gating and accelerator frequency, 15 Hz, resulted in less than 10% dead time due to the bremsstrahlung pulse. The HPGe detectors were then free to count within the remaining time window before the next pulse. Since the MHND detectors recover quickly, within 100 μs following the bremsstrahlung pulse, they required no gating and were able to count during the entire acquisition [20].

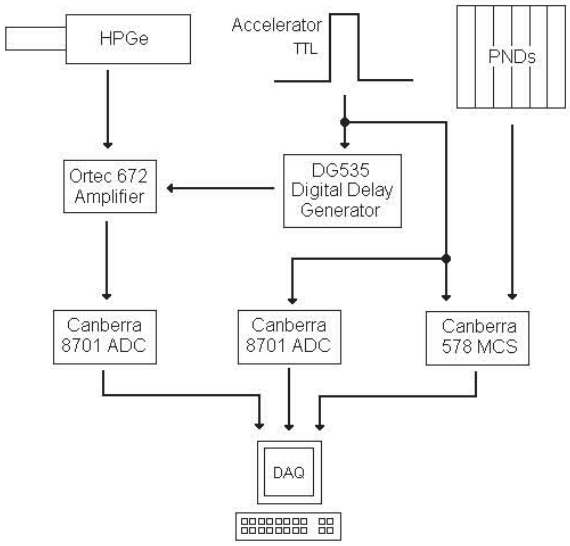

Figure 3.5: Schematic of the electronics portion of the experimental setup. The data acquisition system (DAQ) records both the HPGe and ^{3}He neutron detectors as well as the TTL pulse from the accelerator gun trigger.

Chapter 4

Results and Analysis

4.1 Identifying Fission

Figure 4.1 shows the results of typical energy spectra collected from three 15.4 g·cm^{-2} ^{238}U plates with and without an irradiating bremsstrahlung beam. Both show an elevated γ-ray yield over that of the background, arising from both the natural decay chain and fission products. While the beam-off energy spectrum is dominated by emissions from the decay chain, it also contains contributions from long lived fission products from both spontaneous and prior induced fission events. This is in stark contrast to the beam-on energy spectrum, which appears to be dominated by the emission of high-energy γ-rays from short-lived fission fragments. This elevated yield over the beam-off spectrum continues throughout the entire energy range of the detector and is orders of magnitude greater than that of natural decay. The most significant increase, however, lies in the region above 3 MeV where little to no γ-rays are present from the natural decay of ^{238}U. This overall yield increase is $\sim$ 7000 times that of natural decay of ^{238}U.

The elevated yield above 3 MeV is not unique to fission. Any nonfissionable material will also produce elevated yields of γ-rays above 3 MeV when subjected to an intense and energetic bremsstrahlung photon beam. Figure 4.2 shows energy spectra collected between bremsstrahlung pulses from low mass aqueous targets of ^{238}U, ^{232}Th and H_2O at 22 MeV and 15 Hz. While the fissionable targets of ^{238}U

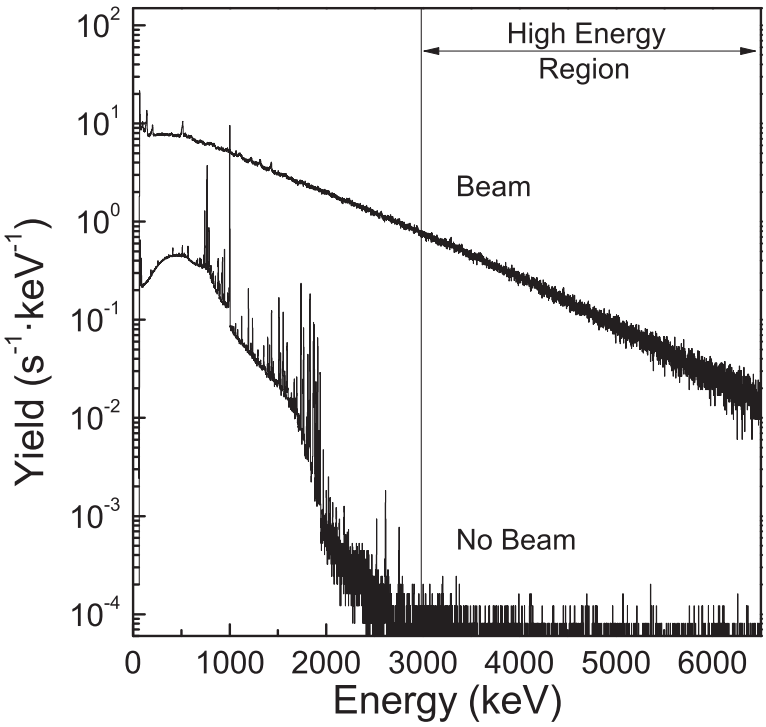

Figure 4.1: Energy spectra of three 15.4 g·cm^{-2} ^{238}U plates with and without incident bremsstrahlung photon beam. For the spectrum with photon beam, the accelerator was operated at 22 MeV and 15 Hz with a charge of 170 nC per pulse. The data was collected for 8 h and 400 s, respectively. A demarcation line at 3 MeV indicates the effective limit of γ-ray emissions from natural decays.

and ^{232}Th exhibit an increase in yield of γ-rays above 3 MeV, Figure 4.2 shows that there are contributions to the energy spectra in this region from non-fission based reactions when a nonfissionable H_2O target is present. These high-energy γ-rays pose a problem due to the potential that they will interfere with the fission signatures thereby limiting the effectiveness of a system based on high-energy delayed γ-rays.

4.1.1 (n,γ) Interference

Figure 4.3 shows the γ-ray rate above 3 MeV as a function of time after the pulse from Figure 4.2. Since there is no fissionable material in the H_2O target, these emissions come from nonfission based nuclear reactions and are most likely due to

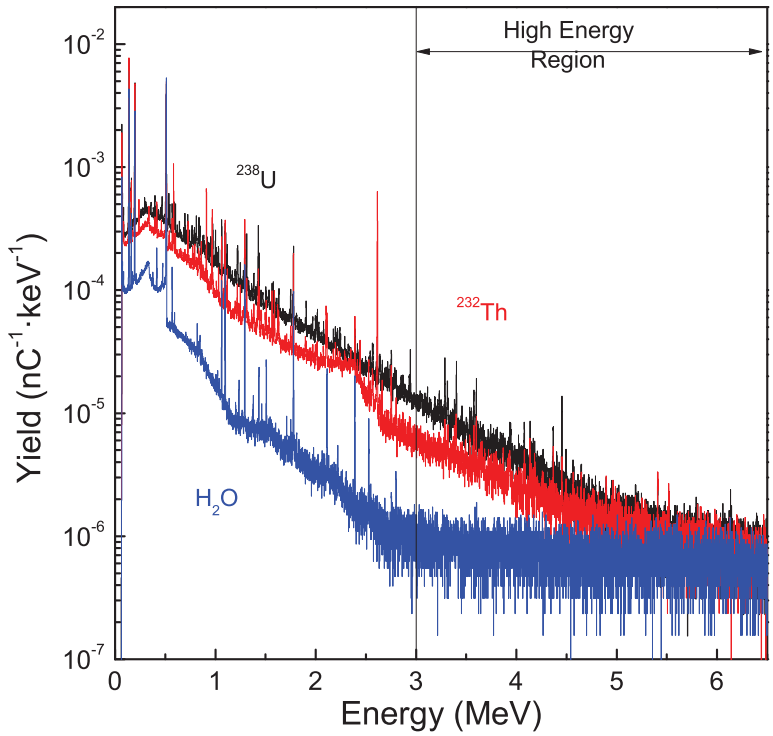

Figure 4.2: Energy spectra of low mass ^{238}U (U-5, 0.41 g·cm^{-2}), ^{232}Th (Th-5, 0.46 g·cm^{-2}) and nonfissionable H_2O collected at 22 MeV and 15 Hz. The accelerator was operated with 4 μs wide pulse containing 150 nC of charge. Total collection time for both spectra is 2 h. Spectra is shown with a demarcation line at 3 MeV.

interactions in the environment. The yield from these reactions decrease to near background levels within 35 ms. In contrast, the yield from the fissionable targets remain elevated for the entire time-span from pulse to pulse. While the emissions from fissionable material are due to short-lived fission fragments, which still emit photons at these timescales, it is not clear what reaction(s) are contributing to the high-energy signal from nonfissionable material. Candidates for these reactions include short-lived products from (γ,n),(γ,2n),(γ,p), etc. as well as the ensuing (n,γ) capture γ-rays.

The neutron detection rate as a function of time enables identification of the reaction responsible for the elevated delayed γ-ray yield in the nonfissionable sample. Figure 4.4 shows the neutron detection rate as a function of time for low mass samples of ^{238}U and ^{232}Th as well as H_2O. Figure 4.4 shows that the neutrons detected by

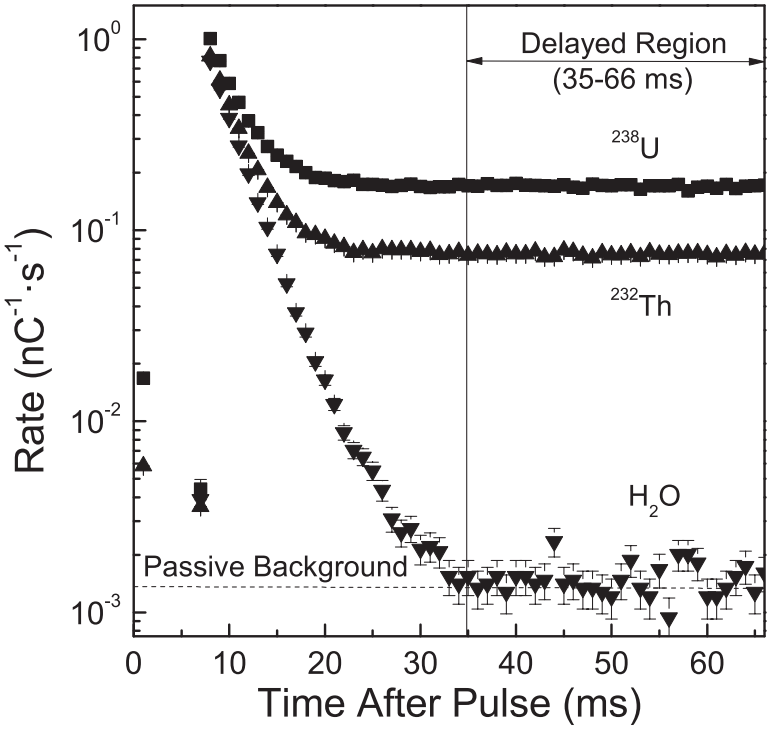

Figure 4.3: The γ-ray rate as a function of time for emissions greater that 3 MeV for low mass ^{232}Th (▲),^{238}U (■) and the nonfissionable sample of H_2O (▼) from the energy spectra in Figure 4.2. The accelerator was operated at 22 MeV, 15 hz with a pulse width of 4 μs, containing 150 nC of charge. Total collection time for each spectrum is 2 h.

the ^{3}He detector array share similar decay properties as the γ-rays above 3 MeV in Figure 4.3 and reduce to background in less than $\sim$ 20 ms. The decay constant seen by the ^{3}He detector array is different due to the fact that the array is unable to measure neutrons below $\sim$ 1 eV. The γ-rays detected above 3 MeV prior to 35 ms are most likely capture γ-rays from neutrons produced by photonuclear reactions in the radiator and any nonfissionable material in the bremsstrahlung beam. These neutrons are captured by material in the environment, i.e. boron in the detector shielding as well as material in the concrete shielding of the experimental cell. The resulting neutron capture γ-rays are then detected by the high purity germanium detector.

Since 22 MeV is beyond the neutron separation energy for most isotopes, this

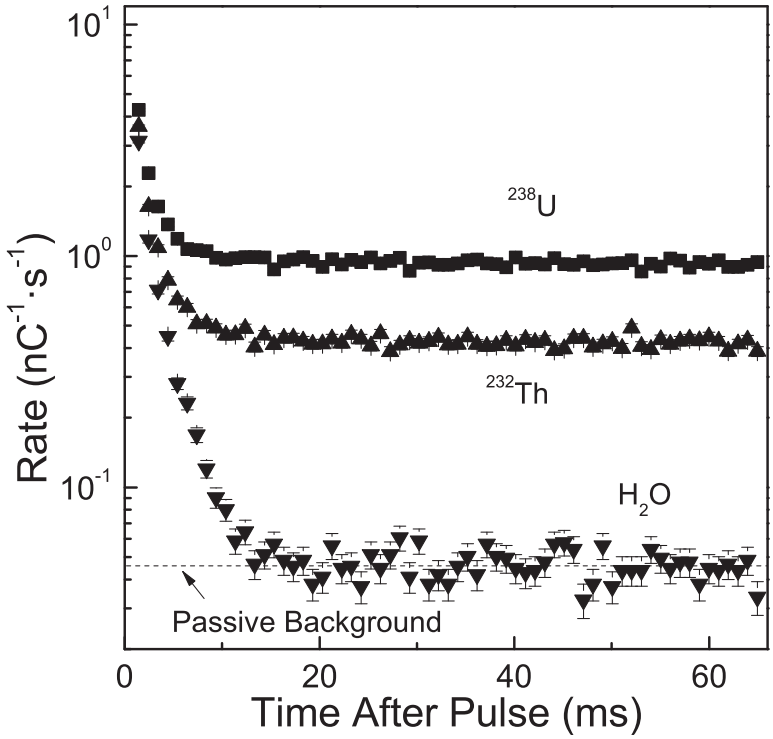

Figure 4.4: Neutron rate as a function of time after the pulse for ^{238}U (■), ^{232}Th (▲) and H_2O (▼). The accelerator was operated at 22 MeV, 15 Hz with a pulse width of 4 μs, containing 150 nC of charge. Total collection time for each spectrum is 2 h.

high-energy γ-ray contribution from neutron capture occurs in any γ-ray energy spectra collected within milliseconds after irradiating pulses. By removing γ-rays detected in the first 35 ms after the pulse, the contribution from non-fission based reactions above 3 MeV are eliminated from the energy spectrum. Because fission fragments still emit photons beyond this timescale, the emissions from ^{238}U and ^{232}Th remain elevated throughout the full 66 ms between pulses. Figure 4.5 shows the result of a time cut on the energy spectra of Figure 4.3. These spectra show γ-rays detected between 35 and 66 ms on aqueous targets of ^{238}U, ^{232}Th and H_2O.

Figure 4.5 shows that the energy spectrum of H_2O has diminished to background in the region above 3 MeV, while the energy spectra of ^{238}U and ^{232}Th remain largely unchanged. Thus, the γ-rays detected in the energy region above 3 MeV and beyond 35 ms are β-delayed γ-rays from short-lived fission fragments. This alone is an

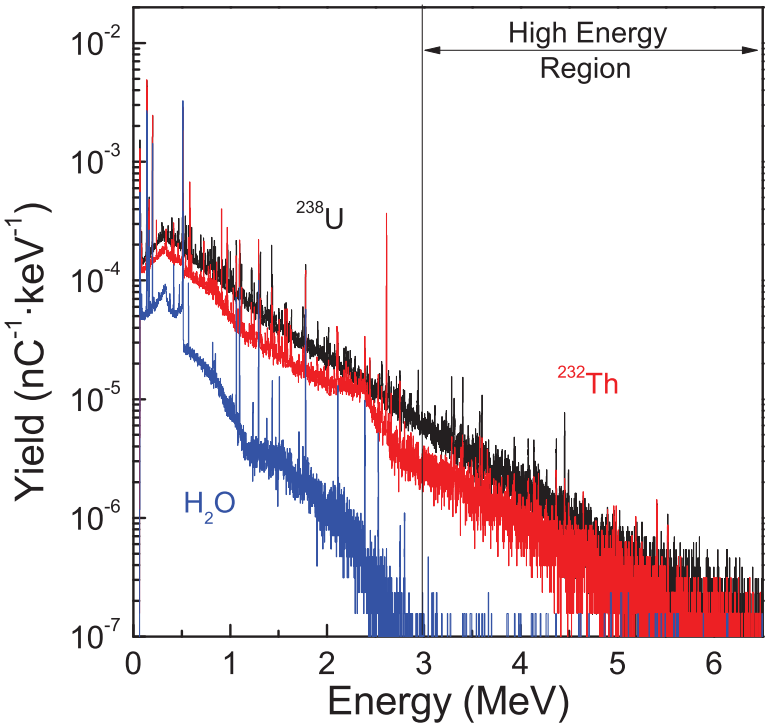

Figure 4.5: Energy spectra of aqueous ^{238}U, 0.41 g·cm^{-2}, ^{232}Th, 0.46 g·cm^{-2} and nonfissionable H_2O from Figure 4.2 with the first 35 ms after the accelerator pulse removed. The accelerator was operated at 22 MeV, 15 Hz with a pulse width of 4 μs, containing 150 nC of charge. Total collection time for each spectrum is 2 h.

indicative signature of fission and can be used as such [30]. While the presence of high-energy γ-rays above 3 MeV and beyond 35 ms provides a useful signal as to the presence of fissionable material, it does nothing to resolve its content. To determine isotopic composition, fingerprints unique to the fissioning isotope must be identified.

4.2 Discrete Line Prediction and Identification via ENDF/B

Figure 4.5 shows the energy spectra from ^{238}U, ^{232}Th and H_2O with the first 35 ms following the accelerator pulse removed. There are discrete lines from fission fragments present in the region above 3 MeV and beyond 35 ms. Due to the prolific

nature of the peaks, identifying the fission fragment responsible for any given discrete line is not easy. In an effort to identify specific peaks, the fission fragment distribution from ENDF/B-VII.0 and the discrete line information from ENSDF were used in conjunction with the response of the HPGe detector to produce simulated energy spectra of ^{238}U and ^{232}Th as discussed in Section 2.3 [3, 8]. These calculated energy spectra allow access to the underlying fission fragment and peak intensity data used to generate it. Hence, overlaying a calculated spectrum with a measured spectrum facilitates the identification of discrete lines.

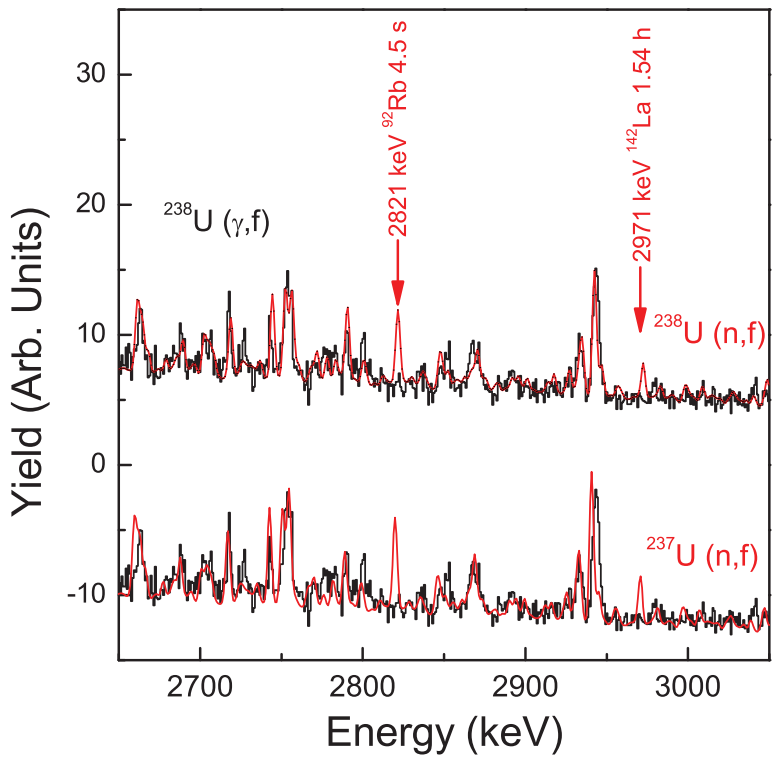

Figure 4.6: Calculated energy spectra from fission fragment distributions for ^{238}U fission with 14.5 MeV neutrons and ^{237}U fast pooled fission overlaid on a measured energy spectrum from a low mass aqueous sample of ^{238}U (U-5, 0.41 g·cm^{-2}). For measured energy spectra, the accelerator was operated at 22 MeV, 15 hz with a pulse width of 4 μs, containing 150 nC of charge. Total collection time was 2 h. The energy spectra are normalized to total charge on radiator and given an artificial offset to accentuate differences between calculated energy spectra. Labeled photopeaks indicate the presence of overly estimated fission fragments in the calculated spectra.

Figure 4.6 shows a portion of two calculated energy spectra using fragment distributions from ^{237}U fast pooled fission and ^{238}U high-energy fission overlaid with the measured photofission spectra of a low mass aqueous ^{238}U target. The average excitation energy of a 22 MeV bremsstrahlung photon beam is 13.2 MeV and lays directly between the excitation energies of high-energy, $\sim$ 19 MeV, and fast pooled, $\sim$ 8.5 MeV, neutron induced fission. Both calculated energy spectra are strikingly similar and align equally well with the measured spectrum. Because of this similarity and a lack of fission fragment distribution data for ^{231}Th fast pooled fission, high-energy neutron induced fission of ^{238}U and ^{232}Th was used to generate spectra for the photofission of ^{238}U and ^{232}Th, respectfully.

Figures 4.7 and 4.8 show the energy spectra calculated from high-energy neutron induced fission of ^{238}U and ^{232}Th overlaid on their respective measured spectra for photofission. These spectra span the energy range from 2650 keV, the limit of decay from naturally occurring radioactive material, to 5850 keV. While the calculated spectra closely align with measured spectra for the energy region from 2650 keV to 4650 keV, above this energy there are sizeable differences. The fission fragment ^{92}Rb is drastically over predicted and emits discrete γ-rays throughout the entire high-energy range. Several isotopes of indium are also predicted but not present, such as ^{124}In, ^{126}In and ^{128}In, as well as the isotopes ^{87}Br,^{94}Rb and ^{142}La. Photopeaks from ^{97}Y are also over predicted in the calculated spectra, but are present in the measured spectra with a lower yield. Three peaks at 3942, 4400 and 4492 keV from unidentified fission fragments are also present in the measured spectra but were not predicted. While a significant number these discrepancies exist between the calculated and measured spectra, overall the calculated spectra match the experimental data well.

D. De Frenne et al. did not report measuring some of these fission fragments including ^{92}Rb and ^{142}La from 20 MeV bremsstrahlung induced fission on ^{238}U [11]. De Frenne utilized a shuttling system to irradiate and measure 0.1 mm thick uranium disks encapsulated in nickel. This measurement includes a transport and cool-down time of 5 to 10 seconds. ^{92}Rb has a half-life of 4.5 s and a large peak intensity at 815 keV, and ^{142}La has a half-life of 1.5 h and a large peak intensity at 641 keV. This places photopeaks from both fission fragments well within their range of interest and

capability of being measured [3,11]. These discrepancies are in part due to the difference between neutron induced fission and photofission. However, some discrepancies are due to how fission fragment yields are calculated and measured. To calculate fission fragment yields, a calculated charge distribution model is used to produce a set of independent yields for a given fissioning nuclei. The yields from this model are then statistically merged with the yields of measured data. Because the model has large errors associated with it and the relevant experiments are incapable of measuring the yield of every fission fragment, large errors exist in the ENDF/B-VII.0 data sets [8, 9].

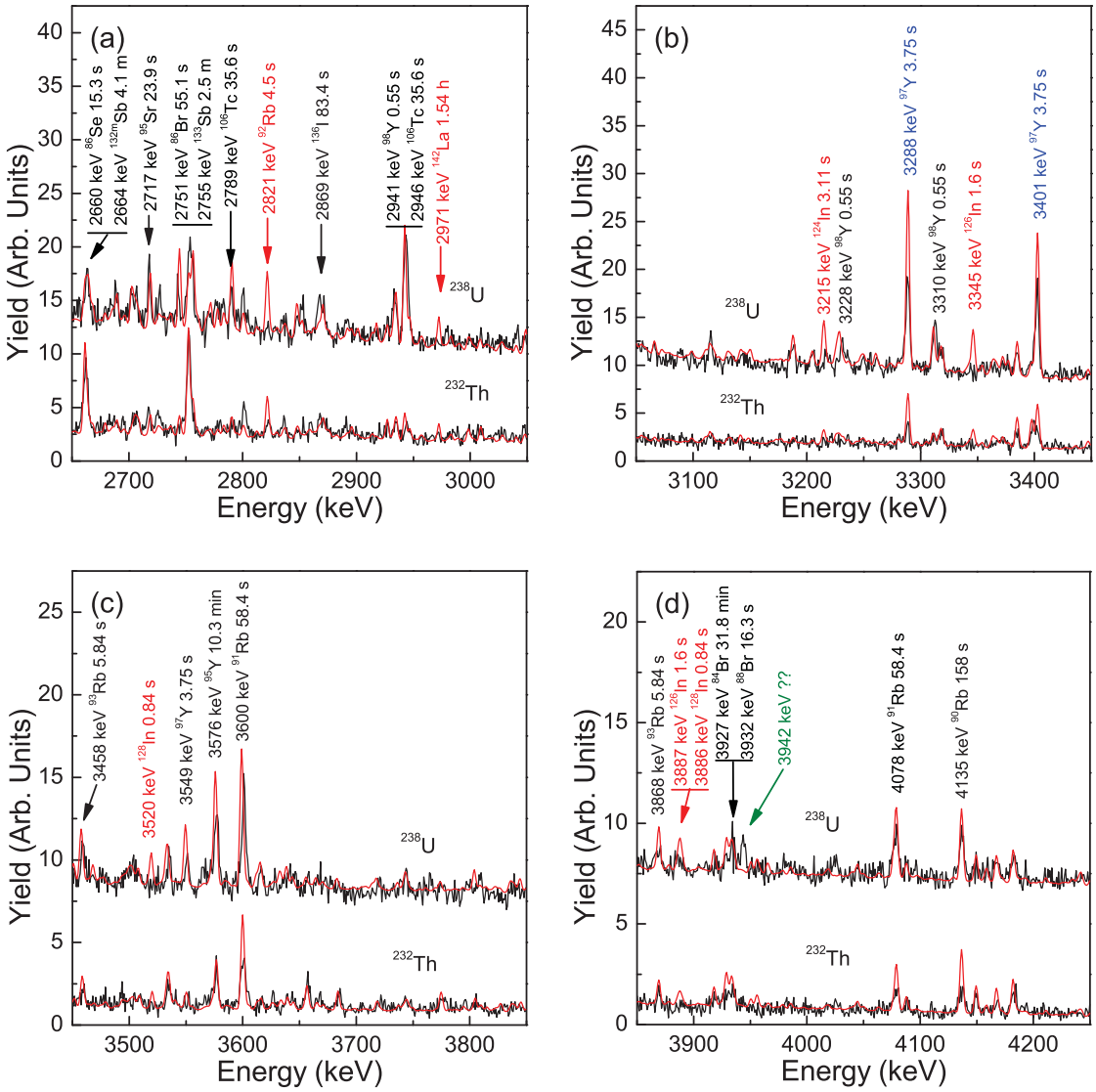

Figure 4.7: Energy spectra of ^{238}U, 0.41 g·cm^{-2}, ^{232}Th, 0.46 g·cm^{-2}, low mass aqueous samples collected at 22 MeV and 15 Hz overlaid with the calculated energy spectra from high energy neutron induced fission on ^{238}U and ^{232}Th, respectively. The measured spectra were collected over a period of 2 h and are normalized to total charge on radiator. ^{238}U spectra are shown with an arbitrary offset to accentuate differences between spectra. Several notable energy peaks are labeled. Those labeled in black have been calculated accurately, red have been predicted but are not present in data, blue have been over predicted but are present in data, and green have not been predicted and thus are not identified.

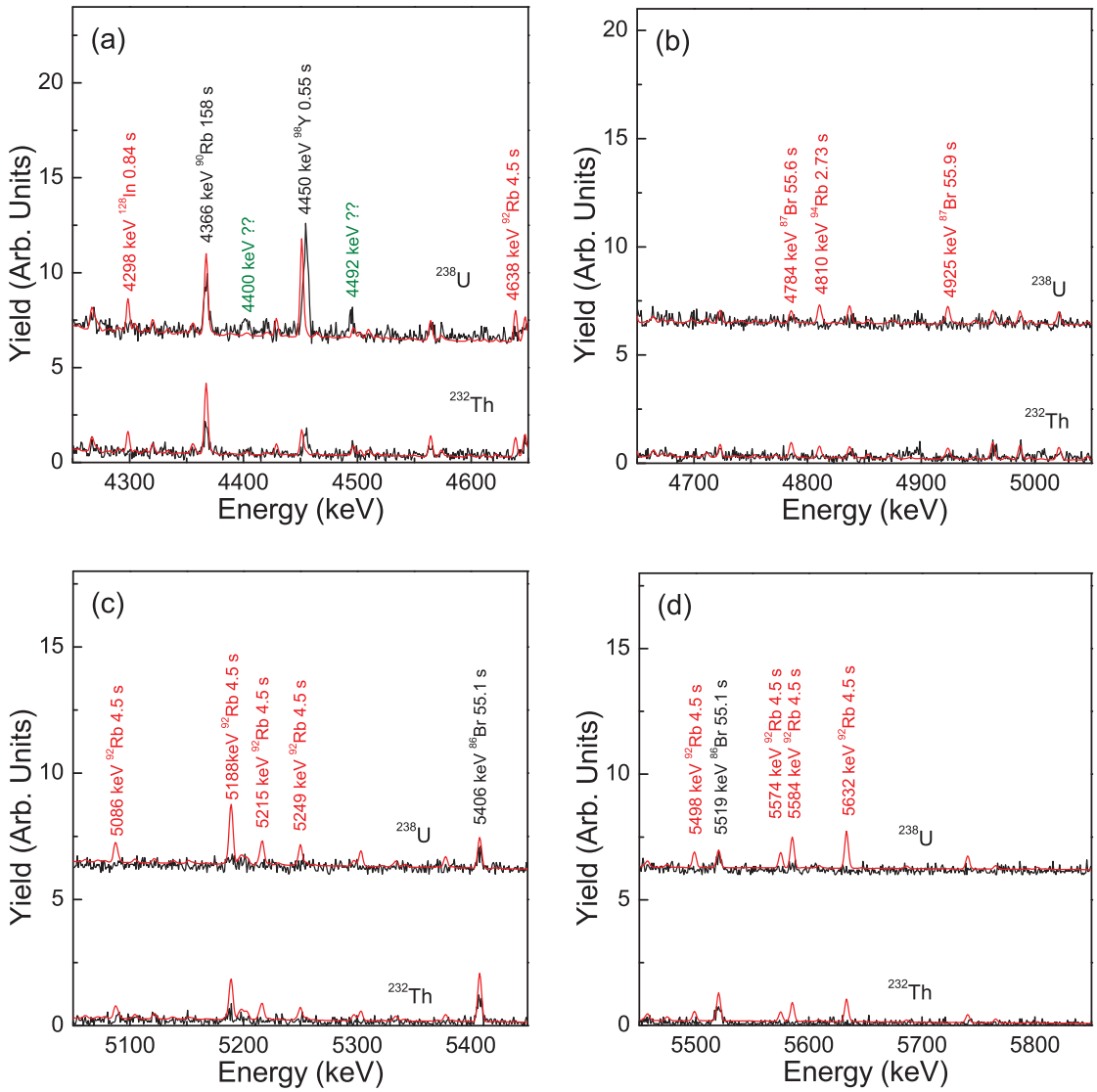

Figure 4.8: Energy spectra of ^{238}U, 0.41 g·cm^{-2}, ^{232}Th, 0.46 g·cm^{-2}, low mass aqueous samples collected at 22 MeV and 15 Hz overlaid with the calculated energy spectra from high energy neutron induced fission on ^{238}U and ^{232}Th, respectively. The measured spectra were collected over a period of 2 h and are normalized to total charge on radiator. ^{238}U spectra are shown with an arbitrary offset to accentuate differences between spectra. Several notable energy peaks are labeled. Those labeled in black have been calculated accurately, red have been predicted but are not present in data, blue have been over predicted but are present in data, and green have not been predicted and thus are not identified.

4.3 Peak Ratio Analysis (PRA)

Peak ratio analysis is a traditional method of determining the isotopic composition of a sample containing two, or more, fissionable isotopes. By identifying a single peak that stays uniform regardless of relative concentration of either fissionable material, this peak can be used as a measure of total fission events in the sample. This works if the two fissioning isotopes share identical, or nearly so, fission yield for the fragment under question. Using this peak as a fiducial, a signal peak can be normalized to a measure of fission reactions. Each signal peak must be unique to one of the fissioning isotopes so as to increase or decrease as the relative concentration is altered accordingly. The ratio of the areas of the signal peak to the fiducial peak is thus a reliable measure of the relative content of the signal peak's contributing fission source.

Figure 4.9 shows energy spectra collected across a set of low mass aqueous targets, which had varied concentration of both ^{238}U and ^{232}Th. The relative ^{238}U concentrations of these samples are 100, 73, 57.5, 39.4, 23.1 and 0% respectively, with the balance being ^{232}Th. Each sample contained an average of $\sim$ 0.40 g·cm^{-2} in the accelerator beam. The combined ^{86}Br/^{133}Sb peak appears constant throughout all energy spectra regardless of the varied relative concentration of ^{238}U and ^{232}Th and presents a potential fiducial peak for peak ratio analysis. A potential signal peak is then found in the combined ^{98}Y/^{96}Tc peak, which grows as a function of the relative ^{238}U concentration. By taking the ratio of these two peaks, a monotonic relationship between this ratio and the relative concentration of ^{238}U is obtained, as seen in Figure 4.10.(a).

Figure 4.10.(a) shows the peak ratio as a function of relative ^{238}U concentration. For a target containing only ^{238}U or ^{232}Th, this ratio would be a constant. As the relative ^{238}U concentration is altered the ratio between peaks changes. Figure 4.10.(a) shows a strong linear relationship between the peak ratio and relative ^{238}U concentration. This linear relationship is expected since the fiducial should be a constant with respect to the relative concentration of ^{238}U and the signal peak increases linearly as

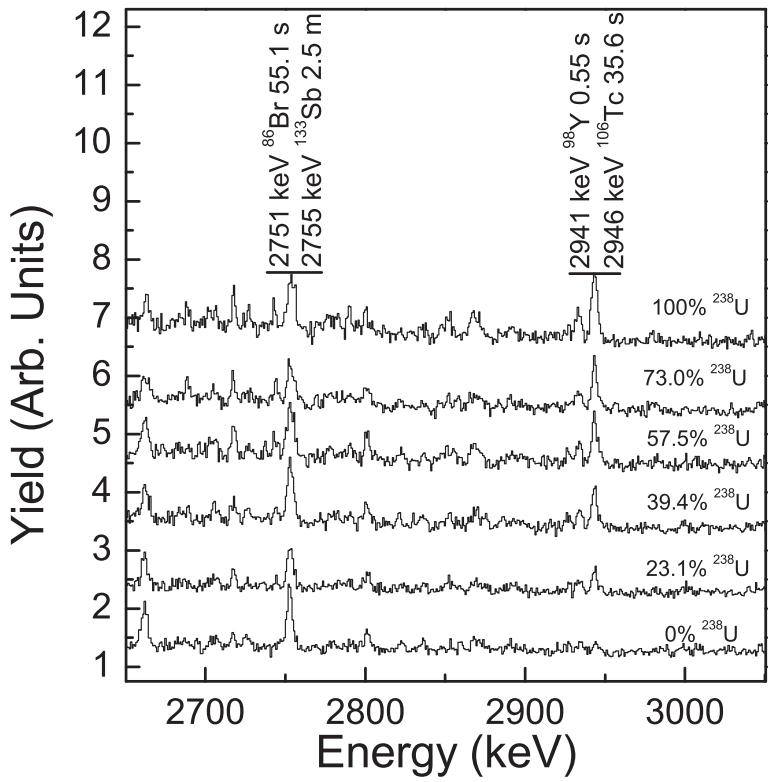

Figure 4.9: Energy spectra of low mass liquid targets U-5, A, B, C, D and Th-5 collected at 22 MeV, 15 Hz. Each spectrum is normalized to total charge on radiator with the first 35 ms following the pulse has been removed. An artificial offset is employed to emphasize differences as well as similarities between energy spectra. The combined photopeaks of ^{98}Y & ^{96}Tc and ^{86}Br & ^{133}Sb are labeled.

the concentration of ^{238}U is increased.

The relative concentration of ^{238}U across the samples are then calculated by calibrating the ratio of the ^{98}Y/^{96}Tc peak to the ^{86}Br/^{133}Sb peak. Because the peak ratio appears linear as a function of relative ^{238}U concentration, a linear fit was applied to the data in Figure 4.10.(a). The inverse of this fit was then used to transform the peak ratio into relative concentration. Figure 4.10.(b) shows the results of this analysis across the six samples containing varied concentrations of ^{238}U and ^{232}Th.

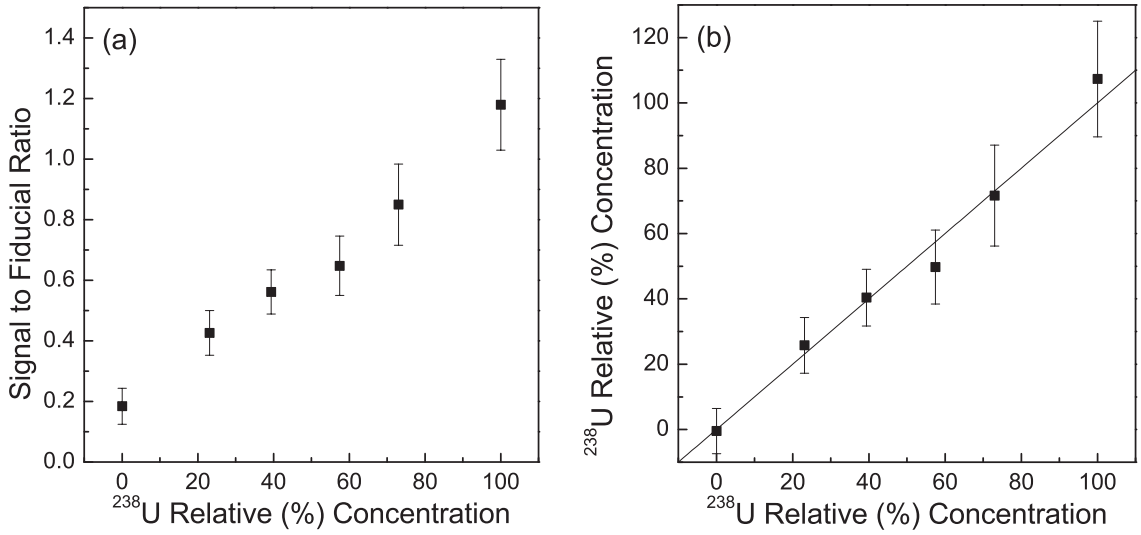

Figure 4.10: a) Graph of the peak ratios of 2941 & 2946 keV and the 2751 & 2755 keV gamma peaks from Figure 4.9. b) Peak ratios have been transformed into Relative ^{238}U concentration. Error bars in both graphs are representative of 1σ standard deviation.

Figure 4.10.(b) shows a 1:1 relationship between the calculated concentration and the true relative concentration of ^{238}U. While this is compelling, the associated errors are too large to make this relationship very useful. At 100% relative ^{238}U concentration the error is nearly 20% and at 0% the error is ~ 8 %. This is in part due to the difficulty in peak fitting because of the high density of peaks in the vicinity of those of interest. The error is dominated, however, by the low number of counts in each peak. While the application of a better fitting algorithm to these peaks may help, there is another underlaying problem. Both the fiducial and signal peaks are convolutions of multiple fission fragments with different fission yields for ^{238}U and ^{232}Th.

Figure 4.11 shows the shift of the ^{86}Br/^{133}Sb peak from 2751 keV to 2755 keV. This shift is due to transition in the dominant fragment from ^{86}Br for fission of ^{232}Th to ^{133}Sb for fission of ^{238}U, resulting in an energy shift of the centroid by ~ 3 keV. Along with this energy shift is a change in the yield. This variance means that the fiducial peak is not truly constant regardless of relative concentration and cannot be used as an accurate measure of the total amount of fission in a sample. If the individual peaks could be resolved, they themselves would act as signal peaks of ^{232}Th and ^{238}U,

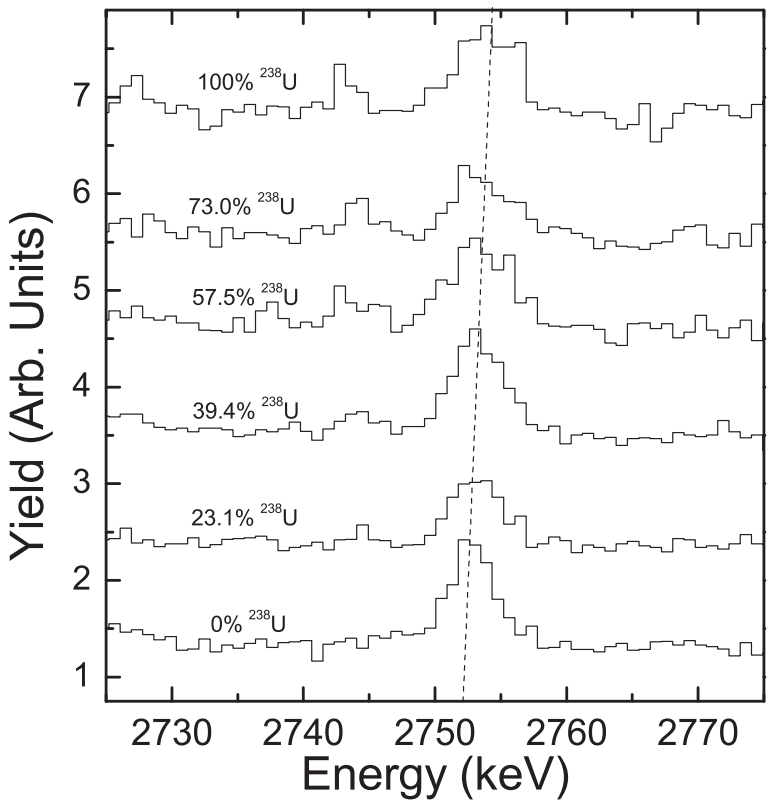

Figure 4.11: A closer look at the combined photopeak of 2751 keV from ^{86}Br and 2755 keV from ^{133}Sb. The dashed line shows the shift in energy due to the transition in dominance from one to the other, respectively.

respectively.

These factors do not readily allow the use of the ^{86}Br/^{133}Sb peak as a fiducial for peak ratio analysis. Further analysis of the energy spectra from Figures 4.7 and 4.8 do not yield any high-energy discrete γ-rays from fission fragments that can be used as a fiducial in this method since multiple fragments produce similar energy γ-rays that cannot be resolved by the detector. Because of the lack of a necessary fiducial and the difficulty in fitting peaks, another analysis method is needed to quantify fissionable material.

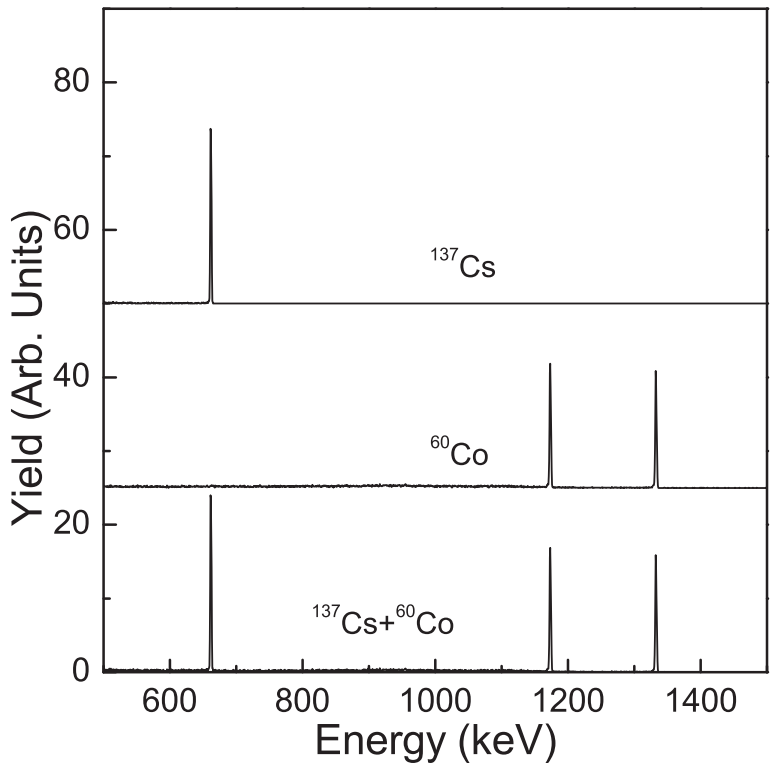

Figure 4.12: Energy spectra of 10 μCi button sources of ^{137}Cs and ^{60}Co taken at 25 cm from the detector both individually and separately. Energy spectra were collected for 1 m each and normalized to time. Spectra are given artificial offset to emphasize individual photopeaks.

4.4 Spectral Contribution Analysis (SCA)

Figure 4.12 shows energy spectra of ^{137}Cs and ^{60}Co both individually and separately. The energy spectrum of the combination of ^{137}Cs and ^{60}Co is identical to the sum of the individual ^{137}Cs and ^{60}Co spectra. The photopeaks from the individual measurements of ^{137}Cs and ^{60}Co are superimposed on one-another to create the total spectra. In simple cases such as this, the energy spectra are easily deconvolved into their base components. The idea of superimposed spectra can be utilized to better isolate components of a mixed fissionable sample. Rather than fitting individual peaks, a portion of the photofission energy spectrum of pure ^{238}U can be used as a fingerprint of ^{238}U and likewise for ^{232}Th. Because a region of a spectrum spans multiple photopeaks, the overall counts utilized are increased and subsequently the errors associated with the counts are decreased. This presents a significant advantage over PRA.

Using superposition, a portion of an energy spectrum (ϕ) from the photofission of a mixed target can be described using the contributing energy spectra of ^{238}U (ϕ_{238}) and ^{232}Th (ϕ_{232}) as a basis set in the equation,

$$\phi = \alpha_{238}\phi_{238} + \alpha_{232}\phi_{232}, \tag{4.1}$$

where the coefficients α_{238} and α_{232} are indicative of the quantity of ^{238}U and ^{232}Th in the target. The energy spectra from the photofission of ^{238}U (ϕ_{238}) and ^{232}Th (ϕ_{232}) are unique due to their different fission fragment distributions. While these basis spectra are unique, they are not orthogonal, since these spectra also share multiple photopeaks from fission fragments. Because of nonorthogonality, regions are selected that are populated by discrete γ-rays that are either unique to each fissioning material or have significant intensity differences. The Levenberg-Marquadt algorithm is then utilized to recreate the energy region for mixed samples containing varied amounts of ^{238}U and ^{232}Th from its base components [29]. This method allows the intensity , i.e. α_{238} and α_{232}, of each contributing energy spectrum to be varied independently and uses a non-linear least squares regression in order to optimize the fit. The resulting parameters α_{238} and α_{232} then indicate the spectral contribution from ^{238}U and ^{232}Th

photofission, respectively. The coefficients satisfy the equations,

$$\phi_{238\ meas.} = \alpha_{238}\phi_{238} = 1 \cdot \phi_{238}, \tag{4.2}$$

and,

$$\phi_{232\ meas.} = \alpha_{232}\phi_{232} = 1 \cdot \phi_{232}, \tag{4.3}$$

where $\phi_{meas.}$ is the measured spectrum of a pure ^{238}U or ^{232}Th target, respectively. Since the fission rate, and subsequently the γ-ray yield, is linearly dependant on mass, this automatically normalizes the coefficients to the mass of fissionable material in the pure target. This normalization allows for a direct comparison of the relative concentrations in the target without the need to compensate for the vastly different photofission rates of ^{238}U and ^{232}Th for 22 MeV bremsstrahlung, a nearly 2 : 1 ratio.

4.4.1 Using Measured Energy Spectra as a Basis Set

The energy region from 2650 to 3050 keV displays several unique and similar discrete lines between the ^{238}U and ^{232}Th photofission spectra. This region was used to form a basis set from the photofission spectra of pure ^{238}U and ^{232}Th low mass aqueous targets. This basis set was then utilized to recreate the same energy region from targets containing varied amounts of ^{238}U and ^{232}Th with relative ^{238}U concentrations of 73, 57.5, 39.4 and 23.1%, as well as the basis set itself. The results of this decomposition algorithm are displayed in Figure 4.13, 4.14 and 4.15.

Figure 4.13 shows the results of spectral decomposition overlaid with the measured energy spectra. The decomposition routine is capable of reproducing the energy spectra of the samples with a great deal of accuracy. While this method reproduces the measured energy spectra, it does not resolve the composition beyond PRA. Figure 4.14 shows the relative spectral contribution or ^{238}U as a function of the relative mass of ^{238}U in the target. While this shows a clear relationship about the line of equality it deviates substantially from a 1:1 correlation for the mixed targets. However, the end points, relative ^{238}U concentrations 0 and 100%, fit exactly. This is because at these relative ^{238}U concentrations the basis set is deconvolving itself.

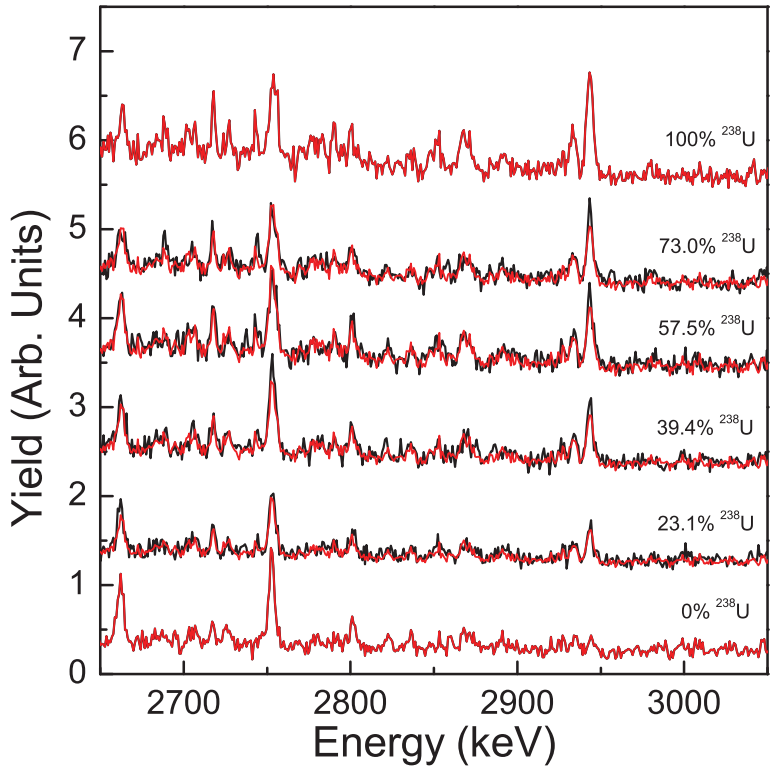

Figure 4.13: Energy spectrum obtained from the fitting algorithm utilizing measured energy spectra as basis sets (red) overlaid on their respective energy spectra (black). Figures to the right indicate the relative percent of ^{238}U present in the sample.

Figure 4.15.(a) and Figure 4.15.(b) show the ^{238}U and ^{232}Th spectral coefficients as a function of mass, respectively. Both coefficients were allowed to vary independently in the decomposition routine. While the ^{238}U coefficient is linear with respect to mass, the ^{232}Th coefficient shows scatter. This scatter about the linear trend of the ^{232}Th coefficient results in the significant discrepancies between the calculated and the actual values in Figure 4.14. This scatter may be caused by a lack of uniqueness of the basis set or a lack of uniqueness from one measured spectra to another. A major factor in the uniqueness of the basis sets is the combined photopeak attributed to ^{98}Y and ^{106}Tc. With little difference in this peak as well as the overall spectra from target to target, the decomposition routine may not be able to resolve the spectra into their ^{238}U and ^{232}Th contributions. The similarity between spectra is evident

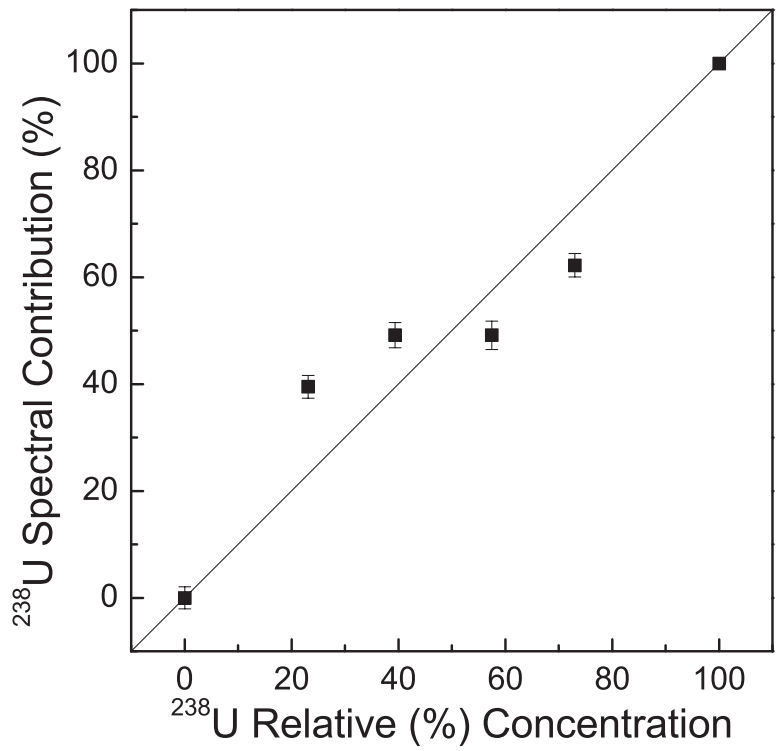

Figure 4.14: Relative spectral contribution from ^{238}U as a function of relative mass in the target. A line is shown at equality between calculated and actual. Error bars are representative of 1σ standard deviation.

in mixes containing relative ^{238}U concentrations of 73 and 57.5%, where the relative concentrations differ by 15.5% but the overall spectra are quite similar.

Figure 4.16 shows the energy spectrum from 1 L of water collected under the same conditions as the low mass aqueous fissionable targets. Two dominant peaks are present from longer lived isotopes produced from neutron capture, a 2754 keV peak from ^{24}Al(n,α)^{24}Na and a combined 2801 keV line from pulse pileup of the 1507.7 keV and 1293.6 keV peaks from ^{115}In(n,γ)^{116m}In. Both materials are present in the high purity germanium detector; aluminum comprises the housing of the detector and indium is a common ingredient in the solder used to make junctions in the preamplifier. While the energy spectra from fission sources is significantly larger than the overall background, the small background peak at 2801 keV is visible in the delayed γ-ray spectra. The 2754 keV peak is buried within the combined photopeak of

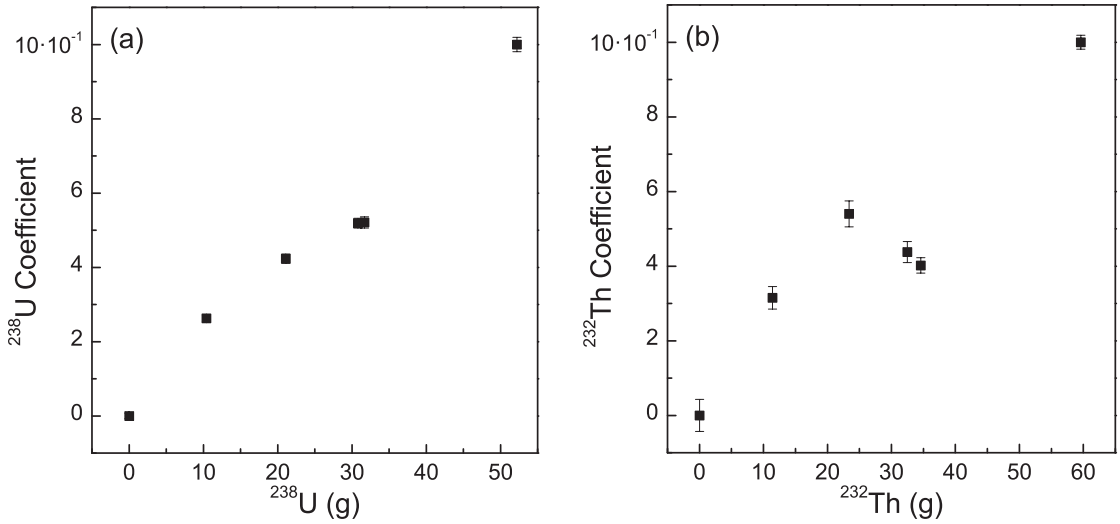

Figure 4.15: Normalized ^{238}U (a) and ^{232}Th (b) coefficients as a function of mass for spectral contribution analysis utilizing measured energy spectra from low mass ^{238}U and ^{232}Th as a basis set. Error bars in both graphs are representative of 1σ standard deviation.

^{86}Br and ^{133}Sb. By including the background along with the fission spectra of ^{238}U and ^{232}Th, the basis set is not independent of the experimental setup. The inclusion of the background peak into both components of the basis set causes it to lose uniqueness. The basis set is no longer dependant solely on the photofission spectra of ^{238}U and ^{232}Th and depends partly on the background caused by the experimental setup.

A measured spectrum, $\phi_{meas.}$, is comprised of its base components times their respective coefficients such that,

$$\phi_{meas.} = \alpha_{238}\phi_{238} + \alpha_{232}\phi_{232}, \tag{4.4}$$

with the coefficients normalized to the amount of mass in the pure targets so that,

$$\phi_{238} = \alpha_{238}\phi_{238} = 1 \cdot \phi_{238}, \tag{4.5}$$

and,

$$\phi_{232} = \alpha_{232}\phi_{232} = 1 \cdot \phi_{232}. \tag{4.6}$$

If the region of interest contains significant background peaks peaks, the basis vectors and measured spectra all contain a background component, ϕ_{bkg}, and a fission com-

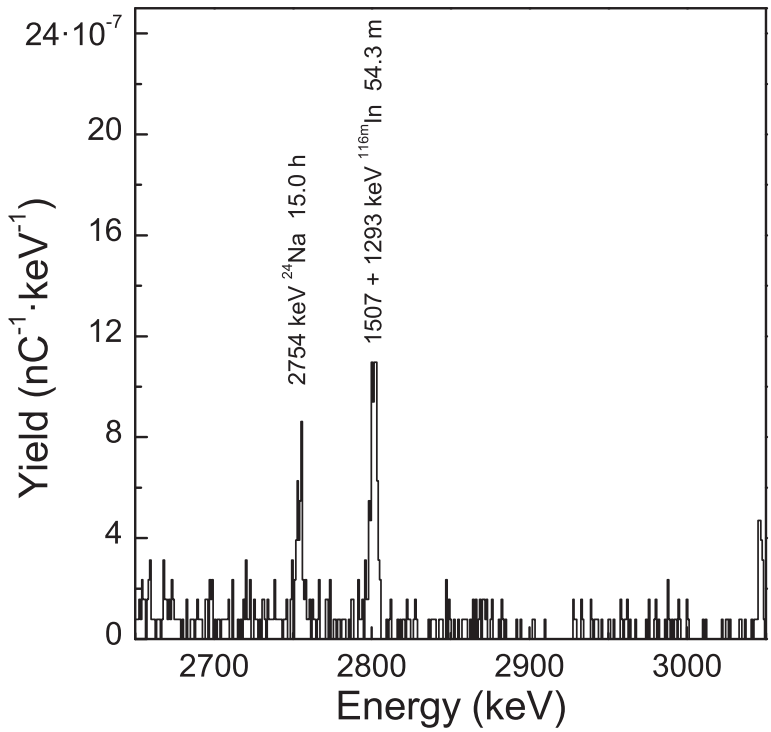

Figure 4.16: A portion of the energy spectrum collected from 1 L H_2O at 22 MeV and 15 Hz. The spectrum is normalized to total charge on the radiator and has the first 35 ms following the accelerator pulse removed. The spectrum was collected over a period of 2 h.

ponent, ϕ'. Assuming that the background is equal across all targets, Equation 4.4 becomes,

$$\phi'_{meas.} + \phi_{bkg} = \alpha_{238}(\phi'_{238} + \phi_{bkg}) + \alpha_{232}(\phi'_{232} + \phi_{bkg}). \tag{4.7}$$

Separating Equation 4.7 into the nonfissionable and fissionable components we obtain,

$$\phi'_{meas.} = \alpha_{238}\phi'_{238} + \alpha_{232}\phi'_{232}, \tag{4.8}$$

and,

$$\phi_{bkg} = (\alpha_{238} + \alpha_{232})\phi_{bkg}. \tag{4.9}$$

Because the coefficients α_{238} and α_{232} are normalized to the amount of mass in the pure targets, the coefficients take the form,

$$\alpha_{238} = \frac{m_{238}}{m^0_{238}} \qquad \text{and} \qquad \alpha_{232} = \frac{m_{232}}{m^0_{232}}, \tag{4.10}$$

Table 4.1: ^{238}U and ^{232}Th aqueous target masses, relative concentration and calculated sum of coefficients α_{238} and α_{232}.

Target	^{232}Th Mass (g)	^{238}U Mass (g)	Relative ^{238}U	Coefficient Sum α_{238}+α_{232}
^{238}U-5	0.0	52.2	100%	1.00
Mixed-A	11.4	30.8	73.0%	0.781
Mixed-B	23.4	31.7	57.5%	1.00
Mixed-C	32.5	21.1	39.4%	0.950
Mixed-D	34.6	10.4	23.1%	0.780
^{232}Th-5	59.6	0.0	0%	1.00

where m^0_{238} and m^0_{232} are the masses of ^{238}U and ^{232}Th in the pure targets, respectively. Substituting these coefficients into Equation 4.9 we obtain,

$$\phi_{bkg} = (\frac{m_{238}}{m^0_{238}} + \frac{m_{232}}{m^0_{232}})\phi_{bkg}. \tag{4.11}$$

While the fission component of the spectrum is unconstrained, Equation 4.11 indicates that any sum of the normalized ^{238}U and ^{232}Th masses that do not equal 1 will fail to reproduce the background, ϕ_{bkg}, in the measured spectrum. Table 4.1 shows the masses and relative concentration of the low mass aqueous targets along with a sum of their calculated coefficients, α_{238} and α_{232}. Only one of the four mixed targets meet the constraint given by Equation 4.11. Thus, the decomposition routine must be altered to account for the inclusion of background.

To eliminate the restriction from Equation 4.11, the background is removed from the basis vectors, ϕ_{238} and ϕ_{232}, and appended to the end of the equation such that the measured spectrum becomes,

$$\phi_{meas.} = \alpha_{238}(\phi_{238} - \phi_{bkg}) + \alpha_{232}(\phi_{232} - \phi_{bkg}) + \phi_{bkg}, \tag{4.12}$$

with ϕ_{bkg} being the active background spectra of an H_2O target from Figure 4.16. Equation 4.12 satisfies the conditions derived from Equation 4.7. Utilizing Equation 4.12, the decoupling algorithm was used to deconvolve the measured spectra from the mixed targets containing the varied relative ^{238}U concentrations of 0, 73, 57.5, 39.4, 23.1 and 100%. The results of the modified decomposition routine are shown in Figure 4.17 and 4.18.

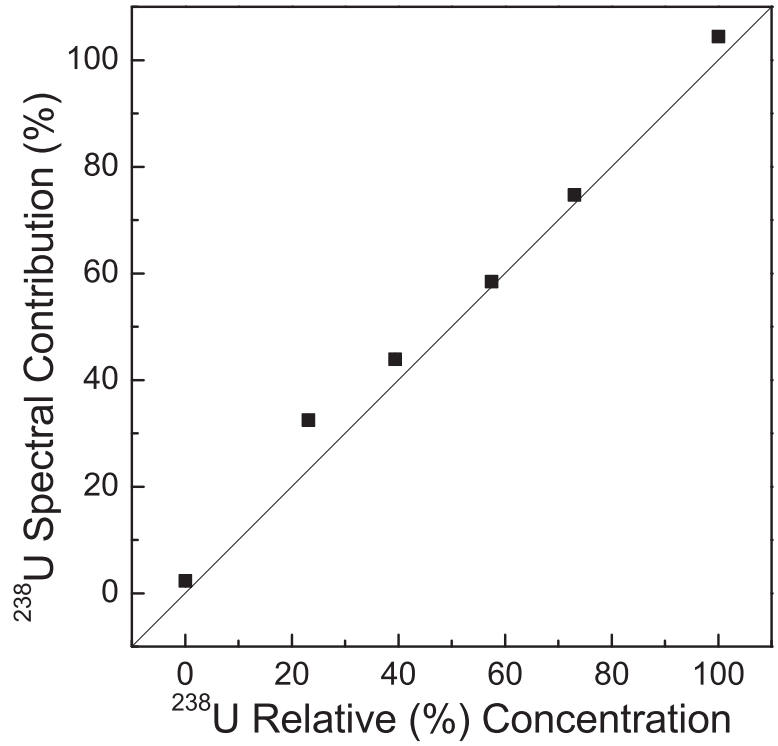

Figure 4.17: Relative spectral contribution from ^{238}U as a function of relative ^{238}U concentration in the target. A line is shown at equality between calculated and actual. Error bars are representative of 1σ standard deviation.

Figure 4.17 shows the relative spectral contribution as a function of relative concentration for ^{238}U. The modified decomposition routine shows significant improvement in accuracy compared to the previous SCA method. This method of measured spectra SCA also shows increased accuracy and precision over peak ratio analysis. Where peak ratio analysis had errors that averaged $\sim$ 15%, the errors from SCA are greatest at 0% relative ^{238}U concentration, an error of 0.2% relative ^{238}U concentration. These errors decrease to 0.1% at 100% relative ^{238}U concentration while maintaining little deviation from the line of equality. While the largest deviation from the line of equality is at a relative ^{238}U concentration of 23.1% and is 9.4% from the true value, the average deviation is less than 4% of the true relative ^{238}U concentration.

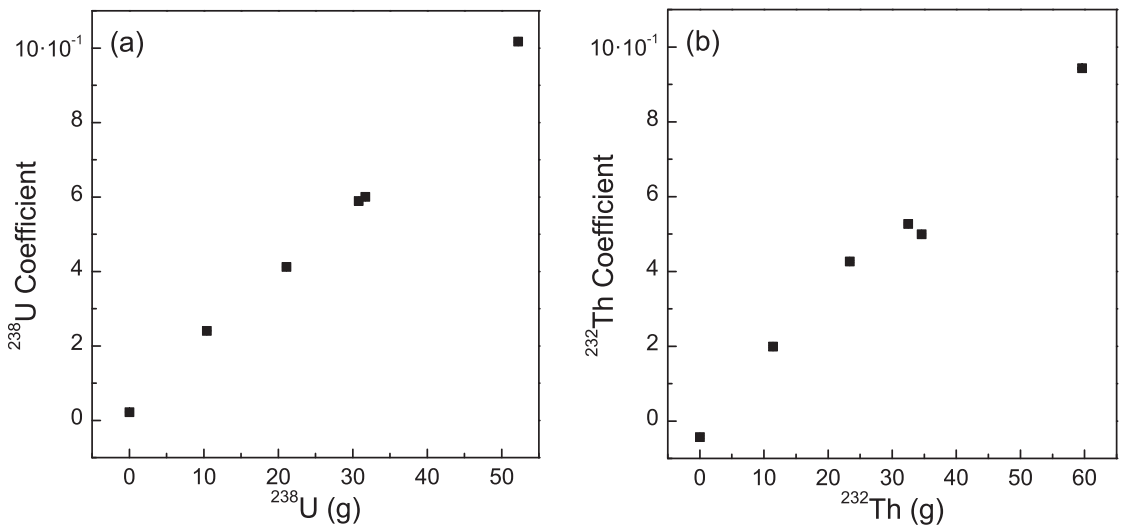

Figure 4.18: Normalized ^{238}U (a) and ^{232}Th (b) coefficients as a function of mass for spectral contribution analysis utilizing measured energy spectra from low mass ^{238}U and ^{232}Th as a basis set. Error bars in both graphs are representative of 1σ standard deviation.

Figure 4.18.(a) and Figure 4.18.(b) show the ^{238}U and ^{232}Th spectral coefficients from the modified SCA routine as a function of mass, respectively. Both the ^{238}U and ^{232}Th coefficient show a strong linear relationship with mass as compared to the prior method of SCA where background was included in the basis set. The only significant deviation from linearity appears in the ^{232}Th coefficient in Figure 4.18.(b). This deviation appears at a ^{232}Th mass of 34.6 g and a relative ^{238}U concentration of 23.1%. This deviation causes the relative ^{238}U concentration to be overestimated in Figure 4.17. This deviation may be due to miss-alignment of the target, inaccurate mixing of the target or changes in the accelerator beam. If the target was miss-aligned or the properties of the bremsstrahlung beam were altered during the experiment both the ^{238}U and the ^{232}Th coefficient would deviate from linearity. However, this sample did have a defect in the stainless steel canister causing the canister to fail shortly after these experiments. Because the targets consist of aqueous solutions of $UO_2(NO_3)_2$ and $Th(NO_3)_4$, the resulting nitric acid reacts with the defect in the stainless and can cause the ^{238}U or ^{232}Th to precipitate out, thus altering the concentration in the target. This or inaccurate mixing of the target are most likely the cause of the

deviation in the ^{232}Th coefficient.

4.4.2 Using Calculated Energy Spectra as a Basis Set

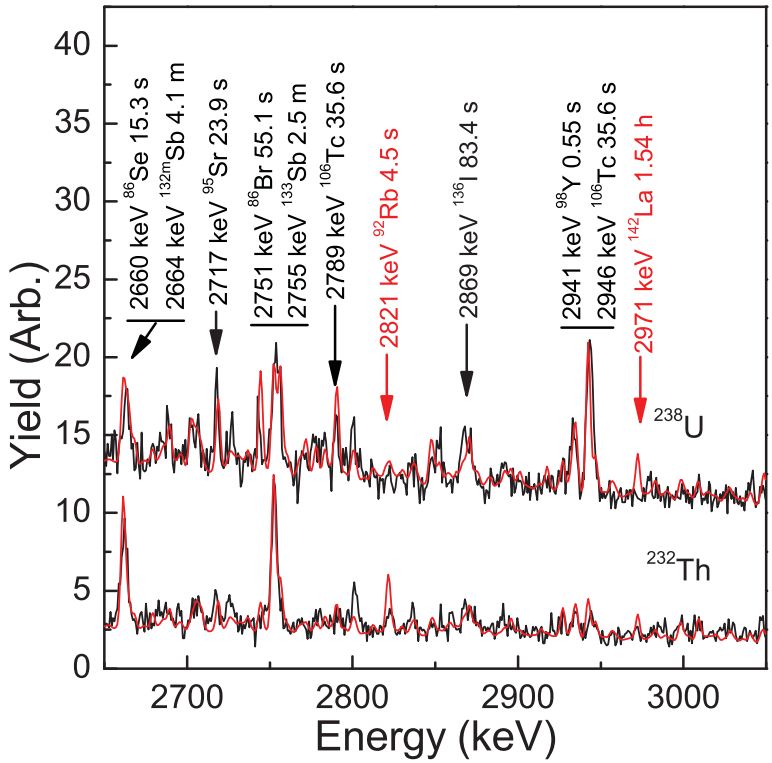

Figure 4.19: The predicted energy spectra overlaid on the respective energy spectra of low mass ^{238}U, 0.41 g·cm^{-2}, and ^{232}Th, 0.46 g·cm^{-2} in aqueous solution. Each spectrum was collected over a period of 2 h at 22 MeV and 15 Hz with the first 35 ms following the pulse removed. Notable discrete lines are labeled above. ^{92}Rb has been removed from ^{238}U calculated energy spectra to better match experimental data. Notable fission fragment contributors have been labeled with their respective energy and half-life.

Figure 4.19 shows the calculated energy spectra using high-energy neutron induced fission fragment distributions for ^{238}U and ^{232}Th overlaid with their respective experimental data for low mass targets of ^{238}U and ^{232}Th. Since ^{92}Rb is greatly over estimated in ^{238}U, it has been removed to better match experimental data. While discrepancies in both ^{238}U and ^{232}Th remain, none are as significant as the presence

of ^{92}Rb in the ^{238}U spectrum. This modified version of the calculated energy spectra for ^{238}U and ^{232}Th photofission from Sections 2.3 and 4.2 were then used as a basis set for the energy region of 2650 to 3050 keV. This basis set was then used to deconvolve the measured energy spectra from the low mass aqueous targets containing relative concentrations 100, 73, 57.5, 39.4, 23.1 and 0% ^{238}U into their base contributors.

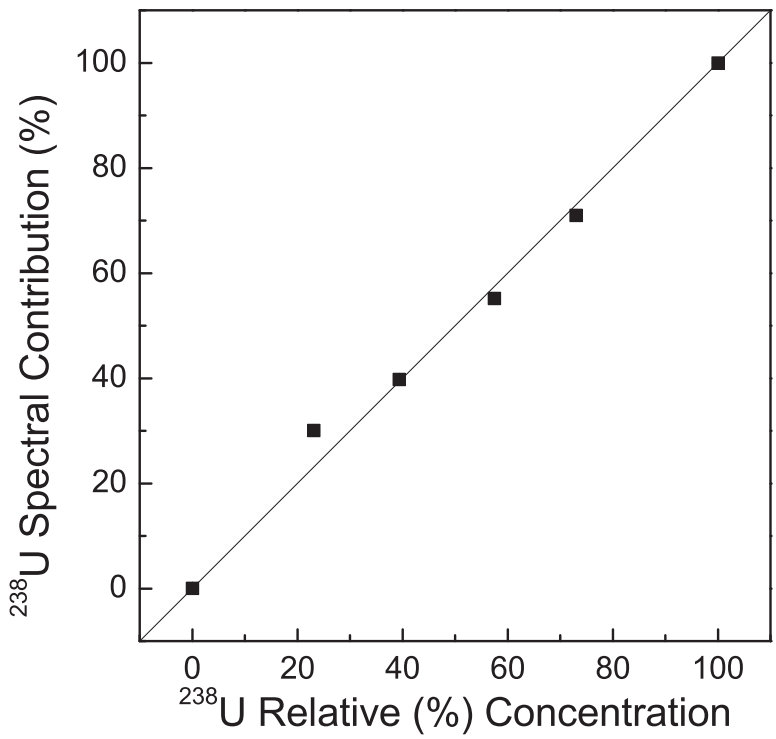

Figure 4.20: Relative ^{238}U spectral contribution as a function of relative ^{238}U concentration. Error bars indicate 1σ standard deviation.

Figure 4.20 shows the relative spectral contribution of ^{238}U as a function of its relative concentration. This shows significant increases in both precision and accuracy over peak ratio analysis as well as measured spectra SCA with the inclusion of background in the basis set. The data points lay close to the line of equality with little deviation and significantly smaller error bars than PRA. The errors from calculated spectra SCA are on the same order as those of measured spectra SCA with background separation, a value of less than 0.2% relative ^{238}U concentration. The deviation observed in measured spectra SCA with background separation is also present

in Figure 4.20. At relative ^{238}U concentration of 23.1%, the relative ^{238}U concentration is over predicted by 7%. The remaining data points, however, lay within 2.5% relative concentration of the actual value.

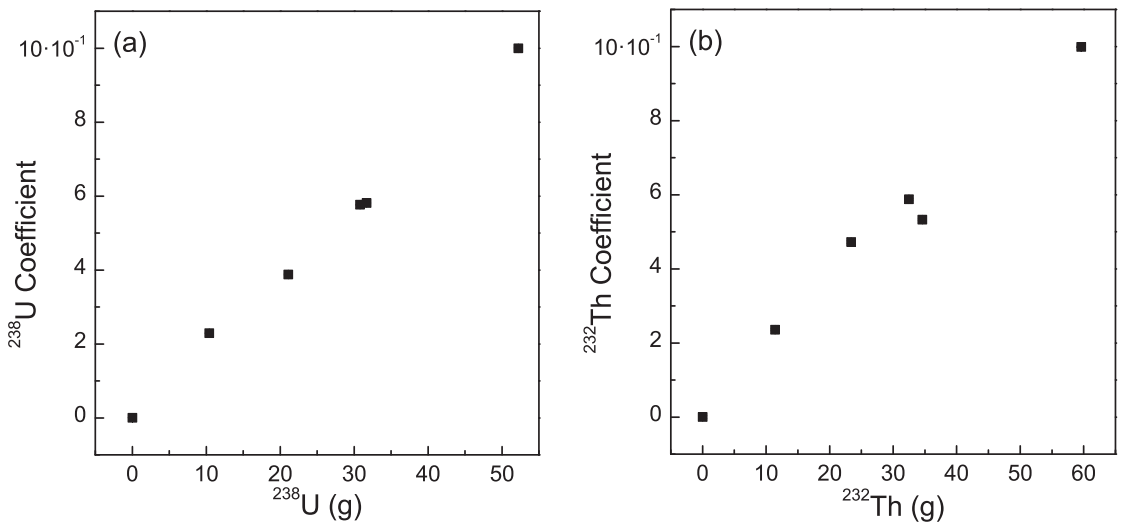

Figure 4.21: Normalized ^{238}U (a) and ^{232}Th (b) coefficients as a function of mass for spectral contribution analysis utilizing calculated energy spectra from low mass ^{238}U and ^{232}Th as a basis set. Error bars in both graphs are representative of 1σ standard deviation.

Figure 4.21.(a) and Figure 4.21.(b) show the ^{238}U and ^{232}Th coefficients as a function of mass, respectively. The linear nature of the coefficients gives rise to accurate measures of the respective ^{238}U and ^{232}Th concentrations. While the ^{238}U coefficient is very linear with respect to mass, Figure 4.21.(b) shows the same deviation of the ^{232}Th coefficient at 34.6 g of ^{232}Th and a relative ^{238}U concentration of 23.1% as previously seen in measured spectra SCA with background separation.

Figure 4.22 shows the results of spectral decomposition overlaid with the measured energy spectra. It is clear that the algorithm fails to reproduce the 2801 keV discrete line from background. This is do to the lack of a background in the decoupling routine. Since the basis set is a calculated energy spectra of only ^{238}U and ^{232}Th

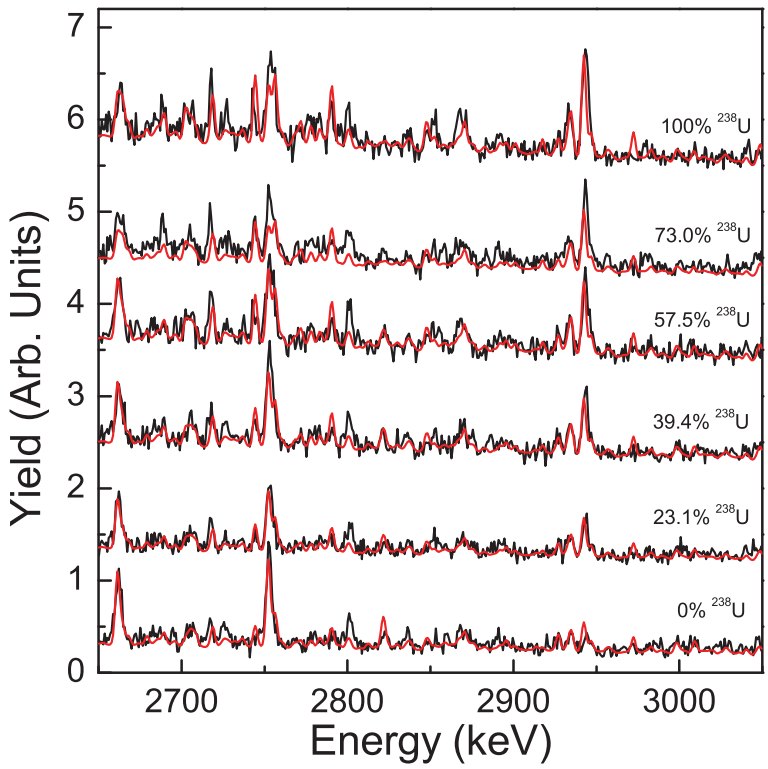

Figure 4.22: Energy spectrum obtained from the fitting algorithm utilizing calculated energy spectra as basis sets (red) overlaid on their respective energy spectra (black). Figures to the right indicate relative percent of ^{238}U present in the target.

fission, Equation 4.7 becomes,

$$\phi'_{meas.} + \phi_{bkg} = \alpha_{238}\phi'_{238} + \alpha_{232}\phi'_{232}, \tag{4.13}$$

where the $\phi'_{meas.}$, ϕ'_{238} and ϕ'_{232} are the fission portions of the energy spectrum and ϕ_{bkg} is the nonfissionable background contribution. To more accurately portray the fission spectrum contribution, ϕ_{bkg} should be removed from the measured spectra of the mixed targets or appended to the end of Equation 4.13 as was done in Equation 4.12 for measured spectra SCA with background separation. However, because the background spectrum is unique, it cannot be reproduced using ϕ'_{238} and ϕ'_{232}. Since the decomposition algorithm cannot reproduce the background, it is treated as an independent and uncalculated third component. In this manner, the background may not need to be considered because it is effectively ignored by the decomposition

routine.

Chapter 5

Conclusions

5.1 Summary/Findings

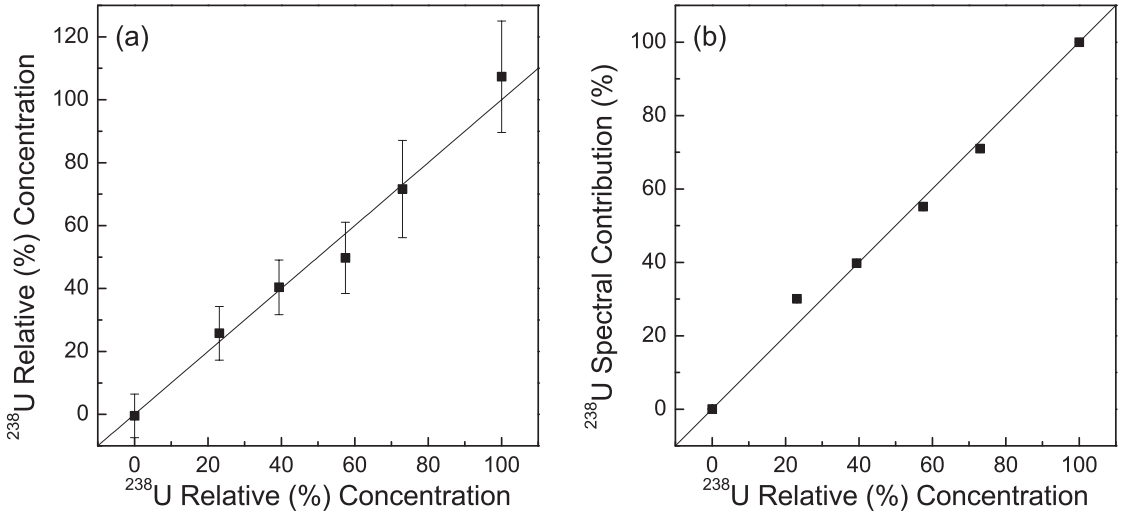

Figure 5.1: Comparison of peak ratio analysis (a) versus spectral contribution analysis (b) utilizing identical data sets.

Figure 5.1 shows a side-by-side comparison between peak ratio analysis (a) and calculated spectrum SCA (b). Since SCA spans an entire region without the need for isolating single peaks, the deconvolution routine provides a more accurate portrayal

of the relative concentration. In addition, the independence of the coefficients allows for the direct measurement of the mass of either ^{238}U or ^{232}Th. Since the coefficients are varied independently, unknown contributors are ignored and additional fissionable contributors can be easily introduced. For the addition of contributions from ^{235}U, ^{239}Pu, etc., a portion of the energy spectra can simply be calculated or measured for inclusion as a potential contributing basis spectrum and added to the equation,

$$\phi = \alpha_{238}\phi_{238} + \alpha_{232}\phi_{232} + \alpha_{235}\phi_{235} + \alpha_{239}\phi_{239} + ... \tag{5.1}$$

The spectral contribution can then be related to the relative concentration of ^{235}U or ^{239}Pu in the target by comparing the coefficients.

5.2 Applications and Future Work

This method proves effective for low mass targets in nonfissionable, low density matrices. Further investigation is needed in to the effect of higher masses of fissionable material. With light mass targets, the spectral contribution from any given isotope can be assumed to be linear with respect to mass. This is not the case with larger mass targets due to self absorption and attenuation within the target. In contrast to the targets investigated here, nuclear weapons require bulk material on the order of several kilograms. However, this method may still be effective for isotopic analysis by investigating the surface of bulk targets provided the target is uniform in concentration.

This method may also be applied to find the fission fragment mass distribution from photofission. Methods for measuring the mass distribution often employ transfer media to move fission fragments from the fission source to a series of detectors. This transfer media does not allow for the transfer of noble gases and can very well miss a significant portion of fission fragments. Utilizing this method, it may be possible to measure the discrete γ-rays of fission fragments to determine a photofission fragment mass distribution between irradiating bremsstrahlung pulses. This allows for the measurement of all contributing fission fragments in situ without the need for transfer media. By the same fitting and prediction methods employed in this thesis, it may be

possible to identify spectral contributions from fission fragments across multiple peaks by creating a basis set from the energy spectra of fission fragments. The normalized coefficients of such a fit would result in those fission fragment's cumulative yield.

Further investigation is planned for this analysis method utilizing multiple components for either the measurement of individual fission fragment yields of a single fissionable isotope or the contributions of multiple fissionable materials such as mixtures containing ^{238}U, ^{239}Pu and ^{235}U. To utilize the full potential of SCA across multiple contributors it may be advantageous to employ the Kullback-Leibler divergence. This divergence allows for a measure of the difference between two probability distributions. The equation,

$$D_{KL}(\phi, \phi_{^{238}U}) = \sum_i \phi(i) \log \frac{\phi(i)}{\phi_{^{238}U}(i)}, \tag{5.2}$$

and the equation,

$$D_{KL}(\phi, \phi_{^{232}Th}) = \sum_i \phi(i) \log \frac{\phi(i)}{\phi_{^{232}Th}(i)}, \tag{5.3}$$

are the Kullback-Leibler equations for divergence between a measured spectra or an unknown (ϕ) and the calculated or measured spectra of ^{238}U and ^{232}Th [22]. It is clear from the equations that if the spectrum S is identical to the ^{238}U or ^{232}Th spectra that the divergence is equal to zero and grows as S diverges from either ^{238}U or ^{232}Th. All that is left is to correlate this divergence to a measure of the concentration of ^{238}U and ^{232}Th. This method of measuring a component's contribution to an energy spectrum is independent of other components' contributions and readily allows for the introduction and independent measurement of additional components.

Appendix A

A Note on Calculated Spectra

Due to an issue in generating the calculated energy spectra for ^{238}U and ^{232}Th, the fission fragment ^{136}Te was, for an unknown reason, not included in the calculated spectra for ^{238}U or ^{232}Th. ^{136}Te has a half-life of 17.5 s and a significant peak intensity at 3235 keV [3]. Figure A.1 shows a region of the calculated spectra overlaid on the measured spectra of ^{238}U and ^{232}Th, respectively. The position of where the 3235 keV peak from ^{136}Te should appear is indicated. In relation to the intensity of the 3401 keV line from ^{97}Y in the predicted ^{238}U spectrum, the peak intensity of the 3235 keV peak from ^{136}Te should be a third this in the predicted ^{238}U spectrum and half of this in ^{232}Th. It is interesting to note, however, that it does not appear in the measured spectra of either ^{238}U or ^{232}Th.

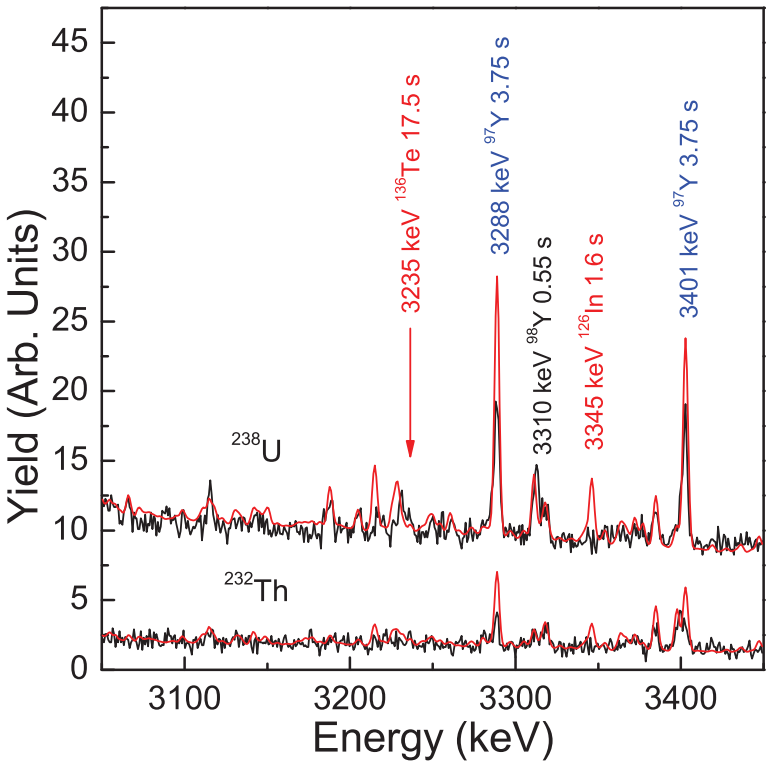

Figure A.1: Energy spectra of ^{238}U, 0.41 g·cm^{-2}, ^{232}Th, 0.46 g·cm^{-2}, low mass aqueous samples collected at 22 MeV and 15 Hz overlaid with the calculated energy spectra from high energy neutron induced fission on ^{238}U and ^{232}Th, respectively. The measured spectra were collected over a period of 2 h and are normalized to total charge on radiator. ^{238}U spectra are shown with an arbitrary offset to accentuate differences between spectra. The position of where the 3235 keV peak from ^{136}Te should appear is indicated

Bibliography

[1] W. Bertozzi, J. A. Caggiano, W. K. Hensley, M. S. Johnson, S. E. Korbly, R. J. Ledoux, D. P. McNabb, and E. B. Norman. Nuclear resonance fluorescence excitation near 2 mev in ^{238}U and ^{239}Pu. *Phys. Rev. C*, 78:041601, 2008.

[2] W. Bertozzi, S. E. Korbly, R. J. Ledoux, and W. Park. Nuclear resonance fluorescence and effective z determination applied to detection and imaging of special nuclear material, explosives, toxic substances and contraband. *Nucl. Instrum. Methods Phys. Res. B*, 261:331, 2007.

[3] M. R. Bhat. Evaluated nuclear structure data file (endf). *Nucl. Data for Sci. and Tech.*, page 817, 1992. Data extracted using the NNDC On-Line Data Service from the ENSDF database, file revised as of 7/22/2009.

[4] Niels Bohr and John Archibald Wheeler. The mechanism of nuclear fission. *Phys. Rev.*, 56(5):426, 1939.

[5] M. C. Brady and T. R. England. Delayed neutron data and group parameters for 43 fissioning systems. *Nucl. Sci. Eng.*, 103:129, 1989.

[6] F. Carrel, M. Agelou, M. Gmar, Lainé, J. Loridon, J. Ma, C. Passard, and B. Poumaréde. Identification and differentiation of actinides inside nuclear waste packages by measurement of delayed gammas. *IEEE Trans. Nucl. Sci.*, 57:2862, 2010.

[7] F. Carrel, M. Gmar, F. Lainé, J. Loridon, J. L. Ma, and C. Passard. Identification of actinides inside nuclear wast packages by measurement of fission delayed gam-

mas. In *Nuclear Science Symposium Conference Record, 2006. IEEE*, volume 2, page 909, Piscataway, New Jersey, 2006. IEEE.

[8] M.B. Chadwick, P. Obložinský, M. Herman, et al. ENDF/B-VII.0: Next generation evaluated nuclear data library for nuclear science and technology. *Nuclear Data Sheets*, 107(12):2931, 2006.

[9] T. R. England and B. F. Rider. Endf-349 evaluation and compilation of fission product yields 1993. Technical Report LA-UR-94-3106, Los Alamos Nationatial Laboratory, Los Alamos New Mexico, USA, 1994.

[10] P. C. Fisher and L. B. Engle. Delayed gammas from Fast-Neutron fission of th^{232}, U^{233}, U^{235}, U^{238}, and Pu^{239}. *Phys. Rev.*, 134:B796, 1964.

[11] D. De Frenne, H. Thiernes, E. Jacobs, P. De Gelder, A. De Clercq, P. D'hondt, and A. J. Deruytter. Charge distribution for the photofission of ˘ with 20 mev bremsstrahlung. *Phys. Rev. C*, 21:629, 1980.

[12] M. Gmar, E. Berthoumieux, S. Boyer, F. Carrel, D. Doré, M. L. Giacri, F. Lainé, B. Poumarède, D. Ridikas, and A. V. Lauwe. Detection of nuclear material by photon activation inside cargo containers. In G. Vourvopoulos and F. P. Doty, editors, *Non-Intrusive Inspection Technologies*, volume 6213 of *Proc. of SPIE*, page 62130F, Bellingham WA, USA, 2006. SPIE.

[13] Tsahi Gozani. Active nondestructive assay of nuclear materials. Technical Report NUREG/CR-0602, United States Regulatory Commission, 1981.

[14] O. Hahn and F. Strassmann. *Naturwissenschaften*, 27:11, 1939.

[15] M. F. James. Energy released in fission. *J. Nucl. Energy*, 23:517, 1969.

[16] M. F. James. The useful energy released in the fission of ^{232}Th, ^{233}U, ^{234}U, ^{236}U, ^{237}Np, ^{238}Pu, ^{240}Pu and ^{242}Pu. *J. Nucl. Energy*, 25:513, 1971.

[17] G. Janssens-Maenhout, F. De Roo, and W. Janssens. Contributing to shipping container security: can passive sensors bring a solution? *J. of Environ. Radioactivity*, 101:95, 2010.

[18] J. L. Jones, B. W. Blackburn, D. R. Norman, S. M. Watson, K. J. Haskell, J. T. Johnson, A. W. Hunt, F. Harmon, and C. Moss. Statue of the prototype pulsed photonuclear assessment (ppa) inspection system. *Nucl. Instrum. Methods Phys. Res. A*, 579:353, 2007.

[19] K. A. Jordan, T. Gozani, and J. Vujic. Differential die-away analysis system response modeling and detector design. *Nucl. Instrum. Methods Phys. Res. A*, 589:436, 2008.

[20] M. T. Kinlaw. *Delayed Neutron Group Parameters From Photofission*. PhD thesis, Idaho State University, December 2007.

[21] Glenn F. Knoll. *Radiation Detection and Measurement*. John Wiley and Sons, Inc., New York, third edition, 2000.

[22] S. Kullback and R. A. Leibler. On information and sufficiency. *The Annals of Math. Stat.*, 22:79, 1951.

[23] L. Meitner and O. R. Frisch. *Nature*, 143:239, 1939.

[24] B. J. Micklich and D. L. Smith. Nuclear materials detection using high-energy γ-rays. *Nucl. Instrum. Methods Phys. Res. B*, 241:782, 2005.

[25] K.J. Moody, I.D. Hutcheon, and P.M. Grant. *Nuclear Forensic Analysis*. Taylor & Francis Group, LLC, Boca Raton, FL, 2005.

[26] J. A. Mullens, J. S. Neal, P. A. Hausladen, S. A. Pozzi, and J. T. Mihalczo. Fast coincidence counting with active inspection systems. *Nucl. Instrum. Methods Phys. Res. B*, 241:804, 2005.

[27] T. Newton Nathaniel, K. Sudarshan, A. Goswami, and A. V. R. Reddy. Non-destructive assay technique for the determination of ^{238}U/^{232}Th ratio in

the mixed oxides of uranium and thorium using prompt gamma-ray neutron activation. *J. of Radioanalytical and Nucl. Chem.*, 279:481, 2009.

[28] E. B. Norman, S. G. Prussin, R. M. Larimer, H. Shugart, E. Browne, A. R. Smith, R. J. McDonald, H. Nitsche, P. Gupta, M. I. Frank, and T. B. Gosnell. Signatures of fissile materials: high-energy γ rays following fission. *Nucl. Instrum. Methods Phys. Res. A*, 521:608, 2004.

[29] William H. Press, Saul A. Teukolsky, William T. Vetterling, and Brian P. Flannery. *Numerical Recipes in C: The Art of Scientific Computing. Second Edition.* 1992.

[30] E. T. E. Reedy, S. J. Thompson, and A. W. Hunt. The detection of delayed γ-rays between intense bremsstrahlung pulses for discriminating fissionable from non-fissionable materials. *Nucl. Instrum. Methods Phys. Res. A*, 606:811, 2009.

[31] D. R. Slaughter, M. R. Accatino, A. Bernstein, P. Biltoft, J. A. Church, M. A. Descalle, J. M. Hall, D. R. Manatt, G. J. Mauger, T. L. Moore, E. B. Norman, D. C. Peterson, J. A. Pruet, and S. G. Prussin. The nuclear car wash: A system to detect nuclear weapons in comercial cargo shipments. *Nucl. Instrum. Methods Phys. Res. A*, 579:349, 2007.

[32] S. J. Thompson, M. T. Kinlaw, J. F. Harmon, D. P. Wells, E. B. Farfan, and A. W. Hunt. Utilization of high-energy neutrons for the detection of fissionable materials. *Appl. Phys. Lett.*, 90:074106, 2007.

[33] R. J. Tuttle. Delayed-Neutron data for Reactor-Physics analysis. *Nucl. Sci. Eng.*, 56:37, 1975.

[34] T. Uckan, J. March-Leuba, C. R. Brittain, D. Powell, J. Benton, and D. Meyers. The role of blend down monitoring system fissile mass flow monitors for the heu transparency program in russia. Technical Report ORNL/TM-2006/99, Oak Ridge National Laboratory, Oak Ridge Tennessee, USA, 2006.

[35] R. B. Walton, R. E. Sund, E. Haddad, and J. C. Young. Delayed gamma rays from photofission of U^{238}, U^{235}, and Th^{232}. *Phys. Rev.*, 134:B824, 1964.

[36] D. K. Wehe, H. Yang, and M. H. Jones. Observation of ^{238}U photofission products. *IEEE Trans. Nucl. Sci.*, 53:1430, 2006.

[37] S. S. M. Wong. *Introductory Nuclear Physics*. John Wiley and Sons, Inc., New York, second edition, 1998.

Appendix C

A M.S. Thesis by Edna S. Cardenas

Detection of Delayed Gamma Rays using $Bi_4Ge_3O_{12}$ and NaI(Tl) Detectors for the Identification of Fissionable Materials

In presenting this thesis in partial fulfillment of the requirements for an advanced degree at Idaho State University, I agree that the Library shall make it freely available for inspection. I further state that permission for extensive copying of my theses for scholarly purposes may be granted by the Dean of Graduate Studies, Dean of my academic division, or by the University Librarian. It is understood that any copying or publication of this thesis for financial gain shall not be allowed without my written permission.

Signature _____

Date _____

Detection of Delayed Gamma Rays using $Bi_4Ge_3O_{12}$ and NaI(Tl) Detectors for the Identification of Fissionable Materials

by
Edna Cárdenas

A thesis
submitted in partial fulfillment
of the requirements for the degree of
Master of Science in the
Department of Physics

Idaho State University

November 2009

©2009 - Edna Cárdenas

All rights reserved.

To the Graduate Faculty:

The members of the committee appointed to examine the thesis of Edna Cárdenas find it satisfactory and recommend that it be accepted.

Major Advisor

Committee Member

Graduate Faculty Representative

Acknowledgments

I would like to express my gratitude to Edward Reedy, Heather Seipel and Dr. Bruce Failor whose help with experiments and discussions of physics have been immeasurable. I appreciate all the hard work and patience from the operators at the Idaho Accelerator Center. I am grateful for the help I have received from Anna Hoskins and Mathew Kinlaw. I am also thankful to my committee members Dr. Tony Forest and Dr. Andrew Holland and I would especially like to thank my adviser Dr. Alan Hunt whose dedication to the research and his students can not be surpassed.

I would like to acknowledge and thank my family and Fil for always believing in me and for all their support. And finally, I would very much like to thank Dr. Daniel Finley and Dr. Stephen Howell who have mentored me and have continually supported my pursuit of physics.

Contents

1 Introduction **1**
1.1 Historical Background 1
1.2 Delayed γ-ray Detection 3

2 Theory **8**
2.1 Theory of Fission 8
2.1.1 Liquid Drop Model 8
2.1.2 Shell Model 9
2.1.3 Energy from Fission 12
2.2 Inducing Fission 13
2.2.1 Bremsstrahlung 13
2.2.2 Fission Cross Sections 15
2.2.3 Other Nuclear Reactions 18
2.3 Detection and Crystal Scintillation Detectors 19
2.3.1 The Photoelectric Effect, Compton Scattering, & Pair Production 21
2.3.2 Photocathode and Photomultiplier Tube 26
2.3.3 Energy Resolution and Efficiency 27
2.4 Decision Levels & Minimum Detectable Mass 29

3 Experimental Setup **36**
3.1 Arrangement of Detectors and Target 36
3.2 Electronic Circuitry and Time Structure 39
3.3 Targets 42
3.4 Efficiency and Energy Resolution 43

4 Experimental Results **46**
4.1 Development of a Unique Signature for Fission 46

4.2 Yield 55
4.2.1 NaI(Tl) Crystal Activation 56
4.3 Background Subtracted Yield 60
4.4 Yield as a Function of Dose 64
4.5 Minimum Detectable Mass 70
4.6 Energy Cut Revisited 71
4.7 MDM, Delayed Neutrons vs. Delayed γ-Rays 74
4.8 Filtering Out γ-Rays 79
4.9 BGO Detector Shielding 81

5 Conclusions and Future Work 89
5.1 Conclusions 89
5.2 Future Work 91

A Neutron Capture Cross Sections 93

B Photonuclear Cross Sections 96

List of Figures

1.1 Energy spectra for ^{238}U. The curve labeled PNDA indicates a passive inspection while the target in the ANDA curve was irradiated using bremsstrahlung photons with an endpoint energy of 14.5 MeV. 4
1.2 ANDA energy spectra for ^{238}U, Pb and ^{9}Be. All targets emit γ-rays with energies throughout the energy range. 5
1.3 ANDA energy spectra for ^{238}U, Pb and ^{9}Be. By removing γ-rays with energies below 2.5 MeV and those that are emitted before $\sim$ 13 ms, ^{238}U can be distinguished from both Pb and ^{9}Be. 6
1.4 High-energy γ-ray yield versus bremsstrahlung endpoint energy using a $\sim$ 13 ms time cut for ^{238}U (■), Pb (▲), Fe (◀) and Be(▼). 7

2.1 Plot of Mass Distribution. 10
2.2 Electron path for bremsstrahlung photons. 14
2.3 Bremsstrahlung Photon Energy 15
2.4 Photofission Cross Sections 16
2.5 Neutron Induced Fission Cross Sections 17
2.6 Scintillation Process 20
2.7 Energy Peaks 24
2.8 Energy Peaks 25
2.9 Schematic of MDM Decision Levels and Risk Assessments. . . 31

3.1 Top view of the detector array and target in relation to the bremsstrahlung beam. 37
3.2 Front view of the detector array with two BGO and two NaI(Tl) detectors. Each detector type was located diagonally from one another. 38

3.3 Photo of the detector array which is shielded with 10.16 cm of lead. 39
3.4 The electronic circuit for the detectors is depicted in (a) while (b) shows the charge circuit. 41
3.5 Time structure of the accelerator beam. 42

4.1 Photon energy spectra for ^{238}U. In the active inspection the bremsstrahlung beam endpoint energy was 13 MeV and ran at a 15 Hz repetition rate. The average electron charge per pulse was $\sim$ 88 nC. The run time was $\sim$ 601 s while that for the passive inspection was $\sim$ 43910 s. 47
4.2 Photon energy spectra for ^{238}U and Pb. The targets were irradiated for 10 minutes with an average charge of 140 nC, a bremsstrahlung endpoint energy of 16 MeV and a 15 Hz repetition rate. The Uranium target has a yield 10 times larger on average than lead for energies above 3 MeV. 48
4.3 High-energy photon yield versus time for Pb (•) and ^{238}U (■). Both targets were irradiated for $\sim$10 minutes with an average charge of 140 nC, a bremsstrahlung beam endpoint energy of 16 MeV, and a 15 Hz repetition rate. The yield drops off for Pb after $\sim$ 22 ms. The error bars are similar in size to that of the symbols for the ^{238}U target. 50
4.4 The measured data in (a) is taken from a Pb target. The bremsstrahlung beam endpoint energy was 16 MeV. The accelerator ran at a 15 Hz repetition rate and a radiation time of $\sim$ 601 s. The MCNPX predicted data in (b) had a tally run time of 40 ms. The initial as well as ending data points were removed from the data to isolate neutron reactions from signal noise and yield from the active background. 51
4.5 Measure data is presented in (a) while results from the MCNPX simulated data is shown in (b). A linear fit is applied to the number of events detected depicted in (a) and the number of particles tallied in (b) and these are graphed as a function of time. The line represents a linear fit of the data. 52
4.6 Time cut energy spectra for Pb and ^{238}U. The yield for Pb remains largely under an energy of 3 MeV. 53

4.7 High-energy photon yield versus time for Pb (★), ^{9}Be (•), deionized H_2O (▲), and Al (◄) and for ^{238}U (■) and ^{232}Th (♦). All targets were irradiated for ∼10 minutes with an average charge of 140 nC. The accelerator operated at an energy of 16 MeV and at a 15 Hz repetition rate. The yield for the non-fissionable materials fall off in ∼ 22 ms. 54
4.8 Charge normalized yield calculated using both the high-energy and time cuts. Data from the BGO detectors are symbolized as ^{238}U (■) and Pb (▼) while ^{238}U (♦) and Pb (★) represent the NaI(Tl) detectors. The average charge over all energies was 124 nC, the accelerator operated at a 15 Hz repetition rate and the targets were irradiated for ∼ 10 minutes. 56
4.9 Energy spectrum for the 20 minute decay of a Pb brick target. The bremsstrahlung endpoint energy was 22 MeV and the accelerator operated at a 15 Hz repetition rate. The average charge on the radiator was 216 nC. At low energies the graph shows a β^- spectrum which inflates the γ-ray counts for the NaI(Tl) detector while the spectrum for the BGO detector shows the natural background. 57
4.10 An energy spectrum for NaI(Tl) crystal recorded by HPGe detector. The energy spectrum shows peaks for ^{128}I and ^{24}Na. The crystal is being activated by neutron capture reactions. . 59
4.11 Data for the BGO detectors are symbolized as ^{238}U (■) and Pb (▼) while ^{238}U (♦) and Pb (★) represent the NaI(Tl) detectors. The average charge over all energies was 124 nC, the accelerator operated at a 15 Hz repetition rate and the targets were irradiated for ∼ 10 minutes. 61
4.12 The data points show the dose normalized to the charge on the radiator as a function of the bremsstrahlung energy. The line is a fit of the data fixed to a cubed energy. 64
4.13 The passive background subtracted yield normalized to dose as a function of energy. Data from the BGO detectors are symbolized as ^{238}U (■) and Pb (▼) while ^{238}U (♦) and Pb (★) represent the NaI(Tl) detectors. 66
4.14 Charge normalized yield for (a) BGO detectors and (b) NaI(Tl) detectors for the non-fissionable targets ^{9}Be (►), Al (★) and Pb (▼). Both graphs compare the yield with ^{238}U. 67

4.15 Cross section for the ^{9}Be(γ,p)^{8}Li reaction. The cross section increases significantly at $\sim$ 17 MeV [15]. 68
4.16 Charge normalized yield for (a) BGO detectors and (b) NaI(Tl) detectors for ^{232}Th (•). Both graphs compare the yield with ^{238}U (■) and Pb (▼). 69
4.17 The minimum detectable mass using deionized water as the active background for the BGO detectors (■) and NaI(Tl) detectors (▼). The MDM is calculated using the a 4.7 % ^{238}U in deionized water. 71
4.18 Yield versus energy cut showing the 4.7 % ^{238}U in deionized water target for the BGO detectors. The bremsstrahlung energy values are represented with a ■, •, ▲, ★, and a ◄ for energies of 10, 13, 16, 19 and 22 MeV respectively. 73
4.19 The MDM versus energy cut for the BGO detectors using 4.7 % ^{238}U in deionized water target. The bremsstrahlung energy values are represented with a ■, •, ▲, ★, and a ◄ for energies of 10, 13, 16, 19 and 22 MeV respectively. 74
4.20 The yield versus energy cut for the NaI(Tl) detectors showing the 4.7 % ^{238}U in deionized water target. The bremsstrahlung energy values are represented with a ■, •, ▲, ★, and a ◄ for energies of 10, 13, 16, 19 and 22 MeV respectively. 75
4.21 The MDM versus energy cut for the NaI(Tl) detectors using the 4.7 % ^{238}U in deionized water target. The bremsstrahlung energy values are represented with a ■, •, ▲, ★, and a ◄ for energies of 10, 13, 16, 19 and 22 MeV respectively. 76
4.22 Location of PNDs in relation to γ-ray detector array. The PND's are located $\sim$ 0.6 m from the target. 77
4.23 Minimum detectable masses versus energy for delayed neutrons (•) and delayed γ-rays (■) using the PNDs and BGO detectors respectively. 78
4.24 Cross section for the ^{18}O(γ,p)^{17}N reaction [32]. 79
4.25 Yield versus time. Data was collected where lead filters were placed directly in front of the BGO detectors. The thickness used were 0 cm (black), 0.32 cm (red), 0.95 cm (green) and 2.54 cm (blue). 80
4.26 MDM for various Pb filter thicknesses. 81
4.27 Compton scattering and photoelectric absorption cross sections for lead. 83

4.28 Cross sections showing the (n,γ) reactions for ^{10}B (|) and ^{11}B($\cdots$). 83
4.29 High-energy yield for the Pb (■) and ^{238}U targets (•). The targets were irradiated for 10 minutes while the accelerator operated with a bremsstrahlung endpoint energy of 19 MeV and a 15 Hz repetition rate. For all three shielding arrangements presented no material was placed on the front surface of the detectors. 84
4.30 The neutron capture cross section for ^{114}Cd shows a large cross section for thermal neutrons. 85
4.31 High-energy yield for the Pb (■) and ^{238}U targets (•). The targets were irradiated for 10 minutes while the accelerator operated with a bremsstrahlung endpoint energy of 19 MeV and a 15 Hz repetition rate. The three arrangements included detector front face shielding labeled with an 'f' in parenthesis and side shielding labeled with an 's'. 86
4.32 MDM as a function of shielding arrangement. None of the arrangements presented include front face shielding. 87
4.33 MDM as a function of shielding arrangement. All arrangements presented include front face shielding. Arrangement 1 includes 5.08 cm of Pb on the sides, and 10.16 cm of borated polyethylene was placed outside of the Pb shielding around all surfaces of the detector including the front. Arrangement 2 had 5.08 cm of Pb on the sides and included a 0.64 cm thick Pb sheet which was placed on the front surface closest to the detectors with the 10.16 cm of borated polyethylene covering the Pb. Arrangement 3 was similar to arrangement 2 only it included a 0.16 cm thick sheet of cadmium in between the Pb and borated polyethylene. 88

A.1 Neutron Capture Cross Sections for ^{56}Fe. 93
A.2 Neutron Capture Cross Sections for ^{10}B. 94
A.3 Neutron Capture Cross Sections for ^{1}H. 94
A.4 Neutron Capture Cross Sections for ^{208}Pb. 95

B.1 Photonuclear Cross Sections for ^{9}Be. The cross section is for (γ,n) reactions [26]. 96

List of Tables

3.1 Target masses are listed in kilograms. The mass listed for the ^{238}U target is for 3 plates each having a mass of 1.3 kg. Deionized water is abbreviated and listed as DI. The mass value listed for 4.7 % ^{238}U in DI H_2O is only for the ^{238}U. . . . 43
3.2 Efficiency measurements for BGO and NaI(Tl) detectors. The source was set a distance of 25.4 cm from the detectors allowing it to be treated as a point. The full-energy peak efficiency values are standard values for a 1.5″ diameter by 1.5″ thick crystal and are comparable to the measured intrinsic efficiency results. 44
3.3 Energy resolution measurements for BGO and NaI(Tl) detectors. Greater energy resolution corresponds to smaller values. The standard resolution in the third column was collected by a 1.5″ diameter by 1.5″ thick detector crystal [29]. 45

4.1 Background subtracted yield with error for Pb target collected from the BGO detector. 63
4.2 MDM Calculated with the Observed Signal 71

Abstract

The recent need to accurately identify fissionable materials for nuclear nonproliferation purposes and for maintaining national security has led to an increased effort in the development of nondestructive detection techniques. One method in the development of this technology is by detecting β^- delayed γ-rays. In the experiments presented, photoinduced β^- delayed γ-rays were measured and serve as a means of distinguishing fissionable from nonfissionable materials. Targets were irradiated with bremsstrahlung photons at endpoint energies of 7 to 22 MeV in 3 MeV increments. Photon emission spectra for ^{238}U, 4.7 % ^{238}U in deionized H_2O, ^{232}Th, Pb, Al and ^{9}Be were recorded using $Bi_4Ge_3O_{12}$ and NaI(Tl) detectors. While a unique signature for fission was found by both detector types, results from the $Bi_4Ge_3O_{12}$ detector gave higher yields and lower minimum detectable masses leading to a more reliable signature for fission.

Chapter 1

Introduction

1.1 Historical Background

As described by Gozani, detection of nuclear materials was most notably initiated as a means to safeguard nations from the theft and dispersion of those nuclear materials and for quality control [1]. To deter against theft, government agencies required fuel processing/reprocessing centers to account for nuclear materials not only added in the processing cycle but also the material in scrap, waste, and residue left in the processing equipment. Detectors have also been positioned at entry and exit points to stymie potential pathways of theft. To account for nuclear materials, a variety of detection techniques have been utilized including implementing them at shipping and receiving centers to confirm shipping quantities. Detection devices have not only been used to deter and account for theft, but have also be used as a

means of process and quality control in nuclear processing plants.

In recent years, a need has emerged to develop detection devices to analyze the contents of maritime shipping containers. Attention has centered on securing ports of entry against the smuggling and transfer of dangerous nuclear or fissionable materials [2]. Of the U. S. imports, over 90% arrive by sea in ocean shipping containers each container having a carrying capacity of ~ 30 tons and prior to the turn of the 20th century only 2% of these ocean containers were being inspected [3, 2]. In 2003, the Container Security group formulated a plan on ways to prevent the transport of nuclear materials [4]. As a means of prevention, the plan included utilizing detectors as a method to deter entry of nuclear materials into the country. Currently, several national and international agencies are interested in enhancing detection capabilities not only in an aim for the nonproliferation of illicit nuclear materials but also to increase fundamental understandings in nuclear science as a means to combat weapons of mass destruction (WMD). As a result of such efforts, new techniques have been developed in the nondestructive detection of concealed fissionable materials.

Nuclear materials are generally detected by the products of their fission events, most commonly the resulting neutrons and γ-rays. In general, there are two types of nondestructive assay (NDA) or detection: passive (PNDA) and active (ANDA). In PNDA, spontaneous reactions are detected while in ANDA the reactions are induced by probing radiation and the secondary emissions are ultimately detected. PNDA is used when the intensity of γ-rays

or neutrons are sufficient enough to detect usually in no or low shielding situations and when the quantity of material present is substantial. PNDA is also employed when the probing radiation utilized in ANDA can not be permitted; for example when passengers would receive high doses of radiation. ANDA is used when the inspection is limited by time because it stimulates the fission events and when the quantity of material is small.

1.2 Delayed γ-ray Detection

A signature indicating the presence of fissionable materials can be developed by detecting the delayed γ-rays which are emitted following the β^- decay of fission events. To begin to develop a signature for fission, γ-rays can be detected both passively (PNDA) and actively (ANDA). Figure 1.1 compares the γ-ray energy spectra of a ^{238}U fissionable target using PNDA and ANDA. The following data presented was collected with a high purity germanium detector (HPGe) by E.T.E. Reedy *et al.* [31]. In the figure, the spectrum labeled PNDA was obtained before irradiation and that labeled ANDA was recorded between bremsstrahlung pulses with an endpoint energy of 14.5 MeV. The ANDA spectrum shows a significant amount of γ-rays with energy above 2.5 MeV while the PNDA spectrum does not. Because ANDA uses probing radiation to induce fission reactions, γ-rays with energies higher than 2.5 MeV are seen sooner in the collection process than if the reactions were spontaneous. To examine the hypothesis further, non-fissionable targets were

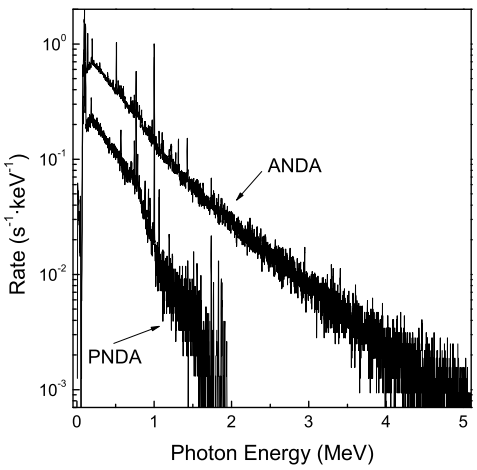

Figure 1.1: Energy spectra for ^{238}U. The curve labeled PNDA indicates a passive inspection while the target in the ANDA curve was irradiated using bremsstrahlung photons with an endpoint energy of 14.5 MeV.

analyzed. Figure 1.2 presents ANDA data for non-fissionable targets, Pb and ^{9}Be and for the ^{238}U fissionable target. While the high-energy γ-ray rate for ^{238}U is 9 times larger, the rate for the non-fissionable targets is significant and if a large mass of the non-fissionable targets were irradiated the rate may overlap with that of the fissionable target. By examining the data, a more unique signature can be obtained by removing γ-rays below 2.5 MeV and those γ-rays emitted before $\sim$ 13 ms. The data from figure 1.2 with the first $\sim$ 13 ms removed is shown in figure 1.3. Hence when using both energy and time cuts, a reliable and unique fission signature from delayed γ-rays is realized. This signature can be more clearly observed in the yield

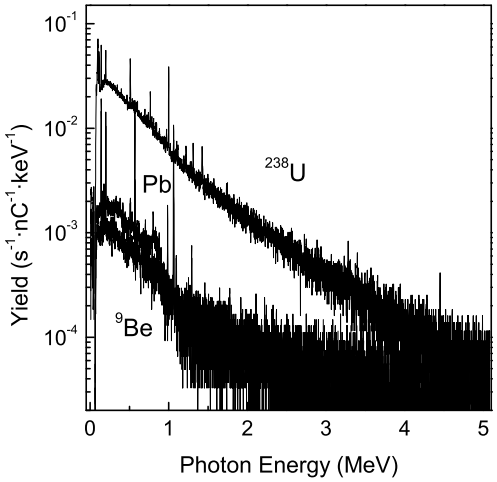

Figure 1.2: ANDA energy spectra for ^{238}U, Pb and ^{9}Be. All targets emit γ-rays with energies throughout the energy range.

data of figure 1.4 which compares the high-energy and time cut yields versus the bremsstrahlung endpoint energy for the fissionable target ^{238}U and the non-fissionable targets Pb, Fe and ^{9}Be. The fissionable target yield is four orders of magnitude higher then the non-fissionable targets at its maximum point. The significant difference in the yield between the non-fissionable and fissionable targets allows for fission targets to be readily determined.

By using the yield to create a unique signature for fission in leu of identifying energy peaks, the superior energy resolution of the HPGe detector was rendered unnecessary. This suggests replacing the HPGe detector with one that has a lower energy resolution and a higher efficiency. The work presented in this thesis expands on the data obtained from the HPGe detector

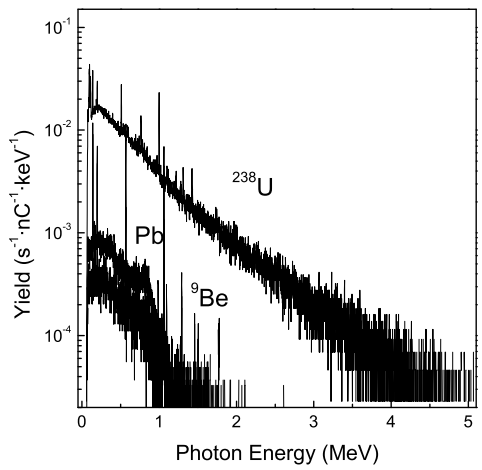

Figure 1.3: ANDA energy spectra for ^{238}U, Pb and ^{9}Be. By removing γ-rays with energies below 2.5 MeV and those that are emitted before $\sim$ 13 ms, ^{238}U can be distinguished from both Pb and ^{9}Be.

and focuses on 3 main areas:

- Determining which high-efficiency detector, the $Bi_4Ge_3O_{12}$ or the NaI(Tl), is more suited in the detection of high-energy γ-rays in an active inspection environment. Detector determination can be made by analyzing not only the yield but also the minimum detectable mass. ANDA experiments along with analysis of the data using high-energy and time cuts are presented for both detector types.

- Shielding experiments were performed to analyze the affect on background radiation.

- Delayed neutrons can also be detected and used to develop a signature

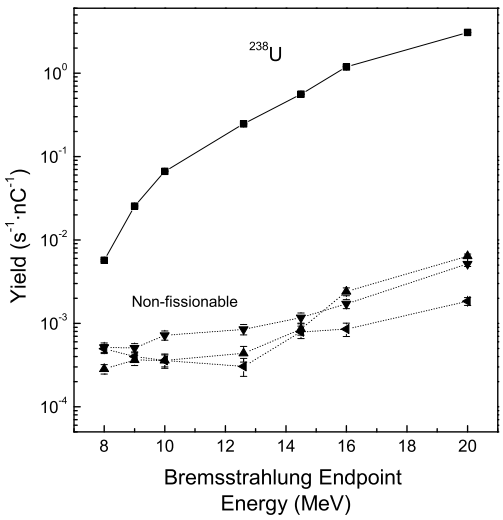

Figure 1.4: High-energy γ-ray yield versus bremsstrahlung endpoint energy using a $\sim$ 13 ms time cut for ^{238}U (■), Pb (▲), Fe (◀) and Be(▼).

for fission. This thesis includes a preliminary investigation comparing yield and minimum detectable masses using delayed neutrons.

Chapter 2

Theory

2.1 Theory of Fission

2.1.1 Liquid Drop Model

In an attempt to characterize fission, in 1939 Meitner and Frisch modeled the nucleus as a drop of charged liquid and termed the analogy "The Liquid Drop Model" [5]. Similar to the surface tension of a liquid drop, the short range nuclear force holds the nucleus together. In opposition to the nuclear force the repulsive Coulomb force drives the protons in the nucleus apart. When these two opposing forces are in balance the nucleus is said to be in a state of equilibrium, however, as the magnitude of the Coulomb force increases to a point near the Coulomb barrier, only a small amount of energy is required to cause the nucleus to begin to deform. As the nucleus deforms its shape stretches from spherical to ellipsoidal while its volume is maintained. The

deformation from spherical to ellipsoidal increases the surface energy (nucleons near the surface are less tightly bound by the increased surface area) and decreases the Coulomb force (owing to the protons being father apart from one another). If the surface combined with the electrostatic binding energies when the nucleus deforms to ellipsoidal is less than that when spherical, the nucleus is likely to undergo spontaneous fission. As described by Bohr and Wheeler, the point at which the nucleus becomes unstable against spontaneous fission can be calculated using the following limiting factor,

$$x = \frac{Z^2}{A} > 47.8, \tag{2.1}$$

where x is a parameter indicating fissility, Z is the number of protons and A is the mass number [5]. Accordingly, the liquid drop model states, that nuclei with an x parameter greater than 47.8 are unstable and can fission spontaneously.

2.1.2 Shell Model

When the nucleus divides the remaining fragments do not generally have an equal distribution of masses. The most probable distribution is the pairing of a light fragment with a heavy fragment where the distribution for the light fragments averages to a mass number of ~ 95 and the heavy fragments at a mass number of ~ 140 for ^{235}U (this region varies for each nucleus) [8]. While it would seem that the region of mass distributions would shift completely

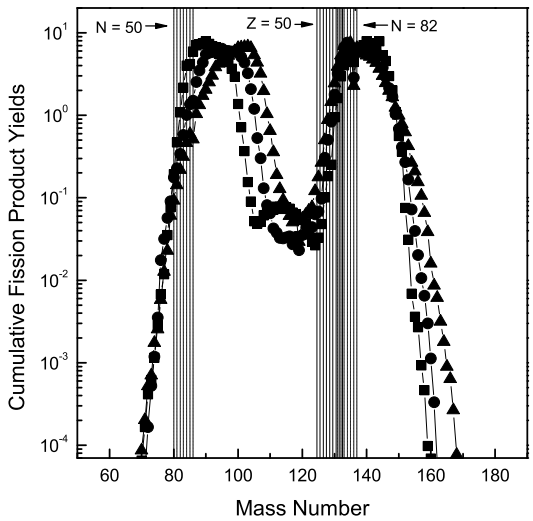

Figure 2.1: The cumulative fission product yield as a function of mass number for the neutron induced fission of ^{232}Th (■), ^{235}U (●), and ^{239}Pu (▲). The shaded regions indicate magic numbers or shell closures for protons (Z) and neutrons (N). The doubly shaded region at $Z = 50$ and $N = 82$ is located at approximately the leading edge of the mass distributions for the heavy fission fragments [8, 13].

and entirely with each differing nucleus, this is not the case. In fact, while the distribution for the light fragments shifts, the heavy fragments do not as seen in figure 2.1. Although the liquid drop model does a good job at characterizing the competing forces that cause fission it does not describe why the mass distribution of the light fragments shifts while the heavy fragments does not.

The shell model extends from the principals of the atomic theory where

electrons fill shells in an order of increasing energy and according to the Pauli Exclusion Principle, where electrons can not occupy the same state. In the shell model, protons and neutrons fill nuclear shells. The theory was formulated by examining proton/proton and neutron/neutron separation energies. In analogy with electron ionization energy, nuclei separation energies increase with increasing neutrons or protons however, drastic decreases in separation energy arise at certain N (neutron) and Z (proton) numbers. These energy decreases occur at the filling of major nuclear shells and are called "magic numbers". The filling of shells occurs at the following magic numbers: 2, 8, 20, 28, 50, 82, 126, and 184.

The shaded regions in figure 2.1 which are labeled N and Z indicate mass number ranges that correspond to magic numbers for neutrons (N) and protons (Z). At $Z \approx 50$ and $N \approx 82$ both the number of neutrons and protons are close or equal to magic numbers signifying filled shells [8]. It is with this N and Z arrangement that the initial edge of the mass distributions curve occurs for the heavy fragments of nearly all nuclei. The nuclear shells that are indicated by magic numbers are in relatively stable states. When an isotope fissions it is most likely to fission into fragments that are close to being in stable configurations. The light fragments however, do not have a similar double magic number region and therefore the mass distributions for various nuclei do not overlap.

2.1.3 Energy from Fission

Energy is released during the fission process. This energy release can be seen in the relationship in mass binding energies of the compound nucleus and the product fission fragments. If the compound nucleus ^{235}U fissions forming ^{90}Kr and ^{143}Ba, the difference in energy in the final fission products is 200 MeV owing to binding energies of -1738 MeV, -754 MeV and -1184 MeV for ^{235}U, ^{90}Kr and ^{143}Ba respectively [7, 8]. Energy conservation necessitates the addition of 200 MeV of energy in the final state. This energy is released not only in the form of kinetic energy ($\sim$80%) but also in the form of the emission of γ-rays and neutrons from the fission fragments [8]. These γ-rays and neutrons are called prompt γ-rays and prompt neutrons and are emitted from the fission fragments 10^{-13} s after fission [9]. The number of neutrons emitted ranges from 0 to 6 and is dependent not only on the compound nucleus and fission products but also on the fission process [11]. On average, two to three neutrons are emitted for ^{235}U [10].

After prompt γ-ray and neutron emission the fission fragments undergo β^- decay to further stabilize. Finally, excess energy is released in the form of the emission of γ-rays and sometimes neutrons. These γ-rays and neutrons are termed delayed γ-rays and delayed neutrons because the time frame of emission is dependent upon the β^- half life of the fission fragments. The half life of the fragments ranges from milliseconds to years [12]. Delayed neutrons are only emitted if the fission fragment is in a highly excited state and enough energy exists to release the neutron from the nucleus. Due to the

energy required for neutron emission, only a fraction of neutrons are emitted compared to γ-ray emission. For ^{235}U only 1 delayed neutron per 100 fission events is emitted [8]. The number of delayed γ-rays is also dependent on the fission fragments and on average 8 γ-rays are emitted per fission event with energy totalling about 7 MeV [1, 11].

2.2 Inducing Fission

2.2.1 Bremsstrahlung

Fission can be induced by exciting the nucleus with energy; typically this energy is supplied by neutrons or γ-rays. Although fission can be induced with neutrons, in the experiments presented in this thesis fission was induced with bremsstrahlung photons. Bremsstrahlung photons are produced by electromagnetic radiation created by the acceleration of electrons near the Coulomb field of a nucleus. The target material, called a radiator, is used to convert incident electrons into electromagnetic radiation or photons. The greater the number of protons in the nucleus of the atom the larger the Coulomb force. Therefore most radiator materials are high-Z.

As an electron travels in the vicinity of the nucleus of an atom, the Coulomb attraction with the protons causes the electron to bend towards the nucleus. This bending or acceleration causes the electron to lose energy in the form of electromagnetic radiation. During the collision of the electron with the nucleus caused by the Coulomb attraction, if the electron is

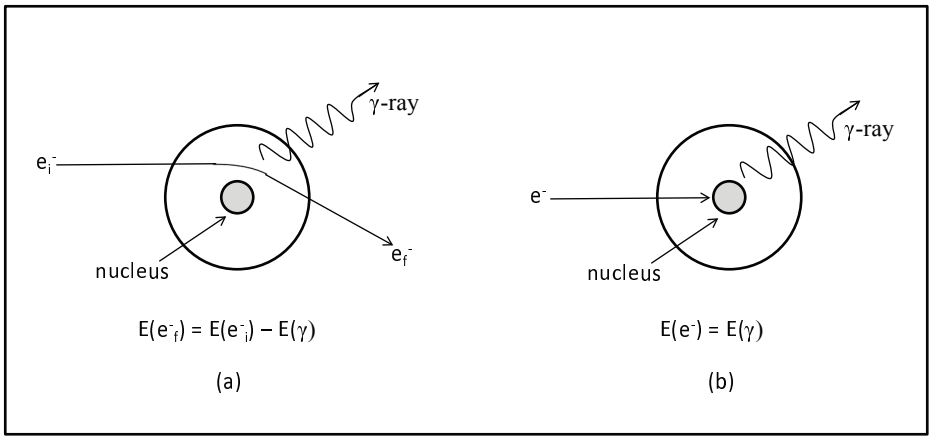

Figure 2.2: Depiction of bremsstrahlung photons. In (a) an incident electron is deflected by the interaction with the atomic nucleus. The resulting bremsstrahlung photon energy is equal to the difference in energy between the electron before and after deflection. In (b) all the kinetic energy of the electron is converted into the energy of the emitted photon. The energy of the resulting bremsstrahlung photon is equal to that of the incident electron.

deflected the energy of the emitted photon will equal the difference in the kinetic energy of the electron before and after deflection (neglecting the small recoil energy of the nucleus). The deflected electron is then free to interact with other atoms in the target material. The electron can also lose all its kinetic energy. This kinetic energy is then transferred to the emitted photon. This scenario is depicted in figure 2.2. As many electrons enter the target material producing many interactions a continuous spectrum of photon energy is produced. Figure 2.3 shows the continuous spectra of photon energy for electron beam energies of 3, 8, 13, and 18 MeV [14].

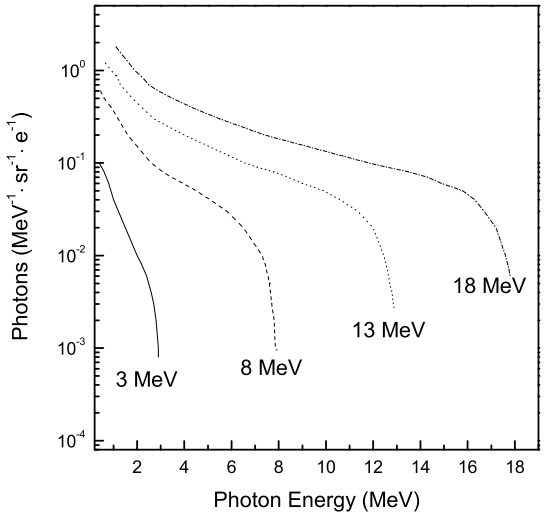

Figure 2.3: The graph shows the continuous energy spectra for photons from electron beam energies of 3, 8, 13, and 18 MeV. The plot was reconstructed from a graph included in INEL-A-9356 [14].

2.2.2 Fission Cross Sections

A cross section gives the probability of the occurrence of an indicated reaction; the larger the cross section, the larger the probability. Although all heavy nuclei can fission with high-energy γ-rays the probability can be large for certain isotopes [1]. The data presented in figure 2.4 was obtained from the National Nuclear Data Center ENDF libraries and gives the photofission cross sections for ^{235}U, ^{238}U, and ^{232}Th [15]. The shape of the cross sections are relatively similar and increase appreciably in magnitude at ~ 5.8 MeV. The peak cross section magnitude for ^{235}U occurs at 13.9 MeV with a value

of 331 mb and that for ^{238}U occurs at 14.4 MeV with a magnitude of 165 mb. The peak cross section magnitude for ^{235}U is about two times greater than that for ^{238}U. The ^{232}Th peak occurs at 14.3 MeV with a value of 56 mb which is about six times smaller than that of ^{235}U.

While bremsstrahlung photons supply the energy for the initial induced fission reactions (in the experiments presented), neutrons from fission products and other nuclear reactions are emitted and can go on to induce additional fission events, thus it is important to also examine neutron induced fission cross sections. Figure 2.5 shows the neutron induced fission cross sec-

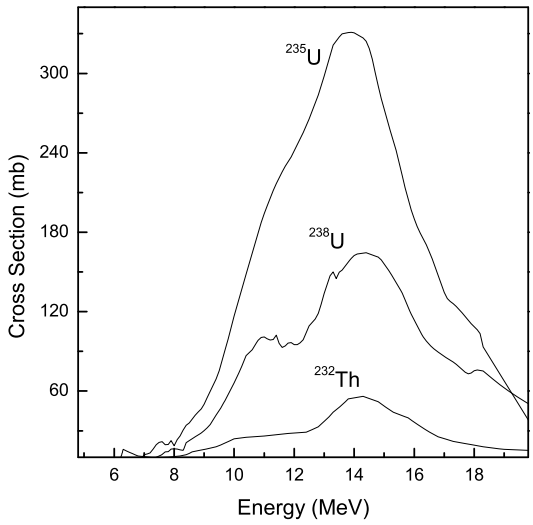

Figure 2.4: The graph shows photon induced fission cross sections for ^{235}U, ^{238}U, and ^{232}Th. The shapes of the three cross sections are relatively similar and indicate peak energies of ∼14 MeV.

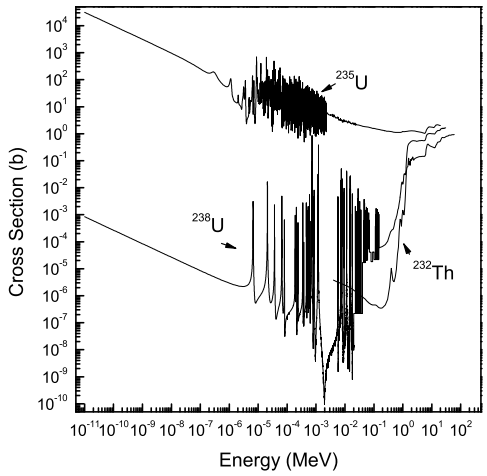

Figure 2.5: The graph shows neutron induced cross sections for ^{235}U, ^{238}U, and ^{232}Th. The majority of fission events are caused by thermal neutrons in ^{235}U while energy is required in the range of approximately 1.5 MeV for a significant number of fission events for both ^{238}U and ^{232}Th.

tions for ^{235}U, ^{238}U, and ^{232}Th [15]. It should be noted that fissile nuclei have a significant cross section for thermal neutron induced fission reactions while fertile nuclei do not. Fertile nuclei are those isotopes that can produce fissile isotopes after the absorption of a neutron. By examining the curve of the fissile isotope ^{235}U, a resonance region occurs from $\sim 10^{-6}$ to $\sim 10^{-3}$ MeV. For ^{238}U, a fertile isotope, the cross section is not appreciable until a neutron energy of ~ 1.5 MeV. The threshold energy for neutrons inducing fission in ^{232}Th is also ~ 1.5 MeV but at this energy the ^{238}U cross section is 5 times larger. The peak of ^{238}U starts at ~ 2 MeV and has a cross section

of ~ 560 mb which extends to about 6 MeV. In this $2-6$ MeV range, ^{235}U has a cross section approximately 2 times larger or ~ 1.13 b. The ^{232}Th cross section in this region is 130 mb which is ~ 9 times smaller than ^{235}U.

2.2.3 Other Nuclear Reactions

Neutron capture reactions can be induced by neutrons emitted either by fission or by other reactions such as (γ, n). In neutron capture reactions the excited compound nucleus stabilizes by emitting γ-rays. Neutron capture undergoes, in a general case, the following process;

$$n +^{A} X \longrightarrow^{A+1} X^{*}$$

$$^{A+1}X^{*} \longrightarrow^{A+1} X + \gamma's,$$

where n is the incident neutron, A is the atomic number, ^{A}X is the target nucleus, and $^{A+1}X^{*}$ is the excited compound nucleus. In examining the reaction, it is the resulting γ-rays that are important. Often times, the resulting nucleus, symbolized by ^{A+1}X, is unstable and will further decay emitting more γ-rays. The resulting γ-rays can have a large amount of energy, for example, ^{54}Fe can emit γ-rays with energies in the range of ~ 0.4 to 9.3 MeV [6]. If there are a significant amount of γ-rays that occur due to nuclear reactions other than fission, the detection system could potentially be overwhelmed by these γ-rays and miss detecting the γ-rays that occur due to fission. These neutron capture reactions can occur in most materials in the environment.

Appendix A shows the cross sections for a few sample materials.

2.3 Detection and Crystal Scintillation Detectors

The ultimate goal of the detection system is to detect the delayed γ-rays which are produced by the fission process. However, the detectors do not differentiate γ-rays emitted from multiple sources. Inorganic crystal scintillation detectors have proven to be reliable in the detection of γ-rays. In the experiments presented, the effectiveness of NaI(Tl) and $Bi_4Ge_3O_{12}$ (BGO) inorganic crystal scintillation detectors were compared.

Crystal scintillation is the process by which a pulse of visible light is produced by a scintillation crystal. The scintillating crystal produces visible light through a process called fluorescence where radiation in the visible spectrum is emitted during the de-excitation of an electron from the conduction band to the valence band. In a pure crystal lattice an electron upon absorption of a discrete amount of energy can transition from the valance band to the conduction band. In the conduction band, the electron can diffuse freely through the crystal. The electron that transitions from the valance band to the conduction band leaves a hole in its place in which a free electron in the conduction band can then fill. Energy is converted into a photon as an electron in the conduction band de-excites back into the valance band. In a pure crystal, this transition energy can be outside the visible spectrum. By

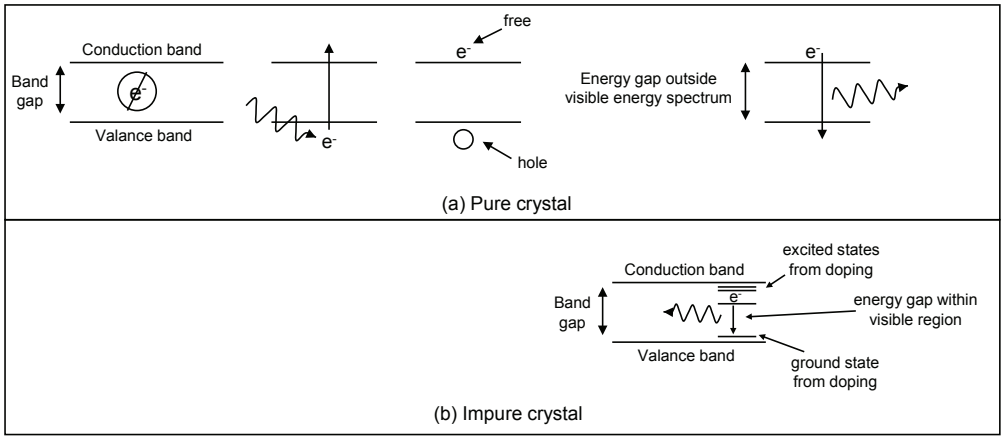

Figure 2.6: The Crystal Scintillation Process. In the crystal scintillation process, upon absorption of energy, an electron in the valence band jumps the band gap into the conduction band. A hole remains in the valence band until a free electron in the conduction band releases energy and transitions back into the valence band. In (a) the pure crystal, the band gap is outside the visible range of the energy spectrum. In (b) a dopant is added to make an impure crystal. Here energy states inhabit the original band gap region. As the electron de-excites energy is now released within the visible region of the energy spectrum.

adding an impurity to the crystal energy levels are added in the band gap region between the pure crystal's valance and conduction bands, thereby decreasing self absorption. The impurity added is called the dopant. Because the energy levels are within the original band gap the electron can now transition from the excited state to the ground state of the dopant. If the right dopant is added, photons in the visible spectrum are emitted. The process is depicted in figure 2.6.

In NaI(Tl) detectors, thallium is the dopant. In its pure crystal form, the band gap spans about 4 eV of energy [8]. When thallium is added energy

states are created within the band gap modifying the maximum emission wavelength from 303 nm to 410 nm, which is now inside the visible electromagnetic spectrum [8]. In contrast, BGO crystals do not require a dopant. Instead the fluorescence is due to an optical transition of the Bi^{3+} ion [17]. The peak fluorescence wavelength is about 475 nm which is also within the visible spectrum [17].

Energy that is required for scintillation is initiated in general by the photoelectric effect, Compton scattering, or pair production. In each process, a high-energy photon transfers energy to an electron which then travels through the crystal losing kinetic energy along the way. As the electrons lose energy it is transferred to electrons within the crystal creating electron-hole pairs. It is the process of electrons filling the holes that leads to the scintillation that was mentioned previously.

2.3.1 The Photoelectric Effect, Compton Scattering, & Pair Production

The photoelectric effect is a process in which photons are absorbed by the detector crystal. The photon energy is transferred and results in the ejection of an electron from an atom in the crystal. This emitted electron is called a photoelectron. The energy of the photoelectron is equal to the difference in the incoming photon energy and the electron binding energy (neglecting an insignificant amount of energy associated with the recoil of the atom).

Typically, electrons are emitted from a K-shell orbital which in high Z materials has a binding energy of tens of keV [19]. Another electron within the atom quickly fills into the hole that remains from the emitted electron. As the electrons are rearranged within the atom, energy equal to the binding energy is released in the form of a characteristic x-ray or Auger electron. The characteristic x-ray is then free to interact with other electrons via this same process. Auger electrons are second outer-orbit electrons that are sometimes emitted by the energy from the characteristic x-rays. This electron then goes on to interact and eventually is absorbed. The energy sum from the photoelectron and the characteristic x-ray or the Auger electron is equal to the total energy of the original photon making the photoelectric effect an ideal process. If all the initial energy is deposited in the detector volume, the energy peak recorded by the photoelectric effect is designated the photopeak.

In Compton scattering the incoming γ-ray scatters from an electron. The resulting energy of the γ-ray is dependent upon the angle of scatter as well as the binding energy of the electron. To simplify the calculation, the equations for this process are based on the scattering of a free or unbound electron. The energy of the recoiled electron is:

$$E_{e^-} = h\nu - \frac{h\nu}{1 + (\frac{h\nu}{mc^2})(1 - \cos(\theta))}. \tag{2.2}$$

Where hν is the energy from the incident γ-ray, θ is the scattering angle, and mc^2 is the rest mass energy of the electron. Based on the scattering angle,

the recoil electron energy can have very little energy ($\theta = 0$) or a maximum energy in which a head-on collision has transpired ($\theta = \pi$). The changes in scattering angle leads to an energy continuum from $\theta = 0$ to $\theta = \pi$. The energy curve is called the Compton continuum which has a maximum energy ending at the Compton edge.

In the final process, pair production, the incoming γ-ray energy is completely transferred to the creation of an electron-positron pair via interaction with the Coulomb field of the nucleus. The incoming γ-ray must carry enough energy to create both the electron and the positron. Therefore the γ-ray must have an energy equal to or greater than the rest mass energy of both the electron and positron which is $mc^2 = 0.511$ MeV. Energy exceeding $2mc^2 = 1.02$ MeV is transferred as kinetic energy of the electron-positron pair. The electron and positron lose their kinetic energy essentially simultaneously causing a summing effect in the detector. The term "double escape peak" refers to the escape of energy resulting from the annihilation of the positron created from the electron-positron pair. As the positron slows to energies in the range of thermal electron energies, the positron will annihilate with a thermal electron creating two photons. If one of the two photons subsequently interacts and loses its energy to the absorbing material, the difference in energy between the original incident γ-ray and the rest energy of the positron ($mc^2 = 0.511$ MeV) is deposited in the detector. The peak resulting from the interaction of this single photon is called the "single escape peak" and occurs at an energy value 0.511 MeV below the photopeak.

If both annihilation photons are absorbed and no energy escapes, all the photon energy is deposited in the detector and is added to the photopeak. A schematic of the peaks characterizing the photoelectric effect, Compton scattering and pair production is shown if figure 2.7.

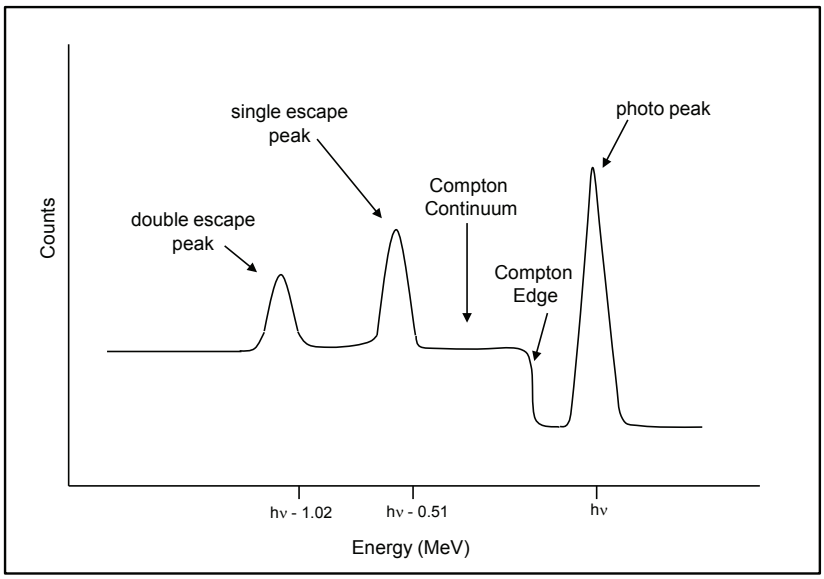

Figure 2.7: Energy peaks resulting from the photoelectric effect, Compton scattering, and pair production. The "double escape peak" results from pair production and the escape of the photons created from positron annihilation. The "single escape peak" is from the escape of one of the photons created from positron annihilation. The Compton continuum ends with the Compton edge and is characteristic of Compton scattering. The photopeak is equal to the full energy of the photon and is a result of the photoelectric effect.

The cross section is the statistical probability of either Compton scattering, pair production or the photoelectric effect interactions occurring. The probability of the interaction occurring is largely dependent on the energy of the incident photon. Figure 2.8 compares the photoelectric, Compton scat-

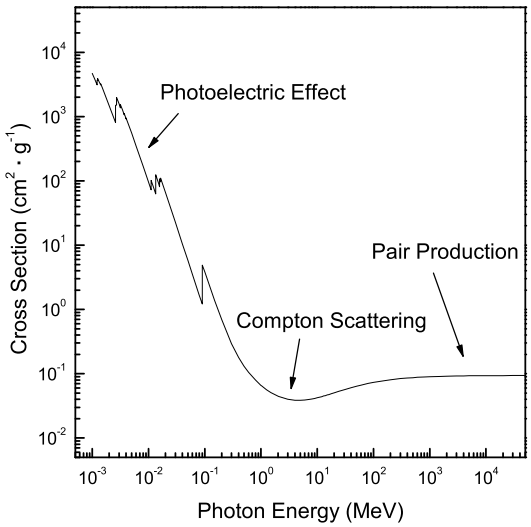

Figure 2.8: Photoelectric, Compton scattering, and pair production cross sections for the BGO crystal [18].

tering and pair production cross sections for the BGO crystal, however, those for the NaI(Tl) crystal are similar. Data for the cross sections was obtained from the NIST XCOM database [18]. The photoelectric effect largely dominates at low incident photon energies from 10^{-3} MeV to 10^{-1} MeV while pair production dominates at high energies starting at ~ 10 MeV. Compton scattering is the dominant interaction for the energies lying in between the photoelectric and pair production interactions. It is the incident photons with energies in the range of Compton scattering interactions which largely includes the delayed γ-rays due to fission that are recorded in the experiments presented in this thesis.

The stopping power is a measure of the energy lost as a result of Compton scattering, pair production or photoelectric effect interactions. The stopping power is associated with the number of electrons in the atoms of the crystal as well as with the density. Since the stopping power is a measure of the energy lost, if the material has a large number of electrons and a higher density, the γ-rays have a greater chance of losing energy. Because a greater charge interaction leads to greater energy loss, a larger atomic number leads to a greater stopping power. Sodium has an atomic number of 11 while Iodine has one of 53 therefore Iodine is largely responsible for the stopping power of the NaI(Tl) crystal. The BGO crystal has an effective atomic number of 74 which leads to a greater stopping power for the BGO detector over the NaI(Tl) detector. The density of BGO (7.13 g/cm^3) is higher than NaI(Tl)(3.67 g/cm^3) which also contributes to a higher stopping power for the BGO crystal [20].

2.3.2 Photocathode and Photomultiplier Tube

Energy from γ-rays can not directly be measured from the scintillation crystal. A photomultiplier tube (PMT) is used to change the energy of the photons into an electrical signal. In the photocathode portion of the PMT, scintillation photon energy is transferred to electrons via the photoelectric effect. These electrons are then focused by an electric field to a dynode. To produce a measurable electric signal, the number of photoelectrons are multiplied using a series of dynodes. Electron multiplication starts with a single

dynode which is an electrode with a voltage applied to it. This voltage is used to accelerate the electrons that have been freed at the photocathode due to the photoelectric effect. If the accelerating voltage is high enough, well over the work function of the dynode metal, many electrons in the dynode will have enough energy to break the surface barrier and be freed by the incident photoelectron. These freed electrons can then be accelerated towards another dynode where a larger voltage relative to the first dynode is applied. The number of electrons emitted from each dynode is equal to the gain of the dynode multiplied by the number of electrons that are accelerated toward it by the previous dynode. As the process continues the number of ejected electrons increases from dynode to dynode creating a multiplying effect. At the end of the dynode chain, an anode is used to collect all emitted electrons. In the experiments presented here, the photocathode for both the BGO and NaI(Tl) detectors is made of bialkali and has a peak sensitivity to blue-green light. The PMT used by both detectors (Electron Tubes 9266B for BGO and 9815B for NaI(Tl)) has a gain of 10^6.

2.3.3 Energy Resolution and Efficiency

The utility of a detector can be measured by its energy resolution (R). A distribution of energies is recorded by the multichannel analyzer (MCA). The MCA sorts the electrical pulses emitted from the PMT according to its amplitude. The distribution is due to statistical fluctuations of the scintillation electrons inside the detector crystal. A wide distribution is an indication

that the detector is not able to discriminate γ-rays of differing energies. The relative energy resolution is measured by the full width at half-maximum (FWHM) of the photopeak and the centroid of the energy (E_γ) of the γ-ray determining the peak. The equation follows:

$$R = \frac{\text{FWHM}}{E_\gamma}. \tag{2.3}$$

The efficiency of a detector is also a good measure of the detector's utility. Two types of efficiency measurements are presented in this thesis, the absolute and the intrinsic efficiencies and both are dependant on the energy of the incident γ-rays. The absolute efficiency (ε_A) is a measure of the number of γ-rays that are detected by the detector (N) to the number of γ-rays that are emitted by the source and can be calculated using the following equation;

$$\varepsilon_A = \frac{N}{\phi \cdot \delta t} = \frac{events\ dectected}{events\ emitted\ from\ the\ source}. \tag{2.4}$$

The symbol δt, is the time that the detector is exposed to the source. The rate, ϕ, of a particular γ-ray transition energy given off by the source can be calculated as follows;

$$\phi = \beta A_o e^{-\lambda t}, \tag{2.5}$$

where β is the branching intensity of the energy peak, A_o is the number of decays per second given off by the source, λ is the decay constant and t is

the time elapsed since the date the source was calibrated.

The intrinsic efficiency includes the angle subtended by the detector from the source (Ω). When the distance (d) from the source to the detector is much much greater than the radius (r) of the detector, the source can be seen as a point source and $\Omega \approx \frac{\pi r^2}{d^2}$. The intrinsic efficiency (ε_I) is determined by the following equation,

$$\varepsilon_I = \frac{\varepsilon_A}{\frac{\Omega}{4\pi}} = \frac{4d^2\varepsilon_A}{r^2} = \frac{events\ detected}{events\ incident\ on\ the\ detector}, \tag{2.6}$$

where ε_A is the absolute efficiency.

2.4 Decision Levels & Minimum Detectable Mass

The minimum detectable mass, MDM, is a measure of the minimum amount of mass required to conclude that a fissionable target has been detected. The MDM can be calculated with the signal collected from the MCA and by using the nomenclature and mathematical definitions of Currie [21]. The signal collected in the MCA is the number of γ-rays collected and includes their energy and the time they strike the detector after the start of the accelerator pulse. The γ-ray counts are then turned into a workable value called the yield.

Unless otherwise specified, the yield in these experiments is the γ-ray

counts divided by the charge on target, Q. The charge on target is a measure of how much charge is incident on the radiator from the beam over the duration of the experiment. In order to develop a unique signature indicting a fissionable target material, it is necessary to isolate delayed γ-rays occurring due to fission from those occurring due to other nuclear reactions. To isolate delayed γ-rays, energy and time cuts are used of 3 MeV and 22 ms respectively and these values are applied to the yield. These cuts are explained in more detail in the Results section.

In developing a unique fission signature, experiments are performed with fissionable as well as non-fissionable targets. The yield resulting from a fissionable material target is symbolized, Y_S while that from a non-fissionable target is Y_B (where B stands for the active background). In a perfect experiment, where no errors are present, a Y_S value above zero would signify the presence of a fissionable target. However, due to counting errors present in the experiment, decisions must be made to determine the level that signifies the presence of fissionable material targets. Currie defines a decision level and a detection limit:(1) the critical level, L_C and (2) the detection limit, L_D [21]. The critical level, L_C is established a posteriori of an experimental observation and includes the risk assessment, α, which sets the false positive probability. The risk value α is used to indicate a confidence interval in which the target can be distinguished from the active background. The detection limit, L_D is established a priori of an experimental observation and uses the value L_C along with the risk assessment, β, which is the converse

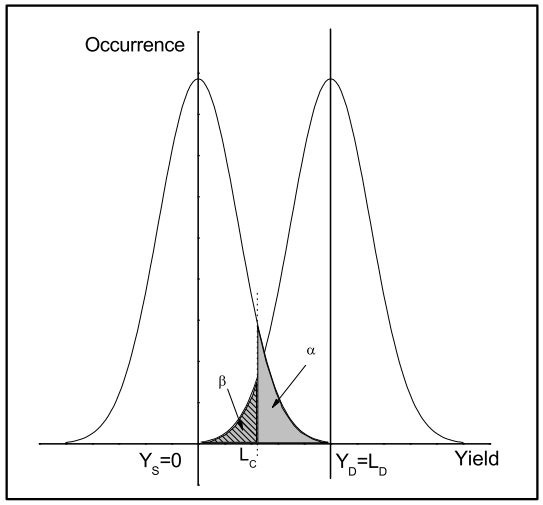

Figure 2.9: Schematic of MDM Decision Levels and Risk Assessments. L_C corresponds to $Y_S = 0$ while L_D corresponds to $Y_D = L_D$. When the yield from the fissionable target is centered around L_D it is represented with a Y_D.

to α and allows for the possibility of a false negative. A false negative is the risk of concluding the target is non-fissionable when in fact it is fissionable. While L_C verifies whether or not a fissionable target can be distinguished from the background, L_D determines whether the experiment is sufficient to lead to detection of the fissionable target and is used to calculate the MDM. Figure 2.9 shows a schematic of a measured signal, L_C, L_D and their associated risks, α and β. In examining the figure, if Y_S is above L_C one can distinguish the fissionable target from the background, if however the signal is above $Y_S = 0$ but below $Y_S = L_C$, one can calculate the confidence level at which the target yield is above background levels and indeed fissionable.

In looking at L_D, one can not say to within the confidence interval specified that the experiment resulted in a fissionable target until the yield is above $Y_{\mathrm{D}} = L_{\mathrm{C}}$ (the figure indicates that the confidence level associated with both α and β is the same and Y_{D} is the yield centered around L_{D}).

Assuming that the number of counts is large (the time of irradiation for the experiments presented in this thesis are long enough to consider this true) then the distribution is Gaussian and the standard deviation measures the statistical error or uncertainty in the measurement. If we assume the error in the charge is negligible, thus allowing the error to be dominated by the number of decay events, the standard deviation is then equal to the square root of the counts divided by Q (not under the square root). Both L_C and L_D include not only this standard deviation but also their associated risk assessments. The value L_C is defined as,

$$L_C = k_\alpha \sigma_o, \tag{2.7}$$

and L_D is,

$$L_D = L_C + k_\beta \sigma_D, \tag{2.8}$$

where σ_o is the standard deviation for a distribution centered around zero and σ_D is that centered around L_D. The abscissa for the risk assessment associated with α is "k_α" and that for β is "k_β". The probability that the measurement falls between negative infinity and "k_α" which is associated

with the yield centered around zero ($Y_s = 0$) is,

$$1 - \alpha = \frac{1}{\sqrt{2\pi}} \int_{-\infty}^{k_\alpha} e^{\frac{-x^2}{2}} dx = \frac{1}{2}(1 + \mathrm{erf}(\frac{k_\alpha}{\sqrt{2}})). \tag{2.9}$$

The probability that the measurement falls between "k$_\beta$" and positive infinity which is associated with the yield centered around L_D ($Y_D = L_D$) is,

$$1 - \beta = \frac{1}{\sqrt{2\pi}} \int_{k_\beta}^{\infty} e^{\frac{-x^2}{2}} dx = \frac{1}{2}(1 - \mathrm{erf}(\frac{k_\beta}{\sqrt{2}})). \tag{2.10}$$

The variance centered around zero, σ_o, includes the variance due to the fissionable and non-fissionable targets and is defined as follows:

$$\sigma_o^2 = \sigma_S^2 + \sigma_B^2 \tag{2.11}$$

If the signal and the active background are measured using the same characteristics, such as having similar run times, similar charges, etc. then they are said to be paired and their standard deviations do not vary. In this case,

$$\sigma_o^2 = 2\sigma_B^2 \tag{2.12}$$

and

$$L_C = k_\alpha \sqrt{2} \sigma_B. \tag{2.13}$$

The critical limit is calculated using the yield which is normalized to a hypothetical charge on target, Q_H. The hypothetical charge on target sets a

standard charge, time of irradiation and repetition rate. Then the standard deviation in terms of the yield is equal to the square root of the yield divided by the square root of Q_H. Therefore,

$$L_C = k_\alpha \sqrt{2 \cdot Y_B / Q_H}. \tag{2.14}$$

The variance for L_D is defined as,

$$\sigma_D^2 = \sigma_{D+B}^2 + \sigma_B^2, \tag{2.15}$$

where σ_{D+B}^2 is the standard deviation of the signal plus the interference of an active background when the yield is centered around L_D. In this case, because the decision is a priori of an experimental observation, the assumption can not be made that the standard deviation, σ_{D+B}^2, does not fluctuate depending on the signal. Therefore,

$$\sigma_D^2 \neq 2\sigma_B^2.$$

By substituting the square root of the yield divided by the square root of Q_H for the standard deviation as defined above,

$$\sigma_D^2 = \frac{Y_D}{Q_H} + \frac{Y_B}{Q_H} + \sigma_B^2 \tag{2.16}$$

Since $Y_D = L_D$ then

$$\sigma_D^2 = \frac{L_D}{Q_H} + 2\sigma_B^2 \tag{2.17}$$

and also by substitution,

$$\sigma_D^2 = \frac{L_D}{Q_H} + \sigma_o^2 \tag{2.18}$$

finally,

$$L_D = L_C + k_\beta \sqrt{\frac{L_D}{Q_H} + \sigma_o^2}. \tag{2.19}$$

Solving for L_D, substituting L_C for $\frac{\sigma_o}{k_\alpha}$, using $k_\alpha = k_\beta$ and also noting that the positive value of the quadratic equation is used because the standard deviation to the background fluctuates and is not constant [21],

$$L_D = \frac{k^2}{Q_H} + 2L_C. \tag{2.20}$$

Finally, the minimum detectable mass is a function of L_D and the amount of mass, M, from the sample that is present in the bremsstrahlung beam. Therefore,

$$MDM = \left(\frac{L_D}{Y_S - Y_B}\right) M. \tag{2.21}$$

Chapter 3

Setup

3.1 Arrangement of Detectors and Target

All the experiments presented in this thesis were performed at the Idaho Accelerator Center using the 25 MeV LINAC and the 90° port. The beam was directed from the main hall, a room housing the accelerator, and into an adjacent room called the experimental cell. Figure 3.1 shows a schematic of the room arrangement. By running the experiments in the experimental cell, a significant amount of accelerator background radiation was eliminated. Separating the two rooms is a 1.22 m thick wall of dirt sandwiched in between concrete 30 cm thick. To induce fission, a bremsstrahlung photon beam was created by directing the electrons produced by the accelerator onto a 4.2 $\mathrm{g \cdot cm^{-2}}$ tungsten radiator located $\sim$ 0.605 m upstream of the concrete wall. Excess electrons exiting the tungsten were swept out of the

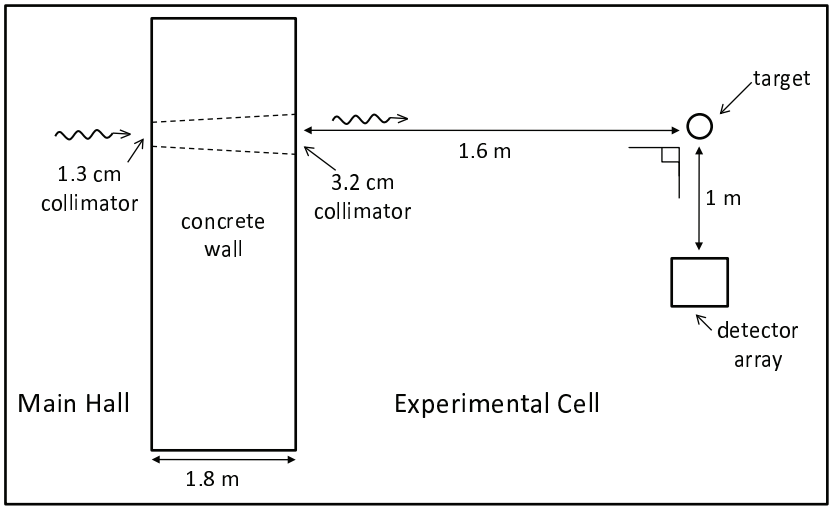

Figure 3.1: Top view of the detector array and target in relation to the bremsstrahlung beam.

bremsstrahlung beam path using a permanent magnet. The beam was collimated into the experimental cell using two collimators 15 cm long. The diameters of the collimators were 1.3 cm and 3.8 cm for the entering and exiting beams respectively. For all the experiments presented, the accelerator operated at a 15 Hz repetition rate. To get a good idea of yield rates at different energies, the bremsstrahlung beam endpoint energies varied from 7 to 22 MeV in 3 MeV increments.

The targets were located ~ 1.6 m from the concrete wall and were centered on the beam axis. The detectors were placed 1 m from the target initially at a 90° angle and then moved to a $\sim 40°$ (from the beam). The change in angle did not affect the yield detected from the targets. Two BGO and two NaI(Tl) detectors were used in the experiments both having crystal

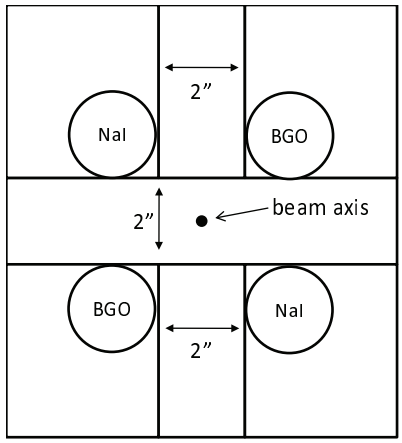

Figure 3.2: Front view of the detector array with two BGO and two NaI(Tl) detectors. Each detector type was located diagonally from one another.

measurements of $2'' \cdot 2''$. The four detectors were placed in a two row and two column array with the center axis of the array level with the center axis of the targets. Each row contained one BGO and one NaI(Tl) detector and each detector of the same crystal type was located diagonally from one another. A schematic of the detector array is depicted in figure 3.2. The detector array was constructed with $(5.08 \times 10.16 \times 20.32)$cm lead bricks with the 5.08 cm side in between the detectors. To reduce background radiation, the detectors were shielded with 10.16 cm of lead which covered all sides except the front of the detector array. The lead enclosure sat on top of a 10.16 cm thick borated polyethylene slab which was used to raise the center height of the detector array level to that of the target center. The geometry of the target, detector and beam arrangement is presented in figure 3.1.

The detectors were kept in place with SillSeal blue styrofoam which can

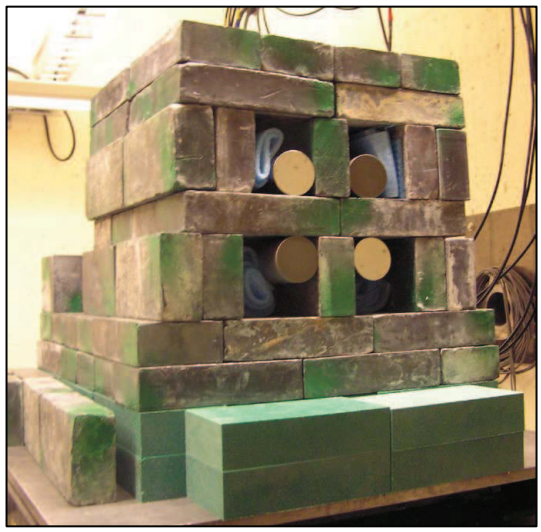

Figure 3.3: Photo of the detector array which is shielded with 10.16 cm of lead.

be seen in a picture of the detector array setup in figure 3.3. The SillSeal has been tested and does not interfere with the detection of γ-rays.

3.2 Electronic Circuitry and Time Structure

The BGO detectors were supplied a voltage of -650 V while the NaI(Tl) detectors were set to $+1150$ V. The capacitance of the preamplifier (Ortec model 113) was used to turn the output charge of the PMT into a voltage pulse and was set to 200 pF for all of the detectors. The voltage pulse produced by the preamplifier is given by

$$V = \frac{Q}{C}, \tag{3.1}$$

where V is the voltage, Q is the output charge by the detector and C is the capacitance of the preamplifier. The preamplifier was then connected to an amplifier (Ortec model 855), which was used for pulse shaping and signal gain. The preamplifier is constructed to drive a 93 Ω impedance while the amplifier has an input impedance of $\sim 1000\,\Omega$ therefor a 93 Ω terminator was placed on the input connection of the amplifier. All the jumpers in the amplifier were set with a time constant of 3 μs and the bipolar output signal was used. The gain varied for each amplifier but was adjusted for a maximum calibration energy in the ADC (Analog to Digital Converter) of ~ 5 MeV. A gate and delay generator was used to inhibit data conversion of the ADC for 1 ms immediately following the accelerator pulse. This gate prevented conversion as the detectors recovered from the large energy deposition of the scattered x-rays from the bremsstrahlung pulse. One ADC was connected to the gun trigger of the accelerator and recorded a time stamp to indicate when the accelerator fired. All other timing information is measured off of the stamp initiated by the gun trigger. The remaining ADCs were connected to the MCA on the computer. Figure 3.4a depicts the detector circuit.

To obtain the charge, which is used to normalize the data and calculate the yield, an induction coil was placed at the end of the accelerator. The coil was connected to an oscilloscope which was then connected to a computer through a GPIB interface. The charge was recorded for each separate run. Figure 3.4b depicts the charge circuit.

The accelerator operated at a 15 Hz repetition rate for all experiments

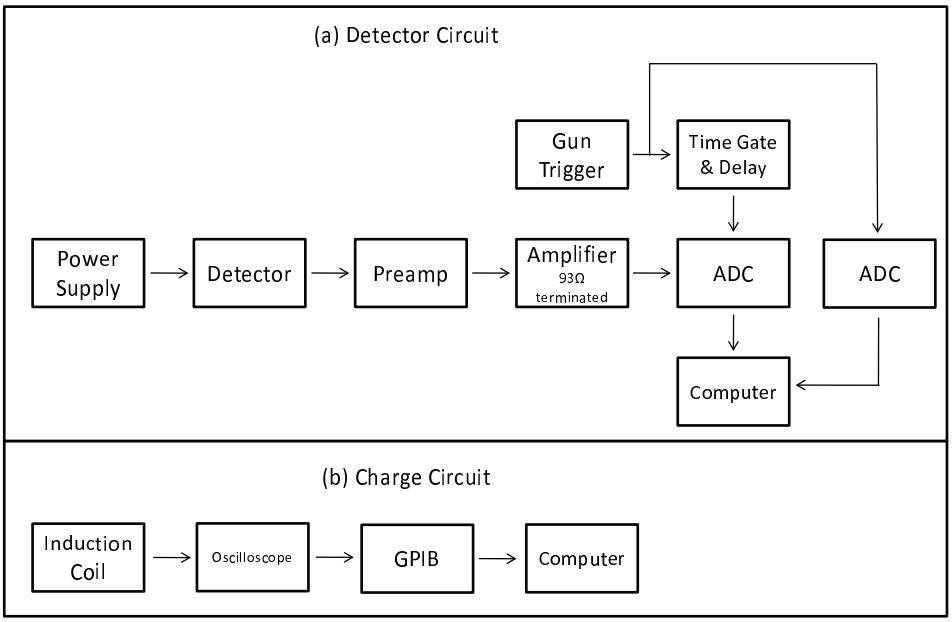

Figure 3.4: The electronic circuit for the detectors is depicted in (a) while (b) shows the charge circuit.

detailed in this thesis leaving 66.6 ms from the start of one pulse to the next. The pulse width of the beam was 4 μs. Data was recorded in between pulses after the 1 ms delay of the ADC. During the 4 μs wide pulse, a large amount of energy is absorbed by the detectors from the scattered bremsstrahlung leaving them inoperable. It is also during this 4 μs, when the detectors are inoperable, that the prompt γ-rays are emitted. Figure 3.5 details the timing structure of the beam.

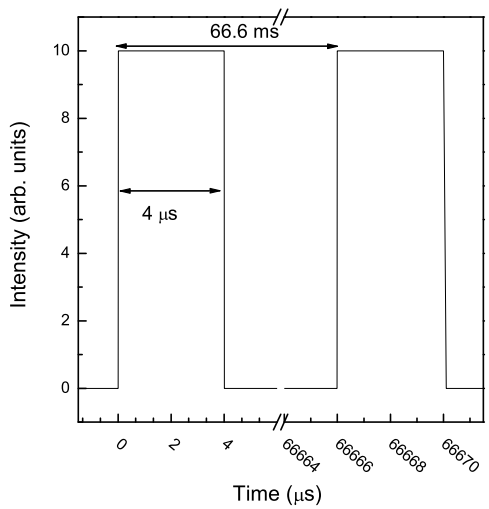

Figure 3.5: Time structure of the accelerator beam.

3.3 Targets

During the experiment, three fissionable targets were used: metallic ^{238}U, 4.7 % ^{238}U in deionized H_2O, and ^{232}Th. The 4.7 % ^{238}U in deionized H_2O target was contained in a Klean Kanteen. Klean Kanteens are made of food grade stainless steel which is a standardized material. The Kanteens are commercially available and do not degrade in the bremsstrahlung beam as quickly as plastic. Non-fissionable targets used were: Pb, Al, ^{9}Be, and deionized H_2O (stored in a Klean Kanteen). The Pb and deionized H_2O targets were used to determine the background. The Pb target is also a common shielding material. Aluminum was used because it is a common

Target	Mass (kg)	Geometry (cm)
^{238}U	3.9	9.1 × 9.1 × 0.635
4.7 % ^{238}U to DI H_2O	0.0523	stored in 40 oz. Klean Kanteen
^{232}Th	1.6	several small cylinders
Pb	6.2	2.5 × 10.2 × 20.3
^{9}Be	3.0	9 diam., 25.4 length (cylinder)
Al	2.8	5.1 × 10.2 × 20.3
DI H_2O	0.89	stored in 40 oz. Klean Kanteen

Table 3.1: Target masses are listed in kilograms. The mass listed for the ^{238}U target is for 3 plates each having a mass of 1.3 kg. Deionized water is abbreviated and listed as DI. The mass value listed for 4.7 % ^{238}U in DI H_2O is only for the ^{238}U.

material. The ^{9}Be target was used because it produces a large amount of neutrons from (γ,n) reactions. The emission of these neutrons could go on to interact with other materials in the environment and create neutron capture reactions which could confound the detection system. Figure B.1 in the appendix shows the ^{9}Be photonuclear cross sections and the target masses and geometries are listed in table 3.1.

3.4 Efficiency and Energy Resolution

The efficiency of the detectors was measured by placing a source a distance of 25.4 cm from the detectors thereby allowing the source to be treated as a point. To reduce backscatter, the detector was elevated 20.3 cm above the surface of the table and placed $\sim$ 0.6 m from the back wall. The source was located on axis with the detector. Absolute and intrinsic efficiencies for

Detector	Energy (keV)	Abs. Eff.	Int. Eff.	Full-Eng. Peak [1]
BGO	661.66	0.15% $\pm$ 0.0004%	60.41% $\pm$ 10.1%	50.00%
NaI(Tl)	661.66	0.06% $\pm$ 0.0002%	22.20% $\pm$ 3.73%	16.05%
BGO	1173.2	0.07% $\pm$ 0.0004%	28.46% $\pm$ 4.78%	30.19%
NaI(Tl)	1173.2	0.03% $\pm$ 0.0001%	10.81% $\pm$ 1.82%	6.44%
BGO	1274.5	0.10% $\pm$ 0.0002%	39.50% $\pm$ 6.63%	28.70%
NaI(Tl)	1274.5	0.03% $\pm$ 0.0006%	10.76% $\pm$ 1.82%	6.00%
BGO	1332.5	0.07% $\pm$ 0.0013%	28.27% $\pm$ 4.77%	26.96%
NaI(Tl)	1332.5	0.03% $\pm$ 0.0001%	10.32% $\pm$ 1.73%	5.70%

Table 3.2: Efficiency measurements for BGO and NaI(Tl) detectors. The source was set a distance of 25.4 cm from the detectors allowing it to be treated as a point. The full-energy peak efficiency values are standard values for a 1.5″ diameter by 1.5″ thick crystal and are comparable to the measured intrinsic efficiency results.

various energies are listed in table 3.2 and are calculated using the intrinsic efficiency equation in section 2.3.3. The errors were added in quadrature. The table also lists standard full-energy peak efficiencies of a 1.5″ diameter by 1.5″ thick for both BGO and NaI(Tl) crystals measured by Evans which are comparable to the calculated intrinsic efficiency [29].

At 661.66, 1173.2 and 1332.5 keV the absolute and intrinsic efficiencies for the BGO detector are ∼2.5 times higher than those for the NaI(Tl) detector. At 1274.5 keV, both the absolute and intrinsic efficiencies are ∼3 times higher for the BGO detector. Therefore, the BGO detector is more efficient than the NaI(Tl) detector. The full-energy peak efficiency is lower at all energies which is expected due to the smaller crystal size.

Energy resolution of the detectors was also measured using the same setup

[1] Data measured by Evans [29].

Detector	Energy (keV)	Measured Resolution	Standard Resolution [2]
BGO	661.6	12% $\pm$ 0.01%	15.4%
NaI(Tl)	661.6	7% $\pm$ 0.07%	8.0%
BGO	1173.2	8% $\pm$ 0.03%	Not Resolved
NaI(Tl)	1173.2	5% $\pm$ 0.03%	Not Measured
BGO	1274.5	9% $\pm$ 0.02%	Not Measured
NaI(Tl)	1274.5	5% $\pm$ 0.13%	Not Measured
BGO	1332.5	9% $\pm$ 0.02%	11.8%
NaI(Tl)	1332.5	5% $\pm$ 0.02%	6.6%

Table 3.3: Energy resolution measurements for BGO and NaI(Tl) detectors. Greater energy resolution corresponds to smaller values. The standard resolution in the third column was collected by a 1.5″ diameter by 1.5″ thick detector crystal [29].

as that for the efficiency. Values are listed in table 3.3 and are calculated using the equation in section 2.3.3. The smaller the value listed, the better the energy resolution. The errors were calculated in quadrature. Similar to the efficiency table, the energy resolution table shows standard energy resolution values observed by Evans [29]. The measured energy resolution is on average (for all energies listed) 4% better for the NaI(Tl) detector.

[2] The 1173.2 keV line was not resolved by the BGO detector and therefor not calculated for the NaI(Tl) detector. The 1274.5 keV line was not measured by either detector in the paper cited.

Chapter 4

Results

4.1 Development of a Unique Signature for Fission

The thrust of these experiments is to create a unique signature indicating fission by detecting delayed γ-rays. However, as mentioned earlier, both NaI(Tl) and BGO detectors do not distinguish γ-rays characteristic of fission from those emitted due to other nuclear reactions. The focus is then to take the data and isolate γ-rays that are emitted due to fission thereby developing a unique fission signature. There are two characteristics of the emitted γ-rays that can be examined: their energy and the time that they are detected (this time is measured from the start of the accelerator gun trigger). In doing experiments similar to those done with a HPGe detector a signature can be developed using the NaI(Tl) and BGO detectors [31].

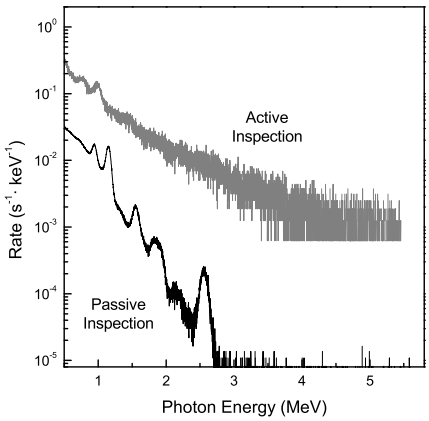

Figure 4.1: Photon energy spectra for ^{238}U. In the active inspection the bremsstrahlung beam endpoint energy was 13 MeV and ran at a 15 Hz repetition rate. The average electron charge per pulse was $\sim$ 88 nC. The run time was $\sim$ 601 s while that for the passive inspection was $\sim$ 43910 s.

Both Reedy and Slaughter eliminate γ-rays due to other nuclear reactions by removing those that have energy below a specific energy cut off [30, 31]. In this thesis a 3 MeV energy cut is used because there is a peak at $\sim$ 2.6 MeV from ^{208}Tl in the ^{232}Th decay chain. The 3 MeV energy cut was developed initially by examining the PNDA and ANDA energy spectrum for ^{238}U as was shown in figure 1.1. In the active inspection spectrum a significant amount of γ-rays were produced with energy above 3 MeV while most of the γ-rays from the passive inspection have energies below 3 MeV. A similar plot can be constructed using data obtained from the BGO detector. Figure 4.1 compares the decay of ^{238}U during a passive and active inspection. The yield was calculated from the γ-ray counts normalized to the run time and

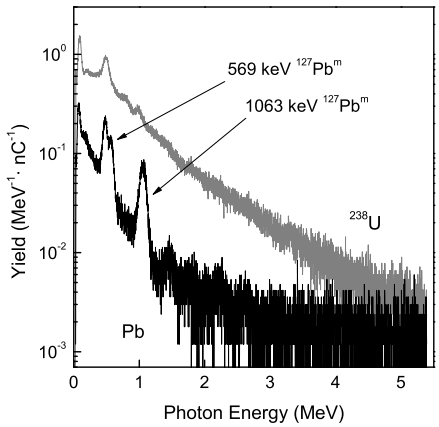

Figure 4.2: Photon energy spectra for ^{238}U and Pb. The targets were irradiated for 10 minutes with an average charge of 140 nC, a bremsstrahlung endpoint energy of 16 MeV and a 15 Hz repetition rate. The Uranium target has a yield 10 times larger on average than lead for energies above 3 MeV.

the energy width per channel. Here again, the active inspection reveals a significant number of γ-rays above 3 MeV which is not the case for the passive inspection. At this point it is necessary to determine whether or not non-fissionable materials will also produce high-energy γ-rays in an active inspection. Figure 4.2 shows the energy spectra for ^{238}U and Pb using the BGO detector. In this case, the yield is calculated by normalizing the counts by the charge on the radiator and the energy width per channel. The intensity for ^{238}U is on average 10 times larger than lead for energies above 3 MeV. The energy peaks in the Pb target at ~ 569 keV and ~ 1063 keV are due to isomeric transitions from ^{207m}Pb, these are metastable states that decay

by γ-ray emission. In a metastable state, the decay process is generally longer than typical γ-ray emissions from excited nuclear states [8]. Although the yield is significantly lower for lead, there are a number of γ-rays above 3 MeV. The concern is that if the mass of lead is increased the number of γ-rays above 3 MeV would also increase. If the mass of the non-fissionable material is large compared to the mass of the fissionable material, there will no longer be a distinction between the materials.

The possibility of confounding the detection system with a large mass of non-fissionable materials led to the examination of using a time cut. To maintain the distinction between fissionable and non-fissionable materials, a time cut is applied along with the energy cut of 3 MeV and is shown in figure 4.3. The figure compares the high-energy yield versus time for ^{238}U and Pb. The yield is calculated by normalizing the counts to the charge on the radiator and the time width per channel. The graph shows that the yield for ^{238}U decays from 0 to $\sim$ 15 ms then remains constant throughout the time period while the yield for Pb falls off in approximately 22 ms to the passive background level. The data is obtained from a BGO detector but the time cut is consistent for the NaI(Tl) detector. An assumption can be made from the data that γ-rays due to nuclear reactions other than fission occur within 22 ms while those due to fission continue throughout the time period. To test this assumption, neutron thermalization times in air were simulated using MCNPX (Monte Carlo N-Particle eXtended) code. The experimental cell was modeled and included a Watt distribution ^{238}U

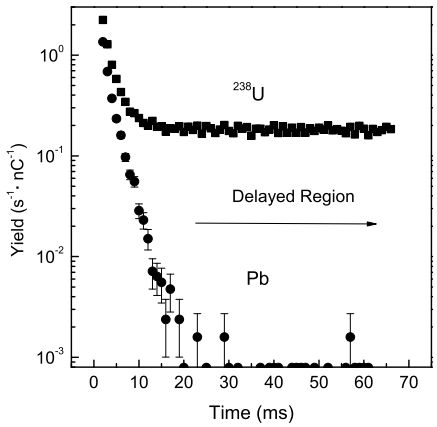

Figure 4.3: High-energy photon yield versus time for Pb (•) and ^{238}U (■). Both targets were irradiated for ∼10 minutes with an average charge of 140 nC, a bremsstrahlung beam endpoint energy of 16 MeV, and a 15 Hz repetition rate. The yield drops off for Pb after ∼ 22 ms. The error bars are similar in size to that of the symbols for the ^{238}U target.

neutron source emanating from the target location. A tally, which calculates the number of neutrons entering or leaving a specified surface, was measured on the surface of the concrete walls in the room and the target. Time bins for the tally measure up to 40 ms. The experimental configuration allowed for two neutron reactions: decay and absorption. The neutron decay half life is ∼ 614.6 s which is well beyond the time frame of the MCNPX tally resulting in essentially zero neutron decays leaving neutron absorption as the most probable reaction [22]. The neutrons are most likely absorbed through interactions in the concrete walls due to the large neutron absorption cross section of hydrogen which is presented in appendix figure A.3. Figure 4.4

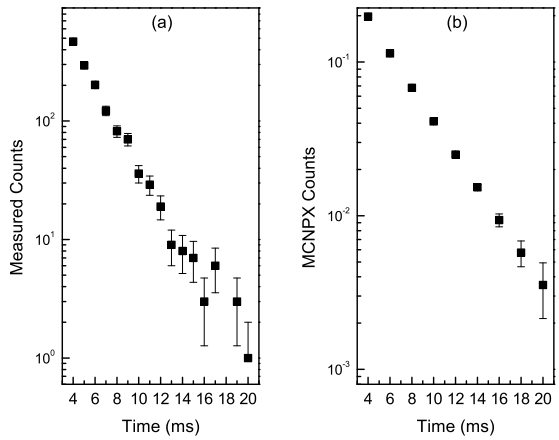

Figure 4.4: The measured data in (a) is taken from a Pb target. The bremsstrahlung beam endpoint energy was 16 MeV. The accelerator ran at a 15 Hz repetition rate and a radiation time of ~ 601 s. The MCNPX predicted data in (b) had a tally run time of 40 ms. The initial as well as ending data points were removed from the data to isolate neutron reactions from signal noise and yield from the active background.

presents a comparison between the measured data to the MCNPX results as a function of time. The measured data were taken from a Pb target. Initial as well as ending data points were removed from both sets of data to isolate neutron reactions to the time frame including the decay rate and the yield associated with the active background in the measured data. A comparison can be made between the measured and MCNPX data by examining the decay rate or slopes of the data presented. Similar decay rates suggest that the measured data is a result of neutron capture reactions analogous to the simulated data. Figure 4.5 shows the measured data in (a) along with the

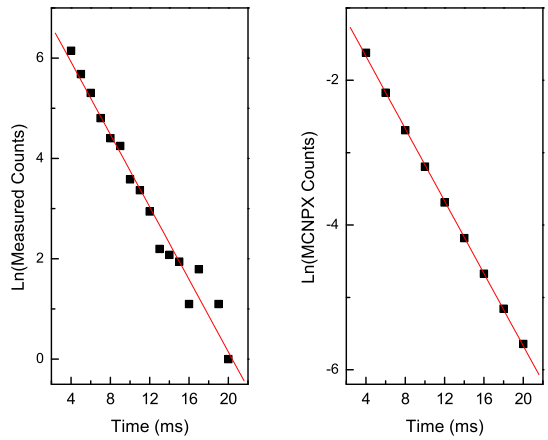

Figure 4.5: Measure data is presented in (a) while results from the MCNPX simulated data is shown in (b). A linear fit is applied to the number of events detected depicted in (a) and the number of particles tallied in (b) and these are graphed as a function of time. The line represents a linear fit of the data.

MCNPX data in (b). To apply a linear fit to the data, the natural log of the number of events detected and number of particles tallied is graphed as a function of time. For exponential functions the natural logarithm of the function becomes linearly proportional to the independent value [27]. The rate of decay of the measured data is $2.769 \pm 0.125\ \mathrm{ms}^{-1}$ and that for the MCNPX simulated data is $3.999 \pm 0.027\ \mathrm{ms}^{-1}$ with a percent difference of $\sim 36\%$. In light of the similarity in the decay rates between the data sets, it is likely that most of the reactions occurring in the non-fissionable targets prior to the 22 ms time cut are due to neutron capture reactions. Differences in the slopes may be due to various neutron absorbers present in the room

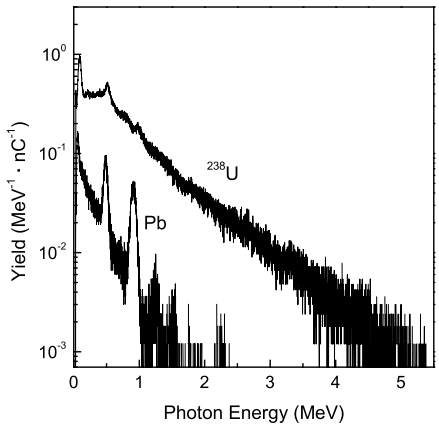

Figure 4.6: Time cut energy spectra for Pb and ^{238}U. The yield for Pb remains largely under an energy of 3 MeV.

during the experiments such as borated polyethylene.

By applying the time cut to the energy spectrum for the Pb and ^{238}U targets shown earlier, it is possible to more easily distinguish the fissionable from the non-fissionable target. Figure 4.6 shows energy spectra for Pb and ^{238}U using the 22 ms time cut. The data shows that the γ-rays detected for the non-fissionable material are largely less than 3 MeV. The signal yield increases over the background yield from an average of 10 times larger before the time cut to 28 times larger when the time cut is applied. Figure 4.2 shows two peaks close together in the Pb target which includes the $\sim$ 569 keV peak along with a peak at $\sim$ 476.9 keV. It is unclear why the first peak in the two peak region is occurring, however, it is no longer present when γ-rays that occur before $\sim$ 22 ms are removed which can be seen in figure 4.6.

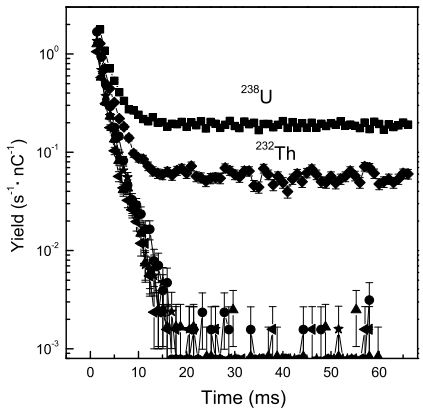

Figure 4.7: High-energy photon yield versus time for Pb (★), ^{9}Be (•), deionized H_2O (▲), and Al (◀) and for ^{238}U (■) and ^{232}Th (♦). All targets were irradiated for ∼10 minutes with an average charge of 140 nC. The accelerator operated at an energy of 16 MeV and at a 15 Hz repetition rate. The yield for the non-fissionable materials fall off in $\sim$ 22 ms.

Additional experiments were performed to verify that γ-rays emitted from various other non-fissionable materials largely occur within 22 ms and to confirm that they remain constant throughout the time period for fissionable materials other than ^{238}U. Figure 4.7 shows the high-energy yield versus time for several non-fissionable materials (Pb, ^{9}Be, deionized H_2O, and Al) and for the fissionable targets ^{238}U and ^{232}Th. The γ-rays from all the non-fissionable materials fall off rapidly in $\sim$ 22 ms while those for the fissionable materials keep a relatively high yield, two (^{232}Th) to three (^{238}U) orders of magnitude higher than the non-fissionable materials, throughout the time period beyond $\sim$ 15 ms.

4.2 Yield

The yield is a measure of the γ-ray counts normalized to the charge on the radiator. By normalizing to total charge on the radiator, each experiment is made comparable to one another. Unless otherwise specified, the following equation was used to calculate the yield for the experiments that follow,

$$Y = \frac{C}{QN_p}, \tag{4.1}$$

where C is the γ-ray counts, Q is the charge per pulse and N_p is the number of pulses fired by the accelerator. By irradiating targets at various energies, a determination can be made as to the best energy suited to distinguish fissionable materials from non-fissionable materials. In figure 4.8, the yield for Pb and ^{238}U are plotted from 7 MeV to 22 MeV in 3 MeV increments. The yield was calculated using both the high-energy and time cuts mentioned earlier. The most important characteristic to note from the figure is that the difference in yield from the ^{238}U and Pb targets recorded by the BGO detectors is larger than that from the NaI(Tl) detectors. At the highest energy, 22 MeV, the BGO detectors show a difference in the yield between the fissionable and non-fissionable targets of three orders of magnitude while in the NaI(Tl) detectors there is only a two order of magnitude separation. The ^{238}U yield for the BGO detectors is higher than that for the NaI(Tl) detectors due to its higher stopping power, however, the yield for the Pb is higher for the NaI(Tl) detector. It is also interesting to note that the yield at

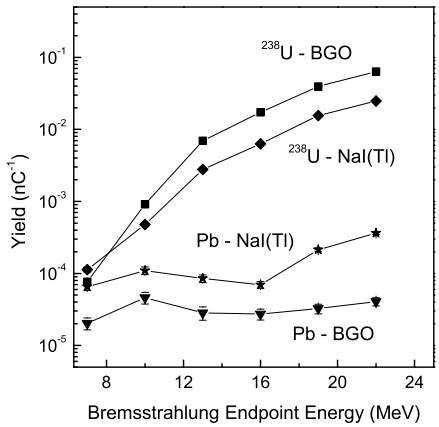

Figure 4.8: Charge normalized yield calculated using both the high-energy and time cuts. Data from the BGO detectors are symbolized as ^{238}U (■) and Pb (▼) while ^{238}U (♦) and Pb (★) represent the NaI(Tl) detectors. The average charge over all energies was 124 nC, the accelerator operated at a 15 Hz repetition rate and the targets were irradiated for $\sim$ 10 minutes.

7 MeV for the ^{238}U target recorded by the NaI(Tl) detectors lies above that for the BGO detectors. In determining why the yield for the Pb target was greater for the NaI(Tl) detector, crystal activation issues were considered.

4.2.1 NaI(Tl) Crystal Activation

Experiments have been performed and work published on the response of both NaI(Tl) and BGO detectors to neutrons. In 1981 O. Hausser *et al.* reports that for neutron energies below 2 MeV the BGO detector is significantly less sensitive than the NaI(Tl) detector and their sensitivity becomes equal around 3.5 MeV. At higher neutron energies the BGO detectors are

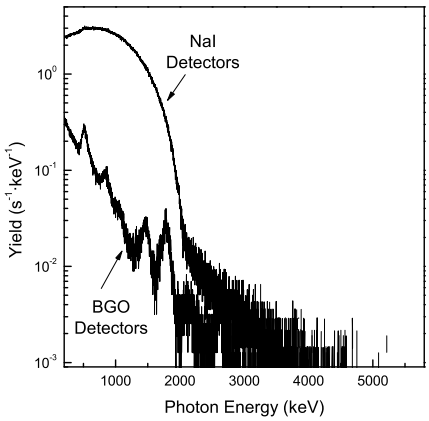

Figure 4.9: Energy spectrum for the 20 minute decay of a Pb brick target. The bremsstrahlung endpoint energy was 22 MeV and the accelerator operated at a 15 Hz repetition rate. The average charge on the radiator was 216 nC. At low energies the graph shows a β^- spectrum which inflates the γ-ray counts for the NaI(Tl) detector while the spectrum for the BGO detector shows the natural background.

slightly more sensitive [28]. Stemming from the results presented in the literature and increased yield values for non-fissionable materials for the NaI(Tl) detector, it was necessary to determine if the NaI(Tl) crystal was indeed being activated and to examine whether or not the BGO detector would also suffer from activation issues. In order to examine the possibility of crystal activation in the detectors, an energy spectrum was collected for a Pb brick which was irradiated for 10 minutes after which its decay was recorded for 20 minutes. The energy spectrum for the 20 minute decay recorded by the NaI(Tl) and BGO detectors is shown in figure 4.9. The energy spectrum

for the NaI(Tl) detector looked suspicious due to the absence of any natural background peaks. It seemed possible that additional energy was being deposited in the NaI(Tl) detector most likely from β^- particles emitted from β^- decay. The energy spectrum for the BGO detector resembled the natural background.

To test the hypothesis of neutron capture reactions within the NaI(Tl) detector a second experiment was performed in which a HPGe detector was used to record an energy spectrum of the NaI(Tl) crystal after being exposed to neutrons. In this second experiment, the NaI(Tl) detector (without electronics hooked up) was placed adjacent to a 1.3 kg metallic ^{238}U target. Although neutrons can be emitted from materials in the environment, the target was used to stimulate excess neutrons in a short period of time which could then be captured by the NaI(Tl) crystal thereby activating it. The target was irradiated for $\sim$ 10 minutes at 19 MeV and at 15 Hz. At the end of irradiation, an energy spectrum of the NaI(Tl) detector was immediately collected by the HPGe detector and is shown in figure 4.10. The figure shows γ-rays of 442.9 keV and 526.4 keV which correspond to ^{128}I which has a half life of 24.99 m and a peak at 1368.2 keV which corresponds to the ^{24}Na radionuclide with a half life of 19.595 h [22]. The presence of these peaks suggest ^{127}I(n,γ)^{128}I and ^{23}Na(n,γ)^{24}Na neutron capture reactions. The 526.4 keV peak is due to the β^- decay of ^{128}I to the 2^+ excited state of ^{128}Xe. The peak results from the decay of the ^{128}Xe* which transitions to an alternate 2^+ state [23]. The 442.9 keV peak is the result of a

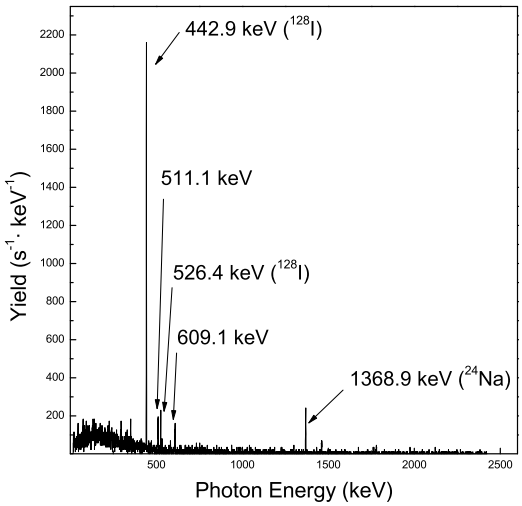

Figure 4.10: An energy spectrum for NaI(Tl) crystal recorded by HPGe detector. The energy spectrum shows peaks for ^{128}I and ^{24}Na. The crystal is being activated by neutron capture reactions.

^{128}Xe* 2^+ state to the ground state [23]. The 1368.2 keV corresponds to the decay of ^{24}Mg* which results from the β^- decay of ^{24}Na. The transition is from a 2^+ state to the ground state [23]. When excess neutrons are present the isotope stabilizes via β^- decay. In this reaction a proton is created from a neutron and to conserve charge an electron is created and emitted from the nucleus the instant of decay. A massless antineutrino is also emitted in the process. From the decay reactions mentioned, β particles or electrons are emitted and free to interact in the crystal. Since 511 keV is close to the rest mass energy of a positron, the 511 keV peak is likely due to the energy emitted from a positron-electron annihilation. Positrons are emitted

following β^+ decays and this type of decay can occur in the target or the crystal itself. For example, the ^{128}I isotope has a β^+ decay path [22]. It is unclear what reaction is causing the 609.1 keV energy peak; it is possible the peak is from impurities in the crystal. The endpoint energy of the emitted β particles for ^{128}I is $\sim$ 2.1 MeV and that for ^{24}Na is $\sim$ 4.1 MeV [23]. Figure 4.9 shows pulse pileup effects for the NaI(Tl) detector from these β particles in coincidence with γ-rays at energies beyond $\sim$ 2.1 MeV.

After performing additional experiments with both the NaI(Tl) and BGO detectors and reconsidering the yield data presented in figure 4.8, it is clear that the greater yield associated with the NaI(Tl) detector for the Pb target is due to NaI(Tl) crystal activation. For energies lower than 2.1 MeV the spectrum is dominated by β^- particles while pulse pileup effects are responsible for counts at higher energies. In re-examining the figure, the rise in the data for the NaI(Tl) detector at 7 MeV for the ^{238}U target occurs because the yield is again inflated due to NaI(Tl) activation issues, it is seen at this energy particularly because the γ-ray count is low.

4.3 Background Subtracted Yield

The yield values plotted in figure 4.8 are calculated using the gross signal. The gross signal is the observed signal which includes both the signal from the target and the active and passive background. There are two backgrounds mentioned in this thesis, the passive background which is the signal coming

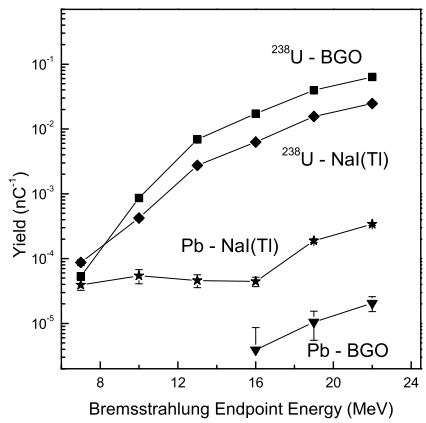

Figure 4.11: Data for the BGO detectors are symbolized as ^{238}U (■) and Pb (▼) while ^{238}U (♦) and Pb (★) represent the NaI(Tl) detectors. The average charge over all energies was 124 nC, the accelerator operated at a 15 Hz repetition rate and the targets were irradiated for $\sim$ 10 minutes.

from the environment in general, in this case the experimental cell, and the active background, which is represented by the active inspection of a non-fissionable target. In the figure, the Pb target is representative of the active background. In order to determine if the yield values for the Pb in the figure are being dominated by the passive background or if they are solely due to the target itself, the passive background signal can be subtracted from the observed signal. Figure 4.11 shows the passive background subtracted yield for all the targets presented. To subtract the passive background from the active background, the following equation was used,

$$Y_B = \frac{C_D - C_{PB}}{Q\omega t}, \tag{4.2}$$

where Y_B is the passive background subtracted yield, C_D are the γ-ray counts collected by the detector from the target, C_{PB} are the passive background counts from the environment and $Q\omega t$ is the total charge on the radiator which includes the repetition rate (ω) and the time of irradiation (t). In order to compare the passive inspection with the active inspection, the following equation was used to calculate the γ-ray counts collected by the detector from the environment (C_{PB}),

$$C_{PB} = \frac{C_B}{t_B} N_P t_{AP}, \tag{4.3}$$

where C_B is the number of γ-ray counts with energies above 3 MeV from the passive inspection, t_B is the total time the detector collected data from the passive inspection, N_P is the number of pulses executed in the active inspection and t_{AP} is the actual time remaining between accelerator pulses after the 22 ms in which the γ-rays are removed. Figure 4.11 shows some interesting properties, most obviously are the points absent (meaning a negative result) from the data at 7 MeV, 10 MeV, and 13 MeV for the Pb target in the BGO detectors. The negative result is indicative that the Pb signal is being dominated by the passive background. To determine whether or not the values for the Pb target are statistically the same, the errors were determined in quadrature and are listed in table 4.1. The yields at 7, 10, 13, and 16 MeV are all statistically zero while the yield at 19 MeV is more than two standard deviations from zero. As was mentioned previously, the passive background

Energy (MeV)	Y_B (nC^{-1})
7	(-2.9±3.8)×10^{-6}
10	(-3.8±8.6)×10^{-6}
13	(-6.9±6.0)×10^{-6}
16	(4.4±4.7)×10^{-6}
19	(11.0±5.0)×10^{-6}
22	(21.01±5.3)×10^{-6}

Table 4.1: Background subtracted yield with error for Pb target collected from the BGO detector.

dominates the yield from 7 to 13 MeV indicated by the negative yield values and while the yield is positive at higher energies, the ratio of passive to active background at both 16 and 19 MeV is greater. The yield at these energies is larger due to a greater detection of γ-rays from the active background. At 22 MeV the yield for the Pb target recorded by the BGO detectors is dominated by the active background. For the Pb target recorded by the NaI(Tl) detector, the active background including the activated crystal dominates the yield at all energies except 10 MeV where the active and passive backgrounds are equal. Although the active background dominates at all energies excluding 10 MeV for the NaI(Tl) detectors, the active background yield increases to over 60% of the total yield for energies starting at 16 MeV. This increase in the ratio of the active to the passive background is responsible for the increase in the yield starting at 16 MeV. The yields at 19 and 22 MeV for the NaI(Tl) detectors are distinguishable from one another while the yields at all the remaining energies are not.

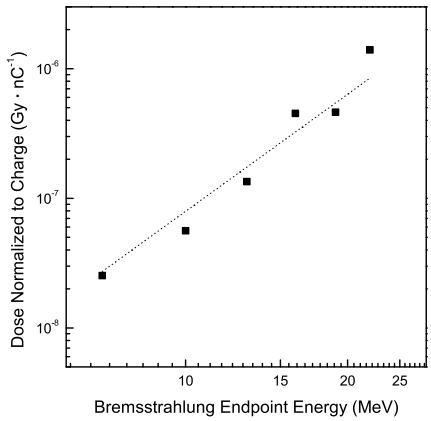

Figure 4.12: The data points show the dose normalized to the charge on the radiator as a function of the bremsstrahlung energy. The line is a fit of the data fixed to a cubed energy.

4.4 Yield as a Function of Dose

Another way to look at yield is by normalizing to dose on target. Dose is a measure of the radiation energy deposited in a material. The dose is measured by placing a dose map directly in front of the beam at the target location. In a dose map, OSLs (optically stimulated luminescence) are placed in a grid arrangement in between two borated polyethylene sheets. The grid is then centered with the bremsstrahlung beam axis at the target location and ultimately irradiated. The dose is calculated by taking an average of the dose recorded by each OSL and dividing by the charge on the radiator. The average charge on the radiator per pulse was 132 nC. The number of pulses is dependent on the charge so as to not over saturate the OSLs. The dose

was normalized to the charge incident on the radiator and was plotted as a function of the bremsstrahlung endpoint energy. A fit was then calculated to resemble a published equation that defines the dependence of dose on the bremsstrahlung energy [24]. The graph with the curve fit is presented in figure 4.12. The dose is proportional to the cube of the energy with a constant that is determined by the number of electrons hitting the target as well as the production efficiency of the target [24]. The calculated curve fit fixes the energy to a cube and determines the leading constant which includes the charge incident on the radiator. The curve fit equation is as follows,

$$D_Q = e^{-23.257 \pm 0.139} E^3, \tag{4.4}$$

where D_Q is the dose per charge on the radiator with units of $Gy \cdot nC^{-1}$ and E is the energy. The constant consequently has units of $Gy \cdot nC^{-1} \cdot MeV^{-3}$. To find the yield as a function of dose, the yield is normalized to dose and calculated in the following way,

$$Y_D = \frac{Y_B}{D_Q}, \tag{4.5}$$

where Y_D is the yield normalized to dose, Y_B is the passive background subtracted yield (equation 4.2) and D_Q is the dose (equation 4.4). The yield as a function of the fitted dose is shown figure 4.13. The characteristics of the graph follow those mentioned earlier in that the yield for the fissionable target is higher for the BGO detector due to its greater stopping power. Also,

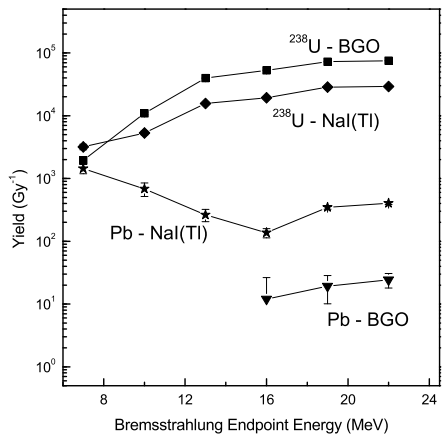

Figure 4.13: The passive background subtracted yield normalized to dose as a function of energy. Data from the BGO detectors are symbolized as ^{238}U (■) and Pb (▼) while ^{238}U (♦) and Pb (★) represent the NaI(Tl) detectors.

the yield for the non-fissionable target for the NaI(Tl) detector is greater due to crystal activation issues. The passive background again is dominant in the Pb target for the BGO detectors up to 22 MeV while the active background dominates the yield recorded by the NaI(Tl) detectors at all energies excluding 10 MeV. Starting at $\sim$ 13 MeV the rate of increase in the yield between energies for the ^{238}U target decreases for both detectors. This suggests that the dose per charge on the radiator has a larger increase with increasing energy than the yield at the respective energy. It would seem that this trend would continue at higher energies, but more experiments are required to prove this statement. Because the Pb target yield is low and fairly level for both detectors up to an energy of $\sim$ 16 MeV as shown in figure 4.11,

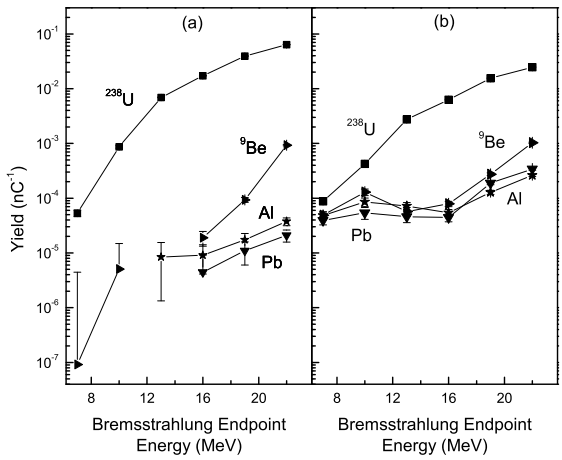

Figure 4.14: Charge normalized yield for (a) BGO detectors and (b) NaI(Tl) detectors for the non-fissionable targets ^{9}Be (▶), Al (★) and Pb (▼). Both graphs compare the yield with ^{238}U.

and the dose per charge on the radiator increases, the yield decreases with increasing energy. While the dose continues to increase for all energies, the increase in the yield is larger than the increase in the dose for energies larger than 16 MeV.

During the experiment other non-fissionable targets including beryllium and aluminum were irradiated. Figure 4.14 shows that all the non-fissionable targets irradiated can be distinguished from the fissionable targets. As previously stated, the yield is background subtracted. For the BGO detectors seen in figure 4.14a, the yield values at 7, 10, and 13 MeV for all three non-fissionable targets have large error bars, which suggests that the time of irradiation was too short at these energies. Longer run times would have to

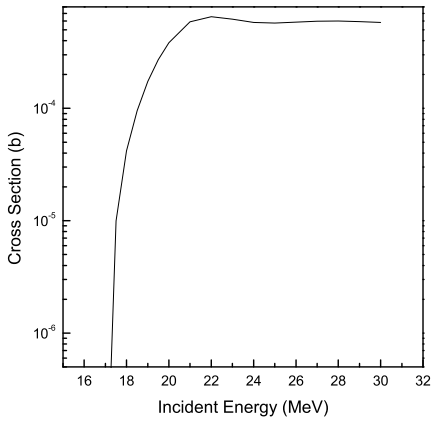

Figure 4.15: Cross section for the ^{9}Be(γ,p)^{8}Li reaction. The cross section increases significantly at $\sim$ 17 MeV [15].

be performed to get reasonable yield values for these targets. At 22 MeV the yield for both Al and Pb is 3 orders of magnitude lower than ^{238}U while that for ^{9}Be is 2 orders of magnitude lower.

For the NaI(Tl) detectors seen in figure 4.14b, the error bars at all energies are reasonable. At 7, 10, 13, and 16 MeV ^{9}Be, Pb, and Al are statistically the same. At 22 MeV, both Pb and Al are two orders of magnitude lower than ^{238}U while the ^{9}Be is one order of magnitude lower.

There is a significant increase in the cross section for ^{9}Be(γ,p)^{8}Li reactions at $\sim$ 17 MeV which is presented in figure 4.15 [15]. The half life of ^{8}Li is 838 ms and decays via β^{-} decay [22]. The increase in the yield for both detector types for the ^{9}Be target after $\sim$ 16 MeV is most likely due to the β particles resulting from the decay of ^{8}Li.

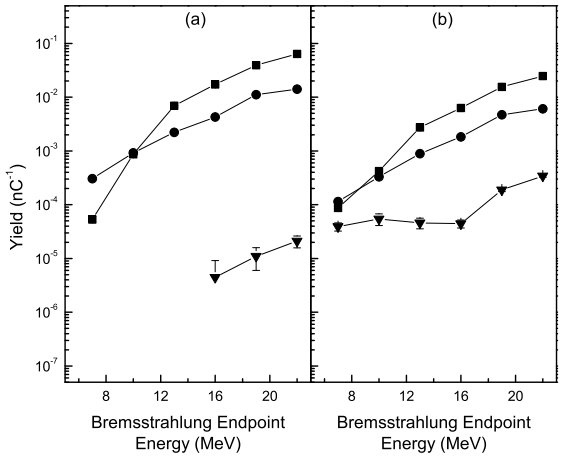

Figure 4.16: Charge normalized yield for (a) BGO detectors and (b) NaI(Tl) detectors for ^{232}Th (●). Both graphs compare the yield with ^{238}U (■) and Pb (▼).

Along with ^{238}U, ^{232}Th was irradiated as an additional fissionable target. Figure 4.16 shows the charge normalized yield for (a) the BGO detectors and (b) the NaI(Tl) detectors. Again all yields are background subtracted. In comparison with ^{238}U, the ^{232}Th yield is within 1 order of magnitude at all energies. While the ^{232}Th yield is below that of ^{238}U for all energies larger than 10 MeV for both detectors, it is above at 7 MeV. The ^{232}Th yield is most likely above the ^{238}U yield at 7 MeV due to its photonuclear cross section. The cross section for ^{232}Th rises above ^{238}U from $\sim$ 6 to 7 MeV which can be seen in the cross section figure in section 2.2.2.

4.5 Minimum Detectable Mass

From the yields the minimum detectable mass can be determined. The Minimum Detectable Mass (MDM) describes how much fissionable mass is required in order to be detected. The MDM is calculated using equation 2.21. Starting with equation 2.14, $k_\alpha = 1.645$ corresponding to a 95 % confidence interval, the hypothetical charge on the radiator (Q_H) is set equal to an average charge of 100 nC multiplied by a 600 s run time and a 15 Hz repetition rate. A deionized H_2O target is used as the active background because it most closely resembles the sample which is obtained from a mass of 2.179×10^1 g (which is the total mass in the beam) of a 4.7 % ^{238}U in deionized water target. Figure 4.17 shows a graph of the MDM as a function of bremsstrahlung energy. Energies calculated are from 10 to 22 MeV in 3 MeV increments. The most important characteristic in the figure to note is that the BGO detectors have a lower MDM for all energy values except at 10 MeV. At 10 MeV the values from both detectors are statistically equivalent. The error bars are large at 10 MeV because the difference in the yields between the deionized H_2O and ^{238}U targets is small. At 22 MeV, ~ 5 times the amount of ^{238}U is required for detection by the NaI(Tl) detectors as opposed to the BGO detectors. Table 4.2 lists the minimum detectable mass in grams for the 4.7 % ^{238}U in deionized water target.

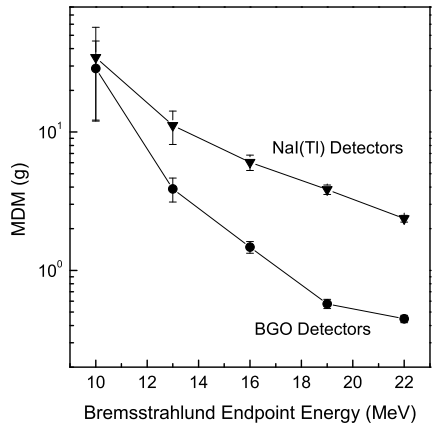

Figure 4.17: The minimum detectable mass using deionized water as the active background for the BGO detectors (■) and NaI(Tl) detectors (▼). The MDM is calculated using the a 4.7 % ^{238}U in deionized water.

Energy (MeV)	Detector	MDM (g)	Ratio of MDM NaI(Tl)/BGO
10	BGO	22.7±16.8	
10	NaI(Tl)	34.6±22.4	1.20±1.66
13	BGO	3.88±0.77	
13	NaI(Tl)	11.2±3.02	2.87±1.34
16	BGO	1.47±0.14	
16	NaI(Tl)	6.04±0.77	4.10±0.91
19	BGO	0.57±0.04	
19	NaI(Tl)	3.84±0.30	6.70±0.99
22	BGO	0.45±0.03	
22	NaI(Tl)	2.37±0.13	5.29±0.64

Table 4.2: MDM Calculated with the Observed Signal

4.6 Energy Cut Revisited

As stated earlier, the 3 MeV energy cut helped to define a signature for fissionable materials based on the energy of the emitted γ-rays. The cut

at 3 MeV was largely used to remove a high-energy peak that corresponded with the decay of ^{232}Th. This section gives a more detailed analysis of the best energy, which should be used, to create a unique signature for fission. By examining the fissionable target yield, along with the MDM, a reliable energy cut can be established. While the yield should be larger for cuts that start at lower energies, the MDM is determined not only based on the fissionable target yield but also on the active background yield, in this case the deionized H_2O target. Since the passive background is included in both the active background and the fissionable target, it is ultimately removed during the active background subtraction. By examining energy cuts at 2.50, 2.75, 3.00, 3.25 and 3.50 MeV for both the yield and MDM a reasonable energy cut can be established. Figure 4.18 shows the yield and figure 4.19 presents the MDM both as a function of energy cut for the BGO detectors. The MDM is lowest for all bremsstrahlung energies at 2.75 MeV. At the 3.00 MeV energy cut the data points for each bremsstrahlung energy are statistically the same with those at 2.75 MeV. When comparing the MDM values with the yield at equivalent energy cuts, the 2.75 MeV energy cut has a higher yield. Since the 2.75 MeV energy cut has both the lower MDM values and the higher yield, it is the best energy cut to use for a unique fission signature for the BGO detectors. The graphs for the NaI(Tl) detectors showing the yield and MDM are presented in figures 4.20 and 4.21 respectively. In the case of the NaI(Tl) detectors, the energy cut with the lowest MDM values at all energies except 10 MeV is at 2.50 MeV and at this

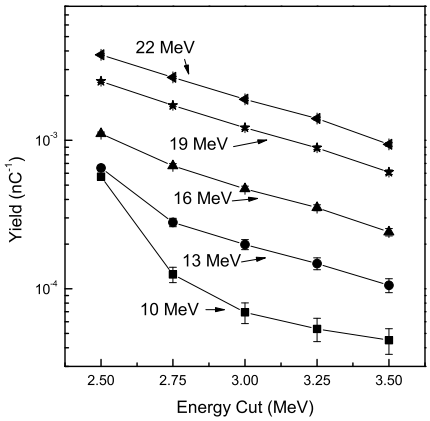

Figure 4.18: Yield versus energy cut showing the 4.7 % ^{238}U in deionized water target for the BGO detectors. The bremsstrahlung energy values are represented with a ■, ●, ▲, ★, and a ◄ for energies of 10, 13, 16, 19 and 22 MeV respectively.

same energy the yield is the highest. At 10 MeV the lowest MDM value is at the 2.75 MeV energy cut. However, because a ^{238}U target is used, the yield does not have counts associated with the ^{232}Th high energy decay peak. The 2.50 MeV energy cut is below the energy of the ^{232}Th decay peak. The next best energy cut to use which does not include the ^{232}Th decay peak is the 2.75 MeV energy cut.

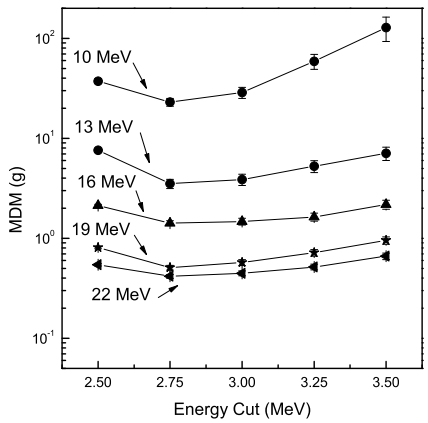

Figure 4.19: The MDM versus energy cut for the BGO detectors using 4.7 % ^{238}U in deionized water target. The bremsstrahlung energy values are represented with a ■, ●, ▲, ★, and a ◄ for energies of 10, 13, 16, 19 and 22 MeV respectively.

4.7 MDM, Delayed Neutrons vs. Delayed γ-Rays

Due to the larger difference in yield between the fissionable and non-fissionable materials and the lower MDM values in the BGO detectors compared with the NaI(Tl) detectors, the BGO detectors are more suited to high-energy delayed γ-ray detection and are therefore the focus of this section and the sections to follow. In a preliminary look, along with detecting delayed γ-rays, photonuclear neutron detectors (PNDs) were used in the experiment for the detection of delayed neutrons. Delayed neutrons may be emitted following

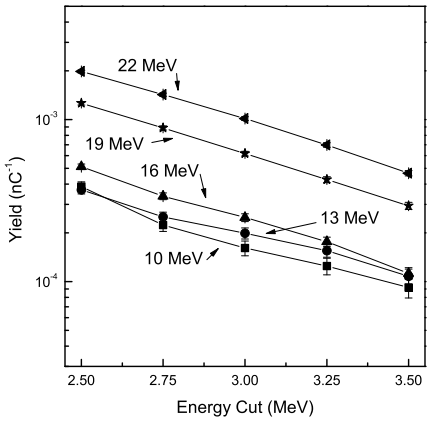

Figure 4.20: The yield versus energy cut for the NaI(Tl) detectors showing the 4.7 % ^{238}U in deionized water target. The bremsstrahlung energy values are represented with a ■, ●, ▲, ★, and a ◄ for energies of 10, 13, 16, 19 and 22 MeV respectively.

the β^- decay of fission fragments and can also be used to develop a unique signature for fission reactions. Six PNDs were used in the experiment and were placed at a 90° angle to the target and at a distance of $\sim$ 0.6 m. All the other characteristics of the setup including the collimator sizes mentioned in section 3.1 are the same. A schematic of the detector to target arrangement in relation to the γ-ray detector array is presented in figure 4.22. Each PND is 10.8 cm in diameter and 53.34 cm tall with an active detection region consisting of a ^{3}He gas tube 2.36 cm in diameter and 20.31 cm in length. The ^{3}He gas tube is surrounded with polyethylene, cadmium and boraflex which serve to moderate neutrons for better detection and to minimize the detection of

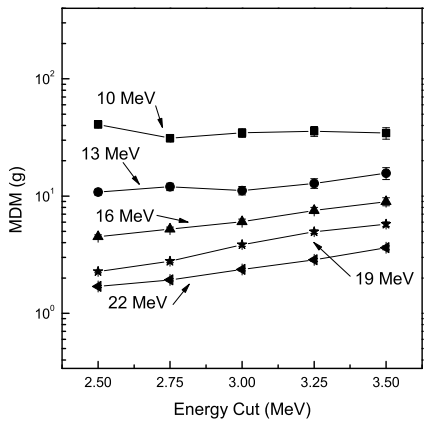

Figure 4.21: The MDM versus energy cut for the NaI(Tl) detectors using the 4.7 % ^{238}U in deionized water target. The bremsstrahlung energy values are represented with a ■, ●, ▲, ★, and a ◄ for energies of 10, 13, 16, 19 and 22 MeV respectively.

low energy neutrons. The detectors operated at −1410 V. The physics detailing the detection of the neutrons is not a topic of this thesis, however, the charged products in the reaction between the ^{3}He and the neutrons initiate the detection signal.

In order to compare the MDM required for both the PNDs and the BGO detectors it is necessary to normalize the yield to solid angle. The yield is calculated using equation 4.2 and utilizes the 4.7 % ^{238}U in deionized water fissionable target along with the active background deionized water target. The area determined for each PND includes the moderating material and is equal to 219.5 cm^2 making the total area for all six detectors $\sim$ 1317 cm^2.

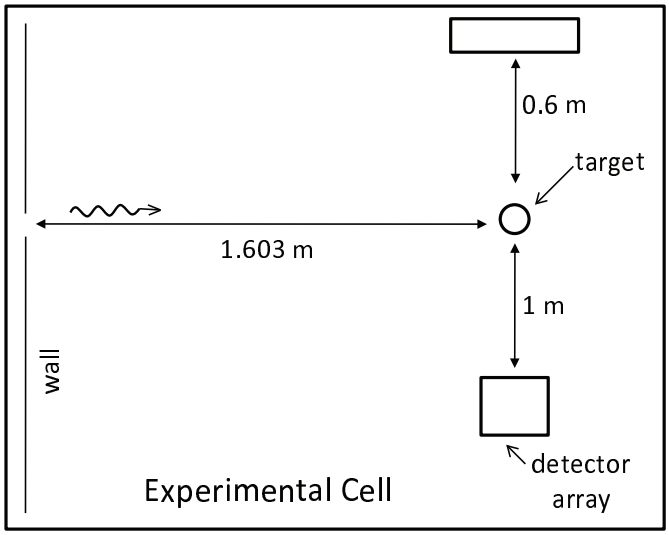

Figure 4.22: Location of PNDs in relation to γ-ray detector array. The PND's are located $\sim$ 0.6 m from the target.

The area of each BGO detector is 20.4 cm^2 making the total area including two detectors $\sim$ 41 cm^2. Both the 3 MeV energy cut as well as the 22 ms time cut are implemented in the data collected from the BGO detectors, however, while a time cut is applied to the neutron data an energy cut is not. To standardize the experiment the hypothetical charge on the radiator includes a charge of 120 nC, a 15 Hz repetition rate and a time of irradiation of 600 s. The hypothetical area used is equal to the area of the PNDs of 1317 cm^2 and the hypothetical distance from the target to the detectors is 1 m. The MDM versus bremsstrahlung endpoint energy for the delayed neutrons and γ-rays are graphed in figure 4.23. While both detectors measure a value for the MDM that decreases with energy, the BGO detectors constantly measure

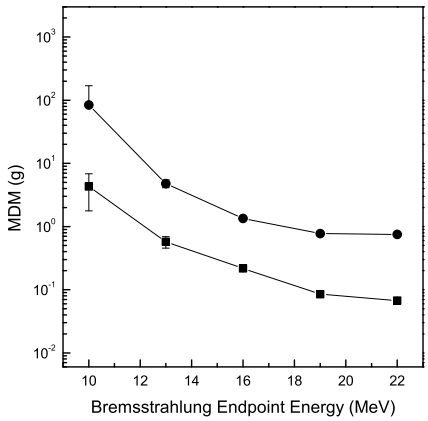

Figure 4.23: Minimum detectable masses versus energy for delayed neutrons (•) and delayed γ-rays (■) using the PNDs and BGO detectors respectively.

a lower MDM. The MDM measurements using the neutron detectors begin to show little improvement from 16 MeV to 19 MeV and then from 19 MeV to 22 MeV. These results are due to the β^- decay of ^{17}N resulting from the ^{18}O(γ,p)^{17}N reaction. The half life of ^{17}N is 4.173 s [22]. The reaction threshold is significant at $\sim$ 16 MeV which is shown in the cross section presented in figure 4.24 [32]. More experiments would need to be performed to see how the MDM values fair with alternate fissionable materials and various active background targets.

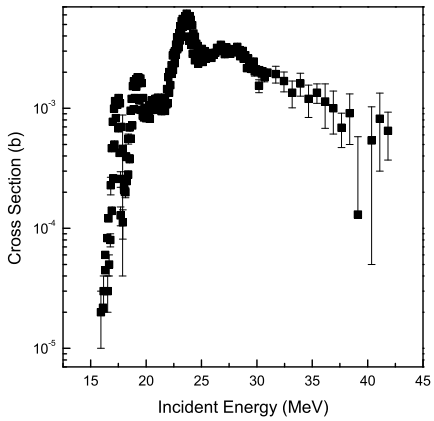

Figure 4.24: Cross section for the ^{18}O(γ,p)^{17}N reaction [32].

4.8 Filtering Out γ-Rays

One primary focus of this thesis is to determine which detector, BGO or NaI(Tl), is better at detecting delayed γ-rays and therefore used to develop a unique signature for fission. Results from the previous experiments show that BGO is a more favorable detector for high-energy γ-ray detection and hence they will be used for future experiments to further develop the technique. The experiments presented in this section were performed prior to the active and passive inspection experiments shown in section 4.1. The discussion of these experiments was delayed and presented at this point to focus attention solely on the BGO detectors.

Initially there was a concern that the detectors were saturated from the large amount of scattered x-rays from the primary bremsstrahlung beam.

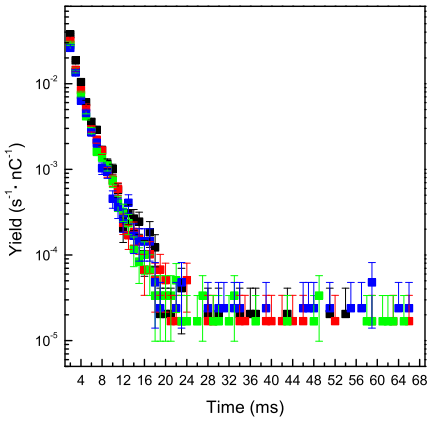

Figure 4.25: Yield versus time. Data was collected where lead filters were placed directly in front of the BGO detectors. The thickness used were 0 cm (black), 0.32 cm (red), 0.95 cm (green) and 2.54 cm (blue).

When these experiments were performed, the origin of the high-energy photon yield occurring before the 22 ms time cut was unknown. The initial thought was that these counts could potentially be an artifact during detector recovery. Lead filters were placed on the front face of the detectors to reduce the energy deposited by the scattered x-rays, thereby decreasing the recovery time. Filters of various thicknesses were applied to examine their affect on the recovery time which could thereby reduce the 22 ms time cut. Lead with thickness of 0.32, 0.95, and 2.54 cm were individually placed directly in front of the BGO detectors. Figure 4.25 shows the yield as a function of time for the lead filters with thicknesses listed above. The results showed that the yield intensity leveled to background levels at $\sim$ 22 ms for

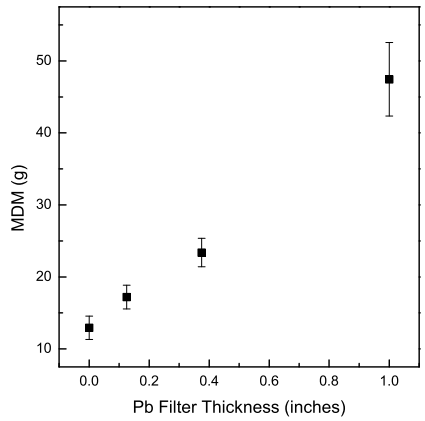

Figure 4.26: MDM for various Pb filter thicknesses.

all the filter thicknesses presented, suggesting the detector recovery was not responsible for the elevated high-energy photon yield prior to ~ 22 ms and therefore the time cut did not change.

The MDM was calculated to examine the affects of the changing yield due to the lead filters. Figure 4.26 shows the MDM as a function of Pb filter thickness. The lowest MDM value exists with no Pb filter which confirms that the Pb filters were unnecessary.

4.9 BGO Detector Shielding

Shielding materials are used to reduce the number of low energy and backscatter γ-rays detected by the detector and to absorb neutrons that create neutron capture reactions. In order to determine whether or not the BGO

detectors would require shielding in future experiments, experiments were performed with different shielding arrangements. Three shielding arrangements were constructed. In the first arrangement, 5.08 cm of lead was placed around the detectors at every side except the front. In the second arrangement, 10.16 cm of borated polyethylene was placed in a similar fashion to the way the lead was arranged. Finally, in the third arrangement, 5.08 cm of lead was placed around the detectors and this lead was then covered with 10.16 cm of borated polyethylene to make the total shielding thickness 15.24 cm. Lead was used as a shielding material because of its large photoelectric absorption and Compton scattering cross sections. The absorption of γ-rays results not only from the photoelectric effect but also as the electrons thermalize from being scattered through Compton scattering reactions. Figure 4.27 shows the sum of the cross sections for these two reactions. The borated polyethylene was used because of its boron content. Boron absorbs neutrons and emits γ-rays through (n,γ) reactions. The γ-rays emitted from the neutron reactions are likely stopped by the Pb that is placed adjacent to the boron material closest to the detectors. There are two stable isotopes of boron that can produce γ-rays, ^{10}B and ^{11}B. Figure 4.28 presents the (n,γ) cross sections for ^{10}B and ^{11}B. The figure shows that γ emitting reactions are probable in the energy region from thermal to fast neutrons and are most likely for thermal neutrons in ^{10}B.

Figure 4.29 presents the yield for Pb and ^{238}U targets as a function of the three shielding arrangements mentioned earlier. For the Pb target, the

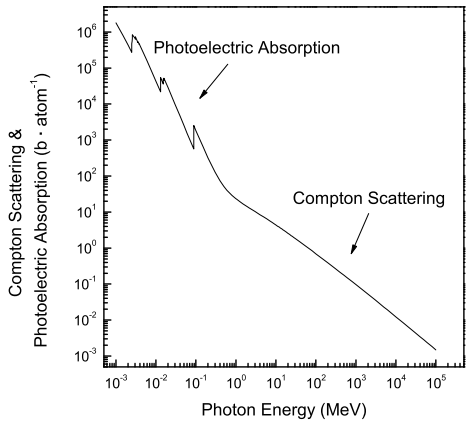

Figure 4.27: Compton scattering and photoelectric absorption cross sections for lead.

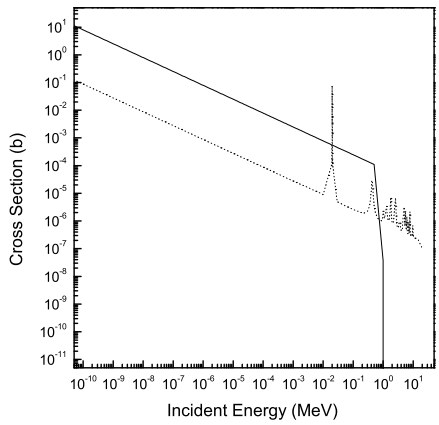

Figure 4.28: Cross sections showing the (n,γ) reactions for ^{10}B (__) and ^{11}B($\cdots$).

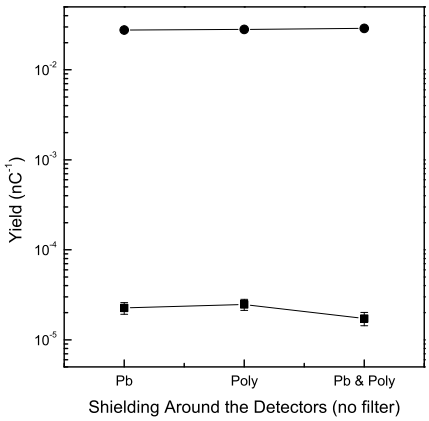

Figure 4.29: High-energy yield for the Pb (■) and ^{238}U targets (•). The targets were irradiated for 10 minutes while the accelerator operated with a bremsstrahlung endpoint energy of 19 MeV and a 15 Hz repetition rate. For all three shielding arrangements presented no material was placed on the front surface of the detectors.

yield for all three arrangements are no more than two standard deviations apart. For the ^{238}U target the arrangements including Pb only and borated polyethylene only are within two standard deviations and therefore statistically the same.

In additional experiments, shielding was added to all sides of the detectors including the front surface. In these experiments, there were again three arrangements. In the first arrangement, 5.08 cm of Pb was placed on all sides of the detectors excluding the front surface, and 10.16 cm of borated polyethylene was placed outside of the Pb shielding around all surfaces of the detector including the front. The second arrangement was similar to

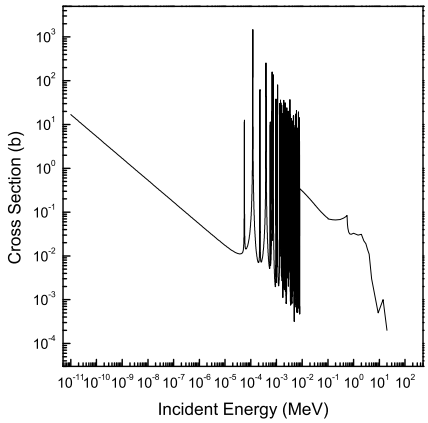

Figure 4.30: The neutron capture cross section for ^{114}Cd shows a large cross section for thermal neutrons.

the first but it included a 0.64 cm thick Pb sheet which was placed on the front surface closest to the detectors with the borated polyethylene covering the Pb. The third arrangement was similar to the second with a 0.16 cm thick sheet of cadmium placed in between the Pb and borated polyethylene shielding.

Cadmium is used as a shielding material to capture thermal neutrons. The neutron capture cross section for the most stable isotope of cadmium, ^{114}Cd, is presented in figure 4.30. The cross section for the neutron capture in ^{114}Cd is quite large for thermal neutrons. Cadmium is placed in between the borated polyethylene and Pb to capture neutrons passing through the borated polyethylene. The Pb then serves to reduce the number of emitted γ-rays from the cadmium. The high-energy yield for the arrangements with

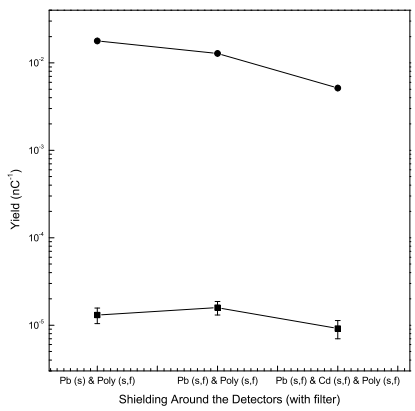

Figure 4.31: High-energy yield for the Pb (■) and ^{238}U targets (•). The targets were irradiated for 10 minutes while the accelerator operated with a bremsstrahlung endpoint energy of 19 MeV and a 15 Hz repetition rate. The three arrangements included detector front face shielding labeled with an 'f' in parenthesis and side shielding labeled with an 's'.

detector front surface shielding is shown in figure 4.31. The figure shows in the ^{238}U target that the yield goes down when more detector front face shielding is added with the largest difference between the first arrangement and the third arrangement with a difference of ~ 3.5 times. The ^{238}U target yields are all differentiable from one another while the Pb target yields are all within two standard deviations and therefore equal.

Again, MDM results can be examined to study the effectiveness of the shielding arrangements. Figure 4.32 presents the MDM as a function of shielding arrangement where no front face shielding is utilized. The lowest MDM corresponds to the arrangement which includes both Pb and bo-

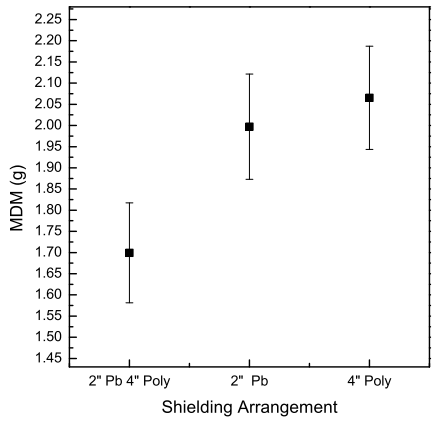

Figure 4.32: MDM as a function of shielding arrangement. None of the arrangements presented include front face shielding.

rated polyethylene however, all values are within two standard deviations and therefore statistically equal. Because the arrangements maintain equal MDM values, no one arrangement is advantageous in relation to the others.

Figure 4.33 shows the MDM values as a function of shielding arrangement for arrangements which include front face detector shielding. Here the lowest MDM value corresponds to the arrangement with the least amount of front face detector shielding, however this MDM value is still above the arrangement with no front face detector shielding. As stated previously, since the MDM value is lowest with no front face detector shielding it does not seem reasonable to use front face detector shielding in future experiments.

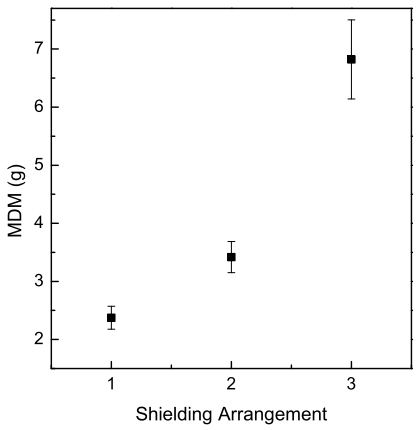

Figure 4.33: MDM as a function of shielding arrangement. All arrangements presented include front face shielding. Arrangement 1 includes 5.08 cm of Pb on the sides, and 10.16 cm of borated polyethylene was placed outside of the Pb shielding around all surfaces of the detector including the front. Arrangement 2 had 5.08 cm of Pb on the sides and included a 0.64 cm thick Pb sheet which was placed on the front surface closest to the detectors with the 10.16 cm of borated polyethylene covering the Pb. Arrangement 3 was similar to arrangement 2 only it included a 0.16 cm thick sheet of cadmium in between the Pb and borated polyethylene.

Chapter 5

Conclusions and Future Work

5.1 Conclusions

While both BGO and NaI(Tl) detectors are reliable choices for γ-ray detection, the experiments in this thesis reveal that the BGO detectors are more suited for high-energy delayed γ-ray detection in active inspection environments with a large neutron flux. As mentioned in section 4.2.1, the ^{127}I(n,γ)^{128}I and ^{23}Na(n,γ)^{24}Na neutron capture reactions of the NaI(Tl) crystal provide a basis for this claim. These neutron capture reactions increase the yield for the non-fissionable materials due to the detection of β^- particles produced from β^- decay. This background decreased the difference between the yield of the fissionable and non-fissionable materials making a less distinguishable signature for fission in the NaI(Tl) detector. With the BGO detector, not only was a lower yield for the non-fissionable materials

recorded, but due to the crystal's higher stopping power the yield for the fissionable materials was higher than that for the NaI(Tl) detector. In calculating the yield, both a high-energy and time cut were used to develop a unique signature for fissionable materials. The high-energy cut was utilized because γ-rays with higher energies are more abundant in induced fission reactions while the time cut was applied as a means to isolate the delayed fission γ-rays from those that occur due to other nuclear reactions. In this examination, while a cut of 3 MeV was applied, a cut of 2.75 MeV could also have been selected. A time cut of 22 ms was also implemented.

A lower minimum detectable mass, MDM, for the BGO detectors was determined at all energies greater then 10 MeV for those energies presented due to the larger difference in the yield from the fissionable and non-fissionable materials. At 10 MeV, the MDM was statistically similar for both detectors. A lower MDM means that less mass of the fissionable material is required for detection, which implies the ability to detect for shorter run times, greater stand off detection distances, and/or reducing the number of BGO detectors in the detector array which has substantial cost advantages. The MDM was not only lower for the BGO detectors in comparison to the NaI(Tl) detectors but it was also lower in relation to the neutron detectors. Fissionable material signatures can also be developed using delayed neutrons, MDM values were calculated using the yield of these neutrons. While the MDM was lower for the BGO detectors in these experiments, more work would have to be preformed to examine the effect on MDM for both delayed neutron and

γ-rays with different target and shielding materials.

The use of filters was also examined in the work presented and it was determined that detector recovery was not responsible for the γ-rays emitted prior to 22 ms. The MDM was examined from these experiments and the results show that the filters were unnecessary. Different shielding arrangements were also tested to examine whether the background radiation reduced by their use would lower the MDM. The analysis shows that when shielding is placed on all faces of the detector except the front face, Pb alone proves to be an adequate shielding material. For the shielding arrangements that included front face shielding, the results show that the additional shielding was not effective at lowering the MDM. These tests proved that the use of front face shielding would not aid in the development of a unique fission signature.

5.2 Future Work

As a result of the work presented in this thesis, six BGO detectors have been purchased and experiments have recently been performed. A recent experiment set out to compare detection results for delayed γ-rays against delayed neutrons. The data obtained from the experiment has yet to be analyzed, but it will be a first in several experiments aimed to determine which detection method (detection of delayed γ-rays or delayed neutrons) will result in a lower MDM for various fissionable materials. A second reasonable step to this experiment is to determine which detection method is more

reliable with different shielding matrices. Future experiments may consist of using the BGO detectors for stand off detection measurements as well as delayed γ-ray coincidence detection.

Appendix A

Neutron Capture Cross Sections

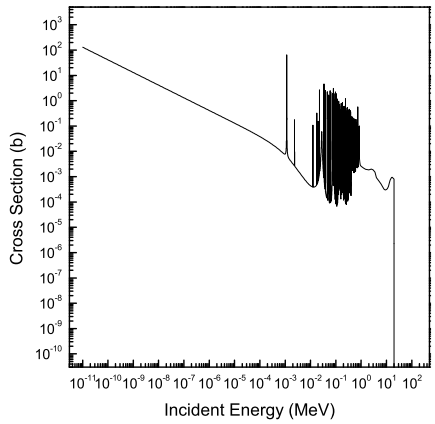

Figure A.1: Neutron Capture Cross Sections for ^{56}Fe.

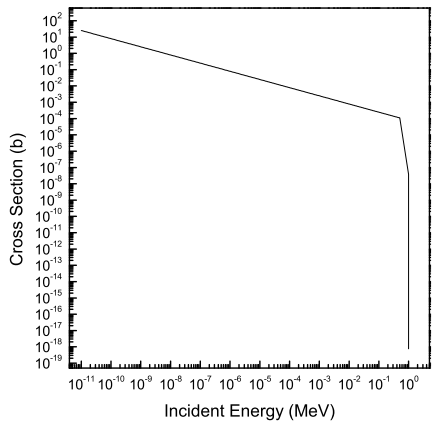

Figure A.2: Neutron Capture Cross Sections for ^{10}B.

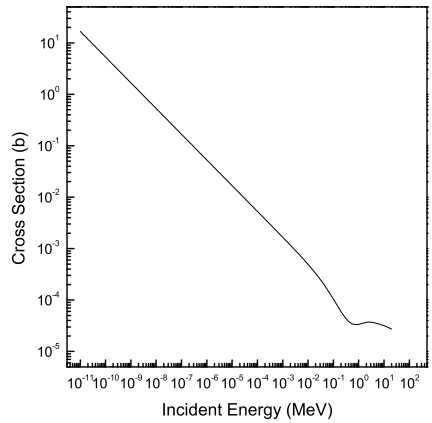

Figure A.3: Neutron Capture Cross Sections for ^{1}H.

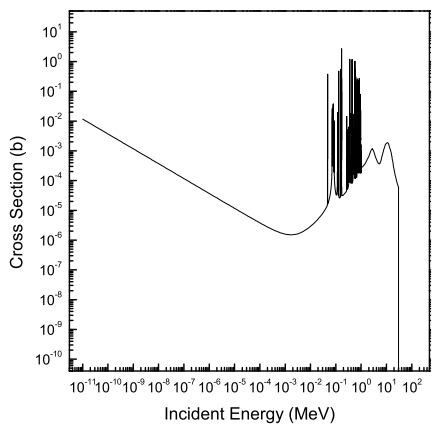

Figure A.4: Neutron Capture Cross Sections for ^{208}Pb.

Appendix B

Photonuclear Cross Sections

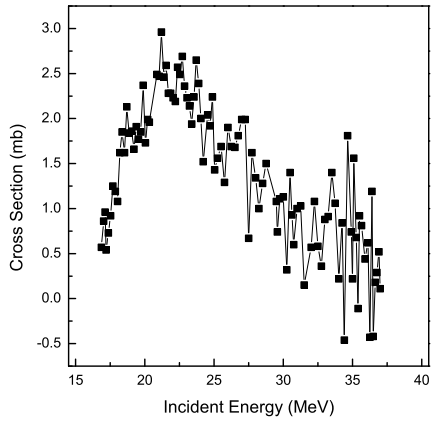

Figure B.1: Photonuclear Cross Sections for ^{9}Be. The cross section is for (γ,n) reactions [26].

Bibliography

[1] T. Gozani, United states Regulatory commission Report No. NUREG/CR-0602, 1981.

[2] Maritime Transport Committee, Organisation for Economic Co-operation and Development, Security in Maritime Transport: Risk Factors and Economic Impact, 2003.

[3] United States General Accounting Office Report No. GAO-03-770, 2003.

[4] Standford Study Group, Container Security Report, 2003.

[5] N. Bohr and J. A. Wheeler, Phys. Rev. **56**, 426 (1932).

[6] M. J. Martin, ENSDF Citation NDS **70**, 315 (1993).

[7] G. Audi and A. H. Wapstra, Nuclear Physics A **A565**, 21-65 (1993).

[8] K. S. Krane, *Introductory Nuclear Physics.* (John Wiley and Sons, Inc., New York, 1988).

[9] D. Reilly, N. Ensslin, J. Hastings Smith, and S. Kreiner, United States Regulatory Commission Report No. NUREG/CR-5550, 1991.

[10] R. Vandenbosch and J. R. Huizenga, *Nuclear Fission.* (Academic Press, New York, 1973).

[11] D. Bodansky. *Nuclear Energy: Principles, Practices, and Prospects. 2nd Edition* (Springer 2004).

[12] M. T. Kinlaw and A. W. Hunt, Appl. Phys. Lett. **86**, 254104 (2005).

[13] T. R. England and B.F. Rider, Los Alamos National Laboratories Report No. LA-UR-94-3106 ENDF-349, 1993.

[14] J. L. Jones, Y. D. Harker, W. Y. Yoon, J. M. Hoggan, and G. J. McManus, Idaho National Engineering Laboratory Report No. INEL-A-9356, 1994.

[15] M. B. Chadwick, P. Obložinský, M. Herman *et al.*, "ENDF/B-VII.0 Next Generation Evaluated Nuclear Data Library for Nuclear Science and Technology", Nuclear Data Sheets, **1**07, 2931 (2006).

[16] S. J. Thompson, M. T. Kinlaw, J. F. Harmon, D. P. Wells, E. B. Farfan and A. W. Hunt, Appl. Phys. Lett. **90**, 074106 (2007).

[17] M. J. Weber and R. R. Monchamp, J. Appl. Phys. **44**, 5495 (1973).

[18] M. J. Berger, J.H. Hubbell, S.M. Seltzer, J. Chang, J.S. Coursey, R. Sukumar, and D.S. Zucker, NIST Standard Reference Database 8 (XGAM), (1990).

[19] Glenn F. Knoll, *Radiation Detection and Measurement. 3rd Edition* (John Wiley and Sons, Inc., New York, 2000).

[20] G. B. Saha, *Physics and Radiobiology of Nuclear Medicine. 3rd Edition* (Springer, 2006).

[21] L. A. Currie, Analytical Chemistry, **40**, 586 (1968).

[22] S. Y. F. Chu, L.P. Ekstrm, and R.B. Firestone, The Lund/LBNL Nuclear Data Search, (1999).

[23] E. Browne, J. Dairiki, R.E. Doebler *et al.*, *Table of Isotopes 7th Edition* (Wiley-Interscience, New York, 1978).

[24] P. I. Kuznetsov, Translated from Atomnaya Energiya **69**, 103 (1990).

[25] S. N. Beljaev, Izv. Rossiiskoi Akademii Nauk, Ser. Fiz., **5**, 953 (1991).

[26] U. Kneissl, G. Kuhl, *et al.*, Nuclear Physics, Section A, **247**, 91 (1975).

[27] John R. Taylor *An Introduction to Error Analysis The Study of Uncertainties in Physical Measurements. 2nd Edition* (University Science Books, California, 1997).

[28] O. Hausser *et al.*, Nuclear Instruments and Methods **213**, 301 (1983).

[29] A. E. Evans IEEE Transations on Nuclear Science (NS-27), 172 (1980).

[30] D. R. Slaughter *et al.*, Nuclear Instruments and Methods in Physics Research B. **241**, 771 (2005).

[31] E. T. E. Reedy, S. J. Thompson, and A. W. Hunt, Nuclear Instruments and Methods in Physics Research A **606**, 811 (2009).

[32] Woodworth, J. G. and McNeill, K. G. *et al.*, Physical Review, Part C, Nuclear Physics **19**, 1667 (1979).

Bibliography

[1] M. T. Kinlaw and A. W. Hunt, *Time dependence of delayed neutron emission for fissionable isotope identification*, Appl. Phys. Lett. **86**, 254104 (2005).

[2] D. R. Norman, J. L. Jones, W. Y. Yoon, K. J. Haskell, J. W. Sterbentz, J. M. Zabriskie, A. W. Hunt, F. Harmon and M. T. Kinlaw, *Inspection applications with higher electron beam energies*, Nucl. Inst. & Meth. in Phys. Res. **B 241**, 787 (2005).

[3] M. T. Kinlaw and A. W. Hunt, *Fissionable isotope identification using the time dependence of delayed neutron emission*, Nucl. Inst. & Meth. in Phys. Res. **A 562**, 1081 (2006).

[4] S. J. Thompson, M. T. Kinlaw, J. F. Harmon, D. P. Wells, E. B. Farfan and A. W. Hunt, *Utilization of high-energy neutron for the detection of fissionable materials*, Appl. Phys. Lett. **90**, 074106 (2007).

[5] D. R. Norman, J. L. Jones, B. W. Blackburn, K. J. Haskell, J. T. Johnson, S. M. Watson, A. W. Hunt, R. Spaulding and F. Harmon, *Time-dependent delayed signatures from energetic photon interrogations*, Nucl. Inst. & Meth. in Phys. Res. **B 261**, 316 (2007).

[6] J. L. Jones, B. W. Blackburn, S. M. Watson, D. R. Norman and A. W. Hunt, *High energy photon interrogation for nonproliferation applications*, Nucl. Inst. & Meth. in Phys. Res. **B 261**, 326 (2007).

[7] B. W. Blackburn, J. L. Jones, C. E. Moss, J. T. Mihalczo, A. W. Hunt, F. Harmon, S. M. Watson and J. T. Johnson, *High energy photon interrogation for nonproliferation applications*, Nucl. Inst. & Meth. in Phys. Res. **B 261**, 382 (2007).

[8] D. R. Norman, J. L. Jones, B. W. Blackburn, A. Fisher, S. M. Watson, K. J. Haskell, A. W. Hunt and M. Balzer, *Radiation safety aspects for pulsed photonuclear assessment techniques in outdoor operations*, Nucl. Inst. & Meth. in Phys. Res. **B 261**, 913 (2007).

[9] T. Gozani, *Active nondestructive assay of nuclear materials*, Tech. Rep. NUREG/CR-0602, United States Regulatory Commission, Washington D.C. U.S.A. (1981).

[10] C. L. Hollas, D. A. Close and C. E. Moss, *Analysis of fissionable material using delayed gamma rays from photofission*, Nucl. Inst. & Meth. in Phys. Res. **B 24-25**, 503 (1987).

[11] J. L. Jones, W. Y. Yoon, Y. D. Harker, J. M. Hoggan, K. J. Haskell and L. A. VanAusdein, *Proof of concept assessment of a photofission based interrogation system for the detection of shielded nuclear material*, Tech. Rep. INEEL/EXT 2000-01523, Idaho National Engineering and Environmental Laboratory, Idaho Falls, Idaho U.S.A. (2000).

[12] J. L. Jones, W. Y. Yoon, K. J. Haskell, D. R. Norman, J. M. Hoggan, C. E. Moss, C. A. Goulding, C. L. Hollas, W. L. Myers and E. Franco, *Photofission-based, nuclear material detection: Technology demonstration*, Tech. Rep. INEEL/EXT-02-01406, Idaho National Engineering and Environmental Laboratory, Idaho Falls, Idaho U.S.A. (2002).

[13] D. K. Wehe, H. Yang and M. H. Jones, *Observation of* ^{238}U *photofission products*, IEEE Trans. Nucl. Sci. **53**, 1430 (2006).

[14] *Preventing nuclear smuggling: DOE has made limited progress in installing radiation detection equipment at highest priority foreign seaports*, United States Government Accountability Office, Report No. GAO 06 389 (2005).

[15] *Combating nuclear smuggling: DHS has made progress deploying radiation detection equipment at u.s. ports of entry, but concerns remain*, United States Government Accountability Office, Report No. GAO 05 375 (2006).

[16] *2006 Quadrennial defense review*, United States Department of Defense (2006).

[17] G. W. Bush, *National security strategy of the United States of America*, Office of the President of the United States of America (2006).

[18] M. F. James, *Energy released in fission*, J. Nucl. Energy **23**, 517 (1969).

[19] M. F. James, *The useful energy released in the fission of* ^{232}Th, ^{233}U, ^{234}U, ^{236}U, ^{237}Np, ^{238}Pu, ^{240}Pu *and* ^{242}Pu, J. Nucl. Energy **25**, 513 (1971).

[20] M. T. Kinlaw, *Delayed Neutron Group Parameters from Photofission*, Ph.D. thesis, Idaho State University (2007).

[21] M. G. Silbert and J. C. Hopkins, *Beta decay of* N^{17} *to bound states of* O^{17}, Phys. Rev. **134**, B16 (1964).

[22] J. G. Woodworth, K. G. McNeill, J. W. Jury, R. A. Alvarez, B. L. Berman, D. D. Faul and P. Meyer, *Photonuclear cross sections for* ^{18}O, Phys. Rev. C **19**, 1667 (1979).

[23] L. A. Currie, *Limits for qualitative detection and quantitative determination*, Ann. Chem. **40**, 586 (1968).

[24] L. A. Kull, R. L. Bramblett, T. Gozani and D. E. Rundquist, *Delayed neutron from low energy photofission*, Nucl. Sci. Eng. **39**, 163 (1970).

[25] R. J. Tuttle, *Delayed-neutron data for reactor-physics analysis*, Nucl. Sci. Eng. **56**, 37 (1975).

[26] M. C. Brady and T. R. England, *Delayed neutron data and group parameters for 43 fissioning systems*, Nucl. Sci. Eng. **103**, 129 (1989).

[27] National Council on Radiation Protection and Measurements, *Radiation Protection for Particle Accelerators Facilities*, NCRP Report No. 144 (National Council on Radiation Protection and Measurements, Bethesda, Maryland U.S.A., 2003).

[28] E. T. E. Reedy, *Discrete γ-rays from Photofission for Nuclear Forensics Applications*, Ph.D. thesis, Idaho State University (2011).

[29] T. R. England and B. F. Rider, *Endf-349 evaluation and compilation of fission product yields 1993*, Tech. Rep. LA-UR-94-3106, Los Alamos National Laboratory, Los Alamos, New Mexico U.S.A. (1994).

[30] R. P. Gardner, E. Sayyed, Y. Zheng, S. Hayden and C. W. Mayo, *Nai detector neutron activation spectra for pgnaa applications*, Appl. Radiat. Isot. **56**, 37 (1975).

[31] E. S. Cárdenas, *Detection of Delayed Gamma Rays Using $Bi_4Ge_3O_{12}$ and NaI(Tl) Detectors for the Identification of Fissionable Materials*, Ph.D. thesis, Idaho State University (2009).

[32] M. Gmar, E. Berthoumieux, S. Boyer, F. Carrel, D. Doré, M. L. Giacri, F. Lainé, B. Poumarède, D. Ridikas and A. V. Lauwe, *Detection of nuclear material by photon activation inside cargo containers*, in G. Vourvopoulos and F. P. Doty, eds., *Non-Intrusive Inspection Technologies*, vol. 6213 of *Proc. of SPIE*, p. 62130F (SPIE, Bellingham WA, USA, 2006).

[33] E. B. Norman, S. G. Prussion, R. Larimer, H. Shugart, E. Browne, A. R. Smith, R. J. McDonald, H. Nitsche, P. Gupta, M. I. Frank and T. B. Gosnell, *Signatures of fissile materials: high-energy γ rays following fission*, Nucl. Inst. & Meth. in Phys. Res. **A 521**, 608 (2004).

[34] D. Slaughter, M. Accatino, A. Bernstein, J. Candy, A. Dougan, J. Hall, A. Loshak, D. Manatt, A. Meyer, B. Pohl, S. Prussin, R. Walling and S. Weirup, *Detection of special nuclear material in cargo containers using neutron interrogation.*, Tech. Rep. UCRL-ID-155315, Lawrence Livermore National Laboratory, Livermore, California U.S.A. (2003).

[35] E. T. E. Reedy, S. J. Thompson and A. W. Hunt, *The detection of delayed gamma-rays between intense bremsstrahlung pulses for discriminating fissionable from non-fissionable materials*, Nucl. Inst. & Meth. in Phys. Res. **A 606**, 811 (2009).

[36] M. B. C. et al., *Endf/b-vii.1 nuclear data for science and technology*, Nucl. Data Sheets **112**, 2887 (2011).

[37] R. B. Firestone and V. S. Shirley, *Table of Isotopes, 8th Edition* (John Wiley & Sons, Hoboken, New Jersey U.S.A., 1999).

[38] A. R. Poletti and J. G. Pronko, *Beta decay of* ^{17}N, Phys. Rev. C **8**, 1285 (1973).

[39] J. K. Tuli, *Evaluated nuclear structure data file*, Tech. Rep. BNL-NCS-51655-01/2-Rev, Brookhaven National Laboratory, Upton, New York U.S.A. (2001).

[40] V. McLane, *Exfor basics: A short guide to the reaction data exchange format*, Tech. Rep. BNL-NCS-63380-2000/5 Rev., Brookhaven National Laboratory, Upton, New York U.S.A. (2000).

[41] N. Soppera, M. Bossant, E. Dupont, H. Henrikson and Y. Rugama, *Recent upgrades to the nuclear data tool JANIS*, J. Korea Phys. Soc. **59**, 1329 (2011).

[42] A. J. Koning and D. Rochman, *Consistent TALYS based evaluated nuclear data library including covariance data*, Tech. Rep. JEFF-DOC 1262, Nuclear Research and Consultancy Group NRG, Petten, The Netherlands (2008).

[43] P. H. Gleick, *Water in Crisis: A guide to the World's Fresh Water Resources* (Oxford University Press, New York, NY U.S.A., 1993).

[44] P. A. Cox, *The Elements: Their origin, bundance and distribution* (Oxford University Press, New York, NY U.S.A., 1989).

[45] K. G. McNeill, J. W. Jury, M. N. Thompson, B. L. Berman and R. E. Pywell, $^{18}O(\gamma,pn+np)$ *cross section*, Phys. Rev. C **43**, 489 (1991).

[46] A. Veyssiére, H. Beil, R. Bergére, A. Leprêtre and A. D. Miniac, *A study of the photoneutron contribution to the giant dipole resonance of s-d shell nuclei*, Nucl. Phys. **A 227**, 513 (1974).

[47] D. Pelowitz (Ed.), *MCNPX User's Manual, Version 2.7.0*, Tech. Rep. LA-CP-11-00438, Los Alamos National Laboratory (2011).

[48] M. Fensin, Private Communication (2013).

[49] S. Mashnik and A. Sierk, *CEM03.03 User Manual*, Tech. Rep. LA-UR-12-01364, Los Alamos National Laboratory (2012).

[50] S. G. Mashnik, M. I. Baznat, K. K. Gudima, A. J. Sierk and R. E. Prael, *Extension of the CEM2k and LAQGSM Codes to Describe Photo-Nuclear Reactions*, Tech. Rep. LA-UR-05-2013, arXiv:nucl-th/0503061v2, Los Alamos National Laboratory (2005).

Department Of Defense

Defense Technical Information Center
8725 John J. Kingman Road, Suite 0944
Ft. Belvoir, VA 22060-6201
ATTN: DTIC/OCA

Defense Threat Reduction Information Analysis
Center 8725 John J. Kingman Road, Suite 0944
Ft. Belvoir, VA 22060-6201
ATTN: DTRIAC

Defense Threat Reduction Agency
8725 John J. Kingman Road
Ft. Belvoir, VA 22060-6201
ATTN: Dave Petersen